Fernando Bello
Stéphane Cotin (Eds.)

LNCS 5958

Biomedical Simulation

5th International Symposium, ISBMS 2010
Phoenix, AZ, USA, January 2010
Proceedings

Springer

Lecture Notes in Computer Science 5958

Commenced Publication in 1973
Founding and Former Series Editors:
Gerhard Goos, Juris Hartmanis, and Jan van Leeuwen

Editorial Board

David Hutchison
Lancaster University, UK
Takeo Kanade
Carnegie Mellon University, Pittsburgh, PA, USA
Josef Kittler
University of Surrey, Guildford, UK
Jon M. Kleinberg
Cornell University, Ithaca, NY, USA
Alfred Kobsa
University of California, Irvine, CA, USA
Friedemann Mattern
ETH Zurich, Switzerland
John C. Mitchell
Stanford University, CA, USA
Moni Naor
Weizmann Institute of Science, Rehovot, Israel
Oscar Nierstrasz
University of Bern, Switzerland
C. Pandu Rangan
Indian Institute of Technology, Madras, India
Bernhard Steffen
TU Dortmund University, Germany
Madhu Sudan
Microsoft Research, Cambridge, MA, USA
Demetri Terzopoulos
University of California, Los Angeles, CA, USA
Doug Tygar
University of California, Berkeley, CA, USA
Gerhard Weikum
Max-Planck Institute of Computer Science, Saarbruecken, Germany

Fernando Bello Stéphane Cotin (Eds.)

Biomedical Simulation

5th International Symposium, ISBMS 2010
Phoenix, AZ, USA, January 23-24, 2010
Proceedings

Springer

Volume Editors

Fernando Bello
Division of Surgery
Department of Surgery and Cancer
Imperial College London
St Mary's Hospital
London, UK
E-mail: f.bello@imperial.ac.uk

Stéphane Cotin
SHAMAN
INRIA Lille, Bâtiment IRCICA
Villeneuve d'Ascq, France
E-mail: stephane.cotin@inria.fr

Library of Congress Control Number: 2009943038

CR Subject Classification (1998): I.6, I.4, J.3, I.3

LNCS Sublibrary: SL 1 – Theoretical Computer Science and General Issues

ISSN 0302-9743
ISBN-10 3-642-11614-0 Springer Berlin Heidelberg New York
ISBN-13 978-3-642-11614-8 Springer Berlin Heidelberg New York

This work is subject to copyright. All rights are reserved, whether the whole or part of the material is concerned, specifically the rights of translation, reprinting, re-use of illustrations, recitation, broadcasting, reproduction on microfilms or in any other way, and storage in data banks. Duplication of this publication or parts thereof is permitted only under the provisions of the German Copyright Law of September 9, 1965, in its current version, and permission for use must always be obtained from Springer. Violations are liable to prosecution under the German Copyright Law.

springer.com

© Springer-Verlag Berlin Heidelberg 2010
Printed in Germany

Typesetting: Camera-ready by author, data conversion by Scientific Publishing Services, Chennai, India
Printed on acid-free paper SPIN: 12842872 06/3180 5 4 3 2 1 0

Preface

To celebrate its 5th edition, the International Symposium on Biomedical Simulation (ISBMS) was organized in conjunction with the International Meeting on Simulation in Healthcare (IMSH). IMSH is the premier simulation in healthcare meeting and largest single gathering of clinicians, educators, administrators and other simulation stakeholders. This unique link-up aimed at bringing together simulation users with those involved in its scientific and technological developments in order to foster closer interaction. The joint meeting was held in Phoenix, Arizona during January 23–24, 2010.

Biomedical modeling and simulation are at the center stage of worldwide efforts to understand and replicate the behavior and function of the human organism. The Physiome Project and Virtual Physiological Human (VPH) initiative aim to develop advanced computational models that will facilitate the understanding of the integrative function of cells, organs, and organisms, with the ultimate goal of delivering truly personalized medicine. At the same time, progress in real-time biomedical modeling and simulation has enabled more complex, interactive simulations, offering the possibility of highly sophisticated task trainers, procedural and patient simulators to support medical training and safer clinical practice. It is in this context that ISBMS seeks to act as an international forum for researchers in this increasingly important area to share their latest work, discuss future trends and forge new collaborations.

We received 41 full paper submissions from 13 different countries. Each was evaluated by at least three members of the Program Committee. Based on these reviews, 19 manuscripts were selected for oral presentation in single track. The manuscripts are organized in four thematic sections covering some of the key aspects of biomedical simulation: soft tissue properties, modeling and segmentation, simulation of biophysical processes and real-time interactive simulation.

The geographical breakdown of the different institutions presenting their research was: Australia, Canada, China, Denmark, France, Switzerland, UK and USA. The quality, diversity and geographical spread of the contributions are a strength of the symposium as it continues to be an important forum for researchers in this field.

In addition to contributed papers, the symposium included discussion panels on model parameter estimation and advances in GPU-based simulation. The panels were chaired by Yohan Payan and Jesper Moosegard, and presented an opportunity to explore in more detail the principles, applications, implementation, and future developments in these two important areas. Steve Dawson gave a keynote presentation on bridging the gap between biomedical simulation scientists / engineers and simulation stakeholders, while Marco Viceconti discussed the Virtual Physiological Human initiative, its importance and implications for biomedical simulation research.

We are extremely grateful to the Program Committee members for volunteering their time to review and discuss symposium papers and doing so in a timely and professional manner. We are also thankful to the Steering Committee for their support in continuing the tradition of a high-quality, focused meeting. Special thanks go to the IMSH organizers and SSH Board for supporting the IMSH - ISBMS link up. The meeting would not have been possible without the help of the ISBMS 2010 Organizing Committee who worked hard to make the event a success. Last but not least, we thank all the authors who submitted their work to ISBMS, and in particular those who shared their work at the symposium. It was a pleasure organizing ISBMS 2010 and we hope that all participants enjoyed the intense and stimulating discussions, as well as the opportunity to renew existing interactions and establish new ones.

January 2010

Fernando Bello
Stéphane Cotin

Organization

The 5th International Symposium on Biomedical Simulation ISBMS 2010 was organized by the department of Biosurgery and Surgical Technology, Imperial College London, and the SHAMAN Group, INRIA Lille North Europe.

ISBMS 2010 would not have been possible without the dedication and hard work of the Organizing Committee: Jérémie Dequidt, Alejandro Granados and Vincent Luboz. We acknowledge the help and contribution of the Department of Biomedical Informatics at the Arizona State University, in particular Jianming Liang and Kanav Kahol who kindly helped with local organisation.

Steering Committee

Fernando Bello, Chair	Imperial College London, UK
Stéphane Cotin, Co-chair	INRIA, France
Nicholas Ayache	INRIA, France
Steve Dawson	CIMIT, USA
Hervé Delingette	INRIA, France
Matthias Harders	ETH Zurich, Switzerland
Dimitris Metaxas	Rutgers University, USA
Gábor Székely	ETH Zurich, Switzerland

Program Committee

Remis Balaniuk	CU Brasilia, Brazil
Cagatay Basdogan	KOC University, Turkey
Elías Cueto	Zaragoza University, Spain
Jérémie Dequidt	INRIA, France
James Duncan	Yale University, USA
Christian Duriez	INRIA, France
Eddie Edwards	Imperial College London, UK
Alejandro Frangi	Pompeu Fabra University, Spain
Miguel A. González Ballester	Alma IT Systems, Spain
Derek Gould	University of Liverpool, UK
Vincent Hayward	McGill University, Canada
Karl Heinz Höhne	University Hospital Hamburg, Germany
Arun Holden	Leeds University, UK
David Holmes	Mayo Clinic, USA
Roy Kerckhoffs	UC San Diego, USA
Vincent Luboz	Imperial College London, UK
Edoardo Mazza	ETH Zurich, Switzerland
Michael Miga	Vanderbilt University, USA

Karol Miller	University of Western Australia
Paul Neumann	CIMIT, USA
Wiro Niessen	Erasmus MC Rotterdam, The Netherlands
Mark Ottensmeyer	CIMIT, USA
Sébastien Ourselin	University College London, UK
Dinesh Pai	University of British Columbia, Canada
Yohan Payan	University Joseph Fourier, France
James D. Rabinov	Massachusetts General Hospital, USA
Joseph T. Samosky	University of Pittsburgh, USA
Luc Soler	IRCAD, France
Thomas S. Sørensen	Århus University, Denmark
Pascal Swider	University of Toulouse, France
Dominik Szczerba	ETH Zurich, Switzerland
Frank Tendick	UC San Francisco, USA
Daniel Thalman	EPFL, Switzerland
Mark Thiriet	INRIA, France
Jocelyne Troccaz	University Joseph Fourier, France
Marco Viceconti	Instituto Ortopedico Rizzoli, Italy
Pierre-Frédéric Villard	University Henri Poincaré, France
Simon Warfield	Harvard and Childrens Hospital, USA
Xunlei Wu	Renci, USA
Guang-Zhong Yang	Imperial College London, UK

Table of Contents

Soft Tissue Properties

LASTIC: A Light Aspiration Device for *in vivo* Soft TIssue Characterization 1
Patrick Schiavone, Emmanuel Promayon, and Yohan Payan

Characterization of Suction and CUSA Interaction with Brain Tissue . . . 11
Di Jiang, Nusrat Choudhury, Vincent Mora, and Sébastien Delorme

Evaluation of a Technique to Estimate the Compliance of Atherosclerotic Intima 20
Hamed Azarnoush, Guy Lamouche, Charles-Etienne Bisaillon, Christian Degrandpre, and Benoit Boulet

Quantifying Mechanical Properties in a Murine Fracture Healing System Using an Inverse Geometric Nonlinear Elasticity Modeling Framework 29
Michael I. Miga, Jared A. Weis, Froilan Granero-Molto, and Anna Spagnoli

Modeling and Segmentation

Optimization of Case-Specific Vascular Tree Models Based on Vessel Size Imaging 38
Bryn A. Lloyd, Sven Hirsch, and Gábor Székely

Efficient Generation of Corresponding Meshes for Biomedical Flow Simulations 49
Robert H.P. McGregor, Bryn A. Lloyd, Dominik Szczerba, and Gábor Székely

Solid Mesh Registration for Radiotherapy Treatment Planning 59
Karsten Østergaard Noe and Thomas Sangild Sørensen

Physics-Based Modeling of the Pregnant Woman 71
Juan Pablo de la Plata Alcalde, Lazar Bibin, Jérémie Anquez, Tamy Boubekeur, Elsa Angelini, and Isabelle Bloch

Semi-automatic Segmentation of Fractured Pelvic Bones for Surgical Planning 82
Jürgen Fornaro, Gábor Székely, and Matthias Harders

Simulation of Biophysical Processes

Development of a Computer Simulation Tool for Application in Adolescent Spinal Deformity Surgery ... 90
J. Paige Little and Clayton Adam

A Fluid-Structure Interaction Index of Coronary Plaque Rupture ... 98
Olusegun Ilegbusi and Eric Valaski-Tuema

Biomechanical Simulation of Human Eye Movement ... 108
Qi Wei, Shinjiro Sueda, and Dinesh K. Pai

A Theoretical Model for RF Ablation of Kidney Tissue and Its Experimental Validation ... 119
Mihaela Pop, Sean R.H. Davidson, Mark Gertner, Michael A.S. Jewett, Michael D. Sherar, and Michael C. Kolios

A Point-Based Simulation Framework for Minimally Invasive Surgery ... 130
Bo Zhu, Lixu Gu, Xiaopeng Peng, and Zhe Zhou

Real-Time Interactive Simulation

Six Degree-of Freedom Haptic Rendering for Dental Implantology Simulation ... 139
Cédric Syllebranque and Christian Duriez

Haptic Simulator for Prostate Brachytherapy with Simulated Ultrasound ... 150
Orcun Goksel and Septimiu E. Salcudean

A Shell Model for Real-Time Simulation of Intra-ocular Implant Deployment ... 160
Olivier Comas, Stéphane Cotin, and Christian Duriez

Endovascular Guidewire Flexibility Simulation ... 171
Vincent Luboz, Jianhua Zhai, Peter Littler, Tolu Odetoyinbo, Derek Gould, Thien How, and Fernando Bello

Comparing Automatic Simulator Assessment with Expert Assessment of Virtual Surgical Procedures ... 181
Stefan Tuchschmid, Michael Bajka, and Matthias Harders

Author Index ... 193

LASTIC: A Light Aspiration Device for *in vivo* Soft TIssue Characterization

Patrick Schiavone[1,2], Emmanuel Promayon[2], and Yohan Payan[2,3]

[1] Laboratoire des Technologies de la Microelectronique CNRS, 17 rue des Martyrs,
38054 Grenoble, France
`patrick.schiavone@cea.fr`
[2] TIMC-IMAG Laboratory, UMR CNRS 5525 and University Joseph Fourier,
Pavillon Taillefer, Faculte de Medecine 38700 La Tronche, France
`Emmanuel.Promayon@imag.fr`
`http://www-timc.imag.fr/Emmanuel.Promayon/`
[3] PIMS, UMI CNRS 3069, University of British Columbia,
Vancouver BC, V6T 1Z2, Canada
`Yohan.Payan@imag.fr`
`http://www-timc.imag.fr/Yohan.Payan/`

Abstract. This paper introduces a new Light Aspiration device for *in vivo* Soft TIssue Characterization (LASTIC). This device is designed to be used during surgery, and can undergo sterilization. It provides interactive-time estimation of the elastic parameters. LASTIC is a 3cm x 3cm metallic cylinder divided in two compartments. The lower compartment is a cylindrical chamber made airtight by a glass window in which a negative pressure can be applied. Put in contact with soft tissues, it can aspirate the tissues into the chamber through a circular aperture in its bottom side. The upper compartment is clinched onto the lower part. A miniature digital camera is fixed inside the upper chamber, focusing on the aspirated soft tissue. LASTIC is operated by applying a range of negative pressures in the lower compartment while measuring the resulting aspirated tissue deformations with the digital camera. These measurements are used to estimate the tissue elasticity parameters by inverting a Finite Element model of the suction experiment. In order to use LASTIC during surgical interventions, a library-based optimization process is used to provide an interactive time inversion.

1 Introduction

Physically based models are now widely used in the field of biomedical engineering, to represent human organs' geometrical and mechanical behavior. These models are mostly used to better understand and validate a given surgical treatment, to model physiological behaviour or to provide virtual simulators for clinicians. While virtual simulators were mostly limited to a single preset model, applications such as Computer Assisted Planning and Computer Aided Surgery sparked the need for patient-specific models. In order to precisely model and

F. Bello and S. Cotin (Eds.): ISBMS 2010, LNCS 5958, pp. 1–10, 2010.
© Springer-Verlag Berlin Heidelberg 2010

simulate a patient's organ or tissue, a specific geometry and a specific biomechanical model of the patient's organ or tissue has to be generated. This implies to build a conforming mesh of the patient's organ geometry, choose the appropriate constitutive law and extract the proper mechanical parameters from the patient tissue.

Organ geometries are in general reconstructed from patient medical image data, such as computed tomography or magnetic resonance imaging. The mechanical behaviors depend on the deformable model parameters, e.g. the spring stiffness in discrete mass-spring models or the constitutive equation in Finite Element models. These parameters are often inferred from image-based deformation measurements (elastography) or experimental mechanical excitations on *ex vivo* or *in vivo* tissues. Mechanical experiments are generally performed on *ex vivo* tissue samples using mainly indentation/stretching devices that exert a stress onto a passive tissue and record its corresponding deformations [1]. With a precise control of the tissue sample size and of the external force directions and intensities, these experiments can provide reliable stress/strain curves, or even determine some tissue anisotropy.

The stress/strain laws provided by experiments on *ex vivo* tissues are very useful for virtual simulators as they mostly need average values for the elastic parameters. The same holds true for other applications such as computer aided planning since getting patient-specific *in vivo* measurements is extremely complex. However, it has clearly been shown ([2],[3]) that the mechanical behavior of soft tissue can differ significantly between *in vivo* and *ex vivo* conditions for a number of reasons, including the vascularization of the tissue and the changes in the boundary conditions. Therefore, *in vivo* measurements seem almost mandatory to take into account patient specificities in Computer Assisted Planning and Surgery.

This paper aims at introducing the latest version of our *in vivo* suction device designed to be used in the context of Computer Assisted Surgery. This device takes into account the application constraints, i.e. full sterilization and interactive-time estimation of the tissues constitutive equations. By interactive time, we mean that the full process is not real time but is fast enough (less than a minute) to be used within the operation theater with no time penalty for the surgeon. The speed limiting factor is here the data acquisition, not the solution of the inverse problem of retrieving the mechanical parameters from the measured data. The next section provides a state of the art of the *in vivo* devices proposed in the literature while section 3 describes our suction device and explains how the constitutive equations are estimated in an interactive time. Section 4 provides some results for a clinical case. Section 5 ends the paper with a discussion and a conclusion.

2 In Vivo Devices: State of the Art

With the design of its Tissue Material Property Sampling Tool (TeMPeST), in parallel with Carter et al. [4], Mark Ottensmeyer [1] pioneered development of an indentation tool that could be used on *in vivo* tissues. The objective was to drastically reduce the size of the device in comparison with what is usually provided by commercial indentation machines. The TeMPeST is a $12\,mm$ diameter minimally invasive instrument, designed to investigate viscoelastic properties of solid material under small deformations. A $5\,mm$ right circular punch vibrates the material surface while recording applied load and relative displacement. Our lab bought a prototype of this device and tried to use it to characterize the elastic properties of tongue and cheek tissues. Despite the nice ergonomy and small size of the TeMPeST, we encountered important difficulties in estimating the elastic parameters of tongue and cheeks tissues. Indeed, it was almost impossible for the subjects to keep immobile while recording the force/displacements curves and of course impossible to stop the organ movements due to inner physiology such as blood flow and the corresponding beating movements. This leads to the loss of a fixed reference between the TeMPeST and the organs. The resulting measurements mixed the controlled TeMPeST punch as well as the organ natural displacements, which generated an error on the measured elasticity.

Other excitation methods including a robotic indenter [5], a torsion device [6] or a ballistometer [7] exist. It is, however, unclear whether the problem of relative displacements between the excitation tool and the organ could be eliminated by these methods. On the other hand, suction techniques provide a full link between the device and the organ that guarantees that there is no uncontrolled relative motion. The principle of suction methods is the measurement of organ elevation caused by the application of a partial vacuum via a circular aperture in a measuring probe. For most human soft tissues, the relevant range for the negative pressure is between $10\,mbar$ to $500\,mbar$. The deformation can be measured with an optical or ultrasound system. Starting from the pioneering work by Grahame and Holt [8], several authors proposed suction cups ([9], [10], [11]). Most devices were developed to be used on external tissues [12], some of them leading to commercial products designed specifically for dermatology market. Very few suction devices were developed and evaluated for tissues that are only reachable during surgery. To our knowledge, only the suction device of Vuskovic [9] was tested on the uterine cervix during surgery and more recently on the liver [13]. This is probably due to the rather drastic sterilization process needed for each ancillary that has to be used in the sterile field of the operation theater. Sterilization is carried out using very rigorous processes such as *(a)* steam under pressure, *(b)* heat or *(c)* chemicals under a liquid, gaseous or plasma form. The fragile parts of a measurement device can be easily damaged under these conditions, especially electronic parts such as sensors, actuators or circuitry which are not very resistant to such severe environments and conditions. Moreover, not only are the parts in close contact with the operating field to be fully sterilized, but also every pieces of the instrument which could come into contact with any projection of liquid during surgery. Design can deal with this to a certain extent. For example, the electronic parts of the suction device of Nava et al. [13] are not sterilized but are integrated in the system and the authors mention that they are never in direct contact with the patient.

We recently developed a suction device that is able to meet the very rigorous sterilization and handling process imposed during surgery [14]. The device, which has no electronic component, is simple, light and can be considered as an ancillary instrument. The deformation of the aspirated tissue is imaged via a mirror using an external camera. The device was used to provided some measurements on a patient brain during a neurosurgery (Figure 1).

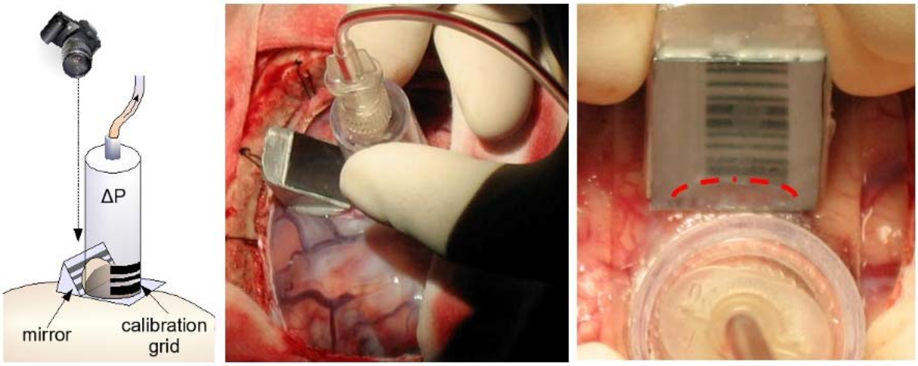

Fig. 1. Light suction device used to measure brain elasticity: Schematic view (a), intra-operative use (b), photo of the aspirated tissue reflected in the mirror (c) - (from [14])

This device was quantitatively evaluated on other organs such as tongue, cheeks and forearm skin. It appeared that the process needed to collect the photos from the camera, to measure the tissues elevation and to estimate the constitutive law was incompatible with an interactive-time use of the device. Such an interactive-time is needed in order to include soft-tissue modeling in Computer Assisted Surgery. In order to achieve interactive-time performance, improvements were sought in two area: *a)* the image capture and segmentation, and *b)* the elastic material parameter estimations. The following section describes these improvements and presents the latest version of our device.

3 Our New Suction Device

3.1 Device Description

The major drawback of the first version of the light suction device is that, since the camera is handheld, the camera optical axis is not always aligned with the mirror. Only the skill of the operator guarantees that the angular offset is close to zero therefore minimizing the parallax error in the aspired tissue height measurement. Another issue lies in the absence of synchronization between the image capture and the pressure measurement. Although the device is operated in static mode, several causes of short term ($< 2\, s$) pressure variation can occur and cause the pressure reading to be shifted in time with respect to the image capture. This turned out to be one of the major cause of error in the measurements performed until then.

The new Light Aspiration device for *in vivo* Soft TIssue Characterization (LASTIC) is designed to overcome these issues while keeping the suction cup as light as possible and maintaining compatibility with the sterilization process required by an intra operative use. The basic design is not very far from the one of Vuskovic [9] except for the compactness. This is a major advantage since it allows using the device even when the access to the tissue is limited in size. The light weight makes the device self positioned as soon as the negative pressure is applied. There is no need for a initial force exerted by the user to hold the suction cup in contact with the tissue. We use a 2 $Mpixel$ mobile phone camera sensor VS6750 from STMicroelectronics. Its overall size is 1 cm. We had it fitted inside a very compact cylindrical case (33 mm in height ×34 mm in diameter) that encloses both the camera and the mirror. A scheme and a picture of the full device can be seen in Figure 2.

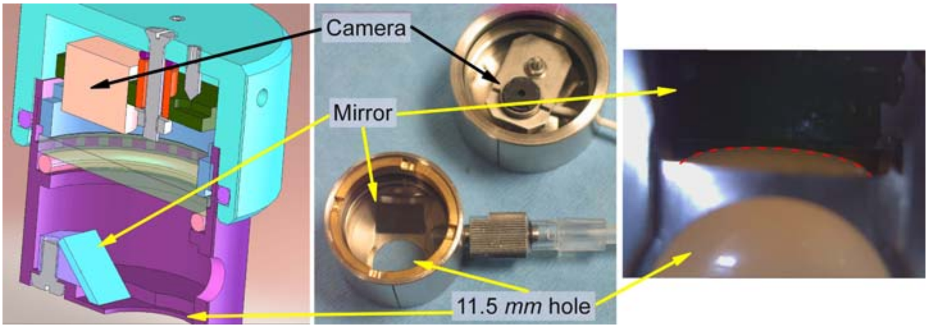

Fig. 2. LASTIC: scheme (left) and picture (center) of the new suction device. Example of an image captured by the camera during a depression of a PVC phantom (right).

It is made of two cylindrical parts that fit together. The lower part is fully passive, it encloses a 45 °mirror and its mount. Its bottom side is drilled with a 10 mm circular hole. A lateral hole equipped with a Luer-Lock connector allows application of a negative pressure to the suction cup. An airtight transparent polycarbonate window closes the top end of this cylinder. This part is expected to withstand the full sterilization treatment.

The upper part encloses the miniature camera and its mount as well as a Light Emitting Diode. The camera is precisely aligned with the mirror using a flexible adjustable mount. Proper focus setting is made by slightly screwing down or unscrewing the built-in camera lens mount. Due to the electronic components, this part cannot withstand elevated temperature. It can be sterilized either using a gas or liquid treatment thanks to a specifically designed air-tight cap that hermetically seals this part. When assembled, both parts constitute an airtight case that is put in contact with the tissues.

In addition to the hardware part of the device, we also significantly improved the data collection as well as the control of the negative pressure and its synchronization with the image capture. The negative pressure is applied using a syringe handled by a software-driven calibrated push-syringe. Since the pressure application is static, there is no pressure lag between the reading from the manometer and the suction cup. We also check for a steady reading from the manometer, which is an indication that no leak occurs. A software program controls the application of the negative pressure, the pressure measurement from an interfaced manometer as well as the synchronisation with the image acquisition. Each one of the three digitally interfacable instruments is connected to the data acquisition board of a laptop computer. A typical measurement takes less than ten seconds during which the pressure is decreased step by step and an image is taken at each step, synchronized with the pressure acquisition from the manometer.

The design of the new suction cup with a built-in miniature camera as well as a fully computer controlled user interface addresses the two major issues of the first version of our aspiration device. The alignment of the camera and the mirror is fixed and once aligned during the initial assembly of the cup, it does not need to be adjusted again. The synchronization of the pressure measurement with the image acquisition is guaranteed by the software controlled data acquisition.

3.2 Interactive-Time Estimation of the Constitutive Equation

The measurements provided by the LASTIC device are used to estimate the tissue elasticity parameters by inverting a Finite Element model of the suction experiment. The aim of this device is to be used *in vivo* in a context of Computer Assisted Surgery. This requires the solution of the inverse problem to be obtained in a very short time of the order of seconds. Since there is no rigorous mathematical solution of the inverse problem, our problem can boil down to a parametric non-linear optimization scheme. The unknown parameters are the coefficients of the mechanical constitutive law. Multiple schemes can be used to solve this optimization problem. The typical time of a Finite Element Model simulation of the suction experiment for one negative pressure value (which we will call the “direct problem”) is approximately 25 seconds on a workstation (Intel Core 2 Quadri-processor Q6600). The exact conditions for the FEM simulation are detailed in [14]. Depending on the initial values, a standard optimization routine would need to run the direct problem several tens to several hundreds times with different parameter values before converging to the best set of parameters. The same order of magnitude holds if a global optimization routine such as a genetic algorithm or simulated annealing is used. Needless to say that the time needed to achieve a single optimization is far beyond the time allotted to this constitutive law determination during a computer assisted surgical intervention. That is the reason why we focussed our attention on a library-based method. The library method proves to be very successful whenever an optimization is required of a problem with a computer intensive direct problem. For example it is widely used to solve the inverse problem of electromagnetic diffraction in the so called scatterometry technique which is a nanometer scale dimensional metrology in the field of microelectronic technology [15]. Other strategies exist that consist of making in advance a large number of time consuming direct problem computations, potentially coupled with a form of preprocessing then restricting the final search of the solution to a much simpler analytical or semianalytical problem. Surface response and neural network approaches are among those. Each one has its own pro and cons, we chose to use the simplest, yet brute force method of the library search.

The choice of the constitutive law as well as the detailed description of the Finite Element simulations have been presented in a previous paper [14], therefore we will not go in great detail here. Note that in order to avoid edge effects during the FEM resolution, the tissue depth should be more than 4 to 5 times the size of the aspiration hole, i.e. about $5\,cm$. Should the tissue be non homogeneous, this could be accounted for in the FEM model at the expense of a larger number of parameters and increased computation time. However, the type of inhomogeneity cannot be completely unknown, a priori knowledge has to be used in order for the FEM model to be described and parameterized. In light of the nonlinear stress-strain relationships given by our previous suction measurements on the brain, the medium was assumed to be an isotropic homogeneous and hyperelastic continuum. We selected a two-parameter Mooney-Rivlin strain-energy function, W, using only the first and third power of the first invariant of the right Cauchy-Green strain tensor. A best fit between the experimental data and the results from the calculation of the deformation vs negative pressure curve was used to determine the material constants a_{10} and a_{30}. In the library method, the calculations are performed in advance and at the time of the measurement, the results are looked up in a file where the computed results have been stored. It can take hours to generate the database, but it takes less than one second to find the best set of parameters in the library. This makes the use in an intra-operative environment fully viable. However, pressure variation is achieved step by step. The simple aspiration control set-up does not allow for dynamic pressure control and dynamic tissue response measurements. All measurements are therefore considered to be fully static.

4 Results

The LASTIC device has not been used yet for an intra-operative use. It was only evaluated in our lab with measurements on tongue and skin elasticities. Compared to the first version of our device described in [14], LASTIC proved much easier to use and install. In addition, the interactive-time estimation of the tissues constitutive equations is a major improvement.

A first quantitative evaluation of this inverse procedure was performed by comparing the results given by the optimization process conducted in Ansys software (Ansys 10 software, Ansys, Inc., Cannonsburg, PA) and by our library based optimization process. The brain measurements described in [14] were used. In Ansys, an advanced zero-order method, which only requires the dependent

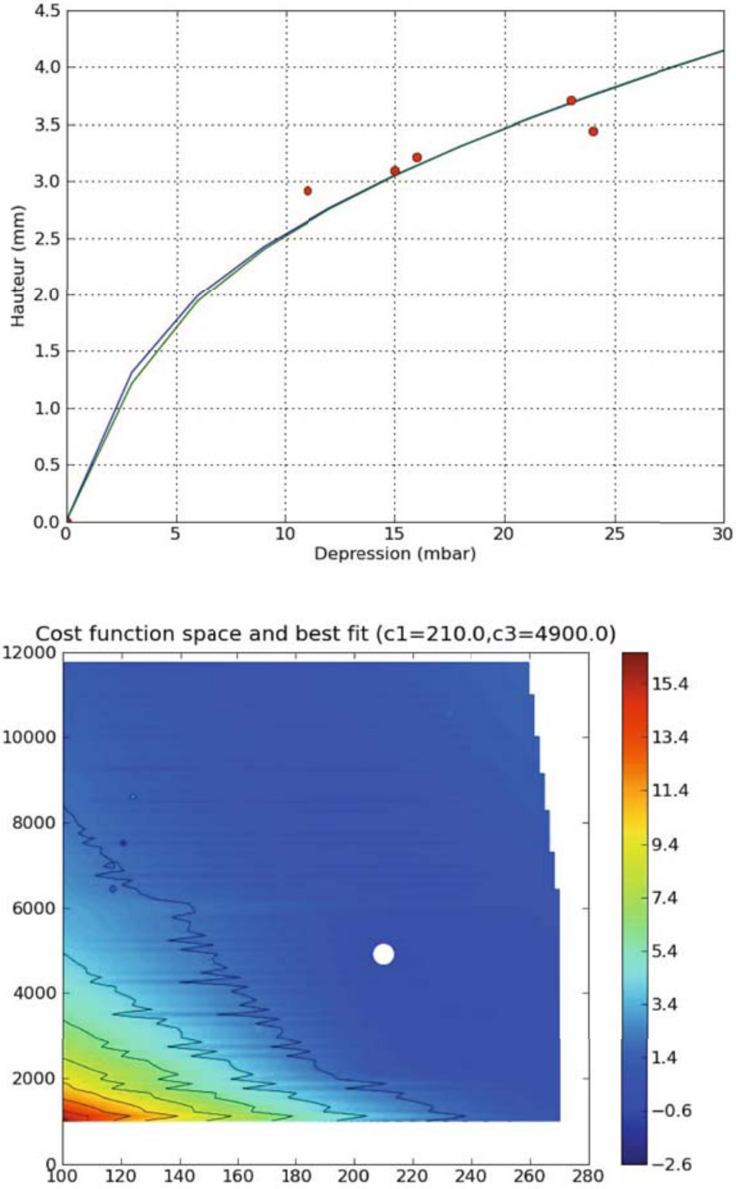

Fig. 3. Comparison of the simulation results for the optimal constitutive laws given by Ansys and by our library-based optimization process, superimposed with measurements points (top). Value of the optimization cost function (least mean square) for the (a_{10}, a_{30}) considered range for the brain tissues characterization (bottom). The white circle corresponds to the local minima found by our method.

variable values, and not their derivatives (Subproblem approximation method), found the optimal values of $a_{10} = 240$ and $a_{30} = 3420$. Our library-based optimization process found $a_{10} = 210$ and $a_{30} = 4900$. The two constitutive laws are not significantly dissimilar in the pressure range considered (Figure 3, top). Furthermore, the cost-function space is rather smooth and free of local minima (Figure 3, bottom).

The computation times are hardly comparable as our optimization takes less than one second to find the best parameters.

5 Discussion/Conclusion

This paper introduced the latest version of our Light Aspiration device for *in vivo* Soft TIssue Characterization (LASTIC). Most of the constraints due to an intra-operative use have been taken into account, with a special focus on the sterilization process and on the interactive time estimation of the elastic parameters. The library search inverse method has been proposed to estimate the tissues constitutive laws and was quantitatively compared with a full optimization direct method based on Ansys Software. Starting from data collected on brain tissues, both methods lead to very similar constitutive laws that match the *in vivo* measurements. A full validation of the device and inversion method is ongoing that includes an estimation of the errors in the parameter determination as well as a comparison with other more conventional rheology instruments. This is first conducted on model materials such as elastomers or hydrogels.

Acknowledgement

The authors wish to thank T. Boudou and J. Ohayon for their contribution to this work, especially the discussion about the aspiration experiment and model inversion.

References

1. Ottensmeyer, M.P.: Minimally invasive instrument for in vivo measurement of solid organ mechanical impedance. PhD thesis, Massachusetts Institute of Technology. Dept. of Mechanical Engineering (2001)
2. Gefen, A., Margulies, S.: Are in vivo and in situ brain tissues mechanically similar? J. Biomech. 37(9), 1339–1352 (2004)
3. Kerdok, A.E., Ottensmeyer, M.P., Howe, R.D.: Effects of perfusion on the viscoelastic characteristics of liver. J. Biomech. 39(12), 2221–2231 (2006)
4. Carter, F.J., Frank, T.G., Davies, P.J., McLean, D., Cuschieri, A.: Measurements and modelling of the compliance of human and porcine organs. Med. Image Anal. 5(4), 231–236 (2001)
5. Samur, E., Sedef, M., Basdogan, C., Avtan, L., Duzgun, O.: A robotic indenter for minimally invasive measurement and characterization of soft tissue response. Med. Image Anal. 11(4), 361–373 (2007)

6. Agache, P.G., Monneur, C., Leveque, J.L., Rigal, J.D.: Mechanical properties and young's modulus of human skin in vivo. Arch. Dermatol. Res. 269(3), 221–232 (1980)
7. Jemec, G.B., Selvaag, E., Agren, M., Wulf, H.C.: Measurement of the mechanical properties of skin with ballistometer and suction cup. Skin Res. Technol. 7(2), 122–126 (2001)
8. Grahame, R., Holt, P.J.: The influence of ageing on the in vivo elasticity of human skin. Gerontologia 15(2), 121–139 (1969)
9. Vuskovic, V.: Device for in-vivo measurement of mechanical properties of internal human soft tissues. PhD thesis, ETH Zürich (2001)
10. Diridollou, S., Patat, F., Gens, F., Vaillant, L., Black, D., Lagarde, J.M., Gall, Y., Berson, M.: In vivo model of the mechanical properties of the human skin under suction. Skin Res. Technol. 6(4), 214–221 (2000)
11. Mazza, E., Nava, A., Bauer, M., Winter, R., Bajka, M., Holzapfel, G.A.: Mechanical properties of the human uterine cervix: an in vivo study. Med. Image Anal. 10(2), 125–136 (2006)
12. Wang, Q., Kong, L., Sprigle, S., Hayward, V.: Portable gage for pressure ulcer detection. In: Engineering in Medicine and Biology Society, 2006. EMBS 2006. 28th Annual International Conference of the IEEE, pp. 5997–6000 (2006)
13. Nava, A., Mazza, E., Furrer, M., Villiger, P., Reinhart, W.H.: In vivo mechanical characterization of human liver. Med. Image Anal. 12(2), 203–216 (2008)
14. Schiavone, P., Chassat, F., Boudou, T., Promayon, E., Valdivia, F., Payan, Y.: In vivo measurement of human brain elasticity using a light aspiration device. Med. Image Anal. 13, 673–678 (2009)
15. Niu, X., Jakatdar, N., Bao, J., Spanos, C.J.: Specular spectroscopic scatterometry. IEEE Transactions on Semiconductor Manufacturing 14(2), 97–111 (2001)

Characterization of Suction and CUSA Interaction with Brain Tissue

Di Jiang, Nusrat Choudhury, Vincent Mora, and Sébastien Delorme

Industrial Materials Institute - National Research Council, Canada
`di.jiang@imi.cnrc-nrc.gc.ca`

Abstract. Basic and ultrasonic aspirators are the most commonly used surgical devices in neurosurgery. In this study, a tissue removal model was adjusted to experimental results of interaction between ultrasonic aspiration and brain tissue-mimicking material. Tissue grasping with a basic aspirator was also further investigated on fresh calf brain tissue obtained from several animals. Tests were conducted on both grey and white matter. The simulation screenshots, compared with the experimental photos, are presented to demonstrate the results.

1 Introduction

Surgical aspirators are one of the most widely used surgical devices in neurosurgery [1,2,3]. Reports on the interaction of aspirators with tissue are scarce and do not provide enough information to develop a suitable model for simulation purposes [4,5,6]. Surgical aspiration is achieved using suction through a tube. The tube includes a keyhole allowing for vacuum pressure to be controlled by the surgeon's thumb. This basic aspirator has three main functions: (1) it can remove liquids, such as blood or cerebrospinal fluid [7]; (2) at low vacuum pressure it can grasp soft tissue [1]; (3) at higher vacuum pressure it can remove some soft tissues [8].

Ultrasonic aspirators, such as the Cavitron Ultrasonic Surgical Aspirator (CUSA) which is commonly used in neurosurgery, are also used to remove tissue that is too stiff to remove with a basic aspirator mentioned above. A general overview of the ultrasound technology in surgery is given in [9]. Briefly, the ultrasonic aspirator differs from the basic aspirator in its ability to generate a high frequency vibration, which liquefies soft tissues in the vicinity of its tip. The liquefied tissue is then removed with vacuum pressure inside the tip. Irrigation is used for tool tip cooling and tissue select allows the surgeon to selectively fragment tissue based on its stiffness. A console is used to control CUSA parameters: vibration amplitude, vacuum pressure, irrigation and tissue select. Unlike the basic aspirator, the CUSA is not used for tissue grasping. It is solely used for the removal of liquids and soft tissues.

A mathematical model of interaction between soft tissue and a basic aspirator has been proposed [10]. This model, comprised of three equations, predicts the

F. Bello and S. Cotin (Eds.): ISBMS 2010, LNCS 5958, pp. 11–19, 2010.
© Springer-Verlag Berlin Heidelberg 2010

grasping and tissue removal behavior of the tool: First, the profile of the grasped tissue in the vicinity of the tool tip is given by

$$||\boldsymbol{u}(r)|| = \frac{h^2}{h + \alpha r^3} \tag{1}$$

where $h = ||\boldsymbol{u}(0)||$, r is the distance between a point on the plane $\mathcal{P}$ tangent to the undeformed tissue surface and the projection of the tool tip center $\boldsymbol{c}$ on that plane, and α is a material parameter (see figure 1).

Second, the reaction force applied by the grasped tissue to the tool tip is given by

$$f(h) = -\beta h^2 \boldsymbol{n} \tag{2}$$

where β is a material parameter and $\boldsymbol{n}$ is a unit vector normal to the plane tangent to the undeformed surface.

Third, the tissue removal behavior of the tool is given by

$$F_{new}(\boldsymbol{x}) = \min(F_{old}(\boldsymbol{x}), ||\boldsymbol{x} - \boldsymbol{t}|| - D/2) \tag{3}$$

where $F_{new}(\boldsymbol{x})$ and $F_{old}(\boldsymbol{x})$ are the current and previous values of the zero iso-surface of a distance field defining the tissue boundary, $\boldsymbol{x}$ is a point in space, $\boldsymbol{t}$ is the position of the tool tip and D is the diameter of a cutting sphere.

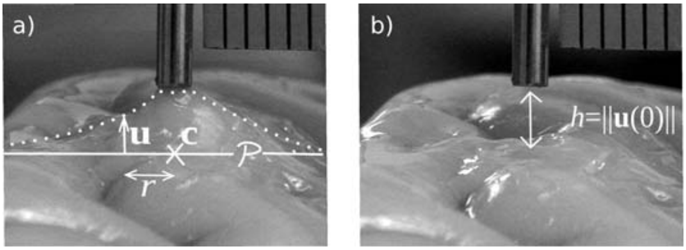

Fig. 1. Definition of h, $\boldsymbol{u}$, r and $\boldsymbol{c}$ in the model [10]

The first objective of this study is to adapt the proposed tissue removal model to the ultrasonic aspirator. Specifically, the parameter D of equation 3 was not characterized and it is likely to depend on tool settings for the ultrasonic aspirator. A second objective is to address some of the limitations discussed in the study [10] such as the fact that the grasping model was adjusted to experimental data obtained from a single specimen of a thawed calf brain and was limited to grey matter. In this study, the proposed grasping model will be characterized on fresh brain tissue obtained from several animals. Furthermore, the behavior of both grey and white matter will be investigated, as there is experimental evidence that the mechanical response differs between grey and white matter [11,12].

2 Methodology

2.1 Tissue Removal

Access to the ultrasonic aspirator was granted to the investigators in this study with the restriction that it be used only on non-biological materials. As such, tissue-mimicking phantoms as in [10] (12.5% mass concentration dessert gelatin) were used in the tissue removal tests with the ultrasonic aspirator. The CUSA EXcel^{TM} system (Radionics, Burlington, MA) with a 36 kHz handpiece was used. The measured tool tip inner diameter was 0.94 mm. The maximum amplitude according to the manufacturer's specifications was 210 μm, and the maximum vacuum pressure was -660 $mmHg$. The tests were carried out for each combination of three levels of vacuum pressure (10%, 30% and 60%) and three levels of vibration amplitude (10%, 30% and 60%), all expressed as a percentage of the maximum. Each test was done three times. The maximum setting was also tested once. The irrigation was held constant at a rate of 2 cc/minute. The tissue select was set for "standard". Each test was conducted using the following methodology:

1. The material sample was positioned on a movable platform underneath a CUSA (which was held at a fixed position and pointing down).
2. A combination of vacuum pressure and vibration amplitude was selected.
3. The platform was raised until the sample either completely obturated the tube tip or was sucked in by the vacuum pressure.
4. The platform was lowered to its original position once tissue was no longer removed.
5. The diameter of the resulting pit on the tissue surface was measured.

The pit diameter was modeled using the following non-linear model:

$$D(p, A) = c_1 + c_2 p + c_3 A + c_4 p A \tag{4}$$

where p is the vacuum pressure (in percentage of maximum), A is the vibration amplitude (in percentage of maximum) and c_i are parameters that are dependent on material properties and tool tip geometry. They were adjusted to the experimental data using the multiple regression module of NCSS statistical software. The coefficient of determination (R^2) was used as a fitting criterion.

2.2 Tissue Grasping

Brains from three calves were obtained from a slaughterhouse, transported in phosphate buffered saline (PBS) and tested within three hours of harvesting for each experiment. Each brain was cut in two hemispheres and the brain stem was removed, while preserving pia mater. One hemisphere per animal was used in the grasping tests.

The grasping tests were carried out with the basic aspirator using a similar setup and methodology as described in [10], shown in figure 2. The tests

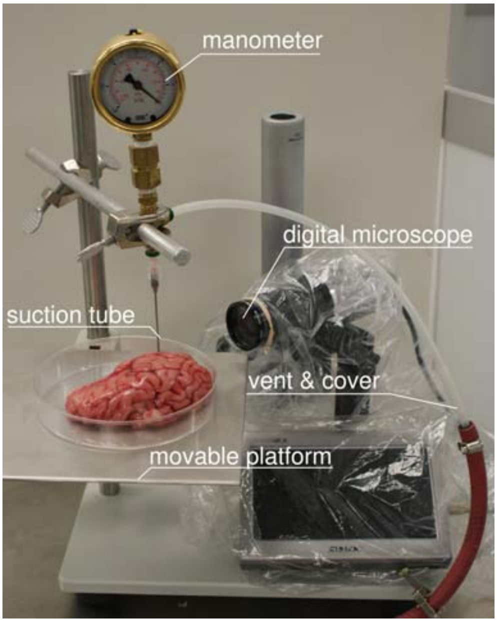

Fig. 2. Experimental setup

were conducted on the surface of the three brain hemisphere specimens at room temperature. Each specimen was kept moist with repeat PBS irrigation. The behavior of grey matter covered by pia mater was measured on 11-21 areas along the convexity of the brain.

The pia mater was then grasped and lifted at a sulcus. In these areas the pia mater is less adhering to the brain tissue. An incision was made using microscissors. The pia mater was gently peeled away from the surface of the brain tissue. Only areas with no visible damage were used for testing. The tests were repeated on 4-7 areas of exposed grey matter. The hemisphere was then flipped over to repeat the test on 5-10 areas of the white matter.

Grasping tests were not performed with the ultrasonic aspirator. It was assumed that when vibration is off, the ultrasonic aspirator behaves like a basic aspirator.

3 Results

Pit diameters in the gelatin specimens are presented in table 1 with respect to vacuum pressure and vibration amplitude. After excluding one outlier (observation 15), a model (equation 4) yielding $R^2 = 0.784$ was obtained with $c_1 = 2.6$, $c_2 = 0.052$, $c_3 = -0.0024$ and $c_4 = -0.00030$.

Figure 3 shows the predicted pit diameter plotted against the observed pit diameter values.

Table 1. Experimental tissue removal results on gelatin with CUSA

Obs.	Vacuum pressure (%)	Vibration amplitude (%)	Pit diameter (mm)
1	10	10	2.8
2	10	10	3.1
3	10	10	3.2
4	10	30	2.8
5	10	30	2.9
6	10	30	3.0
7	10	60	3.0
8	10	60	3.1
9	10	60	2.9
10	30	10	4.3
11	30	10	4.2
12	30	10	3.6
13	30	30	3.5
14	30	30	3.5
15	30	30	2.3
16	30	60	3.4
17	30	60	3.7
18	30	60	3.7
19	60	30	6.0
20	60	30	5.6
21	60	30	5.0
22	60	60	3.6
23	60	60	3.7
24	60	60	3.9
25	100	100	5.0

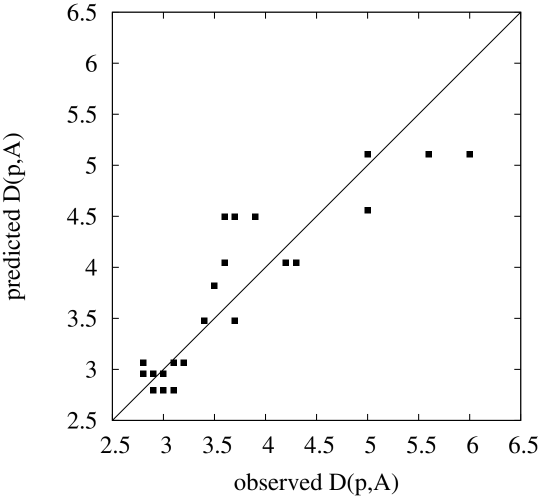

Fig. 3. Predicted vs observed pit diameter (see equation 4)

Deformation profiles $||\boldsymbol{u}||$ as a function of r are shown in figure 4 (a, c, e) for the three tissue types. The deformation profile material parameter (α) was determined for each type of tissue by fitting the experimental data with equation 1, where $\alpha_{\text{grey matter with pia}} = 0.234$ with $R^2 = 0.973$, $\alpha_{\text{grey matter}} = 0.922$ with $R^2 = 0.897$ and $\alpha_{\text{white matter}} = 1.361$ with $R^2 = 0.927$.

The tissue grasping force on the tool tip as a function of h is plotted in figure 4 (b,d,f) for the three tissue types. Experimental results from [10] are also plotted for grey matter with pia. The largest force on each graph is the force at which tissue rupture was observed, i.e. 70 kPa for grey matter with pia, 11 kPa for grey matter without pia and 20 kPa for white matter. The reaction force material parameter β was determined for grey matter with pia by fitting the experimental data to equation 2 where $\beta_{\text{grey matter with pia}} = 0.005$ with $R^2 = 0.793$. A linear fit, $f(h) = -\beta h \boldsymbol{n}$, was also investigated, which resulted in a lower value of $R^2 = 0.774$.

4 Discussion

The goal of this study was to further characterize a neurosurgical aspirator model developed in a previous study [10]. Specifically, to define the tissue removal model according to ultrasonic aspirator tool settings and by characterizing the grasping behaviour of a basic aspirator with fresh tissue.

The previous tissue removal model was developed for a basic aspirator (equation 3) where the value of D (diameter of a cutting sphere) was defined as a material property. In this study, the model was adapted to the ultrasonic aspirator by characterizing the value of D based on two of the four tool settings: (1) vacuum pressure (2) vibration amplitude. Studies on ultrasonic aspirator interaction with tissue have shown conflicting results. It has been reported that only vibration amplitude has an effect on tissue removal [13]. Another study has determined that both vacuum pressure and vibration amplitude work in synergy to optimize tissue removal [14]. The results from the present study indicate that the value of D is dependent on the ultrasonic aspirator tool settings. It was found that both parameters, including their interaction, have a significant effect on the observed pit diameter, which is in agreement with [14]. Another report [15] stated that the CUSA fragments and aspirates tissue within 1-2 mm radius from the tip which is consistent with this study. This can be seen in table 1, where the average from all of the observations excluding the outlier (observation 15) corresponds to a radius of 1.9 mm.

The second objective for this study was to further characterize the behavior of fresh grey and white matter with basic aspiration. Investigations on the biomechanics of brain tissue have shown that the properties of grey and white matter differ, but consensus has not been achieved on which of the two tissues is stiffer [11,12]. Based on our results in figure 4 (b, d and f), denuded grey matter experiences a larger deformation and ruptures at lower vacuum pressures. This indicates that grey matter compared to white is less stiff and easier to remove with basic aspiration. Comparison between figure 4 (b and d) clearly demonstrates that the pia mater has a significant effect on the mechanical properties

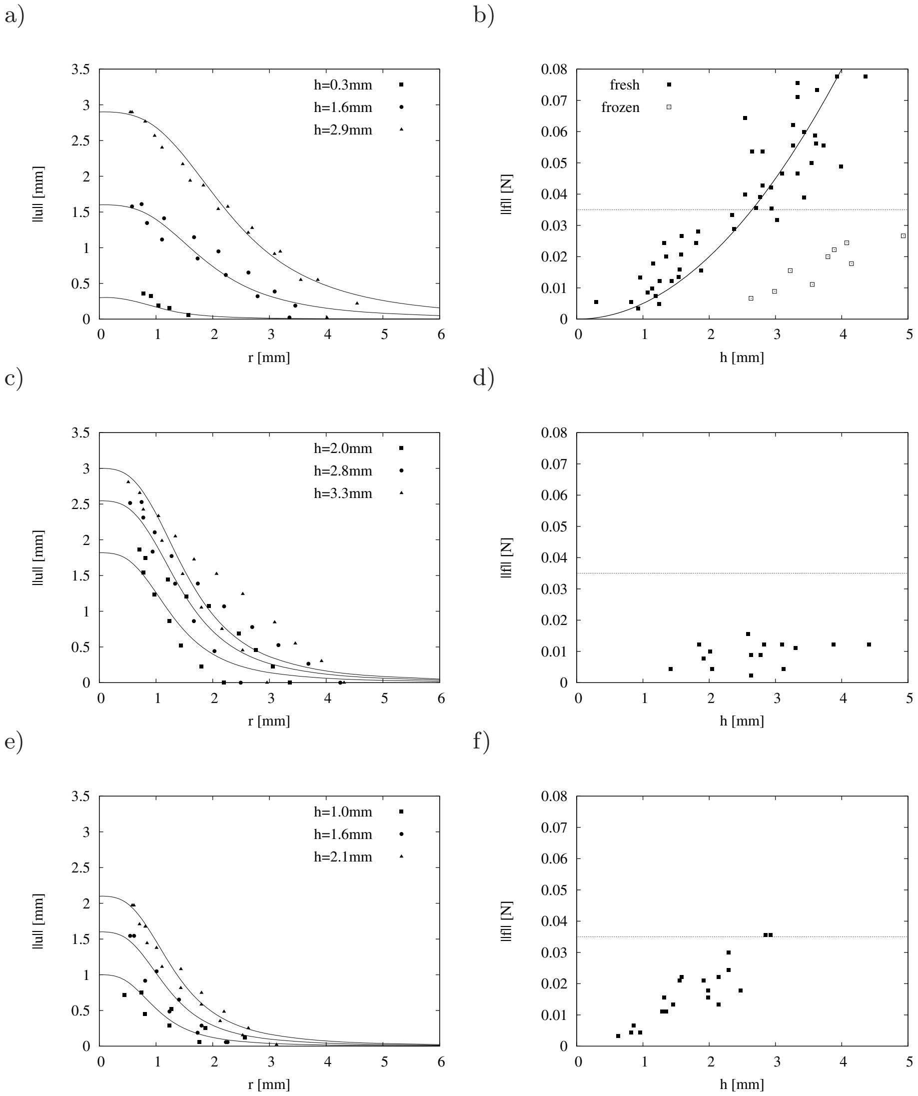

Fig. 4. Deformation profiles for different values of *h* for grey matter with pia (a), grey matter without pia (c) and white matter (e); Force as a function of *h* for grey matter with pia (b), grey matter without pia (d) and white matter (f). Solid lines represent the fitted models, and horizontal dashed lines represent the human touch perception limit.

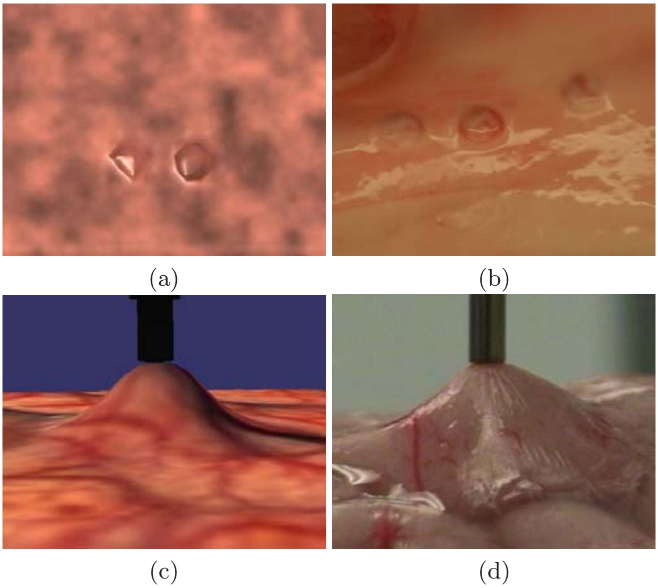

Fig. 5. Simulation results on tissue removal and grasping compared to the corresponding experiment photos

of grey matter. The forces required to rupture grey matter with pia are approximately 4x greater than that required for grey matter alone. Human force perception limit is 10% of the weight of the object [16]. For a CUSA handpiece that weighs about 70 g, this limit is 70 mN. We assumed that a neurosurgeon with exquisite touch perception would not be able to detect a change of 35 mN in force applied on the CUSA. Given that the response of grey and white matter falls below this limit, it was not pertinent to model the forces felt at the tool tip with these tissues. It can be seen that forces can be felt for grey matter with pia at deformation heights approximately greater that 2 mm.

The information obtained from this study was used for simulating surgical aspiration interaction with brain tissue. The deformation profile models were implemented to simulate how brain deforms under the influence of basic aspiration, as can be seen in figure 5 (c and d). The simulated profile is different for each type of tissue. It varies according to the different α found for each type of tissue. Figure 5 (a and b) also demonstrates the simulation results for tissue removal. It can be seen that different tissue removal pit diameters can be achieved in simulation by varying the tool settings.

Based on the results it appears that the aspiration test is not sensitive enough to capture the small forces associated with deformation of white and grey matter. Further exploration using tensile tests will be done with the goal to improve precision of the reaction force equation. This study was limited in that tissue-mimicking phantoms were used to investigate the effect of ultrasonic aspirator parameters on tissue removal. As well, the diameter of the cutting sphere was not characterized for basic aspiration. Future experimentation for both will be conducted on fresh brain tissue.

References

1. Yasargil, M.G.: Microneurosurgery: microsurgery of CNS tumors. Thieme (1996)
2. Cuatico, W.: Neurosurgical suction tips. Acta Neurochirurgica 46, 303–306 (1979)
3. Vällfors, B.: Neurosurgical suction systems, an experimental study. Thesis, Göteborg, Sweden (1976)
4. Vällfors, B.: Suction in neurosurgery. Acta Neurochirurgica 55, 35–42 (1980)
5. Aoki, T., Ohashi, T., Matsumoto, T., Sato, M.: The pipette aspiration applied to the local stiffness measurement of soft tissues. Annals of Biomedical Engineering 25, 581–587 (1997)
6. Schiavone, P., Boudou, T., Promayon, E., Perrier, P., Payan, Y.: A light sterilizable pipette device for the in vivo estimation of human soft tissues constitutive laws. In: Proceedings of the 30th EMBC, pp. 4298–4301 (2008)
7. Vällfors, B.: Efficient atraumatic liquid suction by means of slit suction tubes combined with a pressure control unit. Neurosurgical Review 7, 179–183 (1984)
8. Maxwell, R.E., Chou, S.N.: Convexity meningiomas and general principles of meningioma surgery. In: Operative Neurosurgical Techniques: Indications and Methods, pp. 491–501. Grune and Stratton, New York (1982)
9. O'Daly, B.J., Morris, E., Gavin, G.P., O'Byrne, J.M., McGuinness, G.B.: High-power low-frequency ultrasound: a review of tissue dissection and ablation in medicine and surgery. Journal of materials processing technology (200), 38–58 (2008)
10. Mora, V., Jiang, D., Brooks, R., Delorme, S.: A computer model of soft tissue interaction with a surgical aspirator. In: Medical Image Computing and Computer-Assisted Intervention, pp. 51–58 (2009)
11. Prange, M.T., Margulies, S.S.: Regional, directional, and age-dependent properties of the brain undergoing large deformation. ASME Journal of Biomechanical Engineering (124), 244–252 (2002)
12. Franceschini, G., Bigoni, D., Regitnig, P., Holzapfel, G.A.: Brain tissue deforms similarly to filled elastomers and follows consolidation theory. Journal of the Mechanics and Physics of Solids (54), 2592–2620 (2006)
13. Epstein, F.: The cavitron ultrasonic aspirator in tumor surgery. In: Clinical neurosurgery, pp. 497–505. Wolters Kluwer Health (1983)
14. Cimino, W.W., Bond, L.J.: Physics of ultrasonic surgery using tissue fragmentation: part I. Ultrasound in Medicine and Biology 22(1), 89–100 (1996)
15. Flamm, E.S., Ransohoff, J., Wuchinich, D., Broadwin, A.: Preliminary experience with ultrasonic aspiration in neurosurgery. Neurosurgery 2(3), 240–245 (1978)
16. Jones, L.A.: Perception of force and weight: theory and research. Psychological Bulletin 100(1), 29–42 (1986)

Evaluation of a Technique to Estimate the Compliance of Atherosclerotic Intima

Hamed Azarnoush[1,2], Guy Lamouche[2], Charles-Etienne Bisaillon[2],
Christian Degrandpre[2], and Benoit Boulet[1]

[1] Centre for Intelligent Machines, McGill University
1480 University, Montreal, Quebec, Canada, H2A 2A7
`{Hamed,Boulet}@cim.mcgill.ca`
[2] Industrial Materials Institute, National Research Council of Canada
75 de Mortagne, Boucherville, Quebec, Canada, J4B 6Y4
`{Hamed.Azarnoush, Guy.Lamouche, Charles-Etienne.Bisaillon, Christian.Degrandpre}@imi.cnrc-nrc.gc.ca`

Abstract. We report evaluation of a technique that may be applied to estimate the compliance of atherosclerotic intima. This estimation can help in identification of the type of plaque. It can also be applied in our finite element software, developed to simulate coronary angioplasty. The software accepts segmented intravascular ultrasound images together with each segment's material characteristics. It then simulates the response of the diseased artery, to help choose optimal balloons or stents and also to improve the pressurization strategy. The technique is based on formulating the compliance of two materials in series. A two-layer and two single-layer phantoms were produced to verify the validity of this formulation in practice. The outer layer of the two-layer phantom is chosen with characteristics similar to a real artery. The harder inner layer imitates the intimal thickening. A balloon deployment testing machine, non-compliant balloons and a laser measurement unit were used in experiments.

Keywords: biomedical simulation, pressure-volume measurements, minimally invasive interventions.

1 Introduction

Cardiovascular disease is the leading cause of death in industrialized nations. Percutaneous Coronary Intervention (PCI) is performed on over one million patients in the US, every year [1]. Unfortunately, in spite of the invention of drug-eluting stents (DES), restenosis remains a problem [2]. Considering the large number of cardiovascular patients, addressing this problem is of extreme importance. Decision-making during the PCI is mainly based on the visual feedback from the angiogram; high computational power of today's computers has not been incorporated in the process significantly. Intervention is performed manually and is operator-dependant. Important parameters, i.e. real-time pressurization rates and pressure-volume (P-V) curves for different patients, are not kept in a database. If such information were recorded for

F. Bello and S. Cotin (Eds.): ISBMS 2010, LNCS 5958, pp. 20–28, 2010.
© Springer-Verlag Berlin Heidelberg 2010

millions of patients, who have undergone PCI, strong correlations may have been found between some data characteristics and the clinical events or outcomes of the intervention, i.e. restenosis.

Some researchers have suggested the use of real-time P-V data during PCI, alongside angiography [3]-[6]. The use of such data has also been assessed *in vivo* [7]. However, in general it may not be convenient for the cardiologist to analyze P-V curves during the intervention. Such analysis can be performed by a computer and more tangible results can be provided to the cardiologist.

A finite element software (Angiosoft, Industrial Materials Institute, NRC) was developed, previously, to provide computational as well as visual feedback to the cardiologist. This software is furnished with segmented intravascular ultrasound (IVUS) images, coupled with each segment's material characteristics. Segmentation of IVUS images has already been achieved in the literature [8]. Obtaining information about properties of the thickened intimal segment can be a challenging task. In this paper, we introduce and evaluate a technique by which the compliance of this segment can be estimated. This technique is practiced on a phantom, designed in a way to simulate an atherosclerotic artery. It is common practice among interventional cardiologists to predilate a balloon in the area of stenosis before stent deployment [7]. We explain later, how P-V curves can be monitored during predilation, and help estimate the compliance of the thickened interior layer in the artery. Pressure-volume (P-V) curves can easily be recorded in real-time, without a significant price to pay and without influencing or deteriorating any performance parameter.

The organization of this paper is as follows. In section 2, we introduce our finite element software through simulation of the vessel wall response to stent deployment. We emphasize on existing challenges in using this software. In section 3, we explain how compliance of two materials in series can be formulated. In section 4, we depict the results of some experiments, performed on artery phantoms to verify the formulation obtained in section 3. Section 5 concludes this article.

2 Finite Element Simulation of Tissue's Response

Our finite element software can simulate the tissue's response to balloons and stents of different sizes and models, all already existing in its database. The response can be characterized at a pressure in the range of 0-20 atm. In Fig. 1(a-d), we demonstrate the simulation of stent deployment in an arterial segment with atherosclerotic intimal thickening. Fig. 1(a) provides visual feedback for different sizes of balloons and stents, compared with the size of the lesion, shown by a set of IVUS images in the background. Each division corresponds to 1mm. The blue dashes represent the stent. The stent-supporting balloon in this figure has the dimensions 3.5mm x 20mm (Stent Vision). Three cross-sections of interest can be chosen, which are demonstrated by the horizontal red, yellow and green lines. Fig. 1(b) shows one cross section in the form of a segmented IVUS image. The blue contour depicts the artery and the magenta contour depicts the lumen. The area between these two contours represents the intimal thickening. In order to successfully perform the simulation, information about the properties of the material in this area is needed. Estimation of compliance of this region is addressed in this paper. Fig. 1(c) illustrates sample mappings for the

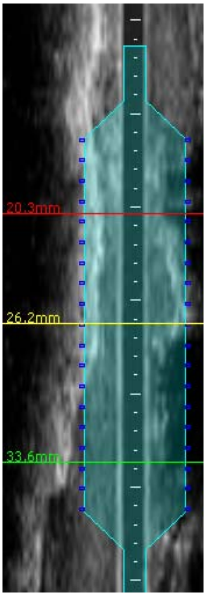

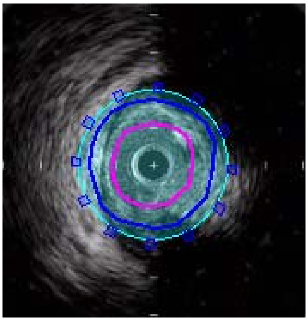

(*b*) Lumen, artery and stent (Cross-sectional contours)

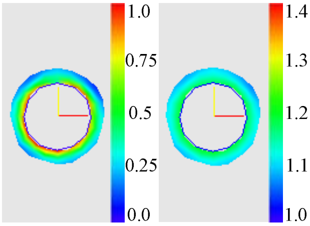

(*a*) Stent vs lumen (Longitudinal view)

(*c*) Mechanical stress in MPa (left) and maximum stretch (right)

Fig. 1. Finite element simulation of the tissue response

mechanical stress (MPa) and maximum stretch (ratio without unit), respectively, at a pressure of 6 atm. Using this software, friction work and endothelial denudation can also be estimated [9]. Such calculations can be helpful for the cardiologist to plan the intervention accordingly. However, these results are only available upon availability of the mechanical properties of the both segments. In the next section, we discuss how the compliance of the intimal thickening can be estimated.

3 Compliance of Interconnected Materials

We have not to this point observed an official formulation of compliance (in physiological sense) for several materials, interconnected with each other. In this paper, we aim at providing such formulation for materials in parallel and in series. Fig. 2 demonstrates the components and their interconnections in our experimental setup. This setup emulates the practice of manual balloon deployment. A syringe is used to inflate the balloon. Although the volume is not commonly measured in PCI, we measure it by determining the position of the plunger. A pressure transducer measures the pressure. The balloon is inflated inside either an excised or a mock (phantom) artery in a saline bath with a temperature of 37°C.

Some researchers [4], [5] have assumed that the compliance of the non-compliant balloon inflated in the air is in parallel with the compliance of the system (composed of pressure transducer, syringe, tubing, etc.). For such a system, the pressure, which is

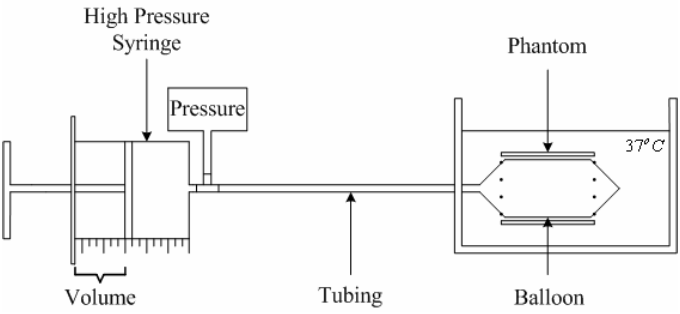

Fig. 2. Interconnection between components in a balloon deployment setup

applied to the balloon and to the system, is the same and is equal to the pressure in the medium. Therefore, representing the system pressure as P_S, the balloon pressure as P_B, and the medium pressure as P, we will have:

$$P_S = P_B = P. \tag{1}$$

The cumulative volume change, ΔV, due to the pressure change, ΔP, will be the summation of the volume change in the system, ΔV_S, and the volume change in the balloon, ΔV_B, obtained from:

$$\Delta V = \Delta V_S + \Delta V_B. \tag{2}$$

If we respectively, define the compliance of the system and the balloon, C_S and C_B, as:

$$C_S = \frac{\Delta V_S}{\Delta P_S},\ C_B = \frac{\Delta V_B}{\Delta P_B}, \tag{3}$$

by using (2), we will obtain the aggregate compliance as:

$$C = \frac{\Delta V}{\Delta P} = \frac{\Delta V_S + \Delta V_B}{\Delta P} = \frac{\Delta V_S}{\Delta P_S} + \frac{\Delta V_B}{\Delta P_B} = C_S + C_B. \tag{4}$$

Next, let us consider a non-compliant balloon being inflated inside an artery with a wall thickened by plaque, which is the focus of this paper. Assume that the compliance of the system (composed of pressure transducers, high pressure syringe, high pressure tubes, etc.) is zero. In the initial phases of inflation, since the balloon is not fully dilated, its compliance can be assumed to be infinity and the balloon can be treated as a pressure transfer medium. Therefore, the aggregate compliance now is equal to the compliance of the diseased artery, composed of arterial wall in series with

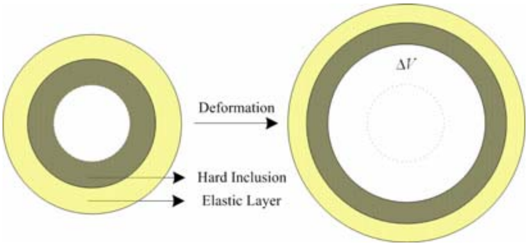

Fig. 3. Intimal thickening to be simulated by a less elastic inclusion inside a rubber phantom

the plaque thickening. The diseased artery is to be simulated by a two-layer phantom, as shown in Fig. 3.

As can be seen in Fig. 3, in the case of having the two materials in series, assuming that the inner layer material is harder than the outer layer material, the volume change for the inner layer, ΔV_I, and for the outer layer, ΔV_O, are equal, shown by:

$$\Delta V_I = \Delta V_O = \Delta V \,. \tag{5}$$

Also the two layers share amongst themselves, the aggregate pressure, P. Hence:

$$\Delta P = \Delta P_I + \Delta P_O , \tag{6}$$

where P_I and P_O are the pressures on the inner surfaces of the inner and the outer layers, respectively. Using the definition of compliance, the equation (6) then leads to:

$$\frac{\Delta V}{C} = \frac{\Delta V_I}{C_I} + \frac{\Delta V_O}{C_O} , \tag{7}$$

where C_I and C_O are the inner layer and the outer layer compliances, respectively. Considering (5) and (7), we will have:

$$\frac{1}{C} = \frac{1}{C_I} + \frac{1}{C_O} . \tag{8}$$

The compliance of the outer layer, C_O, can be estimated from the data in the literature [10]. The aggregate compliance for the diseased artery can also be calculated using the pressure-volume curve, obtained during early pressurization sequences of predilation. Therefore, the compliance of the thickened layer can be calculated using (8). Next, we present the results of some experiments to verify the validity of this equation.

4 Arterial Deformation Simulation Using a Two-Layer Phantom

In this section, we present the results of some experiments, performed on three phantoms. The first phantom was made with a structure, similar to the one, demonstrated

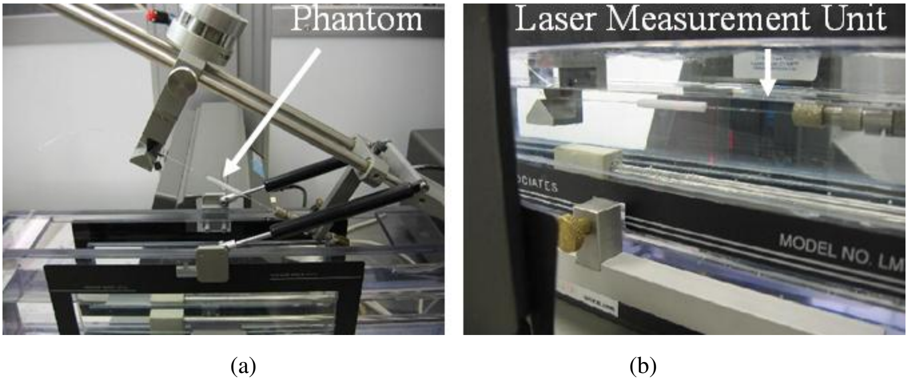

(a) (b)

Fig. 4. The experimental setup (a), and balloon deployment in a heated water bath (b)

in Fig. 3. The lumen diameter of the phantom was 1.5 mm. The thickness of both layers was 0.5mm ± 10%. The outer diameter was measured as 3.6mm. The outer layer was made from a mixture of resin and reactive silicon in proportions of 12:1, respectively. PDMS, resin and reactive silicon were used in proportions of 7.5:15:1, respectively, to make the less elastic inner layer. Two separate phantoms were also generated with dimensions and formulation similar to the inner and the outer layers of the first phantom.

In Fig. 4(a), we illustrate the setup, used in our experiments. All phantoms were pressurized using a deployment testing system (PT-3070, Interface Catheter Solutions) with which the delivered volume and the pressure can be measured, in real-time. The experiments were conducted in a water bath at a temperature of 37^oC (Fig. 4(b)). Non-compliant balloons with 3mm of diameter and 20mm of length were used. These balloons were produced using a computerized balloon-forming machine (9810-H, Interface Catheter Solutions). A laser scan micrometer (LSM-9506, Mitutoyo) was also used to measure in real-time, the outer diameter of the phantom. These measurements help ensure the non-compliant balloon is not fully dilated. Therefore, in experiments we assumed that the balloon is fully compliant. Fig. 5 demonstrates the pressure versus outer diameter, obtained from three experiments for the two-layer phantom (first phantom). In these experiments, initially, the water is flushed through the balloon to remove all air bubbles, followed by closure of the distal end by a pneumatic clamp. Then a vacuum pressure of -0.5 atm is applied. As seen in Fig. 5, the final diameter in all 3 experiments is less than 3.8mm. For a fully deployed balloon the external diameter of the phantom should approach 5mm.

Fig. 6 illustrates the pressure-volume (P-V) data for the same three experiments. Using linear regression, the experiments yield a normalized-over-the-length compliance of 4.81 ± 0.19 [μlitre/atm]/mm for the two-layer phantom. Compliance of the outer-layer corresponds to that of the healthy artery, which in general can be estimated from the data in the literature [10]. In this paper, we demonstrate a P-V data set, as an example, obtained from the experiment with the outer layer phantom (second phantom). This data set is demonstrated in Fig. 6 using squares. According to (6),

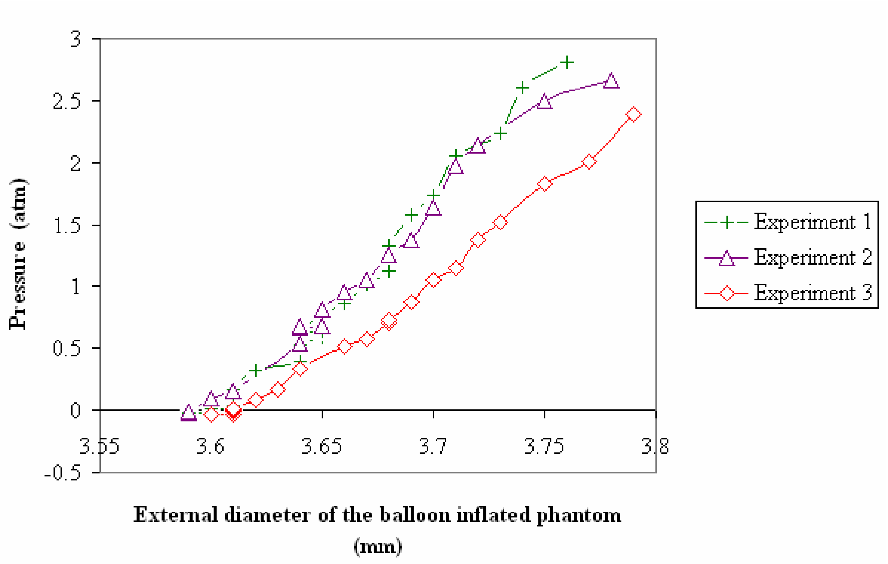

Fig. 5. Pressure vs. external diameter, monitored to ensure the balloon is not fully dilated

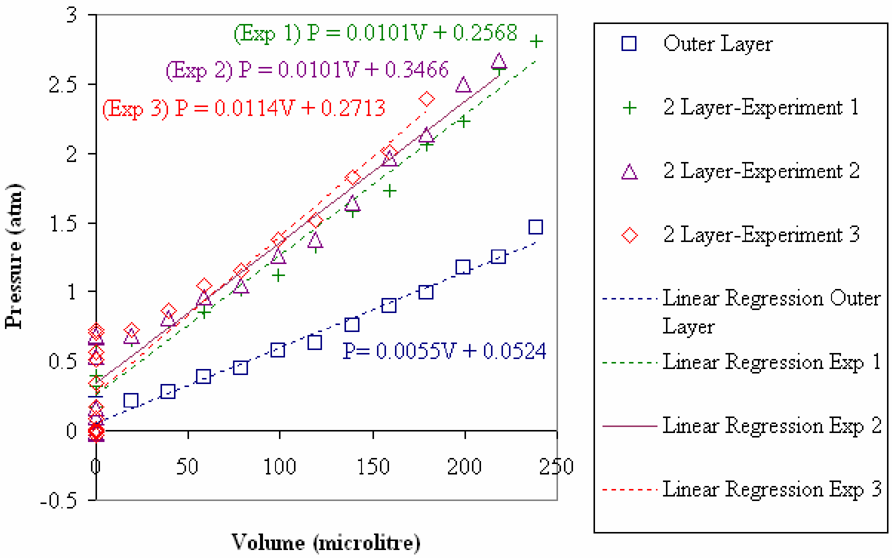

Fig. 6. Pressure vs. volume for the two-layer and the outer layer phantom to estimate the pressure on the inner layer

we can subtract the P-V data set of the outer layer from that of the two-layer phantom to obtain the P-V data set of the inner-layer. This estimated P-V data set is shown in Fig. 7 using circles. The compliance associated to our estimation is 7.94 [μlitre/atm]/mm. An

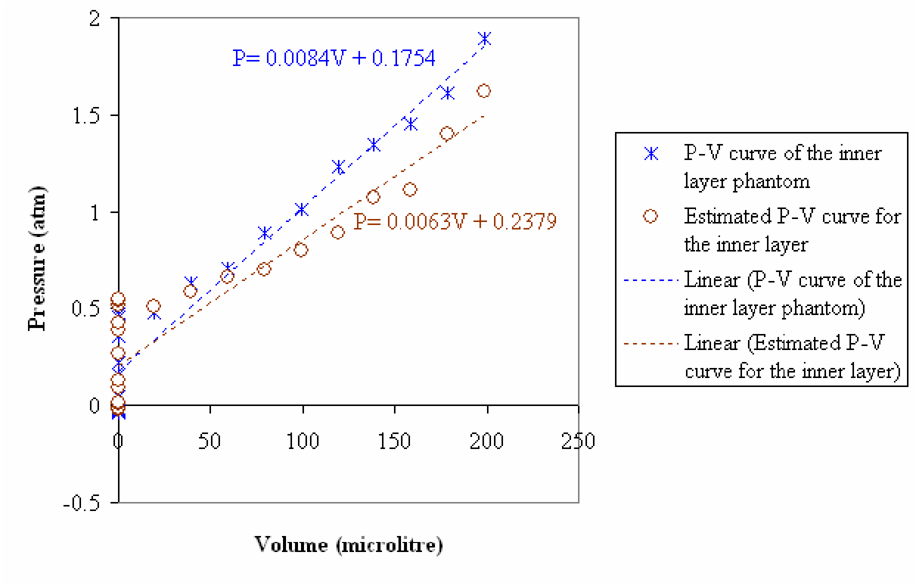

Fig. 7. Estimation of the P-V curve of the inner layer

independent experiment on the inner-layer phantom (third phantom) provides us with a reference that can be compared with our estimation. This reference is shown by stars in Fig. 7. The compliance, obtained from the experiment with the inner layer phantom, is approximated as 5.95 [μlitre/atm] /mm. We calculated the estimation error to be 33.3%. This error can be due to inaccuracies, involved with phantom characteristics or the volume measurements. In this paper, we focused on presenting the methodology. Phantom fabrication and volume measurements can be made more precise to decrease the estimation error.

5 Conclusion

In this paper, we emphasized on recording the real-time pressure-volume data during PCI, as important information which can be statistically related to clinical outcomes of the intervention. As an application of such data, we investigated the possibility of using a technique to estimate the compliance of the atherosclerotic intima. We produced phantoms that were designed to have characteristics similar to a diseased artery. Several experiments were performed on three phantoms to experimentally verify the fact that the summation of the P-V curves of the individual layers yields the P-V curve of the two-layer phantom. As a result, the compliance of the thickened intima could be estimated. This estimation, if improved, can be helpful in achieving a better diagnosis and better treatment, and may help reduce the rate of restenosis.

Acknowledgments. This work is supported by the Natural Sciences and Engineering Research Council (NSERC) and the National Research Council (NRC) of Canada.

References

1. Lloyd-Jones, D., et al.: Heart Disease and Stroke Statistics—2009 Update: a Report from the American Heart Association Statistics Committee and Stroke Statistics Subcommittee. Circulation 119, e21–e181 (2009)
2. Dobesh, P.P., Stacy, Z.A., Ansara, A.J., Enders, J.M.: Drug Eluting Stents: a Mechanical and Pharmacologic Approach to Coronary Artery Disease. Pharmacotherapy 24, 1554–1577 (2004)
3. Zolikofer, C.L., Salmonowitz, E., Bruhlmann, W.F., Frick, M.P., Castenada-Zuniga, W.R., Amplatz, K.: Significance of Balloon Pressure Recording During Angioplasty: an Experimental Study. Rofo. 142, 527–530 (1985)
4. Olbrich, T., Murray, A.: Assessment of a Technique to Determine the Mechanical Properties of Coronary Arteries Using Mock Arteries. Physiol. Meas. 25, 1–15 (2004)
5. Olbrich, T., Murray, A.: Assessment of Computer-Controlled Inflation/Deflation for Determining the Properties of PTCA Balloon Catheters with Pressure-Volume Curves. Physiol. Meas. 22, 299–308 (2001)
6. Shehab, M., Michalis, L.K., Rees, M.R.: Balloon angioplasty optimization: Should we measure balloon volume as well as pressure? Cardiovasc. Intervent. Radiol. 31, 149–157 (2008)
7. Olbrich, T., Williams, D.O., Doig, J.C., Murray, A.: In vivo assessment of coronary artery angioplasty and stent deployment from balloon pressure–volume data. Physiol. Meas. 27, 213–223 (2006)
8. Noble, J.A., Boukerroui, D.: Ultrasound Image Segmentation: a Survey. IEEE Trans. on Medical Imaging 25(8), 987–1010 (2006)
9. Laroche, D., Delorme, S., Anderson, T., DiRaddo, R.: Computer Prediction of Friction in Balloon Angioplasty and Stent Implantation. In: Harders, M., Székely, G. (eds.) ISBMS 2006. LNCS, vol. 4072, pp. 1–8. Springer, Heidelberg (2006)
10. Holzapfel, G.A., Sommer, G., Gasser, C.T., Regitnig, P.: Determination of layer-specific mechanical properties of human coronary arteries with nonatherosclerotic intimal thickening and related constitutive modeling. Am. J. Physiol. Heart Circ. Physiol. 289, H2048–H2058 (2005)

Quantifying Mechanical Properties in a Murine Fracture Healing System Using an Inverse Geometric Nonlinear Elasticity Modeling Framework

Michael I. Miga[1,2,3], Jared A. Weis[1,4], Froilan Granero-Molto[4], and Anna Spagnoli[4,5]

[1] Vanderbilt University, Department of Biomedical Engineering, Nashville, TN, USA
`{Michael.I.Miga, Jared.A.Weis}@vanderbilt.edu`
[2] Vanderbilt University Medical Center, Department of Radiology and Radiological Sciences
[3] Vanderbilt University Institute for Imaging Science, Nashville, TN, USA
[4] University of North Carolina at Chapel Hill, Department of Pediatrics
`granerof@email.unc.edu`
[5] Department of Biomedical Engineering, Chapel Hill, NC, USA
`anna_spagnoli@med.unc.edu`

Abstract. Understanding bone remodeling and mechanical property characteristics is important for assessing treatments to accelerate healing or in developing diagnostics to evaluate successful return to function. The murine system whereby mid-diaphaseal tibia fractures are imparted on the subject and fracture healing is assessed at different time points and under different therapeutic conditions is a particularly useful model to study. In this work, a novel inverse geometric nonlinear elasticity modeling framework is proposed that can reconstruct multiple mechanical properties from uniaxial testing data. This is investigated within the context of a murine cohort (n=3) that are 14 days post fracture. This work is the first to report mechanical properties of a callus using an inverse problem methodology whereby 2758.4 ± 682.5 kPa, 0.467 ± 0.009 were found to be the Young's modulus and Poisson's ratio, respectively. In addition better consistency of the reconstructed metrics over more traditional metrics is demonstrated.

Keywords: fracture healing, murine, finite element, inverse problems, elasticity.

1 Introduction

There is significant morbidity and mortality due to the improper or inhibited healing of bone fractures and is especially relevant to the aging population [1-3]. Restoration of mechanical function to bone is an important healthcare concern and processes to accelerate that process or mediate more successful outcomes is of high significance. In addition, the development of diagnostics that can assess the mechanical function of bone are equally important. Murine systems have become natural platforms for the investigation of therapeutics towards improved healing [4] and ex vivo mechanical testing has served as the primary means to assess efficacy [5, 6]. However, due to confounding geometric effects associated with callus growth and remodeling, robust metrics of evaluation are challenging.

F. Bello and S. Cotin (Eds.): ISBMS 2010, LNCS 5958, pp. 29–37, 2010.
© Springer-Verlag Berlin Heidelberg 2010

To address this, investigators have begun to explore using the detailed structure provided by microCT imaging to facilitate general imaging metrics as well as computational approaches to assess mechanical function using more subject specific models/metrics [7-11]. In this paper, an approach is investigated which looks at the problem more within the context of an inverse problem approach. Similar to work by Shefelbine et al. [9] and Weis et al. [10, 11], a finite element framework is used to generate subject-specific callus models. In this work, an inverse methodology is investigated which represents a significant advance to addressing the problem with computational techniques.

2 Methods

2.1 Inverse Geometric Nonlinear Elasticity Modeling Framework

Hooke's Law is a widely used constitutive law to represent the stress-strain behavior of a material. In the case of uniaxial loading (Figure 1), the full strain state can be expressed with respect to the applied force as shown here,

$$\varepsilon_x = \frac{\sigma_x}{E}, \varepsilon_y = -\nu \frac{\sigma_x}{E}, \varepsilon_z = -\nu \frac{\sigma_x}{E}, \gamma_{xy} = \gamma_{xz} = \gamma_{yz} = 0 \qquad (1)$$

where E is Young's modulus and often referred to as the stiffness, and ν is Poisson's ratio which represents the negative ratio of transverse to axial strain. When conducting mechanical testing, the traditional technique is to prepare a sample with known shape such that the cross-sectional area, A, and reference length, L, are known, and the displacements and forces applied are measured by the testing device. This allows one to take that data and calculate the stiffness of the specimen with, $E = \frac{FL}{A\delta}$ where F is the measured force for the given displacement δ. Typically with this approach a series of displacements are used that span the small strain region of the material characteristic curves and a modulus is fit.

Fig. 1. Uniaxial loading

Of course, the reality is that with the application of an increment of displacement, a change to the cross-sectional area (via Poisson's ratio) is imparted and ultimately affects the measured force. This nonlinear effect is due to the specimen changing shape. To demonstrate, in a simple analytical experiment, a 1 cm cube under tensile loading experienced strains from 0-10% with E=1 MPa (a reasonable approximation to callus stiffness) and a Poisson's ratio of ν=0.3. Figure 2a illustrates the two respective stress-strain curve where 'L' and 'GNL' represent the linear and geometrically nonlinear approaches, respectively. Figure 2b demonstrates the difference in force when taking geometric nonlinearity into account over a range of Poisson's ratio. This is produced by incrementally deforming the specimen cube and accumulating the force at each increment, which is a common strategy to linearize geometric nonlinear

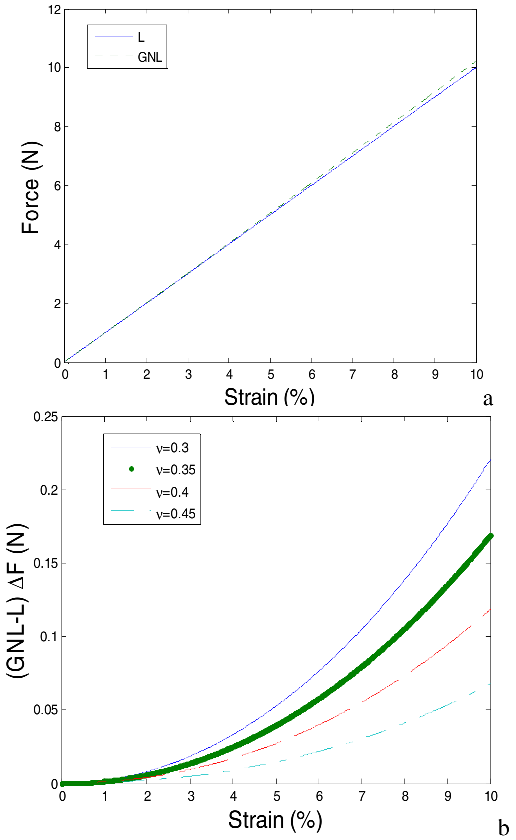

Fig. 2. (a) Force vs strain for linear and geometrically nonlinear problems, (b) the difference in force values over several Poisson's ratios.

problems. As can be seen in Figure 2b, a distinctive force versus strain curve is generated for each Poisson's ratio. This is directly related to the geometric changes to cross-sectional area as reflected by varying Poisson's ratios.

We hypothesize that by taking into account geometrically nonlinear effects within an inverse reconstruction framework that multiple properties can be differentiated from uniaxial testing data. More specifically, we propose to model the geometric nonlinearity in a similar manner as the above analytic example whereby with each increment we deform the mesh and then impart the next increment. The measured forces are then determined by summing the increments. For the application herein concerned with the mechanical integrity of a healing callus, more dramatic changes are expected than the homogeneous example discussed above. In addition, for this paper the callus is being 'lumped', i.e. characterized, as one region with unique mechanical properties. Figure 3 illustrates the typical callus region extracted from µCT data and its geometrical complexity consisting of cartilage (red), new bone (blue), and highly mineralized bone (white). As a dynamic grid finite element model is implemented under tensile load, one can easily note that the geometric relationships between these callus constituents will rapidly change which will manifest in changes to the incremental force.

For the purpose of reconstructing multiple material parameters for the callus region, the

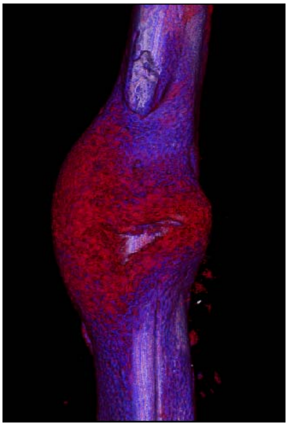

Fig. 3. Image showing callus consistency. Rendering utilizes transparency to reflect bone composition with (red) cartilage, (blue) new bone, and (white) highly mineralized bone.

model for mechanical equilibrium will be expressed in terms of Lame' constants and is stated here,

$$G\nabla^2\bar{u} + (G+\lambda)\nabla(\nabla \bullet \bar{u}) = 0 \quad (2)$$

where G is the shear modulus, λ is the second Lame' constant, and $\bar{u}$ is the displacement vector. With an initial guess at these material parameters, a finite element model of the domain shown in Figure (3) can be constructed, analogous displacements are imposed that match the experimental conditions, and an average force (F_{calc}) is reconstructed from the simulation. A custom-built Levenberg-Marquardt non-linear optimization algorithm is then used to iteratively optimize the material properties such that F_{calc} approaches the experimental material tester generated force (F_{exptl}). In this approach, each strain level is treated as an independent data point with respect to determining the mechanical properties. The important aspect to the approach is that each strain state represents an accumulation effect associated with approximating the geometric nonlinearity. Ultimately this translates to the objective function,

$$\Psi(G,\lambda) = \sum_{i=1}^{N}\left(F_{calc} - F_{exptl}\right)_i^2 \quad (3)$$

where N is the number of displacement data points along the elastic region of the force-displacement curve. The goal is to minimize this objective function with respect to two mechanical properties, G and λ, of the 'lumped' callus region. To optimize this for the callus properties, the derivative of our objective function, $\Psi(G,\lambda)$, is taken with respect to the properties G and λ and set equal to zero, i.e.

$$\begin{bmatrix} \dfrac{d\Psi(G,\lambda)}{dG} \\ \dfrac{d\Psi(G,\lambda)}{d\lambda} \end{bmatrix} = \begin{bmatrix} \dfrac{\partial F_{calc1}}{\partial G} & \dfrac{\partial F_{calc2}}{\partial G} & \cdots & \dfrac{\partial F_{calcN}}{\partial G} \\ \dfrac{\partial F_{calc1}}{\partial \lambda} & \dfrac{\partial F_{calc2}}{\partial \lambda} & \cdots & \dfrac{\partial F_{calcN}}{\partial \lambda} \end{bmatrix} \begin{Bmatrix} F_{calc1} - F_{exptl1} \\ F_{calc2} - F_{exptl2} \\ \vdots \\ F_{calcN} - F_{exptlN} \end{Bmatrix} = \begin{bmatrix} 0 \\ 0 \end{bmatrix}, \quad (4)$$

or simplified as,

$$[J]^T\left\{\bar{F}_{calc} - \bar{F}_{exptl}\right\} = 0 \quad (5)$$

where [J] is the Jacobian matrix. It is important to note that in the above equation each component of the Jacobian is independent and is built over a series of incremental developments. In the case of a fixed mesh/grid counterpart to this approach, each subsequent strain state is just a scalar multiple based on the applied deformations (i.e. double the applied deformation, and double the Jacobian term). The relationship between force and property is just a linear function of applied displacement. However in the GNL approach, each increment provides new information regarding the geometric relationship of the callus constituents. The result is that the standard Levenberg-Marquardt framework contains considerably more information and can be implemented such that multiple mechanical property reconstruction is possible, i.e.

$$\left([J]^T[J] + \alpha I\right)\left[\Delta\bar{P}\right] = [J]^T\left\{\bar{F}_{calc} - \bar{F}_{exptl}\right\}, \quad (6)$$

and

$$\left[\Delta\bar{P}\right] = \begin{bmatrix} G \\ \lambda \end{bmatrix}_{i+1} - \begin{bmatrix} G \\ \lambda \end{bmatrix}_{i}, \quad (7)$$

with the regularization term α defined as,

$$\alpha = \left(\phi * \mathrm{trace}\left([J]^T [J]\right) * SSE^2\right)^{1/2} \tag{8}$$

[12], where ϕ is an empirical factor, and SSE is the sum squared error between measured and calculated force. It should be noted that the Jacobian was determined by a finite difference calculation which was initiated by a 2.5% perturbation from the initial guess of the callus property. The process is iterative until the relative error between iterations converges below a set tolerance or until no improvement in objective function is noted. With respect to reporting the values in this paper, the Lame' constants were converted to Young's modulus and Poisson's ratio for the purpose of comparing with the more traditional metrics. In addition, two other reconstructions were executed whereby Poisson's ratio was fixed (ν=0.45) and Young's modulus was determined using the linear and geometric nonlinear approaches for a single property.

2.2 Murine System

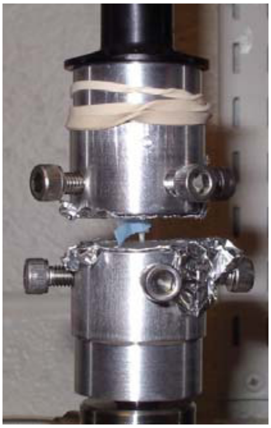

Fig. 4. A murine mouse tibia loaded within the testing apparatus

Three female syngenic FVB mice (FVB-NJ, Jackson Laboratories) 8 to 12 weeks old with a pin-stabilized mid-diaphaseal tibia fracture were generated. Procedural implementation utilized a standard three point bending system for fracture delivery [13], anesthesia, and pain control and was approved by the Institutional Animal Care and Use Committee at Vanderbilt University Medical Center and the University of North Carolina at Chapel Hill. At day 14, the mice were euthanized and tibia fractures were dissected, and wrapped in phosphate buffered saline (PBS) soaked gauzed. The specimens were then placed within a Scanco μCT 40 scanner (Scanco Medical) and an approximate 5 mm section was scanned for each specimen which consisted of callus and bone ends. Once completed, each specimen was prepared for mechanical testing by embedding each end within a customized polymethylmethacrylate cast such that it could be placed within the testing unit while also allowing the callus to remain exposed and free of constraints. The assembly was placed with an Enduratec Electroforce 3100 mechanical tester (Bose, Enduratec Systems Group) and tested in tension at a fixed displacement rate of 0.25 mm/min using a 22 N force transducer (Honeywell Sensotec). Data consisted of displacement and force values and was recorded continuously until failure. Figure 4 shows a murine tibia being tested.

Once the collection of the imaging and displacement data is complete, the bone/callus regions are segmented from the μCT data, a tetrahedral grid is generated, and properties are assigned to mineralized bone and void regions. In this work, highly mineralized bone (white regions in Figure 3) were assigned E=5 MPa, and ν=0.3 MPa [14], while voids within the domain were assigned negligible material properties. With the computational model and data in place, these are then provided to the inverse approach. In this paper, three inverse approaches are generated: (1) a single callus shear modulus reconstruction using the static mesh, (2) a single callus shear modulus value using the dynamic grid, and (3) a dual callus reconstruction of the Lame' constants using the dynamic grid. In addition, the apparent stiffness, and normalized apparent stiffness are reported which are common metrics within the literature. Apparent stiffness is the slope of the best fit line to force versus displacement data within the linear loading phase. Normalized apparent stiffness is the same fitting procedure but with the force and displacement values normalized by the largest cross-sectional area of the callus and overall length, respectively.

3 Results

Figure 5 illustrates a typical result from the model generation process. Figure 6 illustrates the force versus displacement curves for all (n=3) mice. Table 1 reports the

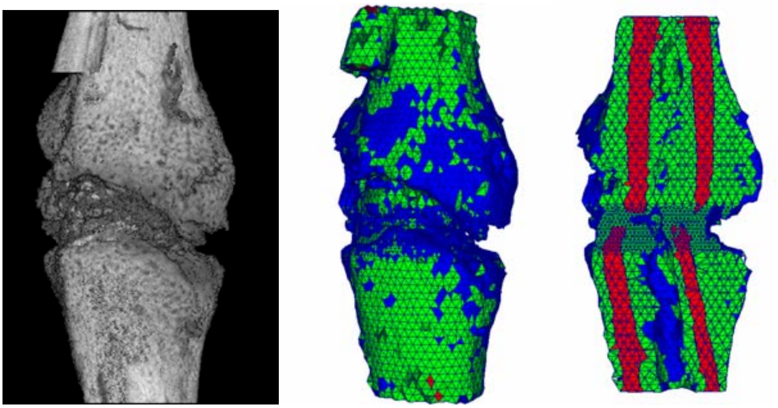

Fig. 5. (left) Volume rendered μCT of callus, (middle) tetrahedral grid of volume, (right)

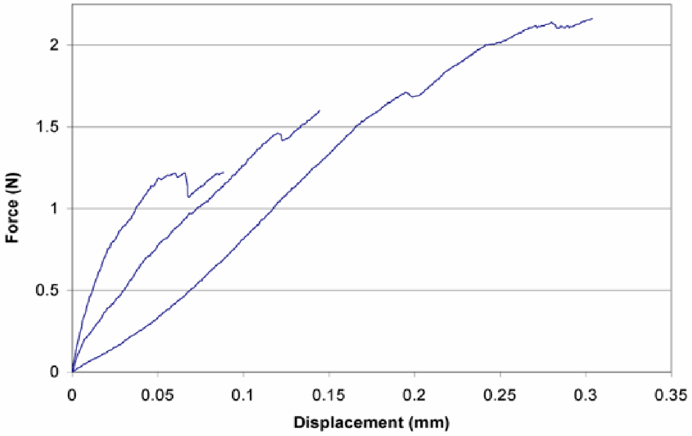

Fig. 6. Force versus displacement for (n=3) mice. Only regions prior to an approximate elastic limit were analyzed as part of the reconstructive analysis.

Table 1. Metrics for mechanical properties assessed over (n=3) mice

PROPERTY	14 d (n=3)	SD as % of mean
Apparent Stiffness (N/mm)	13.95 ± 6.24	44.7%
Normalized Apparent Stiffness (kPa)	8330.1 ± 4941.0	59.3%
$E_{reconstructed}$ (kPa) Linear (ν=0.45 fixed)	2908.3 ± 872.8	30.0%
$E_{reconstructed}$ (kPa) Geometric NonLinear (ν=0.45 fixed)	3230.2 ± 986.7	30.5%
$E_{reconstructed}$ (kPa), $\nu_{reconstructed}$ Geometric NonLinear (dual property)	2758.4 ± 682.5, 0.467 ± 0.009	24.7%, 1.9%

mechanical property metric types in the first column with their corresponding value in the second column. While statistical significance from such a small data set cannot be achieved at this time it is interesting to look at the magnitude of the standard deviations relative to the mean property across the different metrics (reported in column 3 of Table 1).

4 Discussion

The methods reported have shortcomings at this early stage but nevertheless the results are promising. Some of those short comings are: (1) lack of finer discretization of the callus models as shown in Figure 5, (2) the choice of tetrahedral elements as opposed to ones more accurate in mechanics modeling, e.g. hexahedral elements [15], (3) although the grid is dynamic in the geometric nonlinear approach, the lack of re-meshing for the intermediate steps to ensure optimal element aspect ratios, (4) the high strain conditions within the fracture fissure likely need the full-nonlinear strain tensor description, (5) lack of more data necessary to achieve statistical significance, and (6) the inherent experimental error associated with 'potting' tibia fractures and mechanical testing. Despite this however, it is encouraging that the reconstructed values are quite consistent among the widely distributed force/displacement curves. The heterogeneity among these curves can be seen in the considerably large standard deviation of the apparent stiffness and the normalized apparent stiffness as compared to their mean values. Comparing quantitatively, the standard deviations of the apparent stiffness values are approximately 45-60% relative to the mean value while reconstructed values using the inverse approaches are only 25-30% of the mean. This suggests that model-based inverse analysis produces a more consistent metric. The considerable 15% increase in variation when normalizing the apparent stiffness suggests that the process of normalization introduces variability and would seem to confirm the confounding effects of geometry often referred to in the literature. The contribution of the work is that this represents to our knowledge the only inverse elasticity approach to this problem. Because the approach is based on measured force, each result from the three variants to the algorithm represents a quantitative value. As the shortcomings are overcome, better absolute quantification will be achieved, but even as realized here, the approach may serve as an effective means to differentiate and score different treatment groups at different time points. In fact, in recent work not reported here, the ability to differentiate different time (10 day, 14 day post-fracture) points of healing under similar fracture conditions has been found in an expanded cohort (n=6) of mice. Interestingly, the reconstructive analysis was the only method to find statistical significance among the two groups [11].

5 Conclusion

This paper presents a novel inverse approach that takes advantage of geometric nonlinearities to increase the extent of information such that the reconstruction of multiple material properties is achieved. It also goes on to compare different realizations of the approach and compares these to more common metrics to qualify mechanical properties in a murine fracture system. The results indicate a more consistent result across mice using the model-based analysis. Future work will involve investigating if the method can be used to differentiate mice at different healing points and among different treatments.

Acknowledgments. This work was supported by National Institutes of Health (NIH) Grant 5R01DK070929-02 from the National Institute of Diabetes and Digestive and Kidney Diseases (NIDDK).

References

1. Tomak, Y., Kocaoglu, M., Piskin, A., Yildiz, C., Gulman, B., Tomak, L.: Treatment of intertrochanteric fractures in geriatric patients with a modified external fixator. Injury-International Journal of the Care of the Injured 36, 635–643 (2005)
2. Toh, E.M., Sahni, V., Acharya, A., Denton, J.S.: Management of intracapsular femoral neck fractures in the elderly; is it time to rethink our strategy? Injury-International Journal of the Care of the Injured 35, 125–129 (2004)
3. Sharif, K.M., Parker, M.J.: Austin Moore hemiarthroplasty: technical aspects and their effects on outcome, in patients with fractures of the neck of femur. Injury-International Journal of the Care of the Injured 33 (2002); PII S0020-1383(0002)00041-00044
4. Granero-Molto, F., Weis, J.A., Landis, B., Longobardi, L., Miga, M.I., Spagnoli, A.: Mesenchymal Stem Cells Enhance Fracture Healing: Essential Role for Cytokines in Homing and Anti-Inflammatory Response. Journal of Bone and Mineral Research 23, S166–S167 (2008)
5. Gardner, M.J., van der Meulen, M.C.H., Demetrakopoulos, D., Wright, T.M., Myers, E.R., Bostrom, M.P.: In vivo cyclic axial compression affects bone healing in the mouse tibia. J. Orthop. Res. 24, 1679–1686 (2006)
6. Moukoko, D., Pithioux, M., Chabrand, P.: Temporal evolution of mechanical properties of skeletal tissue regeneration in rabbits: an experimental study. Med. Biol. Eng. Comput. 45, 989–995 (2007)

7. Morgan, E.F., Mason, Z.D., Chien, K.B., Pfeiffer, A.J., Barnes, G.L., Einhorn, T.A., Gerstenfeld, L.C.: Micro-computed tomography assessment of fracture healing: Relationships among callus structure, composition, and mechanical function. Bone 44, 335–344 (2009)
8. Reynolds, D.G., Hock, C., Shaikh, S., Jacobson, J., Zhang, X.P., Rubery, P.T., Beck, C.A., O'Keefe, R.J., Lerner, A.L., Schwarz, E.M., Awad, H.A.: Micro-computed tomography prediction of biomechanical strength in murine structural bone grafts. J. Biomech. 40, 3178–3186 (2007)
9. Shefelbine, S.J., Simon, U., Claes, L., Gold, A., Gabet, Y., Bab, I., Muller, R., Augat, P.: Prediction of fracture callus mechanical properties using micro-CT images and voxel-based finite element analysis. Bone 36, 480–488 (2005)
10. Weis, J.A., Granero-Molto, F., O'Rear, L.D., Miga, M.I., Spagnoli, A.: Development of a high-resolution 3D Micro-CT based model to predict fracture callus histological architecture. Journal of Bone and Mineral Research 22, W472 (2007)
11. Weis, J.A., Miga, M.I., Granero-Molto, F., Spagnoli, A.: A finite element inverse analysis to assess functional improvement during the fracture healing process. J. Biomech. (in press, 2009)
12. Joachimowicz, N., Pichot, C., Hugonin, J.P.: Inverse Scattering - an Iterative Numerical-Method for Electromagnetic Imaging. IEEE Transactions on Antennas and Propagation 39, 1742–1752 (1991)
13. Bonnarens, F., Einhorn, T.A.: Production of a standard closed fracture in laboratory animal bone. J. Orthop. Res. 2, 97–101 (1984)
14. Schriefer, J.L., Robling, A.G., Warden, S.J., Fournier, A.J., Mason, J.J., Turner, C.H.: A comparison of mechanical properties derived from multiple skeletal sites in mice. J. Biomech. 38, 467–475 (2005)
15. Benzley, S.E., Perry, E., Merkley, K., Clark, B., Sjaardema, G.: A Comparison of All-Hexahedral and All-Tetrahedral Finite Element Meshes for Elastic and Elasto-Plastic Analysis. In: Proc. 4th International Meshing Roundtable, Sandia National Laboratories, pp. 179–191 (1995)

Optimization of Case-Specific Vascular Tree Models Based on Vessel Size Imaging

Bryn A. Lloyd, Sven Hirsch, and Gábor Székely

Computer Vision Laboratory, ETH Zürich, Switzerland
`{blloyd,shirsch,szekely}@vision.ee.ethz.ch`

Abstract. We analyze a problem, which is relevant for physiological modeling of vascular networks: the initialization and optimization of specific, individual models of a functioning vessel network. We do not try to describe the process of growing vessels. Rather, the model properties are optimized via similarity metrics between the artificial vessel network and suitable image data. A vascular network model has many degrees of freedom to optimize and it can be assumed that there are many different optimal solutions. In order to reduce the variability between different solutions we enforce certain physiological properties, for instance Murray's Law, which must be fulfilled by an optimal network. We propose and validate several similarity metrics, which can be used to optimize the radii of the vascular tree.

1 Introduction

Our ultimate goal is to simulate hemodynamic conditions and blood-tissue exchange of O_2 and CO_2 in specific, individual vascular network models down to the capillary level, while using as much information from images (as acquired e.g. for small animals or patients) and other sources as possible for parameter estimation and evaluation of the models. The first step to individualized models is to create a comprehensive description of the region of interest (e.g. tumor), typically via segmentation of different tissue types (muscle, bone, vessels, etc.), followed by mesh generation and initialization of the physiological state. We are currently acquiring in vivo image data from mice, which can be used for this initialization problem. Vessel size imaging (VSI) provides an estimate for the average vessel diameter per voxel and is a magnetic resonance (MR) based technique which relies on the administration of intravascular contrast agents [1]. While VSI measures vessels smaller than the voxel size, larger vessels are visible in MR angiography (MRA). Therefore, VSI in combination with MRA potentially provides comprehensive local information about the distribution of small and large vessels. It is our goal to use this information to generate a vessel network model with the same distribution of radii as measured in order to estimate the functional state. In this paper we discuss this issue and provide a partial solution. We aim to establish a functionally equivalent vessel network by matching the distribution of radii to the measurements.

F. Bello and S. Cotin (Eds.): ISBMS 2010, LNCS 5958, pp. 38–48, 2010.
© Springer-Verlag Berlin Heidelberg 2010

Many authors have described methods to generate artificial models of vascular systems. The main approaches are typically evolutionary, optimality or data-based. The first tries to express knowledge and assumptions about the biological phenomena as a set of rules or equations describing the temporal behavior (evolution) in reaction to certain factors, including several models of tumor angiogenesis [2],[3], [4].

Many authors have suggested that vascular systems follow certain optimality principles, such as minimal energy dissipation or minimal building material explaining observations from real vessel networks. One example is the bifurcation law (Murray's law) [5], which relates the radii of daughter branches (r_r, r_l) to the radius of the parent branch r_p

$$r_p^\gamma = r_l^\gamma + r_r^\gamma, \tag{1}$$

where γ is the bifurcation exponent. It has been reported that γ is between 2.55 and 3.

The work of Klarbring et al. [6] describes a method to optimize flow network topology and gives access to existing methods for optimizing analogous problems in other fields, e.g. electrical networks and load carrying trusses. They optimize the radii in order to minimize the total dissipation (or pressure loss) within the flow network, while constraining the total volume. Schreiner and colleagues presented a method, which they named constrained constructive optimization (CCO) in order to generate a (visually) realistic vascular system which incorporates both physiological knowledge and hemodynamic conditions [7],[8]. The algorithm builds a binary tree starting from a root node specified by the user. New branches are added by connecting randomly sampled points to existing vessel segments. The branching point is computed by optimizing a minimum volume functional. When a new segment is added, all hemodynamic properties and the vessel radii are updated. Multiple (coupled) trees, for instance a venous and arterial tree can be generated by connecting new points to both trees, with opposite flow direction specified as boundary condition [9]. Kretowski et al. have applied this algorithm to simulate biphasic computed tomography images [10].

Mittal et al. [11] presented a method to reconstruct a model of the coronary arterial tree from detailed morphometric data. Their algorithm constructs a full tree from partial measurements, using cast data for vessel sizes above $40\mu m$ and histological data for vessels below $40\mu m$. The casts of the main arterial trees were measured and sketched manually, noting the connectivity as well as segment length and radius information. Similarly, histological measurements were obtained and added to a database. Since it is not possible to obtain a complete cast of the arterial tree down to the capillaries, they developed an algorithm to reconstruct a possible tree. Subtrees and vessel segments from the database with a similar radius were connected to terminal vessels of the reconstructed tree. Note that since no 3D position information was used, tree segments that originally were very distant might be connected in this algorithm. From the obtained tree they could measure and fit parameters of certain scaling laws, which relate the cumulated length of a tree, with maximal cross section and vessel tree volume [12], [13], [14].

Our underlying assumption is that two vessel networks are functionally equivalent if they share the same larger vessels, while having a similar micro-vasculature in a statistical sense, e.g. similar vessels densities or histograms of vessel radii. It is clear that we cannot reconstruct the exact vascular structure without higher resolution (ex vivo) measurements. Instead we wish to generate a functionally equivalent vessel system from the measured VSI. We plan to do this in a two-step algorithm (possibly in an iterative fashion):

1. Construct a vascular tree by adding and removing vessel segments.
2. Optimize the vessel radii by maximizing the similarity to a measured image.

The first step could be implemented in a way similar to the cited CCO method or one of its extensions. In this manuscript we focus on the second part of this algorithm and assume a vascular tree is given and must be optimized. Due to the number of degrees of freedom of a vascular tree model it is clear that many different optimal solutions exist. In order to allow only biologically meaningful solutions we enforce certain physiological properties, for instance Murray's Law, which must be fulfilled by an optimal network.

2 Methods

Vessel size imaging provides an estimate for the average vessel diameter per voxel and is a MR based technique, which relies on the administration of an intravascular contrast agent [1]. Briefly, the changes of the relaxation rates R_2 and R_2^* are measured using spin echo (T_2) and gradient echo (T_2^*) imaging sequences, before and after injection of a contrast agent. From these four acquisitions VSI can be computed according to

$$VSI_{MRI} = 0.424 \left(\frac{D}{\gamma \cdot \Delta\chi \cdot B_0} \right)^{1/2} \left(\frac{\Delta R_2^*}{\Delta R_2} \right)^{3/2}, \tag{2}$$

where D is the water diffusion coefficient in the tissue, $\Delta\chi$ is the increase in the magnetic susceptibility difference between the extra- and intravascular compartments (induced by the contrast agent). B_0 is the magnetic field strength and γ is the gyromagnetic ratio of the protons. Tropres et al. state that VSI is valid for small blood volume fractions and high contrast agent concentrations [1].

Tropres et al. suggested a formula to estimate the VSI from histological slices [15]. Here, a similar expression is used to estimate the VSI from a vessel network model. At a position (x, y, z) the VSI value is computed from a local average

$$VSI_{model} = \left[\sum_j r_j^{-2/3} f(r_j) \right]^{-3/2} . \tag{3}$$

The above average is computed in a window centered around (x, y, z). The function $f(r_j)$ weights the contribution of individual segments. According to Tropres et al. [1] it corresponds to the normalized blood volume fraction ($f(r_j) \propto l_j\, r_j^2$, and $\sum_i f(r_i) = 1$), therefore,

$$(VSI_{model})^{-2/3} = \sum_j r_j^{-2/3}\, f_j = \sum_j r_j^{-2/3} \frac{l_j\, r_j^2}{\sum_k l_k\, r_k^2}, \tag{4}$$

where l_i is the length of the vessel segment with radius r_i.

For a given vascular network model we would like to minimize the difference between the VSI_{model} and a given vessel size image $VSI_{MRI} = R$. One possibility is to pose the problem as a least square minimization problem

$$E(r_0, r_1, \dots) = \sum_{j=0} (r_j^\alpha - R^\alpha)^2\, f_j. \tag{5}$$

where we introduce the exponent $\alpha = -2/3$ to make the expressions easier to read. Experimentally, we have found this estimator to be biased: the solution has a model VSI, which is larger than R. This has motivated us to investigate the problem. For the analysis we neglect the spatial dependency of R.

Analysis with Full Symmetric Tree: Some important insights are obtained from the analysis of a simpler one-dimensional problem. For this case we assume a full symmetric binary tree, i.e. at all bifurcations both child segments have equal radii. Additionally, we assume uniform segment lengths l_j. Therefore, the tree is completely described by the radius at the root, the number of levels or generations, and the bifurcation exponent γ. According to Equation 1 the segment radius in level n is $r_n = r_0\,(1/2)^{n/\gamma}$ (See Figure 1 a)) and the least square problem for a tree with $N+1$ levels is

$$E(r_0) = \sum_{j=0}^{N} 2^j \left(r_0^\alpha \left(\frac{1}{2}\right)^{\frac{j\alpha}{\gamma}} - R^\alpha \right)^2 f_j. \tag{6}$$

Note that in each level there are 2^j equally sized segments. The problem can be solved analytically. Using the well known expression for geometric series the weight $f_j = \frac{r_j^2}{\sum_k^N 2^k r_k^2}$ can be simplified to

$$f_j = \left(\frac{1}{2}\right)^{j\,2/\gamma} \frac{1}{\sum_k^N \left(\frac{1}{2}\right)^{k(2/\gamma-1)}} = \left(\frac{1}{2}\right)^{j\,2/\gamma} \frac{1}{s_3}$$

and does not depend on r_0. Therefore, the error function in Equation 6 is a quadratic function in r_0^α

$$\begin{aligned} E(r_0) = (r_0^\alpha)^2 \sum_{j=0}^{N} \left(\frac{1}{2}\right)^{j(2\alpha/\gamma-1+2/\gamma)} &- 2R^\alpha r_0^\alpha \sum_{j=0}^{N} \left(\frac{1}{2}\right)^{j(\alpha/\gamma-1+2/\gamma)} \\ + R^{2\alpha} \sum_{j=0}^{N} \left(\frac{1}{2}\right)^{j(2/\gamma-1)} & \\ = (r_0^\alpha)^2\, s_1 - 2R^\alpha r_0^\alpha s_2 + R^{2\alpha} s_3, & \end{aligned}$$

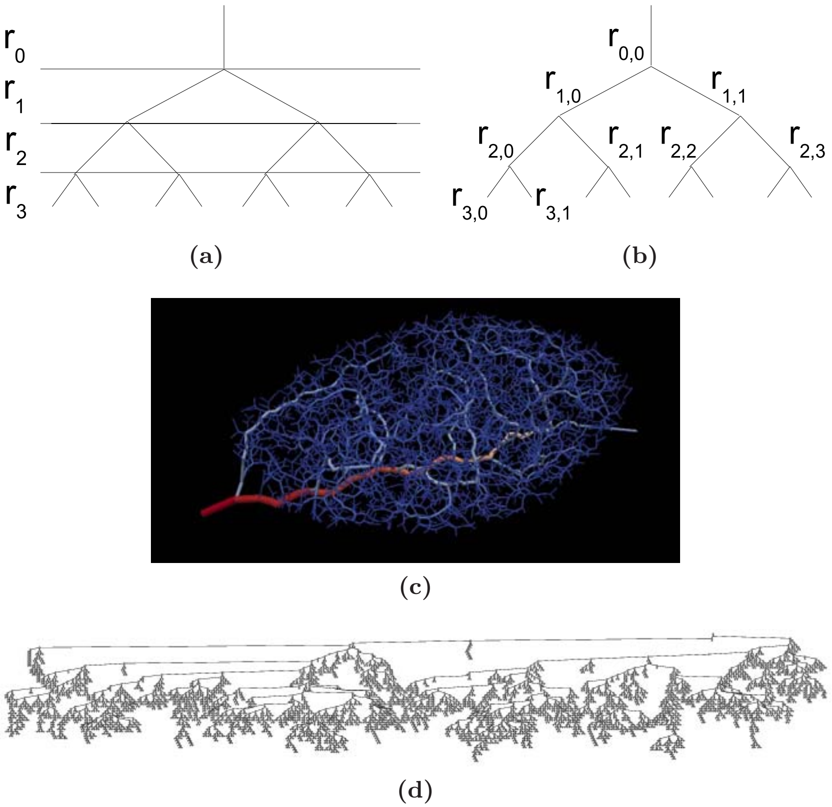

(a) **(b)**

(c)

(d)

Fig. 1. A symmetric full binary is shown in a). Figure b) explains the indexing/counting convention for the 2^N-D case. In c) a tree generated with CCO method is depicted [8]. The topology of the CCO tree is shown in d).

which has a minimum at $r_0^\alpha = s_2/s_1 R^\alpha$. Accordingly, the VSI of the model is

$$VSI_{model} = \left(\sum_j^N r_j^\alpha \, 2^j f_j \right)^{1/\alpha} = \left(R^\alpha \frac{s_2}{s_1 \, s_2} \sum_j^N \left(\frac{1}{2} \right)^{j(\alpha/\gamma - 1 + 2/\gamma)} \right)^{1/\alpha}$$

$$= \left(\frac{s_2^2}{s_1 \, s_2} \right)^{1/\alpha} R,$$

which is larger than R for $N > 0$. This proves that the estimator is biased.

Inversely Weighted Least Squares: An interesting observation is that the solution to the least square error function is given by the equation

$$\frac{\partial}{\partial (r_0^\alpha)} E(r_0^\alpha) = 2 \sum_{j=0}^N 2^j \left(r_0^\alpha \left(\frac{1}{2} \right)^{\frac{j\alpha}{\gamma}} - R^\alpha \right) f_j \, \left(\frac{1}{2} \right)^{\frac{j\alpha}{\gamma}} = 0,$$

which states that at the minimum R^α is a weighted average of the radii r_j^α with weights $W_j = \left(\frac{1}{2}\right)^{\frac{j\alpha}{\gamma}}$, i.e. the small radii are weighted more than the larger ones. Based on this observation we conclude that weighted least square

$$E(r_0) = \sum_{j=0}^{N} 2^j \left(r_0^\alpha \left(\frac{1}{2}\right)^{\frac{j\alpha}{\gamma}} - R^\alpha \right)^2 f_j \, \hat{W}_j,$$

with weights $\hat{W}_j = 1/W_j = \left(\frac{1}{2}\right)^{\frac{-j\alpha}{\gamma}} = \left(\frac{r_0}{r_n}\right)^\alpha$ is an unbiased estimator with a VSI_{model} of R.

Generalization to 2^N-D Case: Until now, it has been assumed that the tree is perfectly symmetric, i.e. that all radii in each tree level have equal sizes. In this section we extend the analysis to non-symmetric full binary trees. The error metric now depends on the arbitrary radius of the leaf segments $r_{i,j}$, where i stands for the layer (=level) of the segment and j is used to count all the segments in a layer. This convention is illustrated in Figure 1 b). There are $N+1$ levels in total. Using the bifurcation law recursively

$$r_{N-k,n}^\gamma = r_{N-k+1,2n}^\gamma + r_{N-k+1,2n+1}^\gamma = \sum_{i=0}^{2^k-1} r_{N,2^k n+i}^\gamma$$

we find that radius $r_{N-k,n}$ depends only on the radii in the subtree of $(N-k,n)$ and only the leaf radii are independent. The total error is decomposed into an error for each layer or segment

$$E(r_{N,0}, r_{N,1}, \dots) = \sum_{k=0}^{N} E_{N-k} = \sum_{k=0}^{N} \sum_{n=0}^{2^{N-k}-1} E_{N-k,n}. \tag{7}$$

The segment least square error can be written as

$$E_{N-k,n} = \left[r_{N-k,n}^\alpha - R^\alpha\right]^2 f_{N-k,n} = \left[\left(\sum_{i=0}^{2^k-1} r_{N,2^k n+i}^\gamma \right)^{\alpha/\gamma} - R^\alpha \right]^2 f_{N-k,n}.$$

The minimum is obtained by setting the derivative (gradient) of Equation 7 to zero. The derivative of the segment error term $E_{N-k,n}$ with respect to the radius $r_{N,q}$ (q is a leaf segment and is an arbitrary descendent of the segment n in layer $N-k$, i.e. $q \in \{2^k n+1, 2^k n + 2^k\}$) is

$$\begin{aligned}\frac{\partial E_{N-k,n}}{\partial r_{N,q}} &= 2 \left[\left(\sum_{i=0}^{2^k-1} r_{N,2^k n+i}^\gamma \right)^{\frac{\alpha}{\gamma}} - R^\alpha \right] \frac{\alpha}{\gamma} \left(\sum_{i=0}^{2^k-1} r_{N,2^k n+i}^\gamma \right)^{\frac{\alpha}{\gamma}-1} \gamma r_{N,q}^{\gamma-1} f_{N-k,n} \\ &\quad + \left[r_{N-k,n}^\alpha - R^\alpha\right]^2 \frac{\partial f_{N-k,n}}{\partial r_{N,q}} \\ &= 2\alpha \left[r_{N-k,n}^\alpha - R^\alpha\right] \left(r_{N-k,n}\right)^{\alpha-\gamma} r_{N,q}^{\gamma-1} + \left[r_{N-k,n}^\alpha - R^\alpha\right]^2 \frac{\partial f_{N-k,n}}{\partial r_{N,q}}.\end{aligned}$$

Unfortunately, unlike in the 1-D case it appears practically impossible to derive a weighted least squares function from the gradient of the error. However, it turns out that by analogy to the 1-D case a goal function with weights $W(r_{N-k,n},\dots) = \left(\frac{r_{0,0}}{r_{N-k,n}}\right)^{\alpha}$ can be used:

$$E(r_{N,0}, r_{N,1}, \dots) = \sum_{k=0}^{N} \sum_{n=0}^{2^{N-k}-1} \left[r_{N-k,n}^{\alpha} - R^{\alpha}\right]^2 f_{N-k,n} \left(\frac{r_{0,0}}{r_{N-k,n}}\right)^{\alpha} \tag{8}$$

Setting the derivative of this error function to zero results in an equation, which has the solution $VSI_{model} = R$. It is difficult to see if also other minima exist. However, it is easy to show that for the symmetric 1-D case this result reduces to the unbiased solution obtained in Equation 2.

Maximum Likelihood Estimation: As an alternative to weighted least squares, we may fit the radii using a maximum likelihood estimator. The radii are Poisson distributed, which is easy to see in the symmetric case. Therefore, the log-likelihood function is [16]

$$L(r_{N,0}, r_{N,1}, \dots) = \sum_{k=0}^{N} \sum_{n=0}^{2^{k}-1} \left(R^{\alpha}\, log(r_{N-k,n}^{\alpha}) - r_{N-k,n}^{\alpha}\right) f_{N-k,n}. \tag{9}$$

The maximum likelihood approach finds the independent (leaf) radii that maximize the function $L(.)$. This is equivalent to generalized least squares based on full iteration [16]. The 1-D symmetric case can be shown to have the solution $VSI_{model} = R$.

Further Generalizations: It can be shown that both the maximum likelihood and weighted least square goal functions can be further generalized to arbitrary binary trees, e.g. with non-uniform segment lengths or leaf nodes with non-uniform depths. An example of such a general tree is shown in Figure 1 c) and d). The numerical experiments performed in the next section also include such general trees.

Experimentally we have found the proposed goal functions, i.e. the weighted least square (Equation 8) as well as the maximum likelihood (Equation 9) metrics, to have multiple local minima in the general case. The unwanted local minima can be interpreted as solutions with a different tree topology, since they contain zero-radius branches and segments. The reason for their appearance is that very small segments have a very small contribution to the total error $E(\cdot)$, or have only a marginal effect on the likelihood function $L(\cdot)$. Therefore, we have developed a scheme to regularize the goal functions and suppress the unwanted solutions.

The maximum likelihood estimator assigns a likelihood to a radius based on a known mean and distribution. In order to regularize this estimator we assign probabilities to the leaf segments. Intuitively, the radii of the smallest vessels usually do not vary very much. This can be expressed as a likelihood function

$$\prod_j p(r_j) = \prod_j exp\left(-\frac{(r_j - \overline{r_{leaf}})^2}{2\sigma^2}\right), \tag{10}$$

where $\overline{r_{leaf}}$ is the arithmetic mean of all leaf radii, r_j are the radii of leaf vessels and the parameter σ controls the standard deviation of the leaf radii, deemed acceptable. Smaller values of σ will penalize large variance in the leaf radii. The regularized log-likelihood function is

$$\begin{aligned} L(r_{N,0}, r_{N,1}, \dots) = &\sum_{k=0}^{N} \sum_{n=0}^{2^k-1} \left(R^\alpha \, log(r_{N-k,n}^\alpha) - r_{N-k,n}^\alpha\right) f_{N-k,n} \\ &- \sum_{n=0}^{2^N-1} \frac{(r_n - \overline{r_{leaf}})^2}{2\sigma^2}. \end{aligned} \tag{11}$$

A similar term can be added to the weighted least square estimator, in order to regularize the solution space.

$$\begin{aligned} E(r_{N,0}, r_{N,1}, \dots) = &\sum_{k=0}^{N} \sum_{n=0}^{2^{N-k}-1} \left[r_{N-k,n}^\alpha - R^\alpha\right]^2 f_{N-k,n} \left(\frac{r_{0,0}}{r_{N-k,n}}\right)^\alpha \\ &+\beta \sum_{n=0}^{2^N-1} (r_n - \overline{r_{leaf}})^2. \end{aligned} \tag{12}$$

The penalty term is scaled by β, which must be chosen by the user and should be large enough to avoid zero-radius solutions, but not too large since this will make the penalty a stiff constraint.

3 Experiments and Results

We have tested and analyzed the discussed goal functions experimentally for both full binary and randomly generated general binary trees (not all terminal nodes are at same level). In addition to the least square (LSQ), weighted least square (WLSQ) and maximum likelihood (ML) estimators, we have also tested the regularized versions of these estimators (RLSQ, RWLSQ, RML). In all experiments we set the reference value R to 25 and the bifurcation exponent γ to 2.55. Numerical optimization was done using Powell's method. For the regularization terms we used the parameters $\sigma = 100$ and $\beta = 1$.

2^N-D Full Binary Tree: The symmetric 1-D problem discussed theoretically is not very interesting and is skipped here. However, already for the full binary tree there are some interesting findings. The first observation is that the numerical solution for the full binary tree is symmetric for all goal functions except for ML and WLSQ, i.e. in each layer the radii are uniform and the solution reduced to the 1-D problem. The reason why ML and WLSQ are not symmetric is because the optimizer got stuck in a local minimum, where some of the tree segments have a zero radius. This issue was already mentioned in the previous section and was the motivation behind the regularization terms. The second observation, which is depicted in Figure 2, is that ML, WLSQ and their regularized versions are unbiased. The LSQ estimator is strongly biased with increasing N.

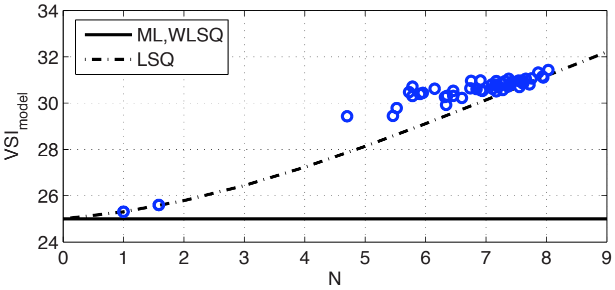

(a)

Fig. 2. This figure shows the optimized mean radius for different sizes of the full binary tree (N is number of levels, i.e. there are 2^N independent leaf radii). The circles represent measured values for several random trees.

General Binary Tree: We generated 100 different random binary trees by building them recursively and creating bifurcations with probability $P = 80\%$. The maximum recursion depth (=number of levels) was chosen as $N = 10$. Note that these trees are not full binary trees, i.e. not all leaves have equal depth. Using these trees we performed tests to evaluate the stability of the solutions. For a given tree we randomly set the initial values using 50 different seeds for the random number generator and optimized using each initial value. For RWLSQ and RML the maximum difference between numerical solutions obtained with different initial values was in the range of the tolerance parameter for Powell's method (10^{-6}). In other words, these goal functions appear to be convex. Again the WLSQ and ML estimators found many different local minima (zero-radius solutions).

The (R)WLSQ, (R)ML estimators were unbiased, while the LSQ was more biased with increasing number of terminal nodes (degrees of freedom), as depicted in Figure 2. Interestingly, although the solutions are stable and unbiased for both RWLSQ and RML, different numerical solutions are obtained by the two methods for a given non-full tree. In Table 1 we provide some quantitative measures characterizing the difference between these two solutions (leaf radii). In general the variability of the independent (leaf) radii is larger for the ML solutions, while the mean is approximately the same and the root radius $r_{0,0}$ is very similar. The correlation between leaf depth and radius shown in the last column is weaker

Table 1. Comparison between numerical solution obtained with ML, WLSQ, RML and RWLSQ

	Leaf Radius					
	mean	std	skew	range	$r_{0,0}$	corr d-r
ML	3.462	7.272	1.625	[0.000,21.675]	60.146	0.003
WLSQ	7.058	7.574	0.234	[0.000,23.748]	70.354	0.166
RML	12.298	0.503	-0.477	[11.065,13.363]	76.956	0.418
RWLSQ	12.329	0.337	0.045	[11.553,13.332]	77.091	0.282

for RWLSQ. Interestingly, although the leaf radii tend to differ for RML and RWLSQ, there is no significant difference for the whole tree. We also measured the radius asymmetry at bifurcations ($\alpha = \frac{r_l}{r_r}$) but did not find differences of the mean, standard deviation, or skewness between RML and RWLSQ.

4 Conclusions and Future Work

The analysis has shown that least square minimization for constructing vascular trees with similar mean radii to a given reference results in a bias. Two alternative optimality criteria have been proposed, which are unbiased. In order to suppress local unwanted minima we added regularization terms, which made the optimization problem convex, as has been verified numerically. For the analysis we have made some simplifications, most importantly that the reference vessel size image (R) has no spatial dependency. For a correct treatment we should consider the VSI of the vessel network in a window of the size of a voxel, which is then compared to the local value of the measured MR VSI. It is also clear that the presented radius optimization needs to be coupled with an algorithm to construct vascular systems, such as the CCO method by Schreiner et al. [7]. The topological operations (adding and removing vessel segments) are more likely to be effective in integrating the spatial dependency of R. We are currently implementing such a strategy, which iteratively performs topological and radius optimization operations in order to maximize the similarity to the measured data. Future work should also address the question of how to integrate the known vessel branches, which are visible in MRA, into the generated tree.

Acknowledgment. This work has been performed within the frame of the Swiss National Center of Competence in Research on Computer Aided and Image Guided Medical Interventions (NCCR Co-Me) supported by the Swiss National Science Foundation.

References

1. Troprès, I., Grimault, S., Vaeth, A., Grillon, E., Julien, C., Payen, J.F., Lamalle, L., Décorps, M.: Vessel size imaging. Magn. Reson. Med. 45(3), 397–408 (2001)
2. Anderson, A.R., Chaplain, M.A.: Continuous and discrete mathematical models of tumor-induced angiogenesis. Bulletin of Mathematical Biology 60(5), 857–899 (1998)

3. Szczerba, D., Székely, G.: Simulating vascular systems in arbitrary anatomies. In: Duncan, J.S., Gerig, G. (eds.) MICCAI 2005. LNCS, vol. 3750, pp. 641–648. Springer, Heidelberg (2005)
4. Lloyd, B.A., Szczerba, D., Rudin, M., Székely, G.: A computational framework for modelling solid tumour growth. Philos. Transact. A Math. Phys. Eng. Sci. (July 2008)
5. Murray, C.D.: The physiological principle of minimum work: I. the vascular system and the cost of blood volume. Proc. Natl. Acad. Sci. USA 12(3), 207–214 (1926)
6. Klarbring, A., Petersson, J., Torstenfelt, B., Karlsson, M.: Topology optimization of flow networks. Computer Methods in Applied Mechanics and Engineering 192(35-36), 3909–3932 (2003)
7. Schreiner, W., Buxbaum, P.F.: Computer-optimization of vascular trees. IEEE Trans. Biomed. Eng. 40(5), 482–491 (1993)
8. Karch, R., Neumann, F., Neumann, M., Schreiner, W.: A three-dimensional model for arterial tree representation, generated by constrained constructive optimization. Comput. Biol. Med. 29(1), 19–38 (1999)
9. Kretowski, M., Rolland, Y., Bézy-Wendling, J., Coatrieux, J.L.: Physiologically based modeling of 3-D vascular networks and CT scan angiography. IEEE Trans. Med. Imaging 22(2), 248–257 (2003)
10. Kretowski, M., Bézy-Wendling, J., Coupe, P.: Simulation of biphasic ct findings in hepatic cellular carcinoma by a two-level physiological model. IEEE Trans. Biomed. Eng. 54(3), 538–542 (2007)
11. Mittal, N., Zhou, Y., Ung, S., Linares, C., Molloi, S., Kassab, G.S.: A computer reconstruction of the entire coronary arterial tree based on detailed morphometric data. Ann. Biomed. Eng. 33(8), 1015–1026 (2005)
12. Kassab, G.S.: Scaling laws of vascular trees: of form and function. Am. J. Physiol. Heart Circ. Physiol. 290(2), 894–903 (2006)
13. Kaimovitz, B., Huo, Y., Lanir, Y., Kassab, G.S.: Diameter asymmetry of porcine coronary arterial trees: structural and functional implications. Am. J. Physiol. Heart Circ. Physiol. 294(2), H714–H723 (2008)
14. Huo, Y., Kassab, G.S.: A scaling law of vascular volume. Biophys. J. 96(2), 347–353 (2009)
15. Troprès, I., Lamalle, L., Péoc'h, M., Farion, R., Usson, Y., Décorps, M., Rémy, C.: In vivo assessment of tumoral angiogenesis. Magn. Reson. Med. 51(3), 533–541 (2004)
16. Carroll, R.J., Ruppert, D.: Transformation and weighting in regression. Monographs on statistics and applied probability. Chapman and Hall, Boca Raton (1988)

Efficient Generation of Corresponding Meshes for Biomedical Flow Simulations

Robert H.P. McGregor[1], Bryn A. Lloyd[1], Dominik Szczerba[1,2], and Gábor Székely[1]

[1] Computer Vision Laboratory, Sternwartstr. 7, 8092 Zürich, Switzerland
`mcgregor@vision.ee.ethz.ch`
`http://www.vision.ee.ethz.ch`
[2] IT'IS Foundation for Research, Zürich, Switzerland

Abstract. The study of hemodynamic conditions in patient-specific geometries is of great interest to the understanding of cardio-vascular pathologies. Performing large-scale studies of these blood flow conditions requires the building of databases with numerous flow simulations in known correspondences. We propose a method for efficient preparation of the imaging data for use in such studies, comprising an automatic high quality mesh generation strategy and a coordinate mapping technique. Our approach deforms a high quality template mesh to fit a patient-specific geometry using a transformation obtained in a registration step. A valuable feature of this technique is that all the generated meshes are by definition co-registered and have the same mesh topology. This, combined with the coordinate mapping makes direct inter-patient comparisons significantly easier. We apply our method to generate patient-specific meshes of the adbominal aortic bifurcation and demonstrate that it is able to provide high quality meshes in a fully automatic way.

1 Introduction

Cardio-vascular diseases are the major cause of death in the developed world and their prevalence is on the rise. This fact, combined with rapidly improving access to high-power computing has led to a large research effort dedicated to simulating blood flow in the human body. Indeed, there is believed to be a significant correlation between the onset and development of cardio-vascular pathologies and local hemodynamic conditions, so understanding these by simulating them could prove to be a key advance in health science. In the long-term it is hoped that such simulations could provide tools for better risk assessment, treatment decision facilitation or even surgical outcome planning.

In this context, there is interest in collecting patient-specific simulation results into databases which could then be used for large scale studies. Such collections of simulations are used e.g. in the @neurIST project[1] or in the measurement enhancement method by McGregor et al. [1]. Building simulation databases

---

[1] @neurIST: European Initiative to Integrate Biomedical Informatics in the Management of Cerebral Aneurysms: *http://www.aneurist.org*

F. Bello and S. Cotin (Eds.): ISBMS 2010, LNCS 5958, pp. 49–58, 2010.
© Springer-Verlag Berlin Heidelberg 2010

requires a lot of pre-processing, mostly to convert the imaging data into model geometries. The requirements for this preprocessing pipeline are as follows: (1) it should be as automatised as possible while still giving the user enough control; (2) it should guarantee high-quality content; (3) the resulting simulations should be co-registered for easy comparison; (4) it should be robust to pathological alterations; and (5) it should accept input images from any modality.

In the case of computational fluid dynamics (CFD) simulations, the first step is the creation of a body-fitting mesh to be used with the finite volume or finite element codes. The quality of these meshes greatly influences the convergence rates and overall accuracy of the numerical calculations. Generating the meshes needed for CFD simulations from patient-specific imaging data is a demanding task and is often the bottleneck in the pre-processing pipeline. Although many meshing tools exist, none are specifically tailored to the requirements of vascular flow simulations, leading to a lot of manual work and lack of efficiency.

The standard patient-specific mesh generation strategy is to produce a surface mesh based on the segmented data and then to use this as input to a volume mesher. Examples of this strategy can be found in [2], [3] and [4]. Unfortunately these are highly sensitive to the quality of the input surface meshes so a large amount of smoothing and mesh repair is performed, often manually, before they can be passed on to the volume meshers. The volume meshing algorithms themselves are difficult to use consistently and balancing the many parameters such as number of elements, refinement possibilities, minimal cell quality or feature preservation can be a challenging optimisation problem.

To overcome these problems it has been proposed to use template-based meshing algorithms. These typically use a synthetically generated high quality base mesh, which is then deformed to fit a patient-specific dataset. Both Baghdadi et al. [5] and Zheng et al. [6] presented such methods for generating successive meshes of the same geometry through time. A promising technique was developed by Barber et al. [7] who generate an image corresponding to a template mesh and then register this image to patient-specific data. This is a very convenient approach as they circumvent segmentation entirely while remaining general enough for any type of geometry. However, depending on the imaging modality, the applicability of the method can be limited, in particular when dealing with badly resolved or low contrast images where the vascular location of interest might not be clearly visible. Also, as no a priori geometric information is used, the method is not robust against pathological alterations where better control of the initialization may be necessary when the patient-specific geometry deviates significantly from the template.

Our contribution. We propose a novel solution to the problem of fast and accurate mesh generation for large databases of patient-specific CFD simulations. Our approach is twofold: in a first step a segmentation and surface meshing of the input image are performed and in a second step a registration is used to deform a high quality template mesh. Our method takes advantage of geometric information, thus making it also applicable to pathological cases. All the meshes produced are by definition co-registered and we also provide a local coordinate mapping technique so as to make the simulated velocity vectors directly comparable. The only constraint is that there must exist an isomorphic mapping from the patient-specific geometry to the template mesh. In this study we demonstrate the effectiveness of our technique using several CT datasets of abdominal aortic bifurcation geometries with and without abdominal aortic aneurysms (AAA).

2 Methods

Our method is a template-based meshing approach using a registration step to deform a base mesh to fit the patient-specific data in a similar fashion to Barber et al. [7]. However, instead of an image-based registration we use a mesh-based registration which exploits a priori information. We also added an end-face flattening step to guarantee that the inflows and outflows are planar, as well as a coordinate mapping step so as to make flow solutions directly comparable across different geometries. The full workflow pipeline can be seen in Figure 1 and a short description of each individual step follows.

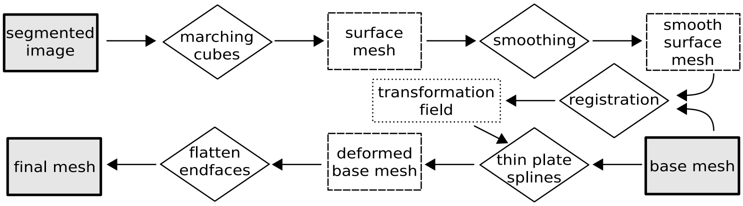

Fig. 1. Method flowchart

Generating the base mesh. The base mesh is produced using ANSYS ICEM-CFD to mesh a bifurcation model made of primitives. This allows for very high quality meshing and any desired level of refinement. A diameter-to-length ratio is chosen for each branch, corresponding to the region-of-interest. For the example case of the abdominal aortic bifurcation we empirically chose 3.1 for the main branch and 3.6 for both child branches as this restricts the geometry to the region distal to the renal arteries and proximal to the bifurcation of the internal and external iliac arteries. An example base mesh can be seen in Figure 2(a).

Generating the surface mesh. The only patient-specific input to the whole procedure is a binary volume resulting from a segmented image. This makes the method general and removes dependence on any specific imaging modality. Based on this image a surface mesh is generated using marching cubes.

Smoothing the surface mesh. The surface mesh is usually very jagged, especially for large or anisotropic voxel size as is often the case in MR images. We perform smoothing in two steps. The first step uses geometric priors and requires a centerline extraction which is performed based on the method by Antiga et al. [8]

implemented in VMTK [2]. This is then used in a regularisation step by Laplacian smoothing of the cylindrical radii: each point p is moved to the average distance from the centerline calculated within its neighbourhood of size ϕ. Parameter ϕ controls the amount of smoothing and we chose this empirically as being $3\times$ the mean edge length of the input surface mesh. In a second step a Taubin filter [9] is applied to remove any remaining high-frequency disturbances. This is also implemented in VMTK and we used a passband of 1 and 30 iterations. Both these smoothing steps are volume-preserving.

Registration. Once a surface mesh with the desired smoothness becomes available registration is performed to find correspondences between it and the surface of the base mesh. This is done by relying on work by Antiga et al. [10] (also implemented in VMTK), who provide a patching algorithm which decomposes bifurcations into their component parts and generates branch-specific coordinates. We can then place any number of points at chosen branch coordinates. Our experience shows that this procedure is robust and reproducible, and results in good correspondences. The same procedure is applied to the base mesh so that we have the direct correspondences between the points on the surface of the base mesh and of the patient-specific surface mesh. So as to ensure that each branch has the correct length, the branch radii are integrated along the centerlines and the surface mesh is cut at the template's diameter-to-length ratio.

Warping the base mesh. Once we have the corresponding points on both the base mesh and the patient-specific surface mesh we can warp the base mesh using thin plate splines (TPS). A convenient feature of this approach is that the transformation is by definition smooth on the inside, thus contributing to maintaining a high cell quality even under deformation. Parameter N, the number of corresponding points, controls the scale-of-detail: the more points are used, the more high-frequency details are transferred from the surface mesh to the deformed result.

Flattening the end-faces. The warped mesh should maintain the flatness of the endfaces in the base mesh. However, some warping does occur and increases with larger deformations. This can make it difficult to apply boundary conditions, especially at the inlet where a flow velocity profile is usually imposed. We therefore flatten the end-faces by snapping their nodes to a plane perpendicular to the centerline and then, to ensure mesh smoothness and avoid low quality elements, we extrapolate this displacement smoothly for all mesh points close to the plane.

Generating a common coordinate system. As very briefly described in [1], we generate a common coordinate system for all meshes so as to make flow velocity vectors directly comparable. This is done by solving the Stokes equation in the mesh with pressure boundary conditions at inlet and outlet which produces a

---

[2] VMTK: the Vascular Modeling Toolkit: *http://www.vmtk.org*

homogeneous vector field with directions aligned to the outer walls. The normalized flow velocity vector is used as our first local coordinate ξ, the second is taken as the vector η pointing from the centerline to any given point and the third is the cross-product ζ of the first two. Such a local coordinate system is represented in Figure 5.

3 Results

For evaluation purposes 3 abdominal CT datasets from patients without AAA and 4 from patients diagnosed with AAA were acquired retrospectively, segmented semi-automatically using ITK-SNAP [3], a level set segmentation tool and then used as input to our method. The voxel size is $0.95 \times 0.95 \times 1.5$ *mm* for all data volumes. The base mesh which was used consists of 9418 nodes and 47729 tetrahedral elements and is shown in Figure 2(a). Figures 2(b), 2(c) and 2(d) show the contour of the initial segmentation, the smoothed surface mesh and the resulting high quality mesh respectively for the first healthy case (*AAN01*). Figures 3(a), 3(b), 3(c) and 3(d) show the final meshes for the three aneurysmal datasets and one of the healthy ones respectively. As may be seen the final meshes are of high quality while preserving the major features of the input data.

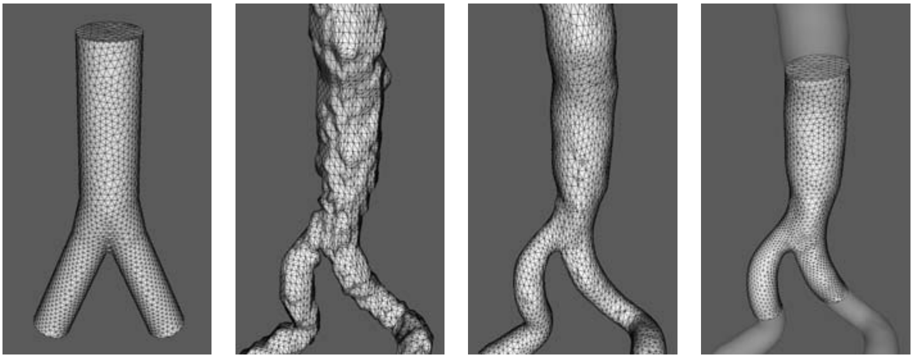

(a) Template. (b) Segmented. (c) Smoothed. (d) Final.

Fig. 2. Mesh generation procedure

We compared the resulting meshes with those produced by two off-the-shelf meshing tools which are frequently used by biomedical simulation researchers: *TetGen* and *NETGEN*. Fedorov and Chrisochoides [11] give a good overview of tetrahedral mesh generation for image-based biomedical simulations and discuss *TetGen* and *NETGEN* in detail, here we only give a brief description. *TetGen* is a constrained Delaunay mesh generation and refinement method by Si [12]. The

---

[3] ITK-SNAP: a tool for segmenting 3D medical images: *http://www.itksnap.org*

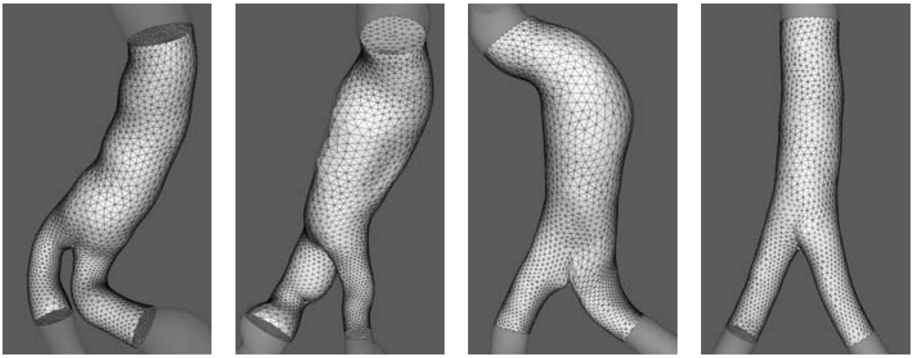

(a) *AAA01.* (b) *AAA02.* (c) *AAA03.* (d) *AAN04.*

Fig. 3. Output meshes for the 3 aneurysmal datasets (on the left) and for a healthy case (last on the right)

algorithm refines tetrahedra which are larger than a user defined size or which have a radius-length ratio worse than a threshold. Since the input surface meshes contain triangles at a higher resolution than desired in the tetrahedral mesh, we first use simplification to reduce the number of triangles [13]. *NETGEN* is an advancing front mesh generator developed by Schöberl [14]. The implementation first generates a new surface mesh and then a tetrahedral mesh using a size parameter to control the resolution. In order to obtain a similar number of tetrahedra as in our base mesh, we experimentally set the size parameter to 3 for Tetgen and 1.8 for Netgen. Additionally, we disabled an option in *NETGEN* to automatically compute a size based on surface curvature, due to excessive local refinement.

Both tools accept triangulated surfaces as input and we employed our smooth surface meshes to this end. A quality measure q, calculated as the in-sphere to out-sphere radius ratio normalised to [0 1] for the meshes generated by all three methods for two representative cases are listed in Table 1. Figure 4 shows quality histograms for all elements in the seven cases for our method and the two standard mesh generators (note the logarithmic scale). The average $min(q)$, $\bar{q}$ and percentage of cells with $q < 1/3$ were 0.325, 0.875 and 0.0125% respectively for the healthy cases and 0.0369, 0.843 and 0.21% for the pathological ones. This clearly demonstrates that the higher deformations do influence the quality - especially the worst elements, however the meshes remain good enough and generally better conditioned than those produced by the standard procedures.

Figure 5 shows the mesh-specific coordinate system for case *AAA01*. As may be observed, the local coordinate system's first component ξ (in white) is aligned to the geometry's main axis and additionally has a radial component η (in grey) and a circumferential one ζ (in black). This local coordinate system stays smooth even in the proximity of bifurcations or sharp angles.

To evaluate the effect of the scale-of-detail parameter N we generated two meshes for the same pathological case (*AAA01*) using a sparse ($N = 504$) and

Table 1. Quality of the meshes produced by our method, *NETGEN* and *TetGen* for a healthy (*AAN01*) and an aneurysmal (*AAA01*) case. N_N: number of nodes. N_C: number of cells. $min(q)$: minimum quality. $\bar{q}$: mean quality. $\%q_{1/3}$: percentage of cells with quality $< 1/3$.

Mesh	N_N	N_C	$min(q)$	$\bar{q}$	$\%q_{1/3}$
AAN01 - our method	9418	47729	0.2828	0.86	0.02
AAN01 - *NETGEN*	10198	44887	0.0039	0.84	0.06
AAN01 - *TetGen*	8449	46521	0.0039	0.73	4.08
AAA01 - our method	9418	47729	0.0753	0.85	0.31
AAA01 - *NETGEN*	9162	39909	0.0246	0.83	0.03
AAA01 - *TetGen*	10576	55316	0.0002	0.73	4.55

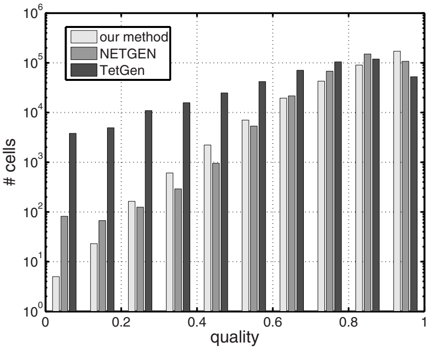

Fig. 4. Quality histograms

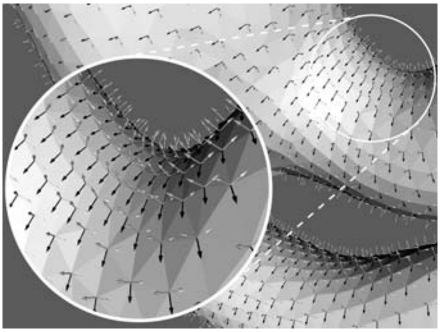

Fig. 5. Local coordinate system

a dense ($N = 4536$) deformation field and compared the distances from the surfaces of the resulting volume meshes to the original smooth surface mesh. The results can be seen in Figure 6(a) and Figure 6(b). As can be seen, using the dense deformation field provides an approximation of the surface mesh which is almost 3× better, thus resolving high-frequency features more accurately.

4 Discussion

We evaluated our method using the example of the abdominal aortic bifurcation. We chose this as it is a common site for flow-related diseases such as aneurysms and atherosclerosis, thus making it a likely candidate for large-scale flow studies. The method as it is implemented here could be directly used for the carotid or any other bifurcating vessel. Moreover, the algorithm could also be applied to any other type of vessel geometry, e.g. incorporating several branchings or trifurcations without any major modifications other than adapting the parameters. The main limitation in this respect is that the studied geometry must always present the same topology: so cases where a specific branching is completely absent due to a pathology or a genetic defect cannot be dealt with. The presented

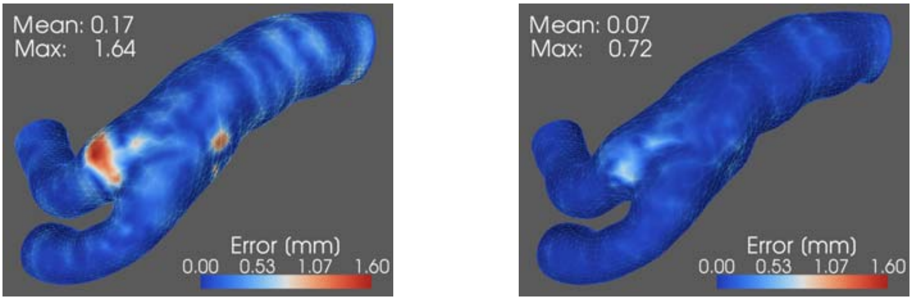

(a) Sparse registration (anterior).

(b) Dense registration (anterior).

Fig. 6. For case *AAA01*: the distance from the smooth surface mesh to the surface of the final mesh generated using 504 registration points (left) and 4536 registration points (right)

method can also be used to register a vascular geometry at one level of loading to itself at other levels of loading, thus recovering the change of shape of the lumen during the cardiac cycle.

There are two main parameters which control the level-of-detail: ϕ which controls smoothness of the surface mesh and N which controls the scale-of-detail in the final mesh, allowing to influence is left as to how much detail is transferred from the image to the volume mesh. We demonstrated that using N, the final mesh's scale-of-detail could be fine-tuned. Unfortunately, using more reference points slows down the TPS interpolation considerably as it requires a dense matrix inversion which scales with $\mathcal{O}(N^3)$. For most CFD applications high frequency features are undesired and considering the numbers in Figure 6(a) one may conclude that the added accuracy is negligible. Nevertheless, the use of TPS is one limitation of this method due to its computational complexity. The use of alternative, more efficient interpolation, using e.g. radial basis functions should be considered to shorten the run times.

As shown in Figure 4 and Table 1, our method generates comparable quality meshes to both considered standard mesh generating tools. It consistently provided a higher minimal quality, which is a significant advantage in the context of numerical simulation and it also generated meshes with a slightly better mean quality than both *NETGEN* and *TetGen*, however the advantage here is minimal. For pathological cases, *NETGEN* seems to produce less elements with quality $< 1/3$ than we do, so clearly the large deformations do contribute to lowering the mesh quality, however, for the given example, we are still only producing 0.31% of such tetrahedrons, which is still very reasonable. *NETGEN* seemed to generally outperform *TetGen*, however the surface caps at inlet and outlets had a large influence on the *TetGen* mesh quality, so a surface remesh would have resulted in improvements. The parameters we used for these meshing tools obviously had a large impact on the quality of the meshes, however, we did not focus on these parameters in particular but strove to produce the best meshes possible with approximately the same size and resolution as the ones generated by our method. The meshes produced by *TetGen* were generally of low quality on the surface; this is due to the constraint we set on the tetrahedron sizes. However, relaxing this constraint would have prohibited fair comparison. One could have optimised the surface mesh in an extra preprocessing step, but we chose not to do this as the complexity of the tool would then become a serious handicap for any potential user. Despite being experienced at using these meshing tools, we generally found that it was difficult to produce consistent meshes and typically these had sharp density changes due to locally small curvature radii. Our mesh registration technique avoids these problems and increases the mesh generation workflow efficiency. So from a mesh quality point of view our method does not radically outperform the standard mesh generators, however it produces meshes of similar quality while still providing many other advantages.

We also described an efficient way to generate a mesh-specific coordinate system which eases inter-patient comparisons of CFD velocity vectors. We only presented unstructured tetrahedral meshes, however any other mesh type e.g. structured or hybrid meshes with hexahedral boundary layers could be used without changing the algorithm.

5 Conclusions and Outlook

We have proposed a novel meshing strategy which generates co-registered meshes for large-scale studies involving numerous CFD simulations. This method fulfils the 5 requirements stated in the introduction and thus constitutes a satisfactory preprocessing pipeline for such studies. We have shown that it produces high-quality elements, even for pathological cases where the deformation is large as compared to the template mesh. To further improve the method, attention will have to be paid to the computational complexity, in particular with regards to the use of TPS. Based on this proof-of-concept, the next step will be application of the method to a large number of patient-specific data for varying vascular locations to further test its robustness and reproducibility.

Acknowledgments. This work was supported by the Indo-Swiss Joint Research Programme. We are also grateful to the Institute of Diagnostic Radiology of the Zürich University Hospital for the CT data which we used.

References

1. McGregor, R.H., Szczerba, D., Muralidhar, K., Székely, G.: A fast alternative to computational fluid dynamics for high quality imaging of blood flow. In: MICCAI, pp. 124–131 (2009)
2. Leung, J.H., Wright, A.R., Cheshire, N., Crane, J., Thom, S.A., Hughes, A.D., Xu, Y.: Fluid structure interaction of patient specific abdominal aortic aneurysms: a comparison with solid stress models. BioMedical Engineering OnLine 5(33) (2006)

3. Cebral, J.R., Yim, P.J., Löhner, R., Soto, O., Choyke, P.L.: Blood flow modeling in carotid arteries with computational fluid dynamics and MR imaging. Academic Radiology 9(11), 1286–1299 (2002)
4. Scotti, C.M., Jimenez, J., Muluk, S.C., Finol, E.A.: Wall stress and flow dynamics in abdominal aortic aneurysms: finite element analysis vs. fluid-structure interaction. Computer Methods In Biomechanics And Biomedical Engineering 11(3), 301–322 (2008)
5. Baghdadi, L., Steinman, D.A., Ladak, H.M.: Template-based finite-element mesh generation from medical images. Computer Methods and Programs in Biomedicine 77(1), 11–21 (2005)
6. Zeng, D., Ethier, C.: A mesh-updating scheme for hemodynamic simulations in vessels undergoing large deformations. Journal of Engineering Mathematics V47(3), 405–418 (2003)
7. Barber, D., Oubel, E., Frangi, A., Hose, D.: Efficient computational fluid dynamics mesh generation by image registration. Medical Image Analysis 11(6), 648–662 (2007)
8. Antiga, L., Ene-Iordache, B., Remuzzi, A.: Computational geometry for patient-specific reconstruction and meshing of blood vessels from MR and CT angiography. IEEE Transactions on Medical Imaging 22(5), 674–684 (2003)
9. Taubin, G.: Curve and surface smoothing without shrinkage. In: ICCV, pp. 852–857 (1995)
10. Antiga, L., Steinman, D.: Robust and objective decomposition and mapping of bifurcating vessels. IEEE Transactions on Medical Imaging 23(6), 704–713 (2004)
11. Fedorov, A., Chrisochoides, N.: Tetrahedral mesh generation for non-rigid registration of brain MRI: Analysis of the requirements and evaluation of solutions, pp. 55–72 (2008)
12. Si, H.: Adaptive tetrahedral mesh generation by constrained delaunay refinement. International Journal for Numerical Methods in Engineering 75(7), 856–880 (2008)
13. Garland, M., Heckbert, P.S.: Surface simplification using quadric error metrics. In: SIGGRAPH, pp. 209–216 (1997)
14. Schöberl, J.: Netgen - an advancing front 2D/3D-mesh generator based on abstract rules. Computing and Visualization in Science 1, 41–52 (1997)

Solid Mesh Registration for Radiotherapy Treatment Planning

Karsten Østergaard Noe[1,3] and Thomas Sangild Sørensen[1,2]

[1] Department of Computer Science, Aarhus University, Denmark
`noe@cs.au.dk`
[2] Institute of Clinical Medicine, Aarhus University, Denmark
[3] The Alexandra Institute, Denmark

Abstract. We present an algorithm for solid organ registration of pre-segmented data represented as tetrahedral meshes. Registration of the organ surface is driven by force terms based on a distance field representation of the source and reference shapes. Registration of internal morphology is achieved using a non-linear elastic finite element model. A key feature of the method is that the user does not need to specify boundary conditions (surface point correspondences) prior to the finite element analysis. Instead the boundary matches are found as an integrated part of the analysis. The method is evaluated on phantom data and prostate data obtained in vivo based on fiducial marker accuracy and inverse consistency of transformations. The parallel nature of the method allows an efficient implementation on a GPU and as a result the method is very fast. All validation registrations take less than 30 seconds to complete. The proposed method has many potential uses in image guided radiotherapy (IGRT) which relies on registration to account for organ deformation between treatment sessions.

1 Introduction

The challenge of registering solid organs to a common reference configuration is often encountered in medical image computing applications. In image guided radiotherapy (IGRT) for example, optimal conformation of radiation dose to tumour tissue is directly linked to the ability to adapt dose delivery to morphological variations encountered during repeated treatment sessions. Accurate conformation is of utmost importance since radiation of healthy tissue may induce severe side effects. On the other hand, failing to deliver a sufficient dose to the tumour results in failure to kill all cancer cells. Ideally organ deformations during and between treatments should be taken into account based on repetitive 3D image acquisitions (CT, CBCT, MRI etc.). By registering the corresponding organs to a common reference configuration, a geometrically resolved view can be obtained and used e.g. to compute the accumulated dose delivered at any given physical point and adjust the treatment plan accordingly.

Due to organ delineation necessary for radiotherapy treatment planning it is in many cases fair to assume that organs have been segmented prior to registration.

F. Bello and S. Cotin (Eds.): ISBMS 2010, LNCS 5958, pp. 59–70, 2010.
© Springer-Verlag Berlin Heidelberg 2010

Having segmented an organ in two configurations however does not imply that a correct surface correspondence function is defined, let alone correspondence of interior morphology. This paper describes an automatic algorithm to register two solid meshes (tetrahedral meshes in the current work), which does not require the user to specify boundary correspondences. The algorithm computes a transformation, which maps boundary nodes in the source mesh onto the boundary of the reference mesh subject to a minimisation of the elastic energy interiorly in the deformed source mesh. The algorithm iteratively deforms the source mesh towards the reference mesh. In each iteration and for each node near the source mesh's surface, a force acting on the corresponding node is computed. This force expression is derived from Euclidean distance field computations and mesh intrinsics. Based on these driving forces a non-linear elastic finite element model (FEM) subsequently computes node displacements for the entire source mesh. The presented work is the continuation of work previously published [1] in which we used a simpler elastic model [2] for regularisation of the organ deformation.

2 Related Work

Since using distance fields and finite element analysis (FEA) for mesh registration is not unique to this paper we reference some representative previous work in the following.

Some authors have used elastic FEA as a regularisation term in intensity based registration. In [3] a linear elastic deformable FEM is applied to the entire image domain, and the image is divided into subvolumes, which are given different material properties. These are connected by appropriate boundary conditions. This technique is used for registering images used in preoperative planning of brain surgery. In subsequent work the linear elastic model is coupled with a model of incompressible fluids via appropriate boundary conditions [4]. Peckar et al. have used linear elastic FEA for finding a smooth transformation that satisfies a number of point constraints. Schnabel et al. [5] have also used a finite element model in connection with intensity based registration, but for creation of images to be registered; their idea was to generate realistic registration problems with a known displacement mapping to evaluate the accuracy of existing registration methods.

Yan et al. used FEA of for quantifying organ motion based on volumetric meshes retrieved from segmentation of CT images. This was used for dose accumulation [6]. Ferrant et al. used active surfaces and distance fields for initial surface matching of brain meshes and FEA for subsequent computation of interior mesh vertex displacements [7]. This model was also used for prostate registration[8]. Brock et al. also use FEA for estimating interior vertex displacements after initial boundary vertex projections [9][10] and have also in earlier work used a linear elastic model for investigating the impact of breathing deformation on the delivered dose to a liver tumour[11]. They use a pre-computed surface correspondence map based on curvature correspondences as boundary conditions to the simulation.

Liang and Yan note that the accuracy of such techniques is limited by the surface projection algorithm [12]. To alleviate this problem they solve for interior and boundary vertices simultaneously by applying extra constraints ensuring that boundary vertices of the deforming organ stay on a triangle mesh describing the surface of the reference organ. Their model requires initial user defined boundary landmark correspondences.

In most work on FEM in image registration a linear elastic tissue deformation model has been applied. For large deformations however, especially those involving rotation, this model induces significant errors [13]. Consequently we have chosen a non-linear model.

Recently Choi et al. published an iterative mesh fitting method which bears many similarities with our method [14]. They define a surface distance term for driving the registration. Unlike our approach their method uses a linear elastic FEM to displace meshes. In order to handle large deformations they utilise a technique called stiffness warping to account for the rotational part of the deformation. Zhang et al. avoid manual definition of landmarks by employing a finite element contact impact analysis [15]. This allows a model of a lung to slide in the pleural cavity. They compute the deformation in multiple steps since their linear elastic model is not able to handle the large deformations of the lung in one step. Also Haker et al. use an iterative FEM [16]. Based on landmarks they project both source and reference organs onto a sphere using an active surface model. The sphere has been triangulated into a tetrahedral mesh, and guided by a few control landmarks, a point correspondence is found for mesh vertices. These are used as boundary conditions for a volumetric finite element analysis. Their work is based on theory in conformal mapping[1][17][18]. Conformal mapping was also used by Warfield et al., who also extended the linear elastic model with inhomogeneous material characteristics which allows fibres to be modelled [19].

Euclidean *distance fields* are used in an N-dimensional space to track the (Euclidean) distance to the closest point of an object in this space. In 3D the field is used to describe the distance to a 2D surface. Besides the already mentioned work by Ferrant et al. [7] and Choi et al. [14], a number of groups working on medical image registration have included the use of Euclidean distance fields in their work. In [20] tissue classification in reference CT images is performed based on fixed Hounsfield units and distance fields to material boundaries are computed. In the source image bones are represented as a point cloud. Based on an SSD measure of distance values bones are rigidly registered to the reference image. This is used for tracking of wrist bones. Marai et al. also minimised a cost function of distance field terms to recover rigid body transformations [20]. In [21] a similarity metric based on the sum of squared difference of distance fields is constructed for shape matching. Here the transformation consists of both a rigid term and a term for local deformable corrections. Xiao et al. use distance fields for rigid registration of surfaces that only partially overlap [22].

---

[1] That the mapping is conformal means that it is bijective and that angles are preserved.

3 Materials and Method

3.1 Mesh Representation

Our aim is to register a volume of interest (VOI), usually an organ, given at two different configurations. Data from a three-dimensional imaging source has been segmented prior to the registration and the VOI in both source and reference datasets are represented as binary volumes. These binary images are initially smoothed using a Gaussian filter. Next, Euclidean distance fields $\phi : \mathbb{R}^3 \rightarrow \mathbb{R}$ are generated for both datasets (Insight Segmentation and Registration Toolkit, ITK)[2].

Based on the distance fields we use an in-house implementation of the isosurface stuffing mesh generation algorithm [23] which produces a tetrahedral mesh. This meshing method guarantees strict upper and lower bounds on the dihedral angles in the generated tetrahedra, which increases the stability of the FEM.

3.2 External Driving Forces

The aim of the registration is to find a transformation of mesh nodes such that the surface nodes of the source body is mapped to the surface of the reference body while interior nodes are at an equilibrium. We propose an iterative algorithm driven by forces computed near the boundary of the source shape. These forces, concatenated in the vector $\mathbf{R}$, are defined for each source mesh node i by

$$\mathbf{R}_i = \gamma(\mathbf{A}_i + \beta \mathbf{B}_i) \tag{1}$$

where β is constant throughout the registration process and γ is iteratively increased until the surface match is achieved.

The force term $\mathbf{A}$ is based on the distance fields that were pre-computed before mesh generation of both the source (ϕ_S) and reference (ϕ_R) VOI. It applies to all mesh nodes less than τ millimetres from the source shape surface and is given by

$$\mathbf{A}_i = \left(\phi_S(\mathbf{p}_i^o) - \phi_R(\mathbf{p}_i^d)\right) \nabla\phi_R|_{\mathbf{p}_i^d} \tag{2}$$

where $\mathbf{p}_i^o$ denotes the initial position of particle i (in the source shape) and $\mathbf{p}_i^d$ denotes the position of particle i in the current configuration of the iterative registration process. The expression $\phi_R|_{\mathbf{p}_i^d}$ evaluates the reference surface distance at the deformed position of particle i. Intuitively Eq. (2) provides force vectors in the direction of steepest descent of the distance field calculated from the reference shape - i.e. towards the reference volume. The forces are weighted with the difference between each particle's current distance to the reference shape and the particles original distance from the surface in the source shape. $\mathbf{A}_i$ vanishes as particle i finds it "desired" distance to the reference surface.

---

[2] See `http://www.itk.org/`

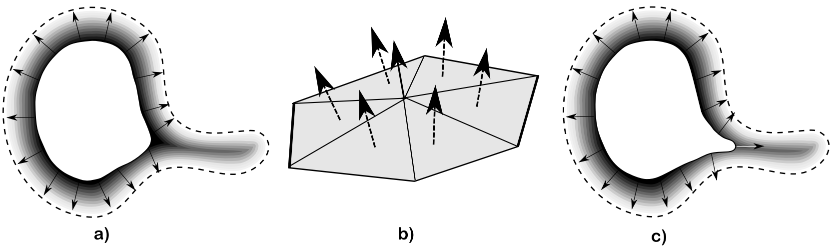

Fig. 1. Illustration of the forces driving the source shape surface vertices towards the surface of the reference shape. a) 2D illustration showing the reference surface (dashed line), distance field (intensity gradient), source shape (white area), and the direction of forces derived from force term **A**. b) a surface patch consisting of 6 surface triangles surrounding a vertex. A normal vector (dashed line) is calculated per triangle, and the mean vector is used in force term **B**. c) 2D illustration of **B** forces showing the same components as in a). Notice how this term allows the source boundary to move into narrow extrusions of the reference surface.

Force term **B** is working normal to the current configuration of the source surface and is calculated for all boundary nodes as the mean of all normal vectors from adjacent surface triangles:

$$\mathbf{B}_i = \left(\phi_S(\mathbf{p}_i^o) - \phi_R(\mathbf{p}_i^d)\right) \frac{1}{N_i} \sum_{\mathbf{f} \in \mathscr{T}_i} (\mathbf{f}_2 - \mathbf{f}_1) \times (\mathbf{f}_3 - \mathbf{f}_1) \tag{3}$$

where $\mathscr{T}_i$ denotes the set of N_i surface triangles which include node i. Each surface triangle $\mathbf{f}$ consists of node points $\mathbf{f}_1$, $\mathbf{f}_2$ and $\mathbf{f}_3$. The significance of force terms **A** and **B** is illustrated in fig. 1.

3.3 Non-linear Elastic Displacement

In each iteration a non-linear elastic FEM is used to displace the source mesh based on the "boundary" forces **R** computed above. This step is based on the work by Miller et al. defining a total Lagrangian explicit dynamics (TLED) FEM formulation [24]. An efficient parallel implementation have been described in detail by Taylor et. al [25]. A summary of their model is provided below.

The TLED FEM on a tetrahedral mesh leads to the standard equations of equilibrium, $\mathbf{M}\ddot{\mathbf{U}} + \mathbf{D}\dot{\mathbf{U}} + \mathbf{K}(\mathbf{U})\mathbf{U} = \mathbf{R}$, where $\mathbf{U}$ is the nodal displacements, $\mathbf{M}$ is a mass matrix, $\mathbf{D}$ is a damping matrix, $\mathbf{K(U)}$ is a stiffness matrix, and $\mathbf{R}$ is the external forces. Notice that $\mathbf{K}$ is a function of $\mathbf{U}$. In this work we omit the dynamic terms $\mathbf{M}\ddot{\mathbf{U}}$ and $\mathbf{D}\dot{\mathbf{U}}$. Hence, for a given load of external forces we search for a configuration of nodal displacements $\mathbf{U}$ in which $\mathbf{K}(\mathbf{U})\mathbf{U} = \mathbf{R}(\mathbf{U})$. In present work $\mathbf{R}$ also depends on $\mathbf{U}$ according to equations (1)-(3).

The TLED FEM method describes shape deformation and displacements with respect to the initial undeformed geometry. Element function derivatives precalculated from the initial mesh configuration are used in each iteration when calculating interior forces (stress and strain) reacting to an exterior load. I.e. with such formulation continuous recalculation of spatial derivatives of the element functions is avoided. Deformation is measured in terms of the *deformation gradient* tensor ${}_0^t\mathbf{X}$ which contains elements ${}_0^tX_{ij} = \frac{\partial^t x_i}{\partial^0 x_j}$. In words, the deformation gradient describes the degree of displacement of material point coordinates ${}^t\mathbf{x}$ with respect to the initial position ${}^0\mathbf{x}$. By convention a left superscript describes at which configuration of the body a quantity is measured and left subscript describes the configuration the measurement is made with respect to. The deformation gradient can be calculated from the node displacements and precomputed element shape function derivatives [24], [25].

The internal forces $\mathbf{K}(\mathbf{U})\mathbf{U}$ are calculated as a sum of elemental forces $\mathbf{K}(\mathbf{U})\mathbf{U} = \mathbf{F}(\mathbf{U}) = \sum_e {}^t\tilde{\mathbf{F}}^{(e)}$ where e denotes the individual elements. For linear tetrahedral elements ${}^\mathbf{t}\tilde{\mathbf{F}}$ can be evaluated as ${}^t\tilde{\mathbf{F}} = {}^0V \; {}_0^t\mathbf{B}_L^T \; {}_0^t\hat{\mathbf{S}}$ where ${}^0V$ is the volume of the undeformed tetrahedron, ${}_0\mathbf{B}_L$ is the strain-displacement matrix, which describes the relationship between nodal displacements and strain in an element, and ${}_0^t\hat{\mathbf{S}} = [{}_0^tS_{11} \; {}_0^tS_{22} \; {}_0^tS_{33} \; {}_0^tS_{12} \; {}_0^tS_{23} \; {}_0^tS_{13}]^T$ is the second Piola-Kirchhoff stress on vector form. As the element deforms ${}_0^t\mathbf{B}_L$ can be found by transforming the initial strain displacement matrix ${}_0\mathbf{B}_{L0}$ using the transformation gradient : ${}_0^t\mathbf{B}_L^{(a)} = {}_0\mathbf{B}_{L0}^{(a)} \; {}_0^t\mathbf{X}^T$ [25]. For ${}_0^t\hat{\mathbf{S}}$ we use a hyperelastic neo-Hookean model given by ${}_0^tS_{ij} = \mu(\delta_{ij} - {}_0^t C_{ij}^{-1}) + \lambda {}^tJ({}^tJ - 1){}_0^tC_{ij}^{-1}$. Here μ and λ are the Lamé constants, δ_{ij} is Kronecker's delta, ${}^tJ = \det({}_0^t\mathbf{X})$, and ${}_0^t\mathbf{C}$ is the Right Cauchy-Green deformation tensor calculated by ${}_0^t\mathbf{C} = {}_0^t\mathbf{X}^T \; {}_0^t\mathbf{X}$.

3.4 Registration Algorithm

The search for a source mesh deformation in which the source and reference surfaces are matched while interior nodes are at equilibrium is based on a gradient descent type approach. In each iteration of the registration algorithm the total forces, $\mathbf{T}(\mathbf{U})$, acting on the source shape is calculated as $\mathbf{T}(\mathbf{U}) = \mathbf{R}(\mathbf{U}) + \mathbf{F}(\mathbf{U})$. Each entry in this vector is used to update displacements ($\mathbf{U}_i \leftarrow \mathbf{U}_i + \delta \cdot \mathbf{T}_i$) with a maximum allowed displacement change of $\Delta_{U,max}$.

The scaling factor γ (Eq. (1)) is iteratively increased by multiplication with constant factor $\Delta_\gamma > 1$ whenever $\mathbf{T}(\mathbf{U})$ is approaching an equilibrium, i.e. when $\max(|\mathbf{T}(\mathbf{U})_i|) < T_1$. The algorithm terminates when all interior nodes are at rest and increasing γ does not increase $\max(|\mathbf{R}(\mathbf{U})_i|)$, at which point all surface nodes of the source mesh have been registered to the surface of the reference mesh. This leads to the termination criterion $\max(|\mathbf{T}(\mathbf{U})_i|) < T_2$.

3.5 Implementation

Compute intensive parts of the proposed registration method was implemented on the GPU using the programming framework CUDA. The GPU implementation of the TLED algorithm is similar to the implementation presented by Taylor et al. [25]. As the internal forces in the FEM are calculated per element the calculations in the TLED model can be massively parallelised. When accumulating forces from elementwise internal force computation, care must be taken

Algorithm 1. Overview of our registration algorithm

```
Let the source organ shape be represented as a tetrahedral mesh with original node distances $\phi_S(p_i^o)$ known
Let the reference organ shape be represented as an Euclidean distance field $\phi_R$
Let $\beta$, $\tau$, $\lambda$, and $\mu$ be known and constant
Let all node displacements $\mathbf{U}$ be initialised to zero
$\gamma \leftarrow \gamma_0$
repeat
    Calculate external forces $\mathbf{R}(\mathbf{U})$ from (2), (3) and (1)
    Evaluate internal forces $\mathbf{F}(\mathbf{U})$ using the FEM
    Calculate resulting force $\mathbf{T}(\mathbf{U}) = \mathbf{R}(\mathbf{U}) + \mathbf{F}(\mathbf{U})$
    Update displacements $\mathbf{U}_i \leftarrow \mathbf{U}_i + \delta \cdot \mathbf{T}_i$, with a maximum displacement change of $\Delta_{U,max}$
    if $\max(|\mathbf{T}_i|) < T_1$ then
        $\gamma \leftarrow \gamma \cdot \Delta_\gamma$
until $\max(|\mathbf{T}_i|) < T_2$ ;
```

to avoid write conflicts. Our solution is to associate four write indices to each tetrahedron which enable us to know where to store the force contributions in elementwise kernels. A per-vertex kernel is subsequently responsible for addition of force contributions.

For evaluation of the expressions of the type $\max(|\mathbf{T}_i|) < T$, a kernel has been written which inspects a $\mathbf{T}_i$ value and stores the value `false` in a fixed global memory position if $|\mathbf{T}_i| > T$. Before invocation of this kernel on all force vectors, `true` is written to the particular memory position, and if it is still `true` after all kernels have terminated the criterion $\max(|\mathbf{T}_i|) < T$ is fulfilled. The running times reported below are measured on an NVIDIA Quadro FX 5600 graphics card in a computer with an Intel core 2 6400 CPU.

3.6 Evaluation Data

Modelling wax phantom: To evaluate the performance of the proposed registration method when registering meshes undergoing large scale deformation, we constructed a phantom data set as a modelling wax cylinder. The phantom was CT-scanned in three configurations: **(a)** straight **(b)** bent approximately 45 degrees and **(c)** bent 90 degrees. The phantom surface was manually delineated. Seven lead markers were positioned on the surface of the phantom for evaluation purposes. The following parameters were used for the registration algorithm: $\beta = 0.01$, $\gamma_0 = 1000$, $\lambda = 5$ kPa, $\mu = 10$ kPa, $\Delta_\gamma = 1.03$, $\Delta_{U,max} = 0.005$ mm, $\tau = 5$ mm, $\delta = 0.01$, $T_1 = 30$ kN, and $T_2 = 3$ kN.

Prostate data set: To evaluate the algorithm on actual morphology acquired in vivo, we registered two manually delineated prostates from successive MRI scans of a prostate cancer patient. As no ground truth about the deformation between the two configurations **(a)** and **(b)** of the organ is available, an evaluation was performed based on inverse consistency of the resulting transformation. For prostate registration parameters were set as above with the following exceptions: $\lambda = 0.33$ MPa, $\mu = 3.3$ kPa, and $\Delta_\gamma = 1.07$.

4 Results

4.1 Modelling Wax Phantom Registration

A mesh consisting of 6034 tetrahedra was constructed from configuration **(a)** of the phantom cylinder and registered to configurations **(b)** and **(c)**. The two registrations were completed in 9 seconds and 17 seconds respectively. The results are shown in fig. 2. The marker positions were expressed in barycentric coordinates on a associated surface triangle and tracked to the final deformed configuration of the mesh. For each marker the registration error was calculated as the length of the difference vector between the registered marker position and the corresponding marker positions in the reference mesh. For the registration from configuration **(a)** to configuration **(b)** the initial error was 14.2 mm ± 12.7 mm (average ± std. dev.). After registration the error was reduced to 1.33 mm ± 1.39 mm. When registering configuration **(a)** to configuration **(c)** the error was reduced from 26.9 mm ± 24.8 mm to 2.03 mm ± 1.03 mm.

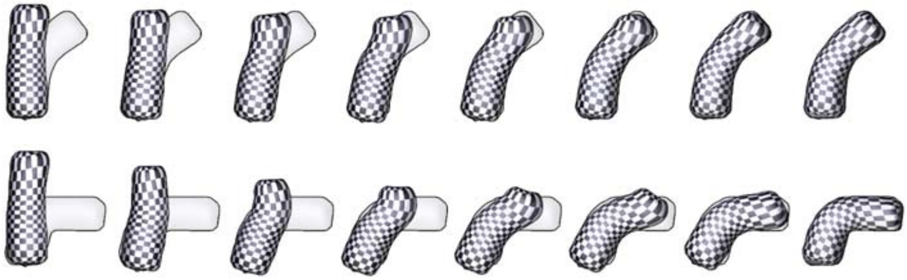

Fig. 2. Iterative registration of a modelling wax cylinder from a straight configuration to two configurations with different degrees of bending (top and bottom respectively). The leftmost images depict the initial source mesh configurations with the reference mesh overlaid transparently. The rightmost images depict the final deformation. Intermediate steps in between show every 1000th iteration (top) or every 2000th iteration (bottom). A checkerboard pattern has been mapped to the surface for visualisation of movement.

4.2 Prostate Registration

From the prostate delineations in two MRI dataset meshes were created consisting of 49005 **(a)** and 50697 **(b)** tetrahedra respectively. Two registrations were made: from **(a)** to **(b)** and **(b)** to **(a)**. The running times of the two registration were 20 seconds and 28 seconds respectively. The results are shown in fig. 3. For

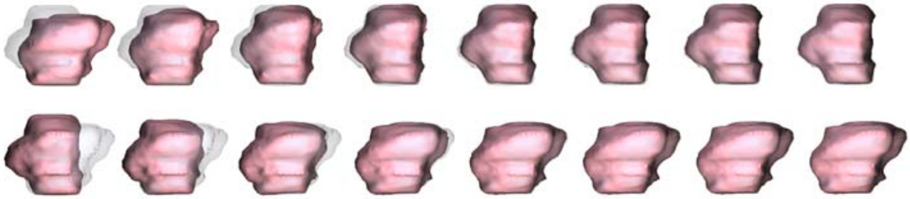

Fig. 3. Two-way registration of two prostate meshes obtained from successive MRI scans of a prostate cancer patient. The leftmost images depict the initial configurations of the source mesh with the reference mesh overlaid transparently. The rightmost images depict the final deformation. Intermediate steps in between show every 1000th iteration.

5000 randomly selected points inside prostate configuration **(a)** registration consistency errors were evaluated by transforming the point from configuration **(a)** to configuration **(b)** and back. The average inverse consistency errors were calculated as the average length of each vector between the initial and final points. The average obtained errors were 0.955 mm ± 0.469 mm (max = 2.62 mm). This should be seen relative to the registration displacements of these same points: 6.25 mm ± 2.83 mm (max = 16.4224 mm). The distribution of the inverse consistency errors can be seen in figure 4.

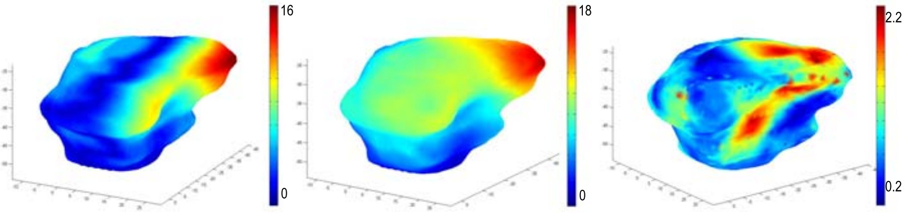

Fig. 4. Inverse consistency errors. Left: distance from source shape surface to surface of reference shape. Middle: Magnitude of deformation found by the registration. Right: Distribution of consistency errors 2 mm below surface. All measures are in millimetres.

5 Discussion

Considering the accumulation of inherent errors such as contouring errors, finite image resolution etc. we are satisfied with the accuracy achieved in the phantom experiment. With respect to the prostate registration we find a mean inverse consistency error of less than 1 mm promising as well. However, as the ground truth in the latter experiment is unknown, this does not necessarily imply that the actual error is this low. Clinical studies including patients with implanted fiducial markers or other consistent anatomical landmarks within the VOI are needed to further evaluate the registration accuracy.

The proposed method includes a number of free parameters that must be defined initially. Based on our experience, the algorithm is quite robust with respect to the choice of most of these parameters. Note however that when different types of tissue are deformed, it is necessary not only to change the material parameters λ and μ but also to adjust Δ_γ which governs rate of increase the driving forces during the registration process.

By incorporating a physically consistent deformation model, it is possible to specify measured material properties for the morphology being registered. When using different parameters for e.g. tumour tissue and surrounding healthy tissue, we can furthermore register non-homogeneous materials. It is left for further studies to investigate this effect on the registration accuracy.

The introduction of the force term **B** was motivated by the inability of the distance field term to lead the surface nodes into narrow boundary concavities. An alternative to introducing the **B** term would be using the *gradient vector flow* approach of Xu and Prince [26]. Based on a diffusion of gradient vectors, their approach creates a vector field which points towards the surface but also points into narrow concavities.

Due to the nature of the proposed algorithm it can easily be parallelised and implemented e.g. on a GPU (as we did in this paper) to achieve high performance. We find that execution times in the order of 20-30 seconds very acceptable for potential clinical use. Due to the parameter $\Delta_{U,max}$, which limits the magnitude of displacement changes in each iteration, the running time is highly dependent on the initial magnitude of deformation between source and reference shapes. Thus registration times do vary from case to case.

Organ registration has multiple uses in the field of IGRT such as dose warping and dose accumulation. Importantly, since the proposed method relies on pre-segmented data, it can be used for multimodal registration of e.g. prostate in the context of functional imaging. Another potential use is creating patient-individual organ deformation models based on principal component analysis [27].

6 Conclusions

We have presented a method for finding point correspondences between organs delineated in successive scans. The method is based on Euclidean distance fields which allow us to evaluate local driving forces independently for each node in a tetrahedral mesh. The correspondence is regularised using a non-linear FEM. Driving force calculation and FEA is massively parallelisable allowing us to implement the method on a GPU. As a consequence the proposed method is very fast. It shows promise as a tool for use in IGRT and an important next step is a further examination of the achieved accuracy.

Acknowledgements

The work presented in this paper has been partly funded by Varian Medical Systems, Inc., Palo Alto, California and the Lundbeck Foundation Centre for Interventional Research in Radiation Oncology (CIRRO). Thanks to Kari Tanderup for the modelling wax phantom data and to Matthias Söhn for valuable discussions during the writing of this paper.

References

1. Noe, K.Ø., Mosegaard, J., Tanderup, K., Sørensen, T.S.: A framework for shape matching in deformable image registration. Stud. Health. Technol. Inform. 132, 333–335 (2008)
2. Marchal, M., Promayon, E., Troccaz, J.: Simulating prostate surgical procedures with a discrete soft tissue model. In: Workshop in Virtual Reality and Physical Simulation (2006)
3. Hagemann, A., Rohr, K., Stiehl, H.S., Spetzger, U., Gilsbach, J.M.: Biomechanical modeling of the human head for physically based, nonrigid image registration. IEEE transactions on medical imaging 18, 875–882 (1999)
4. Hagemann, A., Rohr, K., Stiehl, H.S.: Coupling of fluid and elastic models for biomechanical simulations of brain deformations using fem. Medical Image Analysis 6(4), 375–388 (2002)
5. Schnabel, J., Tanner, C., Castellano-Smith, A., Degenhard, A., Leach, M., Hose, D., Hill, D., Hawkes, D.: Validation of nonrigid image registration using finite-element methods: application to breast mr images. IEEE Transactions on Medical Imaging 22(2), 238–247 (2003)
6. Yan, D., Jaffray, D.A., Wong, J.W.: A model to accumulate fractionated dose in a deforming organ. International Journal of Radiation Oncology*Biology*Physics 44(3), 665–675 (1999)
7. Ferrant, M., Warfield, S.K., Nabavi, A., Jolesz, F.A., Kikinis, R.: Registration of 3d intraoperative mr images of the brain using a finite element biomechanical model. IEEE Transactions on Medical Imaging, 1384–1397 (2001)
8. Bharatha, A., Hirose, M., Hata, N., Warfield, S.K., Ferrant, M., Zou, K.H., Suarez-Santana, E., Ruiz-Alzola, J., D'Amico, A., Cormack, R.A., Kikinis, R., Jolesz, F.A., Tempany, C.M.C.: Evaluation of three-dimensional finite element-based deformable registration of pre- and intraoperative prostate imaging. Medical Physics 28, 2551–2560 (2001)
9. Brock, K.K., Sharpe, M.B., Dawson, L.A., Kim, S.M., Jaffray, D.A.: Accuracy of finite element model-based multi-organ deformable image registration. Medical Physics 32(6), 1647–1659 (2005)
10. Brock, K.K., Dawson, L.A., Sharpe, M.B., Moseley, D.J., Jaffray, D.A.: Feasibility of a novel deformable image registration technique to facilitate classification, targeting, and monitoring of tumor and normal tissue. Int. J. Radiat. Oncol. Biol. Phys. 64(4), 1245–1254 (2006)
11. Brock, K.K., McShan, D.L., Haken, R.K.T., Hollister, S.J., Dawson, L.A., Balter, J.M.: Inclusion of organ deformation in dose calculations. Medical Physics 30(3), 290–295 (2003)
12. Liang, J., Yan, D.: Reducing uncertainties in volumetric image based deformable organ registration. Med. Phys. 30, 2116–2122 (2003)

13. Picinbono, G., Delingette, H., Ayache, N.: Nonlinear and anisotropic elastic soft tissue models for medical simulation. In: Proceedings of IEEE International Conference on Robotics and Automation (ICRA), 2001, vol. 2, pp. 1370–1375 (2001)
14. Choi, J., Szymczak, A.: Fitting solid meshes to animated surfaces using linear elasticity. ACM Trans. Graph. 28(1), 1–10 (2009)
15. Zhang, T., Orton, N.P., Mackie, T.R., Paliwal, B.R.: Technical note: A novel boundary condition using contact elements for finite element based deformable image registration. Medical Physics 31(9), 2412–2415 (2004)
16. Haker, S., Warfield, S.K., Tempany, C.M.: Landmark-guided surface matching and volumetric warping for improved prostate biopsy targeting and guidance. In: Barillot, C., Haynor, D.R., Hellier, P. (eds.) MICCAI 2004. LNCS, vol. 3216, pp. 853–861. Springer, Heidelberg (2004)
17. Angenent, S., Haker, S., Tannenbaum, A., Kikinis, R.: On the laplace-beltrami operator and brain surface flattening. IEEE Transactions on Medical Imaging 18(8), 700–711 (1999)
18. Haker, S., Angenent, S., Tannenbaum, A., Kikinis, R., Sapiro, G., Halle, M.: Conformal surface parameterization for texture mapping. IEEE Transactions on Visualization and Computer Graphics 6(2), 181–189 (2000)
19. Warfield, S.K., Haker, S.J., Talos, I.F., Kemper, C.A., Weisenfeld, N., Mewes, A.U., Goldberg-Zimring, D., Zou, K.H., Westin, C.F., Wells, W.M., Tempany, C.M., Golby, A., Black, P.M., Jolesz, F.A., Kikinis, R.: Capturing intraoperative deformations: research experience at brigham and women's hospital. Medical Image Analysis 9(2), 145–162 (2005)
20. Marai, G.E., Laidlaw, D.H., Crisco, J.J.: Super-resolution registration using tissue-classified distance fields. IEEE transactions on medical imaging 25, 177–187 (2006)
21. Paragios, N., Rousson, M., Ramesha, V.: Non-rigid registration using distance functions. In: Computer Vision and Image Understanding, pp. 142–165 (2003)
22. Xiao, G., Ong, S., Foong, K.: 3d registration of partially overlapping surfaces using a volumetric approach. Image and Vision Computing 25(6), 934–944 (2007)
23. Labelle, F., Shewchuk, J.R.: Isosurface stuffing: fast tetrahedral meshes with good dihedral angles. In: SIGGRAPH 2007: ACM SIGGRAPH 2007 papers, p. 57. ACM, New York (2007)
24. Miller, C., Joldes, G., Lance, D., Wittek, A.: Total lagrangian explicit dynamics finite element algorithm for computing soft tissue deformation. Communications in Numerical Methods in Engineering 23(2), 121–134 (2006)
25. Taylor, Z.A., Cheng, M., Ourselin, S.: High-speed nonlinear finite element analysis for surgical simulation using graphics processing units. IEEE Transactions on Medical Imaging 27(5), 650–663 (2008)
26. Xu, C., Prince, J.: Snakes, shapes, and gradient vector flow. IEEE Transactions on Image Processing 7(3), 359–369 (1998)
27. Söhn, M., Birkner, M., Yan, D., Alber, M.: Modelling individual geometric variation based on dominant eigenmodes of organ deformation: implementation and evaluation. Physics in Medicine and Biology 50, 5893–5908 (2005)

Physics-Based Modeling of the Pregnant Woman

Juan Pablo de la Plata Alcalde, Lazar Bibin, Jérémie Anquez,
Tamy Boubekeur, Elsa Angelini, and Isabelle Bloch

Télécom ParisTech, CNRS UMR 5141 LTCI, Signal and Image Dept,
Paris, France
`{delaplat,lazar.bibin,jeremie.anquez,tamy.boubekeur,`
`elsa.angelini,isabelle.bloch}@telecom-paristech.fr`
`http://www.tsi.enst.fr`

Abstract. High quality obstetric images have become readily available with fast magnetic resonance imaging protocols or new 3D ultrasound probes. These obstetric images provide detailed information which can be used to create realistic models of the fetus at different stages of gestation. Unfortunately, the anatomy of the mother is only partially visible in the obstetric images and a full model of the pregnant woman can only be based on deformations of a non-pregnant woman body. Numerical pregnant women models are useful for a variety of applications, including dosimetry studies to assess the potential health effects of low-frequency electro-magnetic fields generated by power lines and electrical devices, planning of delivery procedure or training of obstetrical echographers. Only few models of pregnant women have been developed up to now, and they all lack realism and medical accuracy in representing the different stages of gestation and the anatomical variability of the fetal anatomy and positioning. This paper describes a novel methodology to create a set of detailed 3D pregnant women based on a series of controlled automatic deformations of a generic woman body envelope to insert pre-segmented utero-fetal units using a physics-based interactive modeler.

Keywords: Anatomical modeling, medical simulation, fetus, ante-natal imaging.

1 Overview of Existing Pregnant Women Models

Numerical models of the adult and infant body used for dosimetry [1] can be categorized into three classes, depending on the type of representation. The first class includes mathematical models, where anatomical structures are described using surface equations. They were proposed for their ease of implementation in pioneer works [2], but they are inherently limited in terms of anatomical realism. For instance, modeling the brain with an ellipsoid remains a coarse simplification of the organ. The second class includes voxelized models, built with segmented medical images, which are now preferred as they accurately represent the human anatomy. However, medical data is not always available and its segmentation requires an important amount of manual interaction. This explains the introduction of a third class: the synthetic models, built using computer graphics

F. Bello and S. Cotin (Eds.): ISBMS 2010, LNCS 5958, pp. 71–81, 2010.
© Springer-Verlag Berlin Heidelberg 2010

software tools such as Blender [3]. The most satisfying models are generated under supervision of experienced anatomists, to ensure their realism [4].

In its 2005 research agenda, the World Health Organization stressed out the need for developing numerical models of the pregnant woman at different stages of pregnancy, in order to study the influence of electromagnetic fields on the fetus. Since whole body medical imaging data sets cannot be acquired on a pregnant patient for ethical reasons (unnecessary fetal exposure) and technical limitations (long acquisition time), two strategies have been employed to build such models. The first strategy consists in elaborating truncated voxelized models. For example, CT images were used to generate models of the maternal trunk between the 12th and the 36th weeks of gestation in [5], distinguishing the uterus, the amniotic fluid, the fetal soft tissues and the fetal bones within the utero-fetal-unit models.

However, whole body models, i.e. representing the pregnant woman from head-to-tow, are desirable and constitute the second modeling strategy. The few works dedicated to model the entire pregnant woman at different stages of pregnancy are based on emerging hybrid modeling, which relies on the combination of mathematical, voxelized and/or synthetic models. In [6], a set of mathematical models of the utero-fetal unit (UFU) at 8, 13, 26, and 38 weeks of gestation [7] were voxelized and embedded in the non-pregnant voxelized model NAOMI. Voxel editing was required to translate and deform NAOMI organs away from the uterus. In [8], hybrid models using the UFU and maternal organs models from [9], the VIP-MAN model from [10] and a synthetic model of the fetus surface were merged to construct 3D surface models of a pregnant woman with detailed organs. Three models were built at 3, 6, and 9 months of pregnancy. To insert the UFU, the maternal organs were manually translated and deformed to avoid overlaps using free-form deformation lattices. Fetal soft tissues, brain and skeleton were distinguished. In [11], a voxelized model of the UFU at 26 weeks of gestation was extracted from magnetic resonance imaging (MRI) data. UFU models at 13 and 18 weeks of gestation were obtained by downscaling. The models are then embedded inside a detailed voxelized non-pregnant woman model [12] using free-form deformations.

Our group has proposed a methodological framework in [13,14] to create UFU models from medical images and generate hybrid pregnant woman models. Several realistic and detailed voxelized models of the UFU were built using MRI and 3D ultrasound (US) data sets, covering the whole pregnancy. Insertion and placement of the UFU into a woman body model was initially performed manually. Automating this task is desirable to enable the generation of multiple models, while limiting manual and subjective interactions.

In this paper, we propose a method to automatically insert the UFU into a synthetic woman body, which is deformed to host the whole uterus. As dosimetry or medical studies may require models represented in a reclined or standing positions, we also want to simulate different positioning configurations, while medical image acquisitions are always performed with patients lying down. To guarantee the realism of our women body models as well as the representation of the major variations in anatomical configurations and morphologies, we decided to design a tool to control the fat distribution on the pregnant woman envelope.

2 Utero-Fetal Modeling

2.1 Image Database

With the collaboration of obstetricians from the hospitals of Port-Royal and Beaujon (Paris, France), we gathered 18 3D ultrasound (US) sequences between 8 and 14 WA with high image quality. These US images have a sub-millimetric and isotropic resolution (typically $0.6 \times 0.6 \times 0.6$ mm^3).

In collaboration with pediatric radiologists from the Saint Vincent de Paul hospital (Paris, France), we gathered 22 MRI Steady State Free Precession (SSFP) sequences [15] between 26 and 34 WA. Strict image quality criteria for inclusion in the database are: large field of view to include the whole uterus, good overall contrast, good spatial resolution ($1 \times 1 \times 4$ mm^3), fast acquisition (less than 30 seconds), and low sensitivity to fetal movement artifacts.

2.2 Image Segmentation

The medical images used to build the UFU models are rather novel and have not yet lead to much work in the image processing community. Therefore, we developed specific tools for their segmentation, combining automatic methods for some tissues and interactive refinements, using the software tools MIPAV (http://mipav.cit.nih.gov/) and Slicer (www.slicer.org).

Regarding the 3D US data, statistical distributions of the tissues were integrated in a deformable model to differentiate automatically the amniotic fluid from the fetal and maternal tissues [16].

For the 3D MRI data, the segmentation procedure is based on shape and appearance models and deformable contours [17]. It was performed automatically for some fetal organs (eyes, brain, ...) and semi-interactively for some others.

These approaches have been validated by our clinical collaborators, who provided the data and work routinely with them to precisely measure fetal growth of individual organs. This validation was performed visually on a number of representative images (both US and MRI ones). This type of validation was considered as sufficient for the targeted application, where a very high accuracy is not mandatory to achieve a good realism of the derived models.

2.3 UFU Surface Reconstruction

To reconstruct the surface mesh of the tissues from the segmentation results of the 3D US images we used a standard marching cubes algorithm. Nevertheless, using this method with the segmentation results of the MRI data provided meshes with staircase effects. To reconstruct smooth meshes, we used multiple point-based graphics tools, in particular the moving least square (MLS) operator, which has recently emerged as an efficient and robust technique in digital geometry processing [13]. All the UFU models were anatomically validated by obstetricians and pediatric physicians.

3 Physics-Based Modeling of Pregnant Women

The developed pregnant women models are composed of three components: (i) a set of pre-segmented UFU, (ii) an empty woman body envelope provided by Daz Studio [18], called Victoria, (iii) the pelvis bone of a pregnant woman, pre-segmented on a CT data set of a subject having the same height as Victoria (167 cm), provided in [5]. The goal is to apply physics-based simulations on the woman body to create realistic and flexible heterogeneous models of pregnant women. We first prepare the models to use them efficiently while running the simulations. Second, we place the models in the right position and finally, we run the simulation to get the final woman models, which can also be interactively sculpted, using physics-based methods, to add a layer of fat.

3.1 Generation of Multimodel Representations

We have chosen the open source medical simulation framework SOFA [19] to perform the physics-based pregnant women body simulations. The SOFA architecture relies on several innovative concepts, in particular the notion of multimodel representations. The simulation components consist of the woman body envelope, the skeleton and the UFU witch are defined with three types of representations (visual, behavior and collision) to respectively optimize rendering, deformation and collision detection tasks.

We use the original surface models of the three components for the visual representation and create new models for the behavior and collision representations:

1. For the skeleton, we do not generate behavior nor collision representations since we only use it as a visual landmark for positioning the UFU.
2. Victoria's body envelope behavior representation is generated from a sparse free-form deformation (FFD) of the bounding box of the visual model's trunk. We focus on the deformations of the abdominal wall, considering that the head, arms and legs do not deform during the simulation. Only the FFD cells containing some matter are considered to generate an hexahedral finite element model (FEM) of a force field while the mass is uniformly distributed.
3. The UFU is considered as a rigid object with six degrees of freedom (3D translation and 3D rotation). It is moved in space using the motion data provided by a Biovision Hierarchy file [20]. For the collision representation between the UFU and the woman envelope, the original models are decimated, which strongly simplifies contact detection computation.

Finally, each representation is connected to each other using standard mappings.

In the following, the segmented fetus will be considered as a rigid structure. Although this is obviously not the case, this assumption allows us to build models where the position and shape of the fetus match the ones viewed in the acquired images, thus guaranteeing the realism and the fidelity between the images and the proposed models.

3.2 Positioning of Anatomical Elements within the Woman's Body

Victoria's representations are positioned in standing positions inside the simulation scene. The skeleton is placed inside Victoria's body interactively, using the free software tool Blender [3]. Three landmark points are manually selected on the skeleton of the generic woman body: the two femoral head centers and the center of the vertebral disk between the L3 and L4 lumbar vertebra (see Fig. 1). The three corresponding points are identified on the MRI images used to segment the UFU, enabling a rigid registration of the UFU collision and visual representations inside Victoria's body. Figure 2 shows four UFU automatically placed in different women models.

3.3 Interactive Pregnant Woman Body Sculpting Tool

An interactive body sculpting tool was designed to model the fat layer on Victoria's body. The idea is to consider that the standard 3D woman model is composed of two different layers of skin and fat. The volume of the fat layer is interactively modified using a mouse pointer. The points of the surface under the pointer are pushed up towards the normal direction by applying a constant force balanced by the Wendland kernel, as in (1). The force applied on the surface is modeled with a radial basis function, centered on the 3D projection of the mouse cursor onto the surface and vanishing within a prescribed Euclidean distance, as detailed in (2). In practice, we use the monotically decaying Wendlend quartic kernel [21].

$$\omega(x) = \begin{cases} \left(1 - \frac{x}{h}\right)^4 \left(4\frac{x}{h} + 1\right) & \text{if } x < h \\ 0 & \text{otherwise.} \end{cases} \tag{1}$$

The surface $\mathcal{S}$ is sampled by the mesh $\mathcal{M} = \{\mathcal{V}, \mathcal{F}\}$ where $\mathcal{V} = \{v_i\}$ are the vertex and $\mathcal{F}$ the faces. In our case, the following displacement field is applied on $\mathcal{M}$:

$$\forall v_i \in \mathcal{V}, f(p_{v_i}) = \alpha\omega\left(q - p_{v_i}\right) n_{v_i} \ . \tag{2}$$

where q is the point of the surface $\mathcal{S}$ under the mouse cursor, p_{v_i} is the 3D position of v_i, h is an user defined support radius, n_{v_i} is the normal to the surface $\mathcal{S}$ at vertex p_{v_i} and α is a user defined weight.

The sculpting process is operational when the mouse cursor is positioned at a point location q on Victoria and any mouse button is clicked. The displacement field is applied, until the button is released, on the surface points p_i that are inside the circle centered at point q and with radius h. The displacement field decreases away from the center point q.

Once the fat layer has been modified, the volume encapsulated between the skin and the fat layers (considered as new an independent closed surfaces) is

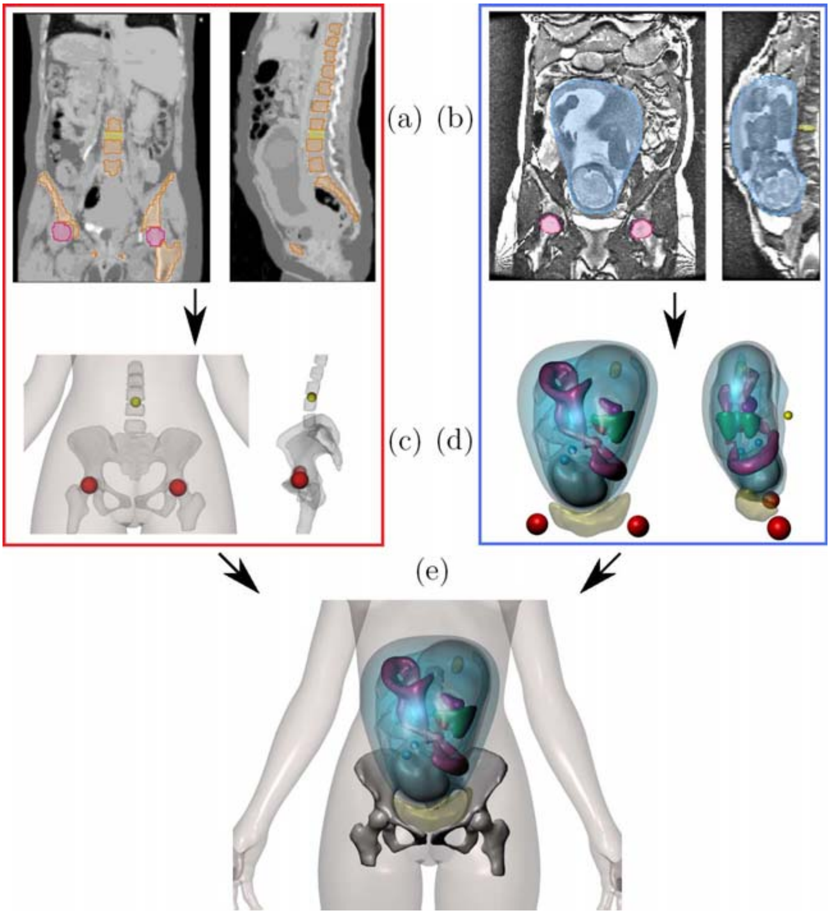

Fig. 1. Insertion of the UFU inside Victoria's body envelope. (a) Segmentation of the skeleton in orange, the femoral heads in red, and the vertebral disk between L3 and L4 in yellow from CT data. (b) Coronal and sagittal views of the reconstructed skeleton and landmark points inserted in Victoria's body. (c) Segmentation of the uterus in blue, the femoral heads in red, and the vertebral disk between L3 and L4 in yellow from from MRI data. (d) Coronal and sagittal views of the reconstructed UFU and landmark points. (e) Final positioning of the UFU. In the red frame, the landmark points identification process is performed one time, whereas in the blue frame the process is performed for each new UFU to insert, generating individual models.

filled with tetrahedras using the Isosurface Stuffing Algorithm [22]. Then, a co-rotational FEM force field is defined to determine its behavior. Points where there is no fat accumulation can also be defined using the mouse. Figure 3 shows with red dots the areas without fat development.

At these point locations, the force applied is always set to zero so that skin and fat layers remain attached together, creating a barrier to the fat expansion

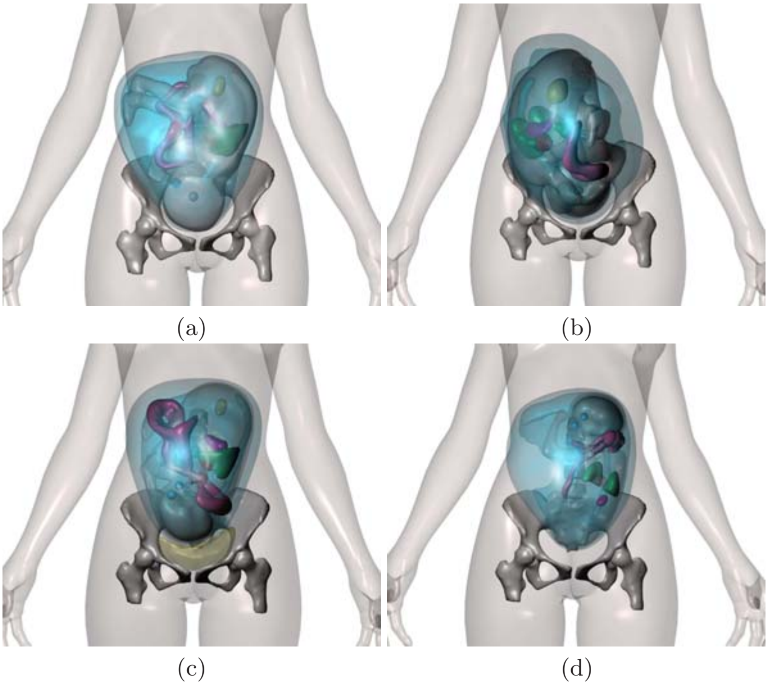

Fig. 2. Four different UFU positioning results using three landmark points. (a) Pregnant woman in supine position. (b) Pregnant woman in lateral position. (c) Pregnant woman with a filled bladder. (d) Pregnant woman with a fetus in breach position.

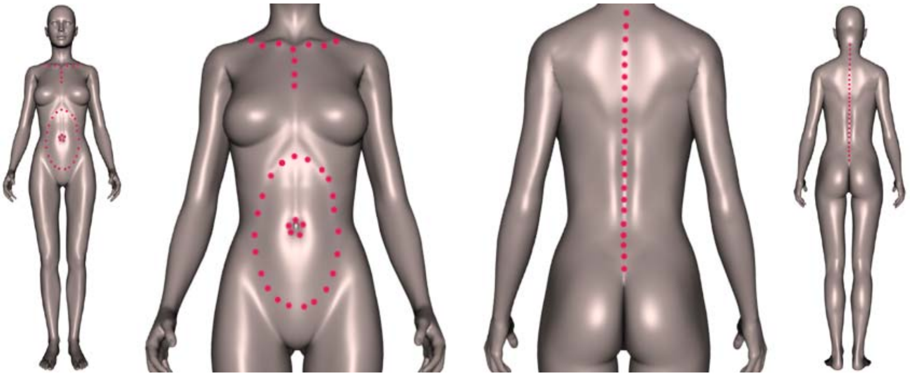

Fig. 3. Body regions without fat accumulation represented by dotted red lines

and accumulation. This procedure is necessary to delimit fat "pockets" and prevent un-physiological fat diffusion under gravitational effects. Figure 4 shows the added fat layers represented by a set of tetrahedras.

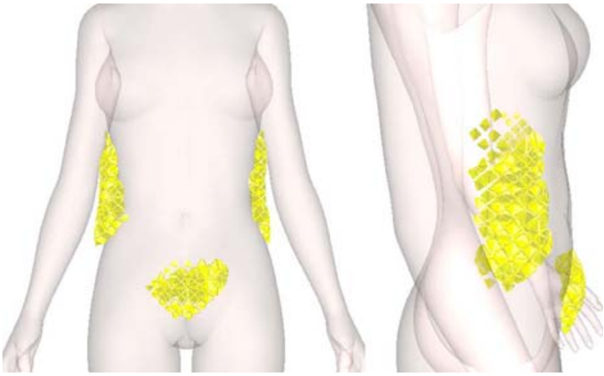

Fig. 4. Set of tetrahedras representing the fat layers

3.4 Simulations Running

The UFU orientation is affected by the laying down position of the mother during the imaging examination. To represent the same mother in a standing position, we need to apply a pendulous movement on the UFU. We first apply a rigid 6 degrees of freedom transformation to align skeleton points of references, as described previously (see Fig. 5). Then, we constrain its position and its rotation

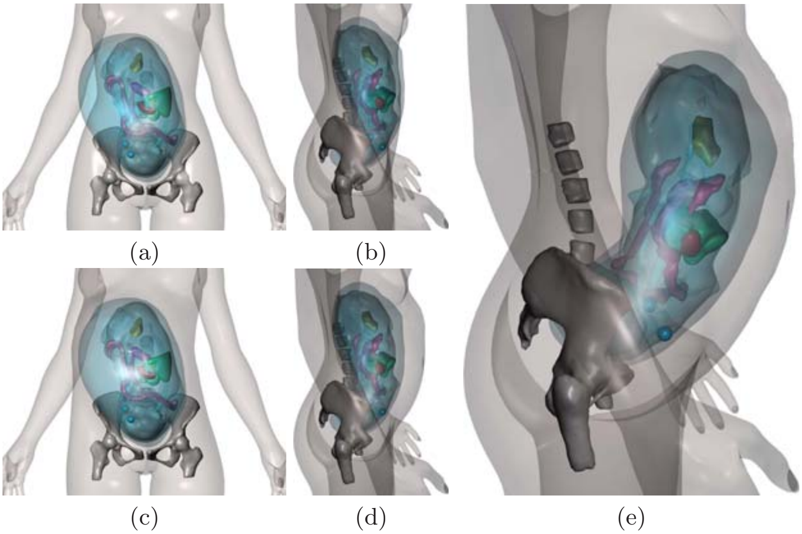

(a) (b) (c) (d) (e)

Fig. 5. Deformations of the Victoria's body envelope to include the UFU: (a,b) UFU positioning without collision detection in coronal and sagittal views. (c,d) UFU positioning using collision detection in coronal and sagittal views. (e) Deformed body of Victoria's body to simulate a standing position, after UFU rotation.

except for a rotation around an axis defined by the two femoral heads, which enables the UFU to rotate while pushing the abdominal walls. We decided to apply a rotation of 35 degrees to the UFU according to our medical experts, using again the Biovision Hierarchy file [20] (see Fig. 5). The coarse model created for the collision detection is used to displace the abdominal wall away from the rotating UFU. At the same time, the added fat layer deforms under the gravitational force field effect, deforming the overall envelope model.

As for the validation of the whole models, it has been performed by our clinical collaborators, who could in particular estimate the accuracy of the positioning of landmark points and the realism of the reconstruction. It should be moreover noticed that the proposed automated positioning method keeps the distance between the skin and the uterus wall constant, thus again guaranteeing the fidelity with the acquired imaging data.

4 Discussion and Conclusion

In this paper, we have proposed a novel automated methodological framework to insert utero-fetal units, segmented on medical images, into a synthetic woman body envelope, which is deformed to host the whole uterus. As dosimetry or medical studies may require models represented in a reclined or standing positions, we also addressed the problem of simulating different positioning configurations. The realism of the UFU was guaranteed by the large database of medical image data sets acquired during this project, covering the whole pregnancy. To guarantee the realism of our women body models as well as the representation of the major variations in anatomical configurations and morphologies, we designed a tool to control the fat distribution on the pregnant woman envelope. Some issues remain regarding the parametrization of such physics-based modeling tool. Indeed, setting the right values for the mass of the fetus and the woman body is a complex task. Finding the right elasticity of the abdominal walls is also difficult to define. For the moment, these parameters are set empirically. Setting all the points where there is no fat needs advanced medical knowledge, and still has to be performed manually. Finally, detailed segmentation of the 3D US and MRI imaging data remains also difficult and still requires manual refinements to include details on the fetal organs.

All our models were anatomically validated by medical experts using visual inspection for the segmentation of the UFU tissues, the insertion of the UFU into the synthetic maternal body, the simulation of the standing position, and the addition of a user defined fat layer.

In conclusion, the proposed approach achieves a significant step further towards hybrid pregnant woman modeling, by proposing both a method to automatically position the fetus inside a generic woman body, and a novel body sculpting tool to simulate fat layers. This allows now studying the influence of the fat thickness for various applications such as dosimetry simulation studies.

References

1. Wiart, J., Hadjem, A., Wong, M.F., Bloch, I.: Analysis of RF exposure in the head tissues of children and adults. Phys. Med. Biol. 53, 3681–3695 (2008)
2. Cristy, M., Eckerman, K.F.: Specific absorbed fractions of energy at various ages from internal photon sources. Oak Ridge National Laboratory Report ORNL/TM-8381/V1-V7 (1987)
3. Blender, `http://www.blender.org/`
4. Human Anatomy, `http://www.3dscience.com/3D_Models/Human_Anatomy/index.php/`
5. Angel, E., et al.: Radiation dose to the fetus for pregnant patient undergoing multidetector CT imaging: Monte Carlo simulations estimating fetal dose for a range of gestational age and patient size. Radiology 249(1), 220–227 (2008)
6. Dimbylow, P.: Development of pregnant female, hybrid voxel-mathematical models and their application to the dosimetry of applied magnetic and electric fields at 50 Hz. Phys. Med. Biol. 51(10), 2383–2394 (2006)
7. Chen, J.: Mathematical models of the embryo and fetus for use in radiological protection. Health Phys. 86(3), 285–295 (2004)
8. Xu, X.G., Taranenko, V., Zhang, J., Shi, C.: A boundary-representation method for designing whole body radiation dosimetry models: pregnant females at the ends of three gestational periods RPI-P3, -P6 and -P9. Phys. Med. Biol. 52(23), 7023–7044 (2007)
9. Shi, C., Xu, X.G.: Development of a 30-week-pregnant female tomographic model from computed tomography (CT) images for Monte Carlo organ dose calculations. Med. Phys. 31, 2491–2497 (2004)
10. Xu, X.G., Chao, T.C., Bozkurt, A.: VIP-MAN: an image-based whole-body adult male model constructed from color photographs of the visible man project for multi-particle Monte Carlo calculations. Health Phys. 78(5), 476–486 (2000)
11. Nagaoka, T., Saito, K., Takahashi, M., Ito, K., Watanabe, S.: Anatomically realistic reference models of pregnant women for gestation ages of 13, 18, and 26 weeks. IEEE Eng. Med. Biol. Soc., 2817–2820 (2008)
12. Nagaoka, T., Watanabe, S., Sakurai, K., Kuneida, E., Taki, M., Yamanaka, Y.: Development of realistic high-resolution whole-body voxel models of Japanese adult males and females of average height and weight, and application of models to radio-frequency electromagnetic-field dosimetry. Phys. Med. Biol. 49, 1–15 (2004)
13. Anquez, J., Boubekeur, T., Bibin, L., Angelini, E., Bloch, I.: Utero-fetal unit and pregnant woman modeling using a computer graphics approach for dosimetry studies. In: Medical Image Computing and Computerized Assisted Intervertion (MICCAI), London, UK. LNCS, vol. 5761, pp. 1025–1032. Springer, Heidelberg (2009)
14. Bibin, L., Anquez, J., Angelini, E., Bloch, I.: Hybrid 3D pregnant woman and fetus modeling from medical imaging for dosimetry studies. International Journal of Computer Assisted Radiology and Surgery (2009)
15. Anquez, J., Angelini, E., Bloch, I., Merzoug, V., Bellaiche-Millischer, A., Adamsbaum, C.: Interest of the Steady State Free Precession (SSFP) sequence for 3D modeling of the whole fetus. IEEE Eng. Med. Biol. Soc., 771–774 (2007)
16. Anquez, J., Angelini, E., Bloch, I.: Segmentation of fetal 3D ultrasound based on statistical prior and deformable model. In: IEEE International Symposium on Biomedical Imaging (ISBI), pp. 17–20 (2008)
17. Anquez, J., Angelini, E., Bloch, I.: Automatic segmentation of head structures on fetal MRI. In: IEEE International Symposium on Biomedical Imaging (ISBI), pp. 109–112 (2009)

18. Daz 3D Studio, `http://www.daz3d.com/`
19. Allard, J., Cotin, S., Faure, F., Bensoussan, P.J., Poyer, F., Duriez, C., Delingette, H., Grisoni, L.: SOFA - an Open Source Framework for Medical Simulation. Medecine Meets Virtual Reality (MMVR'15), pp. 13–18 (2007)
20. Biovision Hierarchy, `en.wikipedia.org/wiki/Biovision_Hierarchy`
21. Wendland, H.: Piecewise polynomial, positive definite and compactly supported radial functions of minimal degree. Adv. Comput. Math. 4(4), 389–396 (1995)
22. Labelle, F., Shewchuk, J.R.: Isosurface Stuffing: Fast Tetrahedral Meshes with Good Dihedral Angles. ACM SIGGRAPH 26(3) (2007)

Semi-automatic Segmentation of Fractured Pelvic Bones for Surgical Planning

Jürgen Fornaro[1], Gábor Székely[2], and Matthias Harders[2]

[1] Institute of Diagnostic Radiology, University Hospital Zurich
`juergen.fornaro@usz.ch`
[2] Computer Vision Lab, ETH Zurich
Switzerland
`{mharders,szekely}@vision.ee.ethz.ch`

Abstract. The segmentation of bones and bone fragments in clinical computed tomography datasets is an important first step in order to carry out computer-based surgical planning using patient-specific anatomical models. While semi-automatic and automatic methods have been proposed for the intact pelvic bone, the segmentation of bone fragments in the fractured pelvic bone still is a challenge due to weak boundaries and the diversity of injury patterns. We propose a semi-automatic multi-step segmentation method using bone and fracture gap enhancement filtering and a graph cut based bone fragment separation approach. The key contribution is a technique for automated detection of incorrect bone fragment separation in the case of incomplete pelvic fractures based on fracture gap planes detected in Hessian filtered images. Moreover, we propose a new sheetness measure based on a modified Hessian matrix. Our system is capable of segmenting fragments of complex hip fractures with only minimal user interaction.

Keywords: Bone segmentation, fractures, surgical planning.

1 Introduction

In our current research we focus on applying simulation techniques for treatment planning in acetabular fractures. These fractures are among the most challenging ones to treat in clinical practice. They typically occur as a result of high-energy traumas such as motor vehicle accidents or falls from a height [1], or less often as a consequence of minor traumas in older patients with osteopenic bone [2]. The anatomy of the pelvis is extremely complex. Moreover, pelvic fractures are diverse and relatively rare, such that patient-individual treatment is often mandatory.

Surgery planning tools for acetabular fracture reduction and fixation have been shown to increase reduction accuracy and to reduce operation times [3, 4]. Advanced simulation-based systems support the adaptation of different types and sizes of osteosynthesis implants to the reduced pelvis as well as mechanical tests of potential intervention plans [5]. For instance, screw trajectories should penetrate fracture gaps at about 90 degrees to prevent displacement of the bone fragments while tightening the

F. Bello and S. Cotin (Eds.): ISBMS 2010, LNCS 5958, pp. 82–89, 2010.
© Springer-Verlag Berlin Heidelberg 2010

screw. This implies that models used for pelvic surgery planning should comprise the cortical as well as the cancellous bone.

In order to carry out computer-based surgical planning, triangular surface meshes of fracture fragments have to be obtained. To this end, appropriate segmentations are required. Simple automatic methods such as thresholding are not sufficient for obtaining these, while manual segmentations are tedious and time-intensive.

Therefore, we have developed a hybrid multi-step pipeline for the semi-automatic segmentation of the fractured pelvic bone as well as the proximal femora, based on clinically obtained CT datasets. The key contribution of our work is a technique for automated detection of incorrect bone fragment separation in the case of incomplete pelvic fractures. Fracture gap planes are detected in Hessian filtered images using an optimized Ransac algorithm. Moreover, we propose a new sheetness measure based on a modified Hessian matrix. Our system is capable of segmenting fragments of complex hip fractures with only minimal user interaction. The obtained segmentations are used as input to our fracture treatment planning software [5].

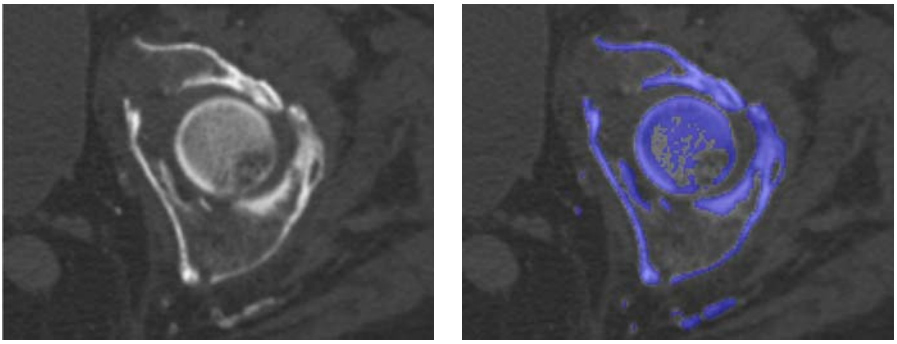

Fig. 1. Fractured left acetabulum in a case with osteopenic bone (left). Result of cortical bone segmentation step (right).

2 Related Work

Several methods have been proposed for the separation of bone components. Kang et al. [6] used a manually positioned sphere to separate the femoral head from the acetabulum, while Zoroofi et al. [7] introduced an involved automatic algorithm to fit a 3D ellipse to the femoral head. Statistical shape models have been applied successfully for the automatic segmentation of the intact pelvic and femoral bones from medical image data [8, 9]. But a priori knowledge from such models is very difficult to use in the segmentation of bone fragments because of the diversity of acetabular fractures [10] with often significant fragment displacements. Wang et al. [11] proposed the use of brittle fracture mechanics based on external stress and the internal intensity gradients for the partitioning of images. Cracks form when the mechanical stress exceeds a threshold that is governed by material properties. While there is an intuitive link to the separation of bone fragments, the solution would be expensive to compute for volumetric datasets. Also the authors showed that their segmentation results are very sensitive to parameter settings such as the window size of stress distribution calculation.

3 Segmentation Pipeline

In the following the individual steps of the complete segmentation pipeline will be introduced in detail. The segmentation was based on CT scans of acetabular fractures. Images were reconstructed with a 512x512 matrix and a slice thickness of 2mm.

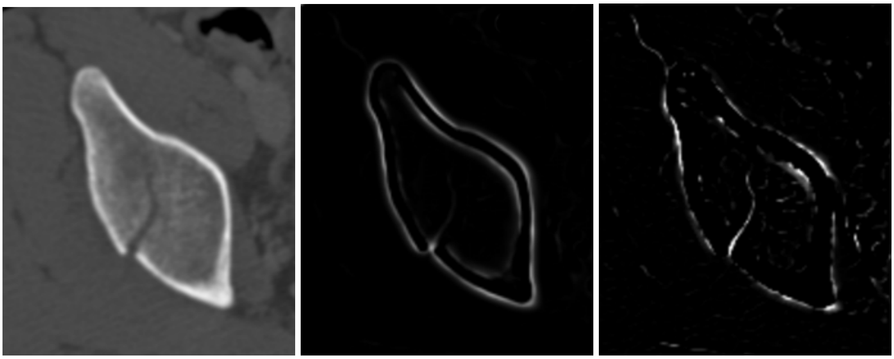

Fig. 2. Axial view of incomplete fracture above right hip joint (left). Original sheetness measure of non-inverted image (middle). New sheetness measure (right).

Segmentation of cortical bone. Simple thresholding of the CT images usually yields dissatisfying results. The CT signal of thin cortical bone sheets is blurred by partial volume effects. In addition, the quantitative accuracy of the signal is decreased by noise. For the segmentation of the cortical bone we therefore applied the adaptive thresholding scheme $t(x) = t_0 - \alpha\, c_{sheet}(x)$ to the input dataset, with $c_{sheet}(x)$ the sheetness measure proposed in [12] and α a weight factor. The method is based on the eigenvalues of the Hessian matrix computed for voxels of the intensity-inverted image at different scales. The scales should cover the range of considered structure sizes. In our case, four different scales Ω={0.75mm, 1.0mm, 1,5mm, 3mm} were chosen.

Applying the sheetness measure generates some false positive candidates at the skin surface, along the CT table, and at the wall of air-filled bowel loops. These false positives were masked by thresholding background air in the original dataset and enlarging the segmented region by morphological dilation. The resulting segmentation is shown for an example case with osteopenic bone in Figure 1.

Segmentation of cancellous bone. Based on the cortical bone segmentation, region growing was applied to the input dataset using the adaptive threshold $t(x) = t_0 + \beta\, c_{min}(x)$, with $c_{min}(x)$ a new minimum sheetness measure and β a weight factor. Just taking the standard sheetness measure of the non-intensity-inverted images to detect the structures results in significant false positive signals at locations with high intensity gradients, e.g. at the boundaries on both sides of the cortical bone (see Figures 2).

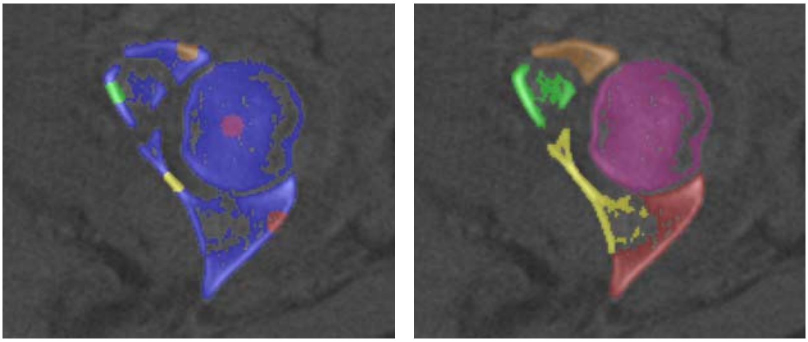

Fig. 3. User seeds added to bone labeling (left). Separated bone fragments using graph cut approach (right).

The new scheme reduces leakage of the segmentation into fracture gaps and joint spaces. Also, the true positives show a low contrast compared to the false positives. In order to reduce the false positive signal we propose a new measure analogous to the standard approach, based on a modification of the Hessian matrix:

$$H_{\min} = \begin{bmatrix} I_{xx} - |I_x| & |I_{xy}| & |I_{xz}| \\ |I_{xy}| & I_{yy} - |I_y| & |I_{yz}| \\ |I_{xz}| & |I_{yz}| & I_{zz} - |I_z| \end{bmatrix} \quad (1)$$

where the I_{j} and I_{jk} are first and second spatial derivatives of the voxel intensities. For the diagonal elements the false positive signal is reduced at edges by subtracting the absolute value of the gradient. Taking the absolute value of the off-diagonal elements fixes them at high positive values for minimum sheets independent of orientation.

Our new minimum sheetness measure increases the contrast of true positives compared to false positives significantly as can be seen in Figure 2 (right). However, it still generates some false positives, e.g. at low density fat tissue layers between bones and muscles. These are taken care of in the next steps.

Separation of bone fragments. The resulting segmentation of the cortical and cancellous bone is a binary partitioning into bone and background. The task of the following steps is to separate the different components. First a simple and fast 3D connected component labeling algorithm [13] is applied. Connected components smaller than 10mm^3 are rejected, representing the minimum size of objects of interest for clinical purposes. In addition, this step also removes small false positive labeled structures.

Unfortunately, between some fragments the boundaries are weak. Their labelings are not separable by a simple connected component algorithm. Therefore, we use graph cuts [14, 15]. This technique provides an energy minimization allowing efficient computation of a globally optimal image segmentation. For the algorithm a smoothness cost function $F_{p,q}(L_p,L_q)$ has to be defined, which gives the cost of assigning a node p to label L_p and the neighboring node q to a different label L_q. We have derived a modified function that pushes the cut surface towards low density structures showing a high minimum sheetness measure:

$$F_{p,q}\left(L_p, L_q\right) = \alpha\left(1 - e^{-\frac{I_p + I_q}{2}}\right) + \beta e^{-\frac{c_{\min}(p) + c_{\min}(q)}{2}} \tag{2}$$

where L_k, I_k, and $c_{\min}(k)$ are label, normalized intensity, and minimum sheetness value of node k. The influence of the sheetness and intensity terms can be controlled by parameters α and β, respectively. In our case both parameters were set to 0.5.

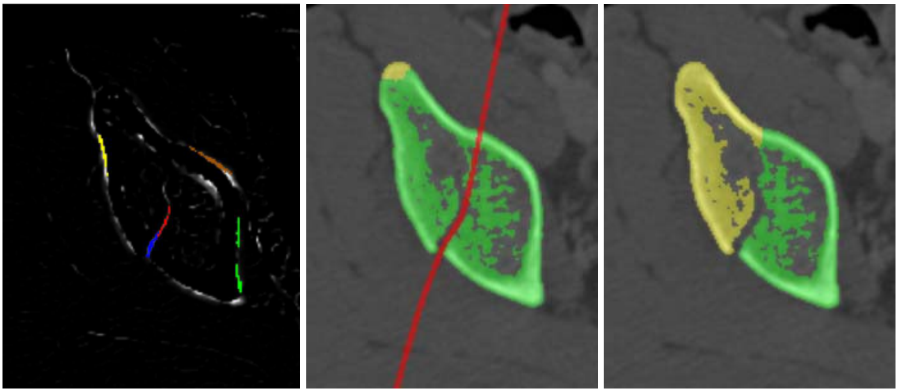

Fig. 4. Detected planes in right pelvic bone (color encoded). True positive fracture planes in blue & red (left). Cross section of TPS based on fracture gap plane (midde). Bone fragments correctly separated along surface after TPS refinement (right).

In order to carry out the graph cut based segmentation, seeds have to be added by a user to each bone fragment in the CT dataset on axial slices or multiplanar reformations. Figure 3 shows multiple bone fragments around the hip joint with user added seeds, as well as the resulting segmentation after applying the graph cut based separation.

Treatment of incomplete fractures. Unfortunately, incomplete fractures of the pelvic bone are quite common. The previously described graph cut technique then usually fails, since a cut into the non-fractured bone is expensive according to the smoothness cost function defined in Equation 2. Therefore, we propose an automated method for detection of incorrect bone fragment separation. The key idea is to first detect fracture planes in Hessian filtered images using an optimized Ransac algorithm [16], and then to use the detected planes as an initial estimate of a fracture surface that will be extended into the non-fractured part of the bone.

The input to the algorithm is a point cloud, corresponding to voxels in the image dataset showing a minimum sheetness measure exceeding a pre-defined threshold. Point normals are derived from the sheetness isosurface. The Ransac algorithm finds plane primitives exceeding a minimum size. Random sampling is performed at different localization scales using an octree implementation. These extracted planes are then used to detect incorrect separations of the graph cut step. A true positive fracture gap plane may be located in between two differently labeled, and therefore correctly separated voxel domains. An incorrect bone fragment separation is indicated by a

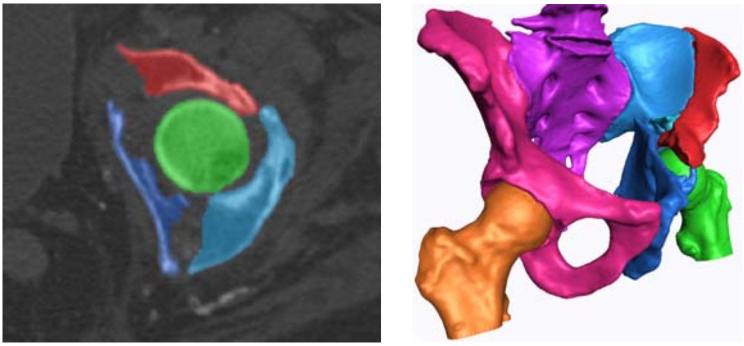

Fig. 5. Final segmentation after refinement of bone fragment contours (left). Surface mesh obtained from segmentation of this example case (right).

plane that is lined by equally labeled voxels on both sides. Finally, any false positive planes exhibit bone-labeled voxels only on one side. An image space method exploiting the graphics hardware was used to differentiate between these cases. Voxel volumes on both sides of a fracture gap plane are considered for an adjacency test. This test is carried out by projecting bone-labeled voxels of the segmented fragment in one such volume at a time onto a plane and testing for overlap in the framebuffer.

A plane is considered for resolving an incorrect bone fragment separation if the overlap is larger than a pre-defined threshold.

The algorithm for fracture gap plane detection produces a considerable number of false positives. These are located along low intensity fat tissue layers lining the cortical bone, in between two nearby and parallel cortical bone sheets, or in between muscles. The first two types of false positives can be filtered out by comparing them to a second set of planes detected in a point cloud derived from the standard sheetness measure of Descoteaux et al. [12] showing high signals at the cortical bone. False positives are then rejected based on a comparison of plane to plane orientations and distances in the two sets as well as testing for overlap using an image space method again. A complete detected set is shown for an example in Figure 4 (left). The planes remaining after the false positive elimination are colored in red and blue.

After removing all false positives, a thin plate spline surface [17] interpolating the constraining points of the true positive candidates is used as an initial estimate of a cut surface resolving the separation. The user may refine the thin plate spline by adding additional constraining points. The bone fragments are then separated along the accepted cut surface (see Figure 4)).

Segmentation refinement. In regions with low bone density, especially in the cancellous bone, the segmentation is still incomplete. This leads to artificial holes in the bone-labeling as well as in open regions (see Figure 4 (right)). In our case, the boundaries of bone fragments are at least partly lined by cancellous bone leading to sometimes quite large segmentation errors. We apply another graph cut based approach to solve both problems at the same time. The key idea is to build a graph from a volume of interest around the fragment currently considered for refinement. Another suitable smoothness cost function that pushes the boundary towards the true fragment outline has been derived:

$$F_{q,p}\left(L_p, L_q\right) = \alpha e^{-\left|I_p - I_q\right|^2} + \beta\left(1 - e^{-\frac{d_f(p)+d_f(q)}{2}}\right) \tag{3}$$

where L_k and I_k, are label and normalized intensity of node k. The minimum distance of node k to voxels of the object is given by $d_f(k)$. Weighting parameters α and β were again set to 0.5. A minimum enclosing axis-aligned bounding box (AABB) padded by 10mm wide margins on all sides was taken as the volume of interest around the object. This segmentation step did not require any user input as the initialization can be obtained from the bone-labelings of the previous steps. The final segmentation result after refinement of bone fragment contours is depicted in Figure 5 (left). The mesh generated from the segmentation is shown in Figure 5 (right).

4 Results

The presented segmentation pipeline was applied in a pilot study to seven clinical cases with complex pelvic fractures involving the acetabulum. The system was used by an expert radiologist. Segmentation times were measured for each step separately and the overall time was computed (see Table 1).

Table 1. Performance time measurements in seconds

Step/Patient	A	B	C	D	E	F	G
1. Cortical bone	79	62	64	74	65	59	69
2. Cancellous bone	19	15	17	18	16	14	18
3. Connected component	4	3	3	4	3	3	3
4a. Separation (graph cut)	212	254	118	201	263	140	127
4b. Separation (spline)	203	211	-	-	206	-	-
5. Contour refinement	54	48	36	39	47	31	34
Overall	359	339	238	336	337	247	251

All cases could be successfully segmented. Note that steps 1, 2, 3 and 5 are carried out automatically, while in step 4a and 4b user interaction, e.g. placement of seeds in the bone fragments is required. Only cases A, B, and E had incomplete fractures, thus step 4b only had to be carried out for these. All but one segmentation yielded excellent results. Only case G required some additional manual refinement due to an anterior column bone fragment that was focally impacted onto the femoral head.

5 Conclusions

We have presented a semi-automatic multi-step segmentation method for the fractured pelvis. The segmentation of bone using local structure enhancement filtering is followed by graph cut based separation of connected components. The key contribution is a technique for automated detection of incorrect bone fragment separation in the case of incomplete pelvic fractures. Additionally we propose a new sheetness measure based on properties of a modified Hessian matrix. This measure enhances minimum sheet-like structures such as fracture gaps and joint spaces.

In a first evaluation with seven clinical CT datasets of complex pelvic fractures our system was able to segment the bone fragments within four to six minutes in all cases, with only minimal user interaction.

References

1. Dakin, G.J., et al.: Acetabular fracture patterns: associations with motor vehicle crash information. J. Trauma 47(6), 1063–1071 (1999)
2. Vanderschot, P.: Treatment options of pelvic and acetabular fractures in patients with osteoporotic bone. Injury 38(4), 497–508 (2007)
3. Citak, M., et al.: Virtual 3D planning of acetabular fracture reduction. J. Orthop. Res. 26(4), 547–552 (2008)
4. Cimerman, M., Kristan, A.: Preoperative planning in pelvic and acetabular surgery: the value of advanced computerised planning modules. Injury 38(4), 442–449 (2007)
5. anonymous
6. Kang, Y., Engelke, K., Kalender, W.A.: A new accurate and precise 3-D segmentation method for skeletal structures in volumetric CT data. IEEE Trans. Med. Imaging 22(5), 586–598 (2003)
7. Zoroofi, R.A., et al.: Automated segmentation of acetabulum and femoral head from 3-D CT images. IEEE Trans. Inf. Technol. Biomed. 7(4), 329–343 (2003)
8. Lamecker, H., et al.: A 3D statistical shape model of the pelvic bone for segmentation. In: Medical Imaging 2004: Image Processing, Pts 1-3, vol. 5370, pp. 1341–1351 (2004)
9. Pettersson, J., et al.: Volume Morphing for Segmentation of Bone from 3D Data. In: Proceedings of the SSBA Symposium on Image Analysis (2005)
10. Letournel, E.: Acetabulum fractures: classification and management. Clin. Orthop. Relat. Res. (151), 81–106 (1980)
11. Wei, W., Ronald, C.: Image segmentation via brittle fracture mechanics. In: International Conference on Image Processing, 2004. ICIP (2004)
12. Descoteaux, M., et al.: Bone enhancement filtering: application to sinus bone segmentation and simulation of pituitary surgery. Comput. Aided Surg. 11(5), 247–255 (2006)
13. Beare, R.: Optimization of connected component labelling. The Insight Journal (2006)
14. Greig, D.M., Porteous, B.T., Seheult, A.H.: Exact maximum a posteriori estimation for binary images. Journal of the Royal Statistical Society. Series B, 271–279 (1989)
15. Boykov, Y., Jolly, M.-P.: Interactive Organ Segmentation Using Graph Cuts. In: Delp, S.L., DiGoia, A.M., Jaramaz, B. (eds.) MICCAI 2000. LNCS, vol. 1935, pp. 276–286. Springer, Heidelberg (2000)
16. Schnabel, R., Wahl, R., Klein, R.: Efficient RANSAC for Point-Cloud Shape Detection. Computer Graphics Forum 26(2), 214–226 (2007)
17. Bookstein, F.L.: Principal warps: thin-plate splines and the decomposition of deformations. IEEE Transactions on Pattern Analysis and Machine Intelligence 11(6), 567–585 (1989)

Development of a Computer Simulation Tool for Application in Adolescent Spinal Deformity Surgery

J. Paige Little and Clayton Adam

Paediatric Spine Research Group, Institute of Health and Biomedical Innovation Queensland University of Technology, Brisbane, Australia

Abstract. Scoliosis is a three-dimensional spinal deformity which requires surgical correction in progressive cases. In order to optimize correction and avoid complications following scoliosis surgery, patient-specific finite element models (FEM) are being developed and validated by our group. In this paper, the modeling methodology is described and two clinically relevant load cases are simulated for a single patient. Firstly, a pre-operative patient flexibility assessment, the fulcrum bending radiograph, is simulated to assess the model's ability to represent spine flexibility. Secondly, intra-operative forces during single rod anterior correction are simulated. Clinically, the patient had an initial Cobb angle of 44 degrees, which reduced to 26 degrees during fulcrum bending. Surgically, the coronal deformity corrected to 14 degrees. The simulated initial Cobb angle was 40 degrees, which reduced to 23 degrees following the fulcrum bending load case. The simulated surgical procedure corrected the coronal deformity to 14 degrees. The computed results for the patient-specific FEM are within the accepted clinical Cobb measuring error of 5 degrees, suggested that this modeling methodology is capable of capturing the biomechanical behaviour of a scoliotic human spine during anterior corrective surgery.

Keywords: anterior scoliosis surgery, spinal deformity, patient-specific finite element model, surgery simulation.

1 Introduction

Adolescent idiopathic scoliosis (AIS) is the most common spinal deformity, and requires surgical correction in progressive cases. Corrective surgery aims to reduce the abnormal spinal curvature and prevent further progression of the deformity via removal of the intervertebral discs, insertion of bone graft material into the cleaned disc spaces and attachment of metal rods to the spine using screws. Post-operative complications (such as screw pullout) or suboptimal correction can occur due to inappropriate choice of surgical levels or the application of excessive corrective force during the procedure. Biomechanical computer models of the spine have the potential to help optimise surgery outcomes and reduce complications, and patient-specific finite element (FE) models have been utilized previously to investigate the biomechanics of AIS surgery [1, 2]. The current study aims to develop more anatomically detailed FE models of scoliosis patients, for subject-specific prediction of the loading and deformation of individual spinal structures (eg ligaments and implants) during surgery.

F. Bello and S. Cotin (Eds.): ISBMS 2010, LNCS 5958, pp. 90–97, 2010.
© Springer-Verlag Berlin Heidelberg 2010

Such mechanical data would provide an improved ability to predict surgical outcomes. An important part of the model development process is the validation of model predictions by comparison with clinical data, and an initial model validation for a single patient is the subject of this paper.

2 Methods

Purpose developed image processing and FE pre-processing tools were developed to allow rapid generation of subject-specific FE models of patients from low-dose preoperative computed tomography (CT) datasets. As an initial step in validation of these computational tools, they were used to create a subject-specific model of a single scoliosis patient, and the model predictions for two clinically relevant physiological load cases were compared with clinical data for this patient. All analyses were performed on a HP xw660 workstation (Intel Xeon 5420, 4GB RAM) using Abaqus/Standard 6.7.1 (Simulia Inc, RI). Analyses were quasi-static with non-linear (finite strain) geometry capability enabled.

2.1 Patient-Specific FE Model Geometry for the Intact Spine

Our method for deriving patient-specific FE models from CT scan data has been previously described [3]. The three-dimensional, pre-operative CT dataset for an AIS patient (14yo female, 65kg, 165cm, pre-op major Cobb angle 44°, Lenke Class 1A) was imported into a custom developed image processing software (Matlab R2007b, The Mathworks, Natick, MA) where the osseous anatomy was thresholded and key bony landmarks were manually selected by the user. These landmarks were imported to a custom FE pre-processing tool (Python 2.5) which generated a parametric FE model of the osseoligamentous thoracolumbar spine, including vertebrae, ribs, sternum, discs, joints, and ligaments (Figure 1a). Seven spinal ligaments were simulated at each vertebral level (Table 1) and these were simulated as either linear connections, or in the case of the anterior and posterior longitudinal ligaments, as a group of spring elements in series and parallel. Note that while the model anatomy is patient specific (derived from CT scan data), all tissue material properties for the spine model are derived from existing literature. Details of the element types and material properties used are provided in Table 1.

2.2 Simulating Surgically Altered Spinal Anatomy

The AIS patient represented in this study underwent a single rod, anterior corrective procedure, with vertebral screws at levels T5 to T12 and discectomies at levels T5-6 to T11-12. The custom pre-processing software was capable of automatically regenerating the surgically altered geometry and FE mesh using user-defined details for the screw location/orientation, discectomy levels and rod size (Figure 1b). The simulated discectomies were represented by removal of half the anulus mesh, and removal of the entire incompressible, fluid filled cavity representing the nucleus pulposus. Contact between the exposed surfaces of the adjacent vertebrae was simulated using both an exponential, softened contact algorithm (normal contact) and a Coulomb

Table 1. Element representations and material properties used in the subject-specific FE model of the thoracolumbar spine

Anatomy	Element type	Material properties	Ref
Bony anatomy			
Cortical bone	3D, 4-node shell	Linear Elastic E = 11.3GPa; ν = 0.2	[4]
Cancellous bone	3D, 8-node brick	Linear Elastic E = 140MPa; ν = 0.2	[4]
Posterior elements	3D, 2-node beams	Quasi-rigid	
Intervertebral discs			
Intervertebral disc anulus ground matrix	3D, 8-node brick	Hyperelastic (Mooney-Rivlin) $C_{10} = 0.7$; $C_{01} = 0.2$	[5]
Intervertebral disc collagen fibres	3D, tension-only link (embedded rebar)	Linear elastic: E = 500MPa; ν = 0.3	[6]
Intervertebral disc nucleus pulposus	3D, 4-node hydrostatic fluid	Incompressible fluid: E ≈ 0, ; ν = 0.5	[7]
Cartilaginous joints			
Zygapophyseal joint surfaces	3D, 4-node shell	Linear Elastic E = 11.3GPa; ν = 0.2	
Costovertebral joints	3D, 2-node beams	Linear Elastic E_{compr} = 245N.mm^{-1} $k_{torsion}$ = 4167Nmm.rad^{-1} $k_{bending}$ = 6706Nmm.rad^{-1})	[8]
Ligaments			
Ligamentum flava, supra-/inter-spinous, capsular, intertrans-verse	3D, 2-node, tension-only connectors	Piecewise, non-linear elastic	[9, 10]
Anterior/posterior longitudinal ligament	3D, 2-node spring	Piecewise, non-linear elastic	[10]
Implant construct			
Rod	3D, 8-node brick	Linear elastic, perfectly plastic: E = 108GPa; ν = 0.3; σ_y = 390MPa	
Screws	3D, 8-node brick & 3D, 2-node beams	Same as for the rod	

friction model, μ=0.3 (tangential contact). Vertebral screws were represented in the vertebral bodies between T5 and T12. The idealized screw shaft representation simulated a perfectly bonded relationship between the screw surface and the underlying cancellous bone elements, without consideration of the screw threads embedded within the bone.

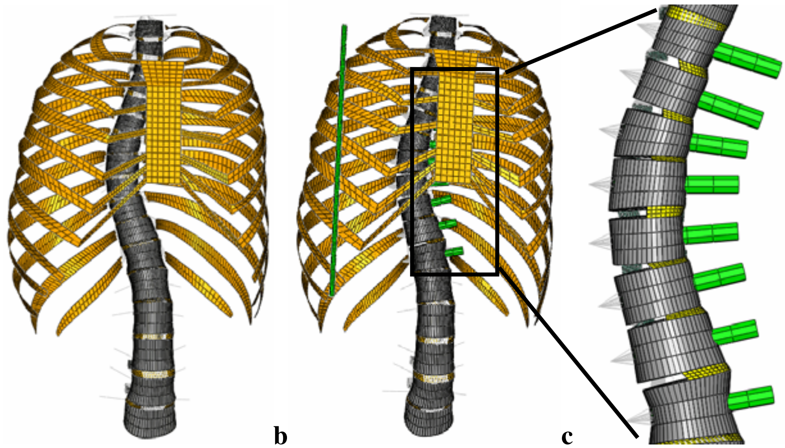

Fig. 1. Finite element mesh a. Intact scoliotic spine; b. Surgically altered spinal geometry with the rod and screws shown in green; c. Surgically altered region of the simulated spine, showing the remaining disc annulus elements (yellow) and screws with beam elements (grey wire) simulating the screw heads (screw ends have been lengthened to visualize screw positioning)

2.3 Simulated Load Cases in the Intact and Surgically Altered Spine

Two loading cases were simulated; (i) pre-operative fulcrum bending test on the intact spine (*intact* model) and (ii) intra-operative implant positioning on the surgically altered spine (*surgery* model).

1. Pre-operative fulcrum bending radiograph. Scoliosis patient spinal flexibility is often assessed clinically using a fulcrum bending radiograph [11] whereby the patient lays laterally over a cylindrical bolster, such that the convex side of their curve is adjacent to the bolster surface. This is a passive correction, which is not driven by muscle activation. To simulate this activity in the *intact* model, patient specific CT-derived segmental torso weights for each vertebral level were determined using custom-developed software (Matlab 2007b) and applied at the centroid of the transverse CT slice corresponding to that vertebral level (tissue density = 1.04×10^{-3} $g.mm^{-3}$). Additionally, load vectors simulating the weight of the full left arm and the upper portion of the right arm were applied at the T1 centroid and a load vector representing the weight of the head/neck was simulated as a point load superior to the T1 vertebra [12] (Figure 2). The bolster was modelled as a rigid body and rigidly constrained. A frictionless contact relationship existed between the ribs and the bolster surface and the spine was free to rotate about a point simulating the contact between the pelvis and the table. Rigid body rotation of the model is prevented by the combination of the translational constraint at the simulated point of contact between the pelvis and the table, and the positive contact pressure between the spine model and the stationary bolster under simulated gravitational loading.

The simulated Cobb angle in the unloaded *intact* model was compared with the pre-operative Cobb angle measured clinically from standing radiographs. The

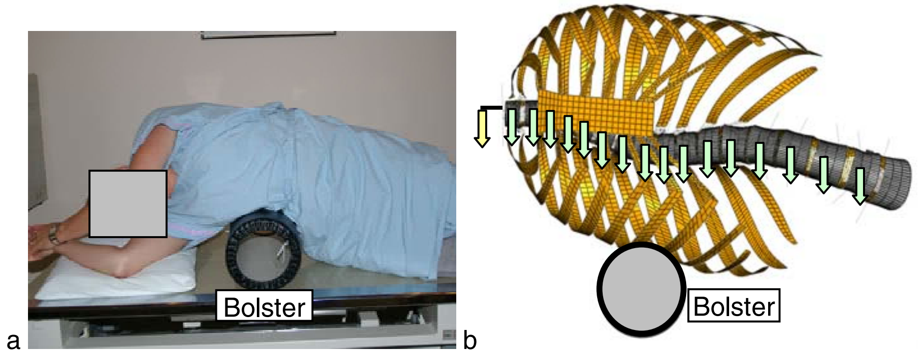

Fig. 2. (a) Patient in position for the fulcrum bending radiograph. (b) *intact* model after simulating the fulcrum bending activity. Green arrows = segmental vertebral torso weights; Yellow arrow = Head weight.

Fulcrum Flexibility (FF[1]) is used clinically to characterise a patients' flexibility during the fulcrum bending test. This parameter was calculated for the simulated deformed shape of the spinal column in the *intact* model and compared with the clinically measured value. An error of 5° between clinical and simulated Cobb angle measurements was considered acceptable since this is the clinically accepted value for accuracy in Cobb angle measurements.

2. Intra-operative implant insertion. Following removal of the discs and insertion of the screws, the anterior surgical procedure involves successive compression of the intervertebral joints within the structural curve. The compressive force is applied between screw heads at adjacent vertebrae, thus resulting in a successive, level-wise decrease in the overall deformity. Data for the corrective forces applied intra-operatively were obtained *in situ* by Cunningham *et al* [13]. These data were utilized in the *surgery* model to simulate the incremental, level-wise compression of adjacent vertebral joints in the thoracic spine. The L5 vertebra was constrained from motion during all load steps. The simulated corrected Cobb angle was compared with the clinically measured corrected Cobb angle obtained immediately post-operative, to ascertain the accuracy of the *surgery* model in predicting the change in coronal deformity following surgery (acceptable error = 5°).

3 Results

3.1 Fulcrum Bending Load Case

Clinically, this patient demonstrated an initial Cobb angle of 44°, which reduced to 26° during Fulcrum Bending, thus giving a pre-operative clinical Fulcrum Flexibility of 40.9%. The simulated initial Cobb angle was 31°, however, it has been shown that

---

[1] Change in Cobb angle between the standing and fulcrum bending radiographs, expressed as a percentage of the standing Cobb angle.

the standing Cobb angle measurement for AIS patients was on average 9° higher than the Cobb angle measured while the patient lays supine [14]. As such, the simulated, corrected-Cobb angle was 40°, which was within the accepted angular measurement error of 5° (Figure 3). The simulated Cobb angle reduced to 23° when the displacement of the spine during the Fulcrum bending radiograph was simulated. This was within 5° of the clinically measured value. Thus the simulated FF was 47.8%, which was calculated using the simulated deformed Cobb angle and the clinically measured standing Cobb angle (Figure 3).

3.2 Intra-operative Load Case

Following surgery, the clinically measured Cobb angle was 14° – this was measured one week post-operative. Results from the surgery simulation demonstrated a simulated corrected Cobb angle of 14° (Figure 3). As such, the computed results for the patient-specific FEM were the same as the clinical data.

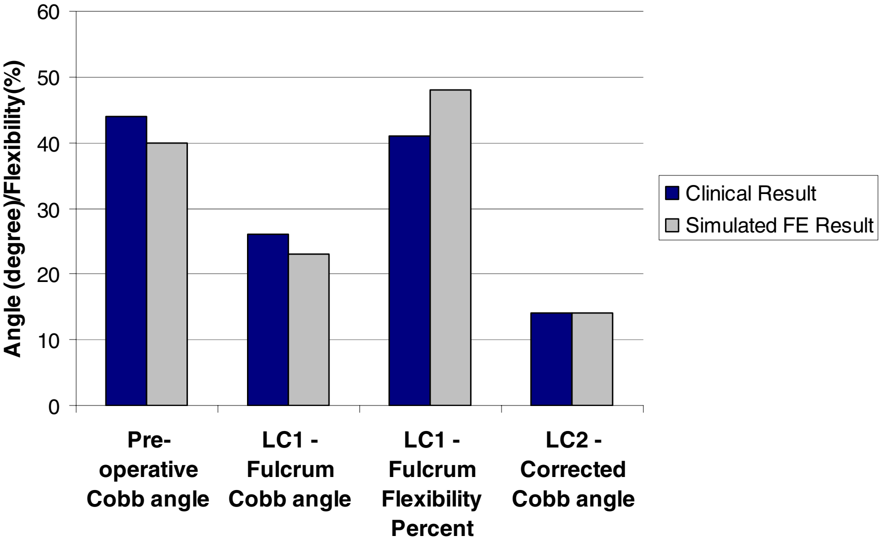

Fig. 3. Comparison of clinical and simulated results for a single AIS patient analysed under the fulcrum bending load case (LC1) and intra-operative correction load case (LC2)

4 Discussion

This paper presents the preliminary validation of a computational tool for developing subject-specific FE models of scoliosis patients, both prior to and immediately following corrective surgery. A patient-specific FE model for a single AIS patient was analyzed for physiological load cases representing both a pre-operative loading condition on the intact spine and an intra-operative loading condition representing intra-operatively applied surgical corrective forces. Comparison between the clinical and simulated data for both the *intact* and the *surgery* models demonstrated good agreement (within 5^o error), suggesting that the patient-specific modeling capabilities hereto developed are capable of capturing the physiological behaviour of a scoliotic spine.

We note that our use of a 5^o criteria for comparison of model predictions with radiographic measurements does not imply that the model results cannot be resolved more finely than 5^o, nor that the model is not sensitive to changes of less than 5^o. Rather, it is well known that radiographic Cobb angle measurements in scoliosis vary by around 5^o due to inter and intra-observer error [15], so this comparison range is necessitated by the uncertainty in the radiographic measurements used for model comparison.

While these patient-specific modeling capabilities currently do not allow the inclusion of patient-specific muscle forces, arguably the physiological loading conditions for which the models have been validated do not include muscle activation. Additionally, this preliminary model validation was carried out using material parameters derived from the literature, which are exclusively for adult spinal tissues. Ideally, material parameters derived for paediatric tissue would be incorporated in the model, however, such data is not available in the literature.

Biomechanically, the fulcrum bending test provides a potentially attractive clinical assessment tool which could be used to help prescribe patient-specific soft tissue properties in the spine model. By adjusting soft tissue properties until the model fulcrum flexibility matches the clinical measured value, the model could be 'calibrated' to match the soft tissue properties of a particular patient. However, there are several difficulties with this approach. Firstly, spinal flexibility is governed not by one soft tissue structure, but by a combination of discs, ligaments, and facet joints interacting in a manner unique to the loading being applied, therefore adjusting the mechanical properties of seven ligaments as well as the intervertebral disc and facet joints to match a single test value (the fulcrum flexibility) will not provide a unique solution to the problem of inversely determining soft tissue properties. Secondly, the manner in which soft tissue properties affect fulcrum flexibility is currently not clear. A previous study by our group using the same model [3] found that reductions of up to 40% in disc collagen fibre stiffness and ligament stiffness produced no measurable increase in fulcrum flexibility. However, complete discectomy did provide a large increase in simulated fulcrum flexibility, suggesting that the discs play an important role in governing fulcrum flexibility.

Future validation studies will develop upon the preliminary validation presented here, to use a larger subset of patient data, thus providing a more detailed and thorough validation of the patient-specific spine FE models. Using patient-specific FEM it will be possible to gain an improved understanding of the biomechanical impact of surgical interventions on the structures within the spine. Many of the complications associated with scoliosis corrective surgery are mechanical in nature and use of a computational tool such as this will provide surgeons with an improved ability to predict the likely outcome following scoliosis surgery.

References

1. Aubin, C.E., et al.: Biomechanical modeling of posterior instrumentation of the scoliotic spine. Comp. Meth. Biomech. Biomed. Eng. 6(1), 27–32 (2003)
2. Dumas, R., et al.: Personalized body segment parameters from biplanar low-dose radiography. IEEE Trans. Biomed. Eng. 52(10), 1756–1763 (2005)
3. Little, J.P., Adam, C.J.: The effect of soft tissue properties on spinal flexibility in scoliosis: biomechanical simulation of fulcrum bending. Spine (Phila Pa 1976) 34(2), E76–E82 (2009)
4. Lu, Y.M., Hutton, W.C., Gharpuray, V.M.: Do bending, twisting, and diurnal fluid changes in the disc affect the propensity to prolapse? A viscoelastic finite element model. Spine 21(22), 2570–2579 (1996)
5. Little, J.P.: Finite element modelling of anular lesions in the lumbar intervertebral disc, in School of Mechanical, Manufacturing and Medical Engineering. Queensland University of Technology, Brisbane, Australia, p. 361 (2004)
6. Kumaresan, S., et al.: Finite element modeling of the cervical spine: role of intervertebral disc under axial and eccentric loads. Med. Eng. Phys. 21(10), 689–700 (1999)
7. Nachemson, A.: Lumbar Intradiscal Pressure: experimental studies on post-mortem material. Acta Orthopaedica Scandinavica, 43 (1960)
8. Lemosse, D., et al.: Characterization of the mechanical behaviour parameters of the costo-vertebral joint. Eur. Spine J. 7(1), 16–23 (1998)
9. Chazal, J., et al.: Biomechanical properties of spinal ligaments and a histological study of the supraspinal ligament in traction. J. Biomech. 18(3), 167–176 (1985)
10. Nolte, L.P., Panjabi, M., Oxland, T.: Biomechanical properties of lumbar spinal ligaments. In: Heimke, G., Soltesz, U., Lee, A.J.C. (eds.) Clin. implant mat., pp. 663–668. Elsevier Science Publishing, Amsterdam (1990)
11. Cheung, K.M., Luk, K.D.: Prediction of correction of scoliosis with use of the fulcrum bending radiograph. J. Bone Joint Surg. 79(8), 1144–1150 (1997)
12. Erdmann, W.S.: Geometric and inertial data of the trunk in adult males. J. Biomech. 30(7), 679–688 (1997)
13. Cunningham, H., Little, J.P., Adam, C.J.: The measurement of applied forces during anterior single rod correction of adolescent idiopathic scoliosis. In: ACSR Annual Meeting, Adelaide, Australia (2009)
14. Torell, G., et al.: Standing and supine Cobb measures in girls with idiopathic scoliosis. Spine 10, 425–427 (1985)
15. Vrtovec, T., Pernus, F., Likar, B.: A review of methods for quantitative evaluation of spinal curvature. Eur. Spine J. 18, 593–607 (2009)

A Fluid-Structure Interaction Index of Coronary Plaque Rupture

Olusegun Ilegbusi[1] and Eric Valaski-Tuema[2]

Department of Mechanical Engineering, University of Central Florida
4000 Central Florida Blvd., Orlando, FL 32816-2450, USA
ilegbusi@mail.ucf.edu
eric_valas_ucf@yahoo.com

Abstract. The impact of coupled blood flow and structural dynamics on coronary plaque is investigated with the objective of defining a unique index for characterizing plaque rupture. Two-dimensional non-circular lumen models of native, moderate and severely stenosed human coronary arteries are investigated. The flow and structural analyses are performed simultaneously using well-validated commercial software. New flow–structure interaction (FSI) indices are defined by normalizing the predicted hemodynamic shear stress with the structural stresses. The results predict that the plaques investigated are potentially vulnerable to rupture at 40-45% stenosis levels. The predicted trend is consistent with clinical observations, indicating that the selected FSI index has the potential to characterize plaque rupture when properly established.

Keywords: Plaque rupture, fluid-structure interaction, stenosis, non-linear elasticity.

1 Introduction

Coronary artery disease (CAD) is the leading cause of death in the developed world [1]. This paper describes a methodology for coupling the principles of fluid mechanics with structural analysis in order to define critical indices for characterizing vulnerability of plaque to rupture under mechanical stress.

Plaque rupture with superimposed thrombosis is the primary cause of acute coronary syndromes of unstable angina, myocardial infarction and sudden death [2]. A highly disturbing statistics is that roughly 68% of patients with myocardial infarction (MI) have moderate stenoses (less than 50% stenosis), with little or no symptom prior to heart attack [3, 4]. In addition, 50 % - 60% of plaque disruptions occur on plaque shoulders [5,6].

Falk et al. [3] studied the silent growth of the disease, its sudden complication to life-threatening thrombosis and its composition and vulnerability rather than the stenosis volume or stenosis severity as the primary determinant of thrombogenesis. The study shows that the smaller rather than the larger plaques are more likely to lead to acute clinical events in case of abrupt occlusion. Equally important, this study

F. Bello and S. Cotin (Eds.): ISBMS 2010, LNCS 5958, pp. 98–107, 2010.
© Springer-Verlag Berlin Heidelberg 2010

suggests that plaque tearing tends to occur at the regions of stress concentrations resulting from biomechanical and hemodynamic forces [2, 7].

Among the other determinants of plaque vulnerability, structural stress is essential in understanding the stenosis tearing mechanism. Increased biomechanical stresses in the arterial wall can lead to rupture of the fibrous cap and, subsequently, myocardial infarction or stroke. However, plaque tearing may not only be related to the site of highest stress but also to the material properties of the plaque. [6,8].

Due to the important role of the arterial compliance wall and high pulsating blood pressure in atheroma rupture, fluid-structure interaction (FSI) phenomenon has been acknowledged as critical in simulating blood flow and plaque stability in stenosed arteries [9-10]. Tang et al. [11-13] used FSI to provide new insights of strain and stress distributions. The results show that severe stenosis causes considerable compressible stress in the arterial wall and affects stress localizations and flow characteristics. Maximum compressive stress and maximum tensile stress are localized within the stenosis.

Although the numerous studies listed above present diverse models of the stenotic artery, none has directly addressed the clinical observation that most patients with myocardial infarction (MI) have moderate stenoses (less than 50%) [3]. In this study, we address this issue by establishing an index for characterizing plaque rupture, using at this initial stage, a 2-D non-circular stenosed segment that is geometrically similar to a coronary artery.

2 Method

This study has three objectives: First, model flow characteristics in the arterial segment; second, model the effects of the mechanical properties of the arterial wall on the stenosed segment; and third, identify a suitable fluid-structure interaction (FSI) index to characterize plaque vulnerability to rupture. We consider a diseased artery segment illustrated in Fig. 1 with the following geometrical data: Total length L= 110 mm, length of the stenosis Ls=10 mm, inner diameter D_i = 4 mm, Ds= diameter of the artery at the stenosis, and wall thickness 0.5 mm. The arterial segment proximal to the plaque is chosen to be 50 mm long ($10\,D_i$), enabling flow development ahead of the plaque. In this study, 5 stenotic segments are considered, representing native (20% stenosis), moderate (30%, 40% and 50% stenosis) and severe (70% stenosis) cases.

2.1 Structural Analysis

The mathematical model assumes bi-linear, isotropic, incompressible material properties. Specifically, bi-linear models [14] are employed for the stenosis constituents. Trilateral (Tri) and quadrilateral (Quad) finite elements are generated for the solid and fluid domains of the arterial segment, respectively, resulting in 8505 to 9354 elements and of 7029 to 7683 nodes per segment.

The following parameters are predicted: endothelial shear stress, and the structural stresses (maximum principal stress “MPS”, Von Mises stress “VMS”, circumferential stress “SZZ”, Maximum Shearing stress “MSS”). Then, by analogy to the concept of

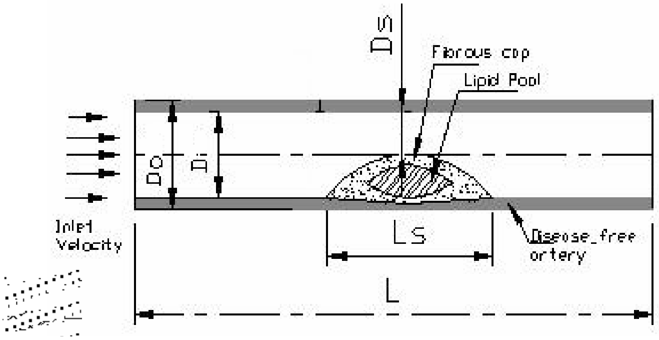

Fig. 1. Schematic representation of stenosed artery segment

buckling in material failure study [15,16,17], the wall shear stress (SS) obtained from the flow model is normalized by each of the above structural stresses for analysis.

The following equilibrium and boundary conditions have been used for the artery wall [11, 18]:

$$\sigma_{ij,j}^{(Sd)} = 0 \tag{1}$$

$$\sigma_{ij}^{(Sd)}.n_j \Big|_{inner\,surf} = \sigma_{ij}^{(fd)}.n_j \Big|_{outer\,surf} \tag{2}$$

$$d^{(Sd)} \Big|_{inner\,surf} = d^{(fd)} \Big|_{outer\,surf} \tag{3}$$

$$d_{\_Y}^{(Sd)} \Big|_{outer\,surf} = 0 \tag{4}$$

$$d_{\_X}^{(Sd)} \Big|_{inlet,outlet\,surf} = 0 \tag{5}$$

where, $d^{(Sd)}(d_{\_X}^{(Sd)}, d_{\_Y}^{(Sd)})$, $d^{(fd)}$ are the displacements (X and Y directions respectively) and $\sigma_{ij}^{(Sd)}$, $\sigma_{ij}^{(fd)}$ are the stress tensors for solid and fluid, respectively.

2.2 Flow Analysis

This study considers steady, viscous, incompressible flow in the asymmetric diseased artery segments illustrated in Fig. 1. The fluid is assumed to be Newtonian at this stage. The Navier-Stokes equations for 2D flow with compliant walls are solved using a commercial software code [19].

The inlet velocity and outlet pressure are prescribed as represented mathematically thus:

$$\mathbf{u}\Big|_{\Pi} = (0,0) \tag{6}$$

$$\frac{\partial \mathbf{u}}{\partial x}\Bigg|_{inlet,outlet} = (0,0) \tag{7}$$

$$u\big|_{x=0} = u_{in} = 0.2 m/s \tag{8}$$

$$p\big|_{x=l} = p_{out} = 0.0\, Nm^{-2} \tag{9}$$

where, $\mathbf{u}$ is the inflow velocity vector, p_{out} the pressure at the outlet, and Π is the interface between fluid and structural domains.

3 Results

The three objectives stated previously for this study, that is, hydrodynamic characteristics, biomechanical stress distribution and fluid-structure interaction analysis will be considered separately in the following presentation of the computed results.

3.1 Fluid-Flow

The distribution of shear stress (SS) is presented in Fig.2 for 20%, 40% and 70% stenosis as a function of X*. The horizontal coordinate X* represents dimensionless longitudinal position along the solid-fluid interface normalized with respect to plaque position such that X*=0 represents beginning of the plaque and X*=1 is the end of the plaque. The vertical thick lines represent the location of the symmetric vertical plane (SP) through the stenosis. Figure 2 shows that the shear stress increases with the stenosis level at the upstream side of the plaque lesion due to the flow acceleration in the reduced channel cross-section. The predicted abrupt decrease in the shear stress distribution, and the subsequent minimum value have been observed in previous studies [11, 20].

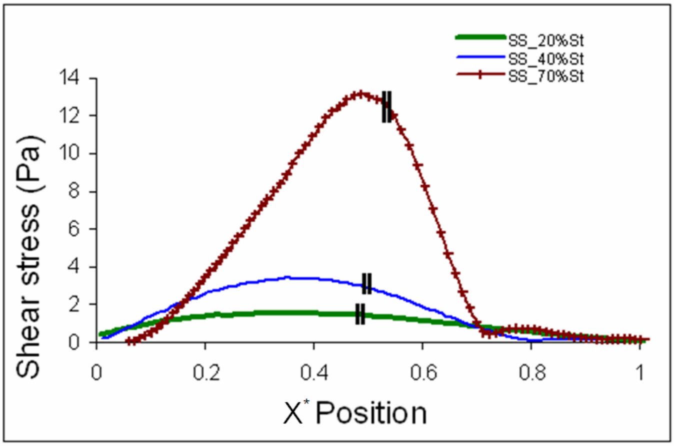

Fig. 2. Shear Stress (SS) distribution along the solid-fluid interface for different stenosis levels

3.2 Structural Analysis

The predicted representative stress contour plots from structural analysis are illustrated in Fig. 3. The plots presented in the figure are the contours of maximum principal stress (MPS) (a), and Von Mises stress (VMS) (b) for the 70% stenosis model. Figure 3-a shows that the plaque undergoes compressive and tensile stress predominantly in the upstream section similar to that observed in Tang [11,13]. Under the same hemodynamic conditions, Fig. 3-b shows the distortionalstress distribution (VMS) in the stenosis.

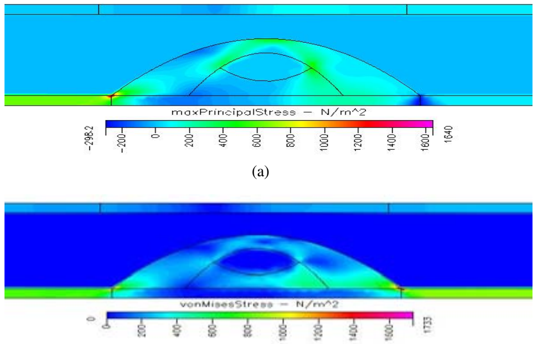

(a)

(b)

Fig. 3. (a) Maximum Principal Stress (MPS) and (b) Von Mises Stress (VMS) band plots

Figure 4 shows the maximum principal stress (MPS) and Von Mises stress (VMS) for 20% (a), 40% (b) and 70% (c) stenosis levels respectively. The distance X is measured along the solid-fluid interface. The incoming flow compresses the plaque proximally while the upstream wall segment is subjected to tension. The compression produces the observed negative MPS. The Von Mises stress (VMS) distribution exhibits three consecutive peaks: one on each side of the SP and one on the SP. The peaks on both sides of the SP increase with the stenosis severity.

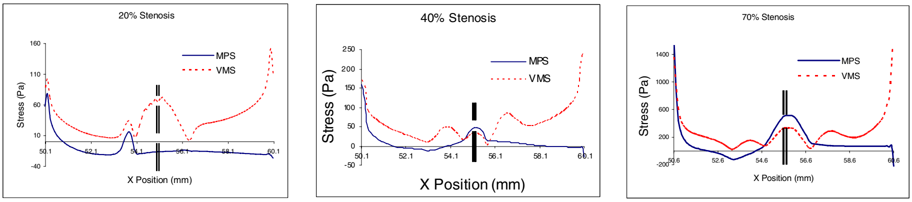

(a)

(b)

(c)

Fig. 4. Maximum Principal Stress (MPS) and Von Mises Stress (VMS) distributions

The plot of the maximum shearing stress (MSS) and circumferential stress (SZZ), not presented here, are quite similar to those in Fig. 4. The similarities, therefore, will be used as an alternative means to support our methodology, and to validate the implication of our results. These issues are addressed in the following section.

3.3 Fluid Structure Interaction (FSI)

Stress normalization. In this section appropriate FSI index is established to characterize plaque potential to rupture under mechanical and fluid stress. The parameters identified for investigation are the stress ratios R_1 and R_2. R_1 is the endothelial shear stress normalized by the maximum principal stress (SS/MPS), and R_2 is the shear stress normalized by the Von Mises Stress (SS/VMS). Figure 5 shows the distributions of the stress ratios R_1 and R_2.

The choice of normalizing the endothelial fluid shear stress by the structural stresses stems from the following three reasons. First, the successive compression and extension of structural stress distribution in the plaque as observed in the previous section. Second, several studies have shown that shear stress and structural stress play important roles in plaque disruption [11-13]. Third, analogy to the mechanism of buckling in material failure studies [16,17] with internal pressure in our vessel related to compressive pressure in the buckled material, and shear stress in our vessel related to perturbation (transverse force) in the material.

The ratio distributions presented in Fig. 5 are for 20% (a), 40% (b) and 70% (c) stenosis levels respectively. The parameter D is the nominal diameter of the normal artery segment proximal to the lesion. The results indicate that the stress ratio R_1 has multiple positive and negative peaks. These peaks are located where R_1 is infinite (discontinuous). This trend is expected since the maximum principal stress (MPS) is zero at these locations.

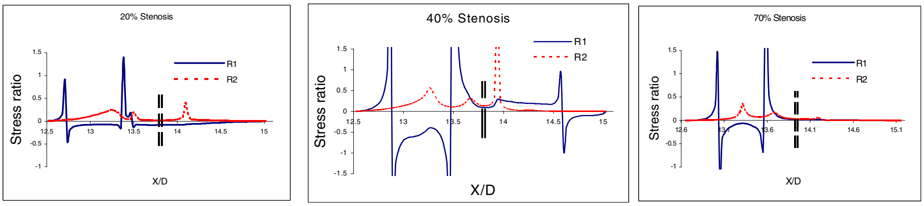

(a) (b) (c)

Fig. 5. Stress ratio R_1 and R_2 distributions

The first peak of R_2 is more interesting to investigate for two reasons. First, it occurs on the shoulder where plaques are most likely to rupture [7,21]. Second, it varies with the stenosis severity. A close look at both ratios show that at the location of the first peak of R_2, the ratio R_1 changes with the stenosis level. The implication of this trend will be described in more detail later in this section. The stress ratios R_3 and R_4 are the ratio of wall shear stress to maximum shear stress (SS/MSS) and the ratio of wall shear stress to circumferential stress (SS/SZZ), respectively. R_3 and R_4 curves have similarities to R_2 and R_1.

Summary: FSI indices. The fluid-structure interaction parameters computed to characterize the stenotic plaque rupture are summarized in Fig. 6. The horizontal axis represents the stenosis range, and the vertical axis represents the monitored stress ratio. Specifically, the plots represent the values of R_1 and R_4 at monitored locations for stenosis levels of 20%, 30%, 40%, 50% and 70%. The monitored locations are the X/D locations where the first R_2 maximum values (alternately R_3 maximum values) occur upstream of the mid plane (SP). These locations are situated on the plaque shoulder where plaque rupture most likely occurs. The magnitude of the stress ratio varies with stenosis severity and, defined as:

$$R_1 = \left| R_1 \left\{ \left(X/D \right)_{R_{2_{Max}}} \right\} \right| \tag{10}$$

$$R_4 = \left| R_4 \left\{ \left(X/D \right)_{R_{3_{Max}}} \right\} \right| \tag{11}$$

The monitored R_1 and R_4 values are presented in Fig. 6 below for comparison

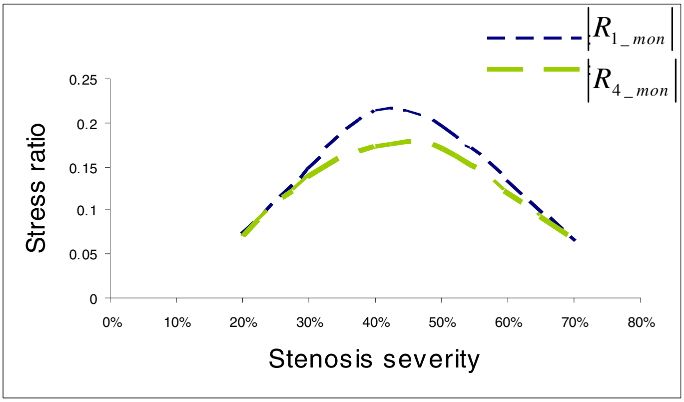

Fig. 6. FSI indices $R_{1\_Monitored}$ and $R_{4\_monitored}$ as a function of stenosis rate

The results show that the two indices predicted to characterize plaque rupture $R_{1\_Monitored}$ and $R_{4\_Monitored}$ exhibit the same trend, but $R_{1\_Monitored}$ is consistently larger than $R_{4\_Monitored}$. In general, the predicted FSI indices are small for both mild (e.g. 20%) and severe (e.g. 70%) stenosis. Interestingly these indices reach a maximum between the extreme stenosis levels at approximately 40%-45% stenosis rate. This stenosis range could be considered at risk to rupture and is consistent with medical observation [3,4]. In other words, the results indicate that the FSI indices investigated here could serve to characterize plaque vulnerability to rupture under mechanical stress. Plaques typically remain asymptomatic until the stenosis level exceeds about 70% of the lumen [4]. However, it has been observed in various studies that nearly 68% of patients with myocardial infarction typically have less than 50% stenosis [3,4]. The results presented here suggest that lipid-laden plaques of about 40-45% stenosis may be at risk to sudden rupture of the fibrous cap under fluid-structural mechanical stresses.

By carefully monitoring the stress ratio R_1 or R_4 at the location of maximum stress ratio R_2 or R_3 respectively, an experimental study can be devised to establish the stability value of R_{1_cr} or R_{4_cr} (critical value) for atheroma rupture. These critical stress ratios combine the interaction of flow and structural parameters on plaque characteristics, and are referred to here as the flow-structure interaction (FSI) stability indices.

The FSI indices need to be associated with the plaque location where the stress ratios become infinite in order for the indices to be meaningful. Specifically, if there is no discontinuity in either R_1 or R_4 distribution, the plaque is likely stable. By the same token, if there is discontinuity in R_1 or R_4 and their magnitude at the location of maximum R_2 or R_3 respectively is smaller than a threshold value (to be determined experimentally), then the plaque is likely stable. Otherwise the plaque is deemed unstable.

4 Discussion

The controlling parameters in this study were inflow velocity, plaque size, material properties, stenosis shape, plaque composition and mechanical boundary conditions. The numerical results were obtained by using a commercial package which has been widely applied and validated for similar biomedical systems [22].

In order to achieve the goal of this paper which is an attempt to establish for the first time a critical index of plaque rupture, the analogy was used of the investigated system to buckling in material failure studies. The parameters R_1 and R_2 (or for the alternative method R_3 and R_4) were predicted, expressing the ratio of endothelial fluid shear stress to Maximum Principal stress and Von Mises stress (or for the alternative method, the ratio of endothelial fluid shear stress to maximum structural shear stress and circumferential stress) in the plaque respectively. It was found that monitoring the R_1 values (or alternatively, R_4 values) at the vicinity of its discontinuity, specifically on the plaque shoulder at the location where the ratio R_2 (or R_3) distribution is maximum, predicts that stenosis levels in the range 40%-45% are most at risk to mechanical rupture. This observation is consistent with the critical stage of lipid-laden plaques.

These findings are quite encouraging since they are consistent with the observed severity of plaque rupture, in spite of the simplifying assumptions made. For example, three-dimensional segments should be considered as well as the full compliance of the walls. Further validation of this critical index would require additional studies that relax some of those assumptions, coupled with systematic experimentation and validation. It could also be applied to conditions reflecting the known risk factors of cardiovascular disease including thin fibrous cap, large necrotic core, high blood pressure, smoking, high cholesterol levels, macrophages effects etc. These studies are being pursued and will be presented in subsequent papers.

References

1. American Stroke Association, 2005 update, Heart Disease and Stroke Statistics, American Heart Association, National Center, Dallas, pp. 3–12 (2005)
2. Ross, R.: Atherosclerosis – an Inflammatory Disease. N. Engl. J. Med. 340(2), 115–126 (1999)
3. Falk, E., Shah, P., Fuster, V.: Coronary Plaque Disruption. Circulation 92, 657–671 (1995)
4. Sorof, S.: Intravascular Atheroma Monitoring: Past, Present and Future of identifying Vulnerable Plaques. Applications in Imaging - Cardiac interventions, 34–39 (2004)
5. Shah, P.K.: Plaque disruption and Coronary Thrombosis: New Insight into Pathogenesis and Prevention. Clin. Cardiol. 20(suppl. II), II-38–II-44 (1997)
6. Loree, H., Kamm, R., Stringfellow, R., Lee, R.: Effects of Fibrous Cap Thickness on Peak Circumferential Stress in Model Atherosclerotic Vessels. Circulation Research 71(4), 850–858 (1992)
7. Huang, H., Virmani, R., Younis, H., Burke, A., Kamm, R., Lee, et al.: The Impact of Calcification on the Biomechanical Stability of Atherosclerotic Plaques. Circulation 103, 1051–1056 (2001)
8. Chen, G., Loree, H., Kamm, R., Fishbein, M., Lee, T.: Distribution of Circumferential Stress in Ruptured and Stable Atherosclerotic Lesions: A structural Analysis with Histopatholigical Correlation. Circulation 87, 1179–1187 (1993)
9. Yamagushi, T., Furuta, N., Nakayama, T., Kobayashi, T.: Computations of the Fluid and Wall Mechanical Interactions in Arterial Diseases. 1996 Advances in Bioengineering, ASME BED 31, 197–198 (1995)
10. Yamagushi, T., Kobayashi, T., Liu, H.: Fluid-Wall Interactions in the Collapse and Ablation of an Atheromatous Plaque in Coronary Arteries. In: Proc. Third World Congress of Biomechanics, p. 20b (1998)
11. Tang, D., Yang, C., Kobayashi, S., Ku, D.: Effect of a Lipid Pool on A Stress/Strain Distributions in Stenotic Arteries: 3-D Fluid-Structure Interactions (FSI) Models. J. Biomech. Eng. 126, 363–370 (2004)
12. Tang, D., Yang, C., Kobayashi, S., Ku, D.: Simulating Cyclic Artery Compression Using a 3D Unsteady Model with Fluid-Structure Interactions. Computers and Structures 80, 1651–1665 (2002)
13. Tang, D., Yang, C., Kobayashi, S., Zheng, J., Vito, R.: Effect of Stenosis Asymmetry on Blood Flow and Artery Compression: A Three Dimensional Fluid- Structure Interaction Model. Annals of Biomedical Engineering 31, 1182–1193 (2003)
14. Beattie, D., Xu, C., Vito, R., Glagov, S., Whang, M.: Mechanical Analysis of Heterogeneous, Atherosclerotic Human Aorta. Journal of Biomechanical Engineering 120, 602–607 (1998)
15. Fred, B., Seely, J.O.: Advanced Mechanics of Materials, 2nd edn., pp. 585–625. John Wiley & Sons, Inc., Chichester (1965)
16. Nicholson, D.: Finite Element Analysis, Thermomechanics of Solids, pp. 185–194. CRC Press, Florida (2003)

17. Vable, M.: Mechanics of Materials, ch. 10. Oxford University Press, New York (2002)
18. CFD-ACE, V2004 Module Manual V1, ESI US R&D. Inc., Huntsville, AL (2004)
19. CFD-ACE, ESI US R&D. Inc., Huntsville, AL (2004)
20. Nosovitsky, V., Ilegbusi, O., Jiang, J., Stone, P., Feldman, L.: Effects of the Curvature and Stenosis-Like Narrowing on Wall Shear Stress in Coronary Artery Model with Phasic Flow. Computers and Biomedical Research 30, 61–82 (1997)
21. Shah, P.: Plaque Disruption and Coronary Thrombosis: New Insight into Pathogenesis and Prevention. Clin. Cardiol. 20(suppl. II), II-38–II-44 (1997)
22. Johnston, M.B., Johnston, R.P., Corney, S., Kilpatrick, D.: Non-Newtonian Blood Flow in Human Right Coronary Arteries: Steady State simulations. Journal of Biomechanics 37, 709–720 (2004)

Biomechanical Simulation of Human Eye Movement

Qi Wei[1,2], Shinjiro Sueda[2], and Dinesh K. Pai[2]

[1] Department of Computer Science, Rutgers University, Piscataway, NJ, USA 08854
[2] Department of Computer Science, The University of British Columbia, Vancouver, BC, Canada V6T1Z4
`pai@cs.ubc.ca`

Abstract. Understanding the neural control and mechanics of human eye movement has significant implications for treating vision disorders. A computational model incorporating physiological properties and nonlinear kinematics of the oculomotor plant's geometry and extraocular muscle (EOM) mechanics is desirable for scientific studies and clinical applications. We simulate realistic three-dimensional eye fixation using a new biomechanical simulation framework. We model EOMs as a collection of "strands," which are modeling elements for musculotendon mechanics based on splines with inertia. Anatomical variations in EOM and globe geometry across individuals can be taken into account. Complicated nonlinear EOM mechanics as well as the recently discovered pulleys are included in the computation. The resulting model generates realistic gaze positions and trajectories given EOM innervations.

Keywords: eye movements, oculomotor plant, computational modeling, biomechanics, computer simulation, 3-dimensional.

1 Introduction

Computation has played an important role in improving our understanding of the mechanics and control of eye movement, which shed light on treating binocular vision disorders, such as strabismus. Robinson [19] performed the first quantitative study of extraocular muscle (EOM) cooperation and prediction of strabismus surgery using digital computers. This model is the foundation of several other three dimensional (3D) models of the oculomotor plant that have been developed in the past three decades. Existing models can be categorized in the following two types, based on their anatomical and physiological realism.

Simplified models. Models using simplified anatomical and EOM mechanical properties of the orbit have been proposed [22,17,14]. These models assume that three pairs of EOMs act on three planes that are orthogonal to each other. They also do not take into account the anatomical variations of different EOMs, such as muscle lengths and cross sectional areas. Another critical assumption for simplifying the analytical solution is that the EOM force is simply proportional to the muscle innervation, whereas the actual EOM mechanics are complex and have

F. Bello and S. Cotin (Eds.): ISBMS 2010, LNCS 5958, pp. 108–118, 2010.
© Springer-Verlag Berlin Heidelberg 2010

nonlinear characteristics [20]. Such models are capable of supporting dynamic simulations and have been used to study the neural control of saccades and the pulley hypothesis [17,14]. These simplifications, however, may limit the models' accuracy and plausibility, as has been illustrated [15] through comparison to an improved model.

Biomechanical models. The first computerized biomechanical model due to Robinson solves for equilibrium of force on the orbit [19]. It incorporates anatomically realistic muscle paths and empirical EOM innervation-length-tension relationships. Two models were developed independently that improved Robinson's model, Miller and Robinson's SQUINT model [9] and Simonsz's model [23]. The SQUINT model was further extended to a widely used software tool, called the $Orbit^{TM}$ gaze mechanics simulation, which provides a graphical user interface and implements passive pulleys [8]. SEE++ [5] is a Windows-based modern software package developed from $Orbit^{TM}$ that aims to provide a highly interactive computer simulation environment for strabismus surgeries. Lately, Quaia et al. [16] presented simulation of superior oblique palsy using a model improved from their previous work by incorporating EOM mechanics and pulleys [15]. All of the above models are restricted to static fixations only and could not simulate dynamic eye movement.

In this paper, we describe a novel 3D biomechanical simulator of the oculomotor plant. One key issue in developing a realistic orbital model is the simulation of EOM mechanics. We represent each EOM as one or more *strands*, which are musculotendon modeling primitives [24]. Our proposed model has the following desirable properties:

- Strand-based EOMs are associated with realistic muscle geometry.
- Physiologically accurate EOM constitutive models are incorporated.
- Revolutionary discoveries of the oculomotor plant, such as the pulley hypothesis, can easily be implemented.
- Contact between EOM tendon and the globe is physically modeled, not only for visualization but also for realistic simulation.
- More importantly, our biomechanical model can simulate dynamic eye movements, which is not possible with previous biomechanical models.

2 Methods

We will first introduce the anatomy and biomechanics of the oculomotor plant (Section 2.1). Then we will review *strand*-based simulation, which is used to model extraocular muscles (Section 2.2). Our 3D biomechanical orbital model will be presented (Section 2.3). Finally, we will discuss how we solve for EOM innervation, i.e., excitation of muscle fibers (Section 2.4).

2.1 Anatomy and Biomechanics of the Orbit

The orbit is a complicated structure. Three agonist-antagonist pairs of muscles insert on the globe (eyeball) and are coupled through complex connective tissues.

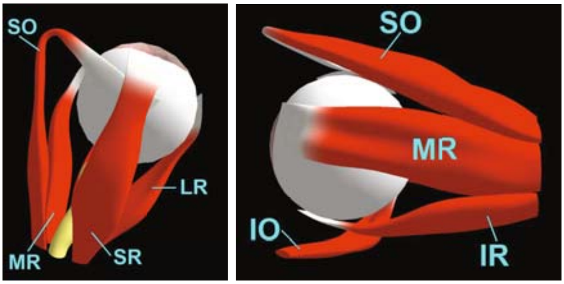

Fig. 1. 3D model of a human orbit reconstructed from MRI [26]. The six extraocular muscles are: LR-lateral rectus, MR-medial rectus, SR-superior rectus, IR-inferior rectus, SO-superior oblique, IO-inferior oblique.

These six muscles, named the extraocular muscles (EOMs), are innervated to generate force and rotate the globe to reach or track a visual target object and to stabilize the image of the object on the retina. The EOMs are bilaminar and consist of two layers with different fiber types [12]. Figure 1 shows a 3D model of a human orbit reconstructed from MRI [26].

The eyeball is nearly spherical. The passive connective tissues of the eyeball apply a restoring force, which brings the globe back to the central position when the net force from the EOMs is zero. The viscoelasticity of the suspensory tissues has been measured experimentally and modeled [21,3,20]. Pulleys refer to the connective tissues that stabilize the eye muscle paths even in extreme eye positions [7], which are believed to play significant roles in simplifying the control of eye movement. Extraocular muscle mechanics has been studied [4,20]. We will present how the EOM mechanics and pulleys are implemented in our model in Section 2.3.

2.2 Strand Musculoskeletal Simulator

One key issue in developing a realistic oculomotor plant model is the simulation of extraocular muscle mechanics. A *strand* is a musculotendon modeling primitive based on a spline with inertia [24]. Each strand represents a part of the musculotendon aligned with the fibers; depending on the level of detail needed, a strand can be as fine as a single fascicle or as coarse as an entire muscle [24]. We model EOMs, consisting of parallel fibers, as a collection of “strands”. EOM orbital and global layers and pulleys can be conveniently incorporated.

The path of a strand is described by a cubic B-spline curve, whose control points are the generalized coordinates, (position, $\boldsymbol{q}_i(t)$ and velocity, $\dot{\boldsymbol{q}}_i(t)$), that define the dynamics of the strand. Given the generalized coordinates, a point on a strand at a parameter s is computed as $\boldsymbol{p}(s,t) = \sum_{i=0}^{3} b_i(s)\boldsymbol{q}_i(t)$, where $b_i(s)$ are the B-spline blending functions. Although a strand can have an arbitrary number of control points, a point on a strand only depends on four control points, due to the local support of the B-spline basis, making the summation a function of only four terms ($i = 0 \ldots 3$). Because of this, the mass matrix of a strand [13] also depends on only four generalized coordinates, making the system mass matrix sparse.

The infinitesimal strain can be computed at any point along the strand. $\varepsilon(s,t) = (\sum_{i=0}^{3} b_i'(s)\boldsymbol{q}_i(t))/L(s) - 1$, where $b_i'(s)$ are the spline derivatives of the blending functions, and $L(s)$ is the rest strain. Based on these quantities, the passive (f_p) and active (f_a) forces acting on the strand control points can be computed, to get the equations of motion of a single strand:

$$M\dot{\boldsymbol{q}}^{(k+1)} = M\dot{\boldsymbol{q}}^{(k)} + h(\boldsymbol{f}_p + a\boldsymbol{f}_a) - G^T\lambda, \tag{1}$$

where M is the generalized mass matrix of rigid bodies and strand control points, h is the step size, a is the activation level, and $G^T\lambda$ is the constraint force.

Constraints are required for muscle origins/insertions and for EOM contact with the globe. Velocity-level constraints on the relative motions of the globe and the EOM strands are used. The combined velocity vector of rigid body and strands is denoted by Φ. A linear system (called a Karush-Kuhn-Tucker system [1]) is solved at each time step to obtain the generalized velocities at the next step.

$$\begin{pmatrix} M & G^T \\ G & 0 \end{pmatrix} \begin{pmatrix} \Phi^{(k+1)} \\ \lambda \end{pmatrix} = \begin{pmatrix} M\Phi^{(k)} + hf \\ -\mu g \end{pmatrix}, \tag{2}$$

where λ is the vector of Lagrange multipliers for the constraints. A direct method based on Gaussian Elimination is used to solve this matrix. Once the new velocities, $\Phi^{(k+1)}$, are computed, the new positions are computed using Rodrigues' formula [10].

2.3 Strand-Based Orbit Model

Each EOM is modeled as one or more strands. Other ocular structures are defined as mechanical constraints. The components in the model are illustrated in Figure 2 and described as follows.

a. The globe is a spherical rigid body with a ball-and-socket joint allowing rotation in 3D. The translational movement of the globe is assumed negligible. Extraocular muscles exert torques on the globe through attachments.
b. Each rectus muscle has two contractile elastic strands modeling the global and orbital layers. The EOM constitutive model will be discussed below. Two strands are chosen as this is sufficient to model the EOM path and mechanics along the principal axis that is functionally most important in moving the eye. Additional strands can be added within our framework if the added complexity is justified by the application.
c. Each EOM, except for the inferior oblique muscle, has a non-contractile, nearly inelastic strand modeling the tendon.
d. EOM origins and insertions are implemented as attachment constraints, which couple their positions to the attachment sites. EOM paths and cross sectional areas are based on 3D models reconstructed from MRI [26] and the *Orbit*^{TM} model [8].

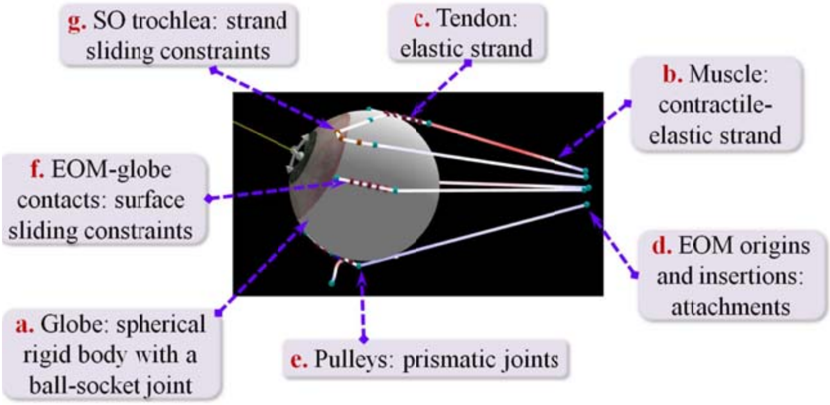

Fig. 2. Biomechanical model of the orbit using strands and mechanical constraints

e. Active pulleys [6] of the four rectus muscles are modeled as prismatic joints in this paper, which allow one-dimensional sliding motion along the joint axis. Our simulator is sufficiently general to allow other implementations of pulleys using elastic suspensions. The pulleys restrict the transverse sideslips of the rectus muscles, which leads to muscle path inflections in secondary and tertiary gazes, consistent with MRI findings [2,6]. In summary, by using prismatic joints, we apply zero longitudinal stiffness and infinitely large transverse stiffness on the pulleys to stabilize rectus muscle paths.
f. A parametric B-Spline surface is used to represent the geometry of the globe for computing contact locations. Surface sliding constraints are added such that extraocular tendons always slide on the globe without penetrating.
g. A sliding constraint is used to enforce the superior oblique to pass through the trochlea, which is fixed in the orbit.

The three-element Hill-type muscle constitutive model, consisting of the contractile element (CE), parallel elastic (PE) element, series elastic (SE) element, has been proposed to describe EOM force generation mechanism [4,20]. However, none of the existing computerized ocular models has included the series elastic component. The SE behavior has not been sufficiently quantified yet due to the lack of physiological data [20]. We follow previous models and only include contractile element and parallel elastic element in the EOM mechanics. Based on the Hill muscle model, the contractile force is formulated as $F_{CE} = a \cdot f_l \cdot f_v$, which is a function of the innervation a, the contractile force-length relationship f_l, and the active force-velocity relationship f_v. We adopt the force-length curves in the Orbit^{TM} 1.8 simulator, and the force-velocity function in [20].

2.4 Simulations

Two kinds of simulations are conducted. In *inverse control simulations*, we compute the EOM innervations that will hold the eye at the target positions or follow the target trajectory. In *forward simulations*, given a set of EOM innervations, the equilibrium eye position or dynamic movement trajectory is computed.

We extend the activation (innervation) solver in [24] to compute innervations of the EOMs, $a \in [0,1]$ a unitless scalar, given the desired trajectory v_x, specified as the desired velocity of the globe:

$$\begin{aligned} \min_{a} \quad & w_a\|a\|^2 + w_x\|(H_x a + v_f) - v_x\|^2 \\ \text{s.t.} \quad & 1 \geq a_i > a_i^0 \; c_v(v_{eye}) \; c_p(p_{eye}) \end{aligned} \tag{3}$$

where w_a and w_x are blending weights and the lower bounds of the constraints are modulated as a function of eye velocity and position as described below.

The first term in the objective function minimizes the total activation such that among the numerous possible solutions, the set of innervations with the minimal summed energy are found. It also adds regularization to the quadratic problem. The second term guides the dynamics of the system towards the target motion. The matrix H_x can be thought of as the effective inverse inertia experienced by the muscle activation levels in order to produce the target motion. The v_f vector is the velocity of the target due to the non-active forces acting on the system.

The constraint terms specify the innervation bounds of each EOM. The lower bound is non-zero to be consistent with the well known fact that the innervation in primary gaze at rest is not zero. We denote this minimal innervation as a_i^0 for EOM_i. This lower bound is reduced to zero with increasing eye velocity so that lower bound is zero during saccades. We define

$$c_v(v_{eye}) = \max(0, \frac{v_{max} - |v_{eye}|}{v_{max}}), \tag{4}$$

$$c_p(p_{eye}) = \max(0, \frac{p_{max} - |p_{eye}|}{p_{max}}). \tag{5}$$

Here v_{max} is the velocity defining the onset and offset of a saccade, which is set to $20°/s$ [25]. The c_p factor linearly decreases the lower bound with the eccentric eye position. p_{max} is the maximum OFF direction eye position, at which the EOM's innervation is completely off; we assume $p_{max} = 30°$ in our experiments.

In order to deal with the redundancy problem (3 degrees of freedom of the eye rotation vs. six EOMs), previous models [8,5] apply Sherrington's Law of Reciprocal Innervation by using a symmetric hyperbola function to explicitly define the innervation relationship of an agonist and antagonist pair. Realizing the deficiency of this symmetry assumption, [16] applies an asymmetric constraint and data-based heuristics to compute the oblique muscle innervations. Our simulator does not incorporate the reciprocal control model but solves for the innervations of the six EOMs simultaneously. Since we have a detailed model of the orbital geometry and mechanics, the reciprocal innervation characteristics is obtained automatically without being added as assumptions.

3 Results

We first verify the invertibility of the computed muscle innervations, using simulated fixations. We then demonstrate simulations of saccadic movements. Finally, we show that our model produces realistic longitudinal EOM strains during smooth pursuits.

3.1 Verification of Invertibility

We first verify that the computed EOM innervations are sufficient in fixating the eye at desired positions. We first simulate fixations at nine eye positions in a 3 × 3 grid. The EOM innervations that drive the eye to each position are first computed from the inverse activation solver described above. Applying the computed innervations, we then perform a forward simulation and record new eye positions. Figure 3 shows the forward simulated fixation positions as black cross markers, which are close to the target positions in blue circles. The mean error was 0.016 degrees with standard deviation 0.02 degrees. We conclude that the estimated EOM innervation sets are accurate in driving the plant as expected.

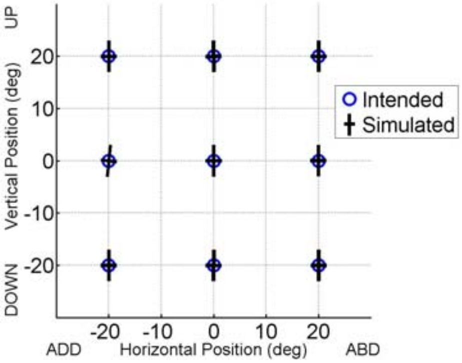

Fig. 3. Simulated fixations

3.2 Simulation of Saccades

The neural drive to produce a rapid saccadic eye movement can be characterized by a *pulse* component to overcome the viscoelasticity of the orbital plant, a *step* component to stabilize the eye in the new position, and a *slide* component that models the gradual transition between the pulse and step [18].

The abducens motoneurons (ABNs) activities, expressed as neural discharge rates, have been recorded and modeled as a linear equation $FR = b + kE + r\dot{E}$ [18,25]. The equation indicates that the ABNs firing rate FR is linear in the eye position E and velocity $\dot{E}$. b is a bias constant, which is the neural activity at stationary central eye position. In order to test the plausibility of our biomechanical model, we use the above empirical ABN discharge model as innervation input of the lateral rectus (LR) muscle to drive the plant. We then compare simulated eye trajectory to desired motion.

Figure 4 plots simulated abduction saccades of 10, 20, and 30 degrees respectively, while the eye is elevated by 20 degrees. For each tested saccadic movement, the left panel shows its simulated path starting from a secondary position in 20 degree elevation. The blue curves in the right panel show the desired position and velocity profiles, based on recorded traces from a monkey [25]. The middle panel

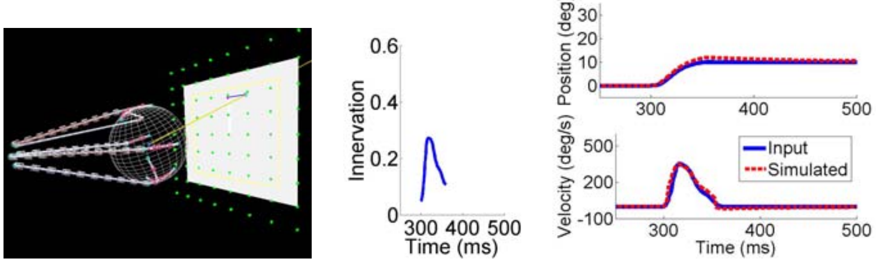

(a) Simulated saccade of 10 degrees

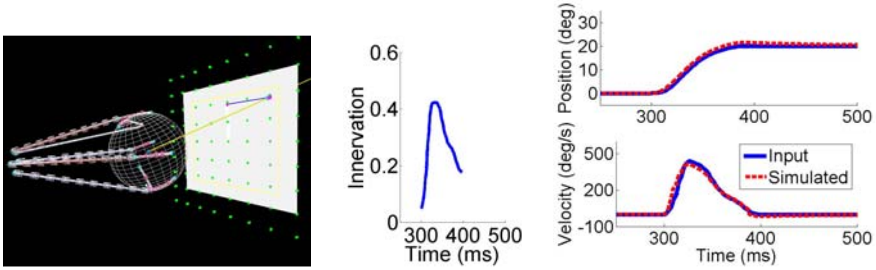

(b) Simulated saccade of 20 degrees

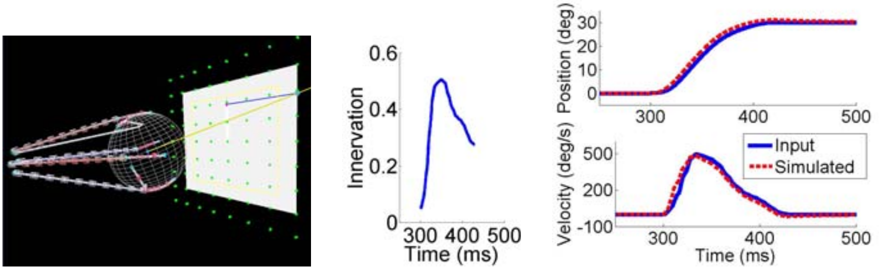

(c) Simulated saccade of 30 degrees

Fig. 4. Simulated abduction saccades of (a) 10 degrees, (b) 20 degrees, and (c) 30 degrees

shows the LR muscle innervation profile computed based on the ABNs firing rate model; it clearly exhibits pulse-slide-step characteristics of saccadic neural control signals. Finally, the red curves in the right panel show the simulated saccades, which follow the desired trajectories reasonably well. This preliminary result shows that our biomechanical model produces plausible eye movements and innervations; more detailed comparisons with specific subjects is beyond the scope of the current paper.

3.3 EOM Deformation

EOM deformation as a function of gaze and time is an important parameter in studying extraocular mechanics. We compare simulated EOM deformation to *in* *vivo* EOM motion data. Motion-encoded MRI was recently proposed to assess EOM motion during smooth pursuit eye movement [11]. Along the longitudinal axis in primary eye position, each EOM is divided into three segments of equal length. Stretch ratio, defined as the ratio between the deformed muscle length and initial length, is used to quantify the EOM deformation [11].

We simulate the same smooth pursuit movement as in [11]. The eye moves horizontally from 20 degree in abduction to 20 degree in adduction with zero vertical movement. The velocity is a sinusoidal function with 2 second period. Applying the same analysis schemes, we show the simulation results in Figure 5, which is overlaid on top of the *in vivo* EOM motion data averaged for 7 subjects for comparison. Our simulated deformation of the two horizontal EOMs, lateral rectus and medial rectus muscles, is consistent with the published data. The EOM segments show nearly sinusoidal deformation patterns. Nonuniform shortening and elongation are observed in the two EOMs. The middle segment, which has larger cross sections, deforms more than the posterior segment. The anterior part consists of more tendon and deforms the least.

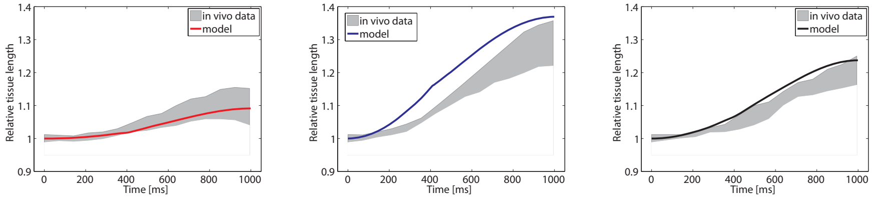

(a) LR anterior segment (b) LR middle segment (c) LR posterior segment

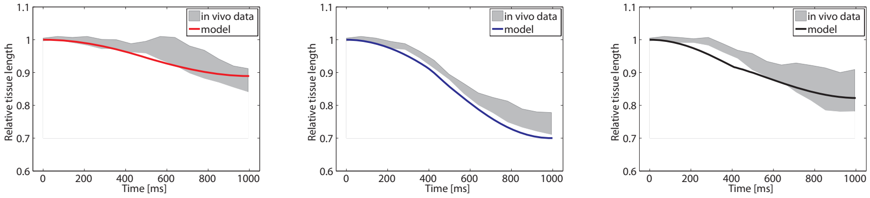

(d) MR anterior segment (e) MR middle segment (f) MR posterior segment

Fig. 5. Comparison of lateral rectus (LR) and medial rectus (MR) muscle strains from simulation and image data. Shaded regions show the average stretch ratios (mean $\pm 1 S.D.$) from 7 subjects (redrawn from [11]). Solid curves show simulated strains. Values larger than one indicate muscle lengthening.

Due to limited availability of data in [11], we only make comparisons for the horizontal EOMs in sinusoidal smooth pursuits. In future studies, once more comprehensive motion-encoded MRI data is available, we would like to validate simulated EOM strains of the vertical and oblique EOMs in different movement trajectories.

4 Conclusion

To better understand the mechanical and neural factors contributing to human eye movement, it is important to have a computational model that implements our current knowledge of the oculomotor plant and tests different hypotheses. We present a 3D biomechanical model of the oculomotor plant that takes into account the realistic EOM muscle geometry. EOM constitutive model based on empirical data is incorporated. The model implements pulleys with infinite transverse stiffness; it generates realistic gaze positions and trajectories given EOM innervations. Simulated EOM deformation shows inhomogeneity, consistent with motion encoded MRI data. In the future, we plan to investigate the clinical applications of the model in predicting outcomes of surgical treatments for strabismus. We will also study the functions of the pulleys in ocular motility.

Acknowledgment. We thank Dr. Joel M. Miller and Dr. Joseph L. Demer for very helpful discussions.This research was supported in part by NIH grant R01NS050942, Canada Research Chairs Program, NSERC, Peter Wall Institute for Advanced Studies, Canada Foundation for Innovation, BC KDF, and MITACS.

References

1. Boyd, S., Vandenberghe, L.: Convex Optimization. Cambridge University Press, Cambridge (2004)
2. Clark, R.A., Miller, J.M., Demer, J.L.: Three-dimensional location of human rectus pulleys by path inections in secondary gaze positions. Investigative Ophthalmology & Visual Science 41, 3787–3797 (2000)
3. Collins, C.C.: Orbital mechanics. In: The control of eye movements, pp. 283–325. Academic Press, New York (1971)
4. Collins, C.C., O'Meara, D., Scott, A.B.: Muscle tension during unrestrained human eye movements. Journal of Physiology 245(2), 351–369 (1975)
5. Haslwanter, T., Buchberger, M., Kaltofen, T., Hoerantner, R., Priglinger, S.: SEE++: Biomechanical model of the oculomotor plant. Annals of the New York Academy of Sciences 1039, 9–14 (2005)
6. Kono, R., Clark, R.A., Demer, J.L.: Active pulleys: Magnetic resonance imaging of rectus muscle paths in tertiary gazes. Investigative Ophthalmology & Visual Science 43, 2179–2188 (2002)
7. Miller, J.M.: Functional anatomy of normal human rectus muscles. Vision Research 29, 223–240 (1989)
8. Miller, J.M., Pavlovski, D.S., Shamaeva, I.: Orbit^{tm} 1.8 gaze mechanics simulation. Eidactics, San Francisco (1995)
9. Miller, J.M., Robinson, D.A.: A model of the mechanics of binocular alignment. Computers and Biomedical Research 17(5), 436–470 (1984)
10. Murray, R.M., Sastry, S.S., Zexiang, L.: A Mathematical Introduction to Robotic Manipulation. CRC Press, Inc., Boca Raton (1994)
11. Piccirelli, M., Luechinger, R., Rutz, A.K., Boesiger, P., Bergamin, O.: Extraocular muscle deformation assessed by motion-encoded MRI during eye movement in healthy subjects. Journal of Vision 7(10), 1–10 (2007)

12. Porter, J.D., Baker, R.S., Ragusa, R.J., Brueckner, J.K.: Extraocular muscles: basic and clinical aspects of structure and function. Survey of Ophthalmology 39, 451–484 (1995)
13. Qin, H., Terzopoulos, D.: D-nurbs: A physics-based framework for geometric design. IEEE Transactions on Visualization and Computer Graphics 2(1), 85–96 (1996)
14. Quaia, C., Optican, L.M.: Commutative saccadic generator is su_cient to control a 3-D ocular plant with pulleys. Journal of Neurophysiology 79, 3197–3215 (1998)
15. Quaia, C., Optican, L.M.: Dynamic eye plant models and the control of eye movement. Strabismum 11(1), 17–31 (2003)
16. Quaia, C., Shan, X., Tian, J., Ying, H., Optican, L.M., Walker, M., Tamargo, R., Zee, D.S.: Acute superior oblique palsy in the monkey: effects of viewing conditions on ocular alignment and modelling of the ocular motor plant. Progress in Brain Research 171, 47–52 (2008)
17. Raphan, T.: Modeling control of eye orientation in three dimensions:i. role of muscle pulleys in determining saccadic trajectory. Journal of Neurophysiology 79, 2653–2667 (1998)
18. Robinson, D.A.: The mechanics of human saccadic eye movement. Journal of Physiology 174, 245–264 (1964)
19. Robinson, D.A.: A quantitative analysis of extraocular muscle cooperation and squint. Investigative Ophthalmology & Visual Science 14, 801–825 (1975)
20. Robinson, D.A.: Models of the mechanics of eye movements. Models of Oculomotor Behavior and Control, 21–41 (1981)
21. Robinson, D.A., OMeara, D.M., Scott, A.B., Collins, C.C.: Mechanical components of human eye movements. Journal of Applied Physiology 26(5), 548–553 (1969)
22. Schnablok, C., Raphan, T.: Modeling three-dimensional velocity to position transformation in oculomotor control. Journal of Neurophysiology 71, 623–638 (1994)
23. Simonsz, H.J., Spekreijse, H.: Robinson's computerized strabismus model comes of age. Strabismus 4(1), 25–40 (1996)
24. Sueda, S., Kaufman, A., Pai, D.K.: Musculotendon simulation for hand animation. ACM Transactions of Graphics (Proc. SIGGRAPH 2008) 27(3) (2008)
25. Sylvestre, P.A., Cullen, K.E.: Quantitative analysis of abducens neuron discharge dynamics during saccadic and slow eye movements. Journal of Neurophysiology 82, 2612–2632 (1999)
26. Wei, Q., Sueda, S., Miller, J.M., Demer, J.L., Pai, D.K.: Subject-specific reconstruction of the human orbit from magnetic resonance images. In: Proceedings of the IEEE International Symposium on Biomedical Imaging, pp. 105–108 (2009)

A Theoretical Model for RF Ablation of Kidney Tissue and Its Experimental Validation

Mihaela Pop[1], Sean R.H. Davidson[2], Mark Gertner[2,3], Michael A.S. Jewett[4],
Michael D. Sherar[1,2], and Michael C Kolios[1,3]

[1] Department of Medical Biophysics, University of Toronto, Toronto, Canada
mihaela.pop@utoronto.ca
[2] Division of Biophysics and Bioimaging, University Health Network, Toronto, Canada
[3] Department of Physics, Ryerson University, Toronto, Canada
[4] Division of Surgical Oncology, University Health Network, Toronto, Canada

Abstract. Radio-frequency (RF) ablation is a minimal invasive thermal therapy, currently considered as an alternative to surgery to eradicate small solid kidney tumors. Our aim is to understand the kinetics of thermal lesion growth in kidney tissue exposed to RF energy by taking into account dynamic time-temperature changes in electrical properties of multiple tissues (i.e. kidney, surrounding fat, muscle). We present a computer model designed to calculate the voltage distribution and the temperature rise in kidney. The model further calculates the RF lesion size based on kinetic processes, which correctly describe coagulative necrosis process. The simulated transient temperatures and lesion size were experimentally validated with good agreement in a porcine kidney model, *ex vivo*. The expected increase in electrical conductivity of kidney (approximately 3 times) during heating resulted in predicted lesion width and depth that were larger (by as much as 20% and 30% respectively) than those predicted for constant properties. Simulation results also show how the lesion size and shape can be affected by the proximity to the RF electrode of a surrounding layer of fat, which acts as an electro-thermal insulator. The results of this pre-clinical investigation may be useful for treatment planning of RF thermal therapy of kidney tumours.

Keywords: computer modelling, radio-frequency ablation, kidney, thermal damage.

1 Introduction

Radio-frequency ablation (RF ablation) is currently being investigated clinically as a minimally invasive alternative to surgery for the treatment of solid renal masses of about 3cm in diameter, but the success rate is controversial. Clinical studies showed that the size and shape of RFA renal lesions are not reproducible [1]. The aim of the RFA is to elevate tissue temperature beyond 50°C, where protein coagulation causes cell death [2]. Computer models could help to better understand the kinetics of lesion formation and to predict the extent of necrosis (i.e., lesion).

F. Bello and S. Cotin (Eds.): ISBMS 2010, LNCS 5958, pp. 119–129, 2010.
© Springer-Verlag Berlin Heidelberg 2010

Theoretical models incorporate electrical and thermal factors influencing the lesion growth could. Any change in tissue electrical conductivity, σ, is expected to affect the RF energy deposition which is known to be directly proportional to electrical conductivity of tissue, and, consequently, the temperature distribution and tissue damage [3]. We have previously demonstrated that σ changes significantly for kidney and fat tissues at ablation frequencies (i.e. 460 kHz) during heating to high temperatures [4]. These changes were due to reversible, temperature–dependent and permanent structural changes (e.g. protein coagulation, melting of fatty acids) that occur during heating. Such dynamic changes characterize the thermal transitions and are very important for biological tissues. Computer models have been developed to predict the RF energy deposition in tissue and subsequent temperature rise in heart and liver tissue for different RF electrode designs, as summarized in [5]. Some models have included reversible, temperature-dependent changes in electrical conductivity of liver, with coefficients derived from NaCl solutions [6]. Permanent, irreversible changes of electrical properties during heating could play an important role in the theoretical predictions, and thus, they should be taken into account. Only one study [7] has incorporated such dynamic changes into a model of RF kidney ablation, but the validation of the predictions was limited to a few point temperature probes. Moreover, these authors compared the simulated lesion size with the experimental lesion based on the 42ºC iso-dose temperature, although it is well known that the critical temperature where protein coagulation starts to cause the death of cells is beyond 50°C. For kidney tissue, we previously demonstrated [4], via gross examination and histological analysis, that low temperatures (i.e. 42-47ºC) cannot be associated with irreversible thermal effects.

In this paper, we present a computer model that includes the temperature-dependant as well as permanent changes in kidney tissue electrical conductivity due to thermal damage. We predicted this damage using the Arrhenius formalism which appropriately describes the coagulative necrosis. In addition, layers of fat and fat were incorporated into the computational domain, to mimic the anatomy of kidney. Our calculations were validated by measuring the temperature rise during RF heating in pig kidney, *ex vivo*, using a thermographic technique, which is superior to point temperature sensors as it offers surface iso-temperature maps instead of sparse point measurements. The calculated extent of damage was validated by comparison with the size of RF lesions also created in porcine kidney tissue.

2 Methodology

2.1 Mathematical Model and Computer Implementation

Our numerical model contains three components: 1) calculation of the RF energy absorbed by the tissue using electromagnetic field theory; 2) calculation of the transient tissue temperatures using Pennes bio-heat equation; and 3) calculation of the extent of the thermal damage using the Arrhenius formalism. For the first step (i.e., modelling of the RF energy distribution), the RF energy deposited in tissue can be expressed in terms of *absorbed power density* $P(Wm^{-3})$ and is given by [3]:

$$P = \sigma \, | \, E \, |^2 = \frac{| \, j \, |^2}{\sigma}, \tag{1}$$

where σ is the tissue electrical conductivity (S m^{-1}), and $| \, E \, |$ and $| \, j \, |$ are the magnitudes of the electrical field (V m^{-1}) and current density (A m^{-2}), respectively.

The electrical field $\vec{E} = -\nabla V$ can be calculated if the voltage distribution, V, is known. At the operating frequency of the RF applicator used in this study (i.e. 460 kHz), the tissue is considered source-free and the displacement currents are neglected. This is known as *quasi-static approximation*.

The voltage is calculated by solving the Laplace equation: $\nabla \cdot \sigma \nabla V = 0$ [3], for which Dirichlet boundary conditions are applied: a specified value 35.5 V rms on the electrode surface, and zero on the outer domain boundary corresponding to the ground electrode. For complex geometries there is no analytical solution for Laplace equation, therefore, we employed the finite element method (FEM).

The RF energy absorbed by the tissue in the vicinity of the electrode causes a localized rise in temperature. This thermal gradient causes thermal conduction from the electrode into the surrounding tissue. The balance of thermal energy in time and space can be modeled by the *bio-heat transfer equation* (BHTE) given in [8]:

$$\rho_t c_t \frac{\partial T}{\partial t} = P + \nabla \cdot (k_t \nabla T) - c_b w_b (T - T_b) - Q_m, \tag{2}$$

where ρ_t is the tissue mass density (g cm^{-3}), k_t is the thermal conductivity of tissue (W $cm^{-1}K^{-1}$), c_t and c_b are the specific heat of tissue and blood (J g^{-1} K^{-1}), T and T_b are the local tissue and blood temperatures (°C), w_b is the volumetric perfusion rate (g $cm^{-3}s^{-1}$), P is the heat deposited (W cm^{-3}) and Q_m is the metabolic heat (W cm^{-3}), which is very small (thus is usually neglected). To solve the BHTE, a constant temperature at the boundary of the domain was assumed. The volumetric perfusion term was set to zero in this study. Most of the physical properties were taken from [10].

Next, the degree of tissue damage at a tissue location *r*, is calculated using [9]:

$$\Omega(r,t) = \ln\left\{\frac{[C(r,0)]}{[C(r,t)]}\right\} = \int_0^t A e^{-\frac{E_a}{RT(r,\tau)}} d\tau, \tag{3}$$

where $\Omega(r,\tau)$ is the thermal damage index (dimensionless), τ denotes the exposure time (s), A is the frequency constant (s^{-1}), E_a is the activation energy (J mol^{-1}) and R is the universal gas constant (8.314 J $mol^{-1}K^{-1}$). The thermal damage is defined as the logarithm of the ratio of the original concentration of native tissue at time zero, C(r,0), to the remaining native state tissue at time τ, C(r,τ), A value of 1 for Ω represents 63% of the cells in a damaged state (e.g. cell death, protein coagulation).

A FEM solution of the coupled electro-thermal problem was implemented in a computer program that incorporated the Diffpack C++ FEM class library (inuTech GmbH, Nurnberg, Germany). The Laplace equation and BHTE were solved separately. At each time step, the power input to the tissue was calculated by the electrical solver and transferred to the thermal solver (Fig. 1).

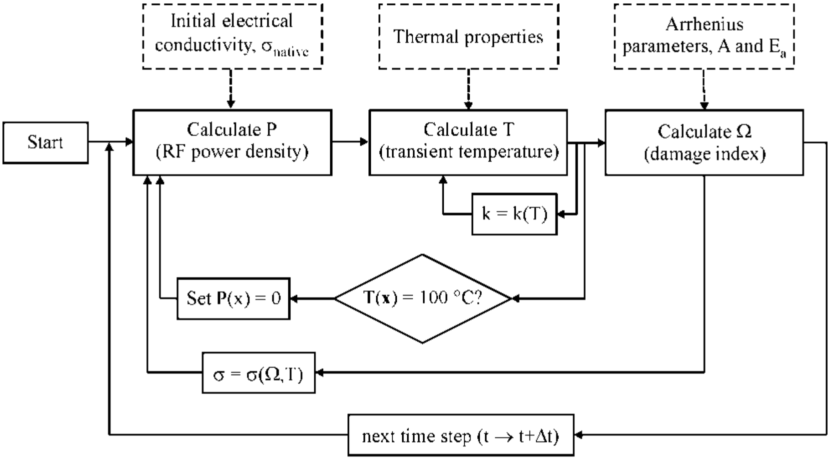

Fig. 1. Flowchart for the non-linear electro-thermal solver

The damage calculated from the thermal solver was then used to update the electrical properties in the electrical solver. The solution of the electro-thermal problem is non-linear due to the dynamic changes in tissue properties σ and k during heating. At time (t), the heat source P(x,t) is calculated and fed into the calculation for T(x,t), which is then used to determine the thermal damage Ω(x,t). Both T and Ω affect the tissue property values, which are re-evaluated *after* each time step. Then, the model re-calculates at the next time iteration (t+Δt) the heat source P(x,t+Δt) based on the new distribution for σ, then re-estimates the local temperature T(x,t+Δt) based on the new values for P and k, and calculates the accumulated thermal damage Ω(x,t+Δt). The calculation of σ is based on tissue measurements up to 78°C [4], however σ is also known to decrease dramatically as tissue desiccates and approaches vaporization temperatures. To implement this effect, the power P was set to zero when T reached 100°C.

The temperature-dependent thermal conductivity of the tissue, $k(T)$, was calculated after each time step according to: $k(T) = k_0 \cdot [1+\beta \cdot (T(t)-T_0)]$, where k_0 is the thermal conductivity of at $T_0 = 22$°C and β is the temperature coefficient (°C^{-1}) [10].

A mesh of triangular elements was generated over the computational domain using Geompack (ZCS Inc., Calgary, Canada). The mesh automatically produces smaller elements around complicated structures (e.g. tissue/electrode interface, electrode tip). The treatment duration was divided into multiple time steps. After convergence tests, a time step of 0.1s and a mesh of 35048 triangular elements were used in all simulations.

Materials and tissue properties (electrical, thermal and mechanical) were included to Table 1.

Table 1. Electrical and thermal properties used in simulations: electrical conductivity σ (at 460 kHz), heat capacity c, thermal conductivity k, mass density ρ, and temperature coefficients, α and β, for electrical and thermal conductivity, respectively.

Material/Tissue [reference]	σ S cm^{-1}	c Jg^{-1} K^{-1}	k Wcm^{-1}K^{-1}	ρ_t g cm^{-3}	α %°C^{-1}	β %°C^{-1}
Electrode (stainless steel) [6]	8×10^4	4.7×10^{-2}	2×10^{-1}	8	0	0
Catheter (polyurethane) [6]	1×10^{-7}	1.05	2×10^{-4}	7×10^{-2}	0	0
Kidney (pig) [4] and [10]	2.2×10^{-1}	3.89	4.8×10^{-3}	1.05	1.6	0.3
Fat, porcine [4] and [10]	2×10^{-2}	2.6	1.7×10^{-3}	0.96	1.7	0.2
Muscle [10]	3×10^{-1}	3.9	4.9×10^{-3}	1.06	2.1	0.2
0.2% NaCl sol. [10]	2.2×10^{-1}	4.18	5.1×10^{-3}	1.0	2	0.2

2.2 Experimental Validation

Freshly excised porcine kidneys were used for the experimental part. The RF lesions were created using a LeVeen™ electrode (2 cm diameter tip-to tip) with eight stainless steel tines (4 mm thickness) deployed in an ‘umbrella’ fashion in the kidney (Fig. 2). The electrode has an insulated catheter (polyurethane, 2 mm diameter) and the needle tip has an un-insulated section (1 mm length, 2 mm diameter). The LeVeen electrode was connected to an RF 2000™ generator. The tissue electrical impedance rises when tissue desiccates the power falls to zero.

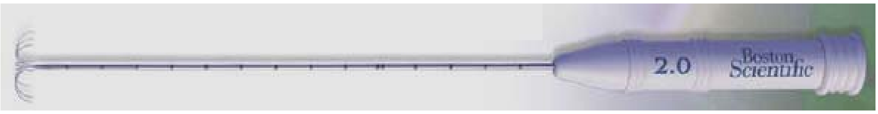

Fig. 2. RF ablation electrode (LeVeen needle, 2cm diameter; Boston Scientific, USA)

2D temperature patterns were measured using a thermographic technique. The kidneys were cut into two pieces in coronal plane and a 2cm RF electrode was placed between them; only two opposite tines were used to compare with the 2D calculation. After applying a voltage of 35.5V rms for 7s or 60 s, the top portion of the kidney was removed and the surface of the bottom part was exposed. An infrared (IR) camera (FLIR systems, model SC2000, accuracy 0.2°C) was used to measure the temperature on the exposed surface. The camera recorded continuously at a rate of 5 frames/s rate. A cooling delay between end of heating and temperature acquisition starting time was estimated to 0.5s (and was also taken into consideration in theoretical calculations).

Before each measurement, calibration measurements were made using objects of known dimensions. The 2D temperature maps were converted into contour plots using Matlab (Mathworks, CA).

For the thermal damage assessment, RF lesions were created ex vivo in porcine kidney, with and without a surrounding layer of fat. The lesions were produced by applying a power of 40W (35.5 V r.m.s.) to a 2cm electrode LeVeen electrode deployed into the kidney. The kidney was immersed in 0.2% saline solution at 37ºC (having the same electrical conductivity as kidney, 0.0022Sm^{-1}) and placed on a layer of muscle tissue that, in turn, was placed on a grounded electrode. Several lesions were also produced in kidney surrounded by a layer of fat (4-5 mm thickness) sewn to the kidney using surgical thread to ensure good contact. The lesion extent was assessed by gross pathology. The thermal lesion usually appear as a whitened area of coagulated tissue surrounded by a red rim (due to collapsed and ruptured red blood cells), beyond which tissue is normal [2]. The size of the RF ablation lesion was compared to the thermal damage predicted by simulations.

3 Results

The 2D computational domain used in simulations is shown in Fig. The 7x7 cm domain was segmented into regions (kidney, fat, muscle, etc) to replicate the experiment. The voltage solution is shown in Figsures 3b (no fat) and 3c (with fat included). An asymmetry in voltage distribution is created around the electrode tine placed in the vicinity of fat (fig 3c) because σ of fat is ~1/10 that of kidney.

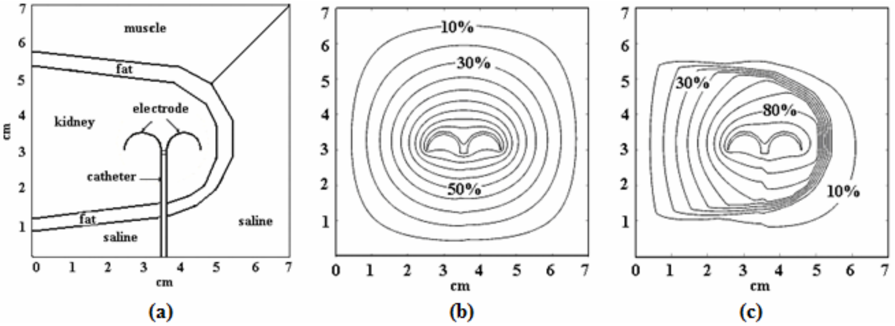

Fig. 3. The computational domain used in simulations (a). The voltage solution: (b) with the layer of fat not included, and (c) with fat surrounding the kidney.

Figure 4 shows contours of temperature measured on the exposed surface of the kidney immediately after 7s heating (4a) and 60s heating (4c). The predictions for the same heating durations are shown in Figs 4b and 4d, respectively. Both measured and predicted maximum absolute temperatures are given in Table 2.

Table 2. Maximum absolute temperature predicted and measured using the thermographic technique. Experimental results are given as mean ± standard deviation (3 or 4 experiments).

Thermal treatment time (s)	Maximum absolute temperature (°C)	
	Simulations (dynamic case)	Experiments
7s heating +		
a) 0s cooling	45.9	N/A
b) 0.5s cooling	41.1	43.6 ± 4.1 (3)
60 s heating +		
a) 0 s cooling	91.8	N/A
b) 0.5 s cooling	87.7	84.9 ± 4.0 (4)

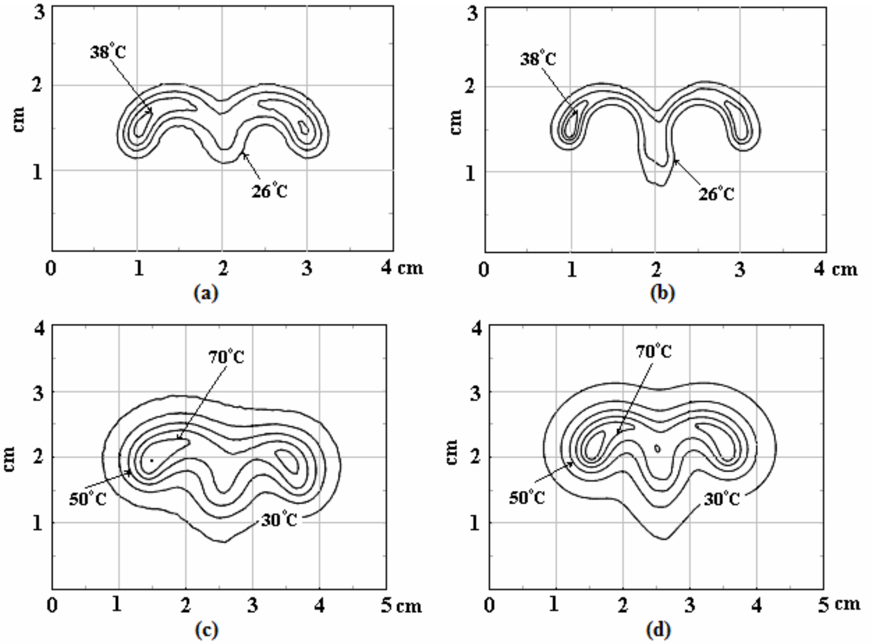

Fig. 4. Iso-temperature contours (a) measured after 7s heating, (b) predicted for 7s heating + 0.5s cooling using the dynamic properties model, (c) measured after 60s heating and (d) predicted for 60s heating + 0.5s cooling using the dynamic properties model

The measured and calculated maximum temperatures were in a good agreement for the 7s heating. However, the experimental contours (fig 4a) are slightly wider than the theoretical contours (fig. 4b). This difference may be due to the limited spatial resolution (1 mm) of the camera or to the noise in the thermographic images. The depths and widths of temperature iso-contours at 60 s (figs 4c and 4d) were in very good agreement. After 0.5 s cooling, the calculated maximum absolute temperature was 2.8°C higher than the experimental value, representing a difference of 4.5%. In all cases, the maximum temperature occurs at the electrode tip.

A comparison of the transient temperatures after 120 s of heating (plots not shown) for the 3 models, showed that for the dynamic case, an increase in σ with respect to time and temperature caused an increase in maximum P value from 2751 Wcm^{-3} to 7980 Wcm^{-3}, being maximum at the electrode tip. The dynamic model showed an increase of ~8% in both depth and width of the 50°C contour in comparison with the static model. Moreover, when the fat was included, the area encompassed by the temperature contours changed (e.g. the 50°C contour was 10% larger in width than in dynamic case) due to the thermal insulation property of the fat.

The calculated extent of damage after a 6 min thermal treatment (2 min heating + 1 min cooling + 1 min heating + 2 min cooling) is shown in Fig 5.

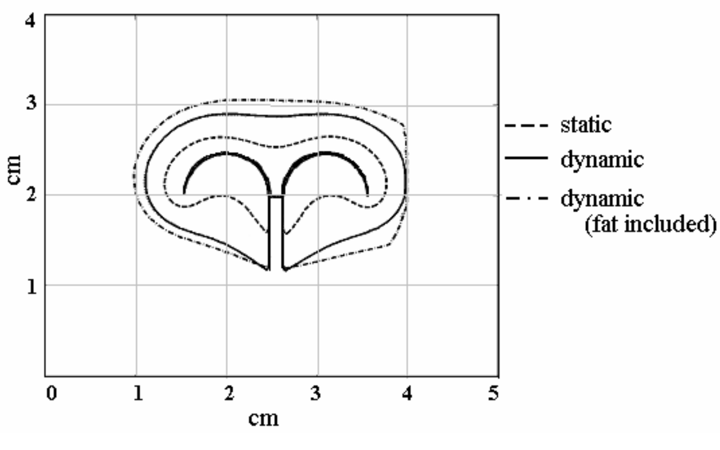

Fig. 5. RFA lesion predicted for different models; the outer line corresponds to a dynamic case with fat, the middle line to a dynamic case with no fat, and the inner line to a static case.

The predicted depth (D) and width (W) of the lesions for each model are included in Table 3.

The extent of damage predicted by the dynamic model was ~20% larger in width and ~35% larger in depth, and almost double the area of the lesion predicted by the constant model. The largest area of damage was predicted for the dynamic properties model in which the layer of fat was incorporated, as also seen in the gross (visual) inspection of the specimens Figure 6 (a and b).

Table 3. Theoretical predictions and experimental measurements of the RF lesion size, for different models. Experimental results are given as the mean ± standard deviation of 5 experiments.

Model	Theoretical predictions		Experimental measurements (mean ± S.D.)	
	W (cm)	D (cm)	W (cm)	D (cm)
1. Static properties	2.4	1.2	N/A	N/A
2. Dynamic properties	2.9	1.8	2.7 ± 0.3	1.9 ± 0.2
3. Dynamic (with fat)	3.0	2.0	2.8 ± 0.2	2.3 ± 0.2

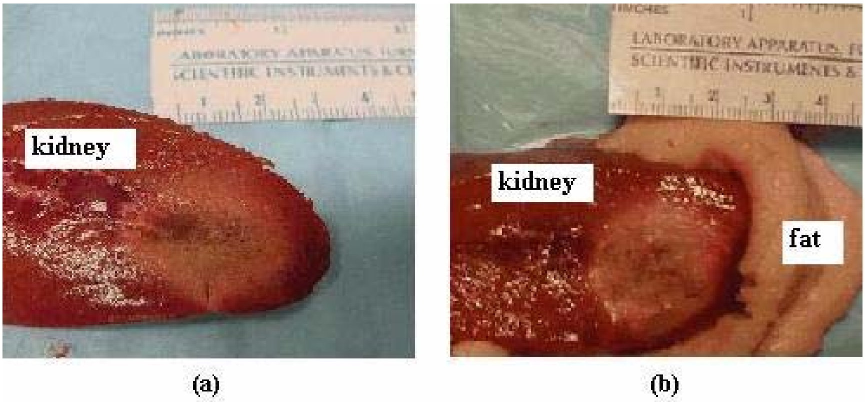

(a) (b)

Fig. 6. Gross pathology of the RFA lesion: (a) fat not included, and (b) fat surrounding the kidney (white areas correspond to coagulation)

4 Discussion and Future Work

The deposition of RF energy is considered to be mainly resistive, i.e. the heat arises from the ionic agitation caused by the RF heating and the displacement currents are neglected [2]. The incorporation of tissue properties is known to be very important in order to accurately predict the extent of the thermal lesions [12]. As a result, the energy absorbed by tissue depends on the changes in electrical conductivity, which further affects the temperature distribution and the extent of the thermal damage, as demonstrated by comparing the results between the dynamic and static models. We calculated the thermal lesion size using Arrhenius equation instead of iso-dose temperatures, and validate it experimentally. Our results suggest that a damage model based on this formalism is more accurate for kidney tissue than a model based on temperature alone. In a study for RFA of liver [6], the authors considered a 50°C iso-contour as the margin of 'coagulated area' and an overestimation of lesion size calculated based on the 47°C contour compared to Arrhenius model was observed. Additional evidence from theoretical and experimental results obtained in liver tissue, showed that 42-47°C isotherms give wrong estimates of the extent of the damage, and so, the iso-dose damage should be carefully considered instead of the traditional iso-dose temperature [5].

Results from our study also suggest that RF lesions produced in kidney are affected by a surrounding layer of fat acting as both an electrical and thermal insulator. Such an observation is important for clinical studies since the peri-renal fat surrounding the human kidney can have a thickness of up to 2 cm, thus the fat could protect the anatomical structures surrounding the kidney [1]. In addition, the electrode position relative to the peri-renal fat plays an important role in defining the final size and shape of the RF lesion in kidney. Preferential heating of the tumors surrounded by fat has also been demonstrated by others via simulations and experimental studies for RF ablation in breast tissue, emphasizing the importance of incorporating fat into the domain geometry for realistic simulations [12].

Our model has certain limitations. The implementation of the model was limited to a 2D case. Thus, we considered only two tines of the RF needle since it was advantageous for designing the experiment validating the temperature contours. In reality, this RF electrode has 8 tines each contributing to the lesion growth in 3D; this most likely accounts for the difference between predicted and experimentally generated thermal damage. Desiccation and contraction of the tissue may contribute to smaller dimensions obtained in the experiments versus simulations. We also limited the study to un-perfused scenarios.

In the future, we will extend the model to a 3D case and include the perfusion term in the BHT equation, as well as experimental validation in a perfused kidney model. Treatment optimization and designing new and improved heating applicators as well as their placement relative to the target (i.e., tumours), are ongoing challenges for a better thermal therapy planning [13, 14].

References

1. Stern, J.M., Svatek, R., Park, S., Hermann, M., Lotan, Y., Sagalowsky, A.I., Cadeddu, J.A.: Intermediate comparison of partial nephrectomy and RFA for clinical T1a renal tumours. British Journal of Urology 100, 287–290 (2007)
2. Thomsen, S.: Qualitative and quantitative pathology of clinically relevant thermal lesions. Critical Reviews of Optical Science and Technology CR75, 425–458 (2000)
3. Strohbehn, J.: Temperature distributions from interstitial RF electrode hyperthermia systems: theoretical prediction. Int. J. Radiation Oncology 9, 1655–1667 (1983)
4. Pop, M., Molkovski, A., Chin, L., Kolios, M., Jewett, M., Sherar, M.: Changes in dielectric properties at 460 kHz of kidney and fat: importance for radio-frequency thermal therapy. Phys. Med. Biol. 48, 2509–2525 (2003)
5. Chang, I., Nguyen, U.D.: Thermal modeling of lesion growth with radio-frequency ablation devices. Biomedical Engineering OnLine 3, 27 (2004)
6. Tungjikusolmun, S., Staelin, S.T., Haemmerich, D., et al.: 3D finite-element analyses for RF hepatic tumor ablation. IEEE Trans. Biomed. Eng. 49, 3–9 (2002)

7. Meyer, M., Velte, H., Lindenborn, H., Bangert, A., Dahlhaus, D., Albers, P.: Radiofrequency ablation in renal tumors improved by preopeartive ex-vivo computer simulation model. Journal of Endourology 21, 886–890 (2007)
8. Pennes, H.: Analysis of tissue and arterial blood temperatures in the resting forearm. Appl. Physiol. 85, 5–34 (1998)
9. Pearce, J., Thomsen, S.: Rate process analysis of thermal damage. Optical-thermal Response of Laser-Irradiated Tissue, pp. 561–605. Plenum, New York (1995)
10. Duck, F.A.: Physical Properties of Tissue, A Comprehensive Reference Book. Harcourt Brace Jovanovich, London (1990)
11. Van de Kamer, J.B., Van Wieringen, N., De Leeuw, A.C., Lagendijk, J.W.: The significance of accurate dielectric tissue data for hyperthermia treatment planning. Int. J. Hyperthermia 17, 123–142 (2001)
12. Ekstrand, V., Wiskell, H., Schultz, I., Sandtstedt, B., Rotstain, S., Eriksson, A.: Influence of electrical and thermal properties on RF ablation of breast cancer: is the tumour preferentially heated? Biomedical Engineering OnLine 4, 41 (2005)
13. Berjano, E.J.: Theoretical modelling for radio-frequency ablation state-of-the-art and challenges for the future. Biomedical Engineering OnLine 5, 24 (2006)
14. Chen, C.R., Miga, M.I., Galloway, R.L.: Optimizing Electrode Placement Using Finite-Element Models in Radiofrequency Ablation Treatment Planning. IEEE Trans. Biomed. Eng. 56, 237–245 (2009)

A Point-Based Simulation Framework for Minimally Invasive Surgery

Bo Zhu[1], Lixu Gu[2], Xiaopeng Peng[1], and Zhe Zhou[1]

[1] School of Software, Shanghai Jiao Tong University, China
[2] Med-X Research Institute, Shanghai Jiao Tong University, China
`{boolzhu,gulixu,season129,ziziamy}@sjtu.edu.cn`

Abstract. In this paper, we present a physically-based simulation framework to build up real-time Minimally invasive surgery (MIS) simulators using point-based techniques. In our framework, simulations of organ contacts, collisions, deformations and haptic feedbacks are all based on discrete physics points. We propose a new smoothed particle hydrodynamics (SPH) approach to simulate non-linear biological soft tissues with a specified tensor computation scheme and experimentally measured organ parameters. We employ a uniform grid method to handle collisions and contacts between organs and surgical instruments represented by particles in real-time. Additionally, a point-based smoothing method for contact feedback is proposed. Our framework could simulate complex surgical scenes in MIS simulation in a unified way, and improve the time efficiency of the entire system without loss of physics accuracy, as shown in our experiment results.

Keywords: Minimally invasive surgery simulation, deformable modeling, point-based simulation, SPH, physically-based modeling.

1 Introduction

Computer-based training system for Minimally invasive surgery (MIS) plays a more and more important part in today's surgical residents' education. And the realism of the virtual surgery scenarios significantly affects the effects of training. In common surgical simulators, different parts of simulation are usually based on different physics or computation models (e.g. FEM [5], BEM [1] or mass-spring [136]) and different data representations (e.g. volume mesh, surface mesh or particle systems). Because there exists hardly any direct correlation between these models, the interaction between them becomes a bottleneck of simulation. To couple these heterogeneous models in one system and let them work together with high performance is a challenging task in today's real-time surgical simulators.

Considering all these drawbacks of model diversity in surgical simulation, in this paper we present a unified framework to represent models and simulate physics behaviors in surgical environment. Our framework is mainly based on point-based simulation techniques, which draws a lot of attention in the field of computation physics,

F. Bello and S. Cotin (Eds.): ISBMS 2010, LNCS 5958, pp. 130–138, 2010.
© Springer-Verlag Berlin Heidelberg 2010

computer graphics over the past years ([2], [3], [7], [10]). Since most existing point-based applications are focusing on video games, computer animation and off-line physics simulation, there are few research works ([11], [12]) concerning with applying these techniques in the field of real-time biomedical simulation. In our work, a physically-based simulation framework purely using discrete physics points instead of surface or volume meshes is applied in simulating laparoscopic surgery procedures, including simulating organ deformation, controlling instrument movement, detecting collision and computing haptic feedback.

Comparing with the point-based modeling methods used in computer graphics and video games, whose mainly concerns are time efficiency, our modeling approach focus on simulating human organ deformations realistically in virtual surgical environment. To achieve this goal, a new strain-stress tensor computation scheme is combined with SPH method, and material properties of different organs are determined via biomechanics experiments. Our framework contains four main parts: medical data segmentation and point extraction, point-based deformable modeling, collision and haptic handling and visualization feedback. We will discuss each of them in the following.

2 Medical Data Segmentation and Point Extraction

In this stage, organ models necessary for constructing virtual surgery scenes are segmented from the CT image data, and then discrete physics points are extracted from the set of pixels of each segmented organ by using an adaptive sampling algorithm. Different number of sampled points could meet the efficiency requirements in different detail-levels (as in Fig.1). Additionally, surface meshes of organs for visualization are reconstructed by employing marching cube method. In simulation steps, visualization mesh and physics points are combined together by a simple interpolation method (in section 4).

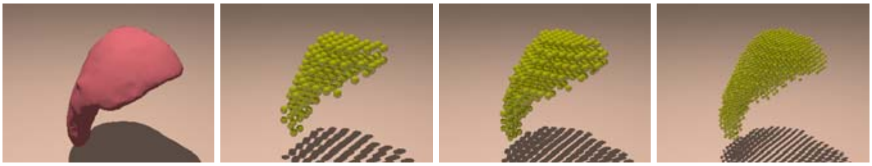

Fig. 1. Surface mesh (first figure on the left) and physics points with different detail levels (three figures on the right) of a liver model are extracted from raw medical data

3 Point-Based Deformable Modeling

With the extracted physics points in the previous step, we use Smoothed Particle Hydrodynamics (SPH), a mesh-free particle system approach to simulate the elasto-mechanical properties of soft bodies in a physically motivated way. Recently similar works in computer graphics could be seen in [3] [2] [7].

3.1 SPH-Based Elasticity Model

SPH method is an interpolation method to approximate properties carried by discrete particles. In SPH method, a deformable object is replaced by a set of particles, and each of them carries a series of physics properties. The local physics property $f(\mathbf{x}_i)$ and its gradient $\nabla f(\mathbf{x}_i)$ of particle i could be approximated by interpolating the properties of its neighbors using the following function:

$$f\left(\mathbf{x}_i\right)=\sum_j \frac{m_j}{\rho_j} f\left(\mathbf{x}_j\right) W\left(\mathbf{x}_i-\mathbf{x}_j, h\right) \tag{1}$$

$$\nabla f\left(\mathbf{x}_i\right)=\sum_j \frac{m_j}{\rho_j} f\left(\mathbf{x}_j\right) \nabla W\left(\mathbf{x}_i-\mathbf{x}_j, h\right) \tag{2}$$

in which $W(\mathbf{x}_i-\mathbf{x}_j, h)$ is kernel function and h is influence radius. In our approach, we use the spiky kernel function as in [3]. The neighbor information and density of each particle is pre-computed before simulation loops.

The way we use to compute the organ deformation based on SPH is similar to [2], in which deformable model is assumed as a Hookean material. The strain ε and the stess σ follow the following rules:

$$\sigma=\mathbf{C}\varepsilon \tag{3}$$

in which **C** is a rank four tensor. As for isotropic materials, **C** could be represented by a 6x6 matrix determined by Young's Modulus and Poisson Ratio of linear elastic materials as in [2] and [7]. In our case, we use coefficients λ_1, λ_2 and λ_3 determined from non-linear anatomical tissue experiments (in Part 3.2) to compute the tensor C.

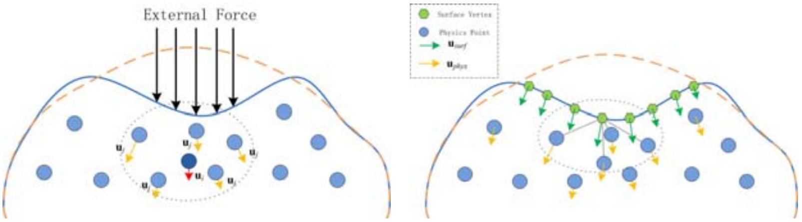

Fig. 2. The left figure shows a solid (blue lines) deforms from the rest shape (orange line) due to the external force. The displacement of each physics point is computed according to the displacements of its neighbors within distance h. The right figure illustrates the displacements of surface vertices (green) are computed based on the displacements of the neighbor physics points (blue) as in section 5.

SPH method is employed to approximate the derivatives of displacement of each particle:

$$\nabla \mathbf{u}_i=\sum_j \frac{m_j}{\rho_j}\left(\mathbf{u}_j-\mathbf{u}_i\right) \nabla W\left(\mathbf{x}_i^0-\mathbf{x}_j^0, h\right)^T \tag{4}$$

where ρ is the density of particle *i*, which is pre-computed using the information of the referenced rest shape of the object.

With $\nabla \mathbf{u}_i$, ε_i is computed as Green-Saint-Venant strain tensor with the form

$$\varepsilon = \nabla \mathbf{u} + \nabla \mathbf{u}^T + \nabla \mathbf{u} \nabla \mathbf{u}^T \tag{5}$$

Stress tensor σ_i is calculated using equation (3). With both strain and stress, we could get the strain energy density on each point and the elastic force is computed as the derivative of the energy density with respect to the direction of displacement **u** as in [2]. In detail, the elastic force $\mathbf{f}_{ji}$ exerted on particle j by particle *i* is computed as

$$\mathbf{f}_{ji} = -\nabla \mathbf{u}_i U_i = -\frac{m_i}{\rho_i}(\mathbf{I} + \nabla \mathbf{u}_i)\sigma_i \mathbf{d}_{ij} \tag{6}$$

With

$$\mathbf{d}_{ij} = \frac{m_j}{\rho_j} \nabla\left(\mathbf{x}_i^0 - \mathbf{x}_j^0, h\right) \tag{7}$$

In each time step, the forces including elastic force, body force and external force on each particle are summed up and applied in a common ODE solver to evolve the system with time (in Fig. 3). To improve the numerical stability, we employ XSPH [4] to smooth the interpolation values and use a second order Runge-Kutta integration scheme in the ODE solver.

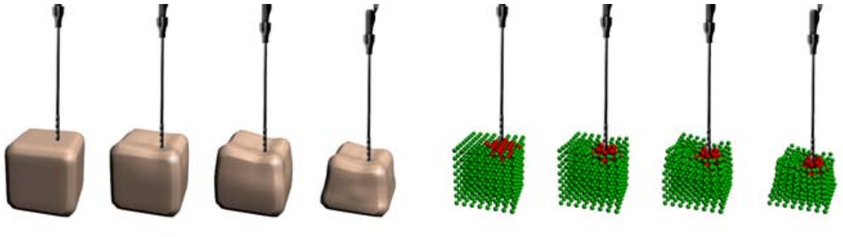

Fig. 3. An elastic cube deforms under pressure of a nipper. Our point-based elastic model and the experimental material parameters are employed. Images are taken every 20 timesteps with (left 4 pictures) and without (right 4 pictures) combined surface rendering.

3.2 Physically Accurate Organ Elastic Tensor

In most applications simulating soft body in computer graphics, the material properties are simply controlled by the Poisson Ratio and Young's Modulus embedded in tensor **C**. However, as for non-linear materials such as biological soft tissues, this is not accurate enough. In our method, we compute the tensor **C** based on polynomial energy functions with parameters determined by biological mechanics experiments. The tensor **C** is computed using the following equation

$$\mathbf{C} = \begin{bmatrix} \eta+2\mu & \eta & \eta & & & \\ \eta & \eta+2\mu & \eta & & & \\ \eta & \eta & \eta+2\mu & & & \\ & & & \mu & & \\ & & & & \mu & \\ & & & & & \mu \end{bmatrix} \tag{8}$$

where

$$\mu = -2\lambda_2 \tag{9}$$

$$\eta = 4\lambda_1\lambda_3^2 e^{2\lambda_3(\varepsilon_{11}+\varepsilon_{22}+\varepsilon_{33})} + 4\lambda_2 \tag{10}$$

We determine the coefficients λ_1, λ_2 and λ_3 for different anatomical organs by measuring the displacement-load relations of tissues sampled from different parts of porcine kidney and liver on INSTRON mechanics equipment and fitting the strain-stress curve using polynomial interpolation method. We get the parameters for kidney and liver model used in our surgical environment as in Table 1.

Table 1. Empirical parameters for different organ models

	λ_1	λ_2	λ_3
Liver	1788.32	-1981.95	6.712
kidney	1646.02	3503.93	5.569

With the measured parameters to represent tensor C, it is possible to describe the specific deformation behaviors of specific organs and tissues.

4 Collision Handling, Haptic Feedback and Visualization

Detecting collision and simulating the interactions between organs and surgical instruments is a very important part in real-time surgical simulation. In our point-based framework, all the objects are represented as points carrying physical properties, so we use a uniform grid to compute their interactions.

The uniform grid (as in Fig.4) subdivides the space of the laparoscopic surgical environment into N^3 voxels with the same size. N is computed as N = L / h, in which L is the longest length of space and h is the influence radius used in SPH. In each time step, for each particle *i*, the indexes x, y, z of voxel **b**(x, y, z) where it locates is updated and the collisions of particle *i* is detected and handled locally within the 27 neighbor voxels. Uniform grid method requires more memories, but it is a highly parallelizable method which could be easily implemented on GPGPU.

After detecting collisions in uniform grid, a correct response should be made both visually and haptically. Since our collision response method is impulse-based as in [9], drastic changes of response force usually occur when the time step is large, which

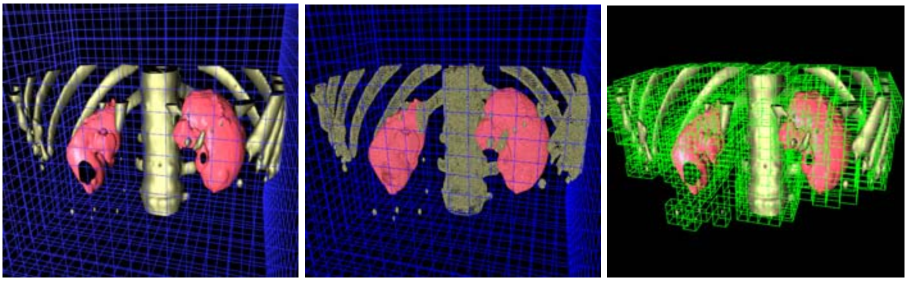

Fig. 4. The surgical environment is modeled as a uniform grid (blue grid in left and middle picture). The model is visualized as a surface mesh (left), physics points are inserted in to the grid (middle), and the voxel containing physics points (green) are updated in each time step (right).

will make the haptic feedback discontinues. On the other hand, in point-based methods, external force is usually added on one discrete physics point, which will lead to various inconsistencies because the contact area is a finite area rather than a infinite point in real world. To overcome these drawbacks, we integrate pressure mask, a method used in boundary element method [1] to smooth the force distribution on the surface, into our framework to get a smoothed haptic feedback from the deformed anatomical organ.

The basic idea of pressure mask is very simple: a smoothed scalar function is used to distribute a vector on a single discrete point to a continuous local area. The scalar function should satisfy the normalizing condition and smoothness condition with compact support. In our framework, we simply reuse the SPH kernel function in deformable solid simulation as the force mask. The external force exerted on each neighbor particle is calculated as

$$\mathbf{f}_j = \frac{W\left(\mathbf{x}_i - \mathbf{x}_j, h\right)}{\sum_j W\left(\mathbf{x}_i - \mathbf{x}_j, h\right)}\mathbf{f} \tag{11}$$

After mask the external force in a local area, the force exerted on one single point is distributed smoothly on a set of neighbor points. And we can get the continuous haptic feedback over time steps (illustrated in Fig. 6).

Visualization in our framework is implemented by combining physics points and renderable surface mesh in real-time. The combine method is based on interpolation between vertexes of surface meshes and physics points. The SPH kernel function is used to sum up the weighted displacements of neighbor physics points and this sum is regarded as the displacement of the surface vertex:

$$\mathbf{u}_i^{surf} = \frac{\sum_j W\left(\mathbf{x}_i - \mathbf{x}_j, h\right)\mathbf{u}_j^{phyx}}{\sum_j W\left(\mathbf{x}_i - \mathbf{x}_j, h\right)} \tag{12}$$

in which $\mathbf{u}_i^{surf}$ is the displacement of surface vertex and $\mathbf{u}_j^{phyx}$ is the displacement of its neighbor physics points (illustrated in Fig. 2). This method is very fast and easy to implement. And high resolution visual feedback of surgical scenes (in Fig. 5) could be provided from a small number of physics points. But this method is weak in preserving the deformation details of the surface. To improve this condition, adaptive particle methods [13] could be applied.

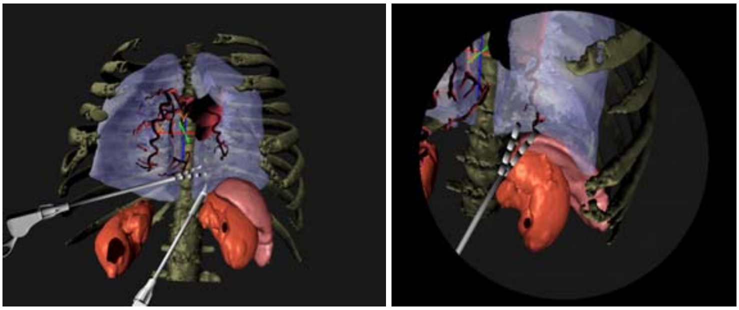

Fig. 5. A Minimally invasive surgery simulator based on our point-based simulation framework

5 Experiments and Results

As the physics accuracy of visualization and haptic feedback are demonstrated in section 3 and 4, in this part we will focus on the scalability and time performance of our framework. All the experiments were carried out on a 2.26GHz Pentium M notebook PC with GeForce 9650M graphics card and 2 GB of memory.

First, we test the scalability of our deformable model by simulating models with different number of physics points. We generate deformable cubes (Fig. **3**) with physics points increasing linearly from 500 to 3000. Then an external force is added on its surface and the time cost of processing deformation is recorded in each time step. The process includes deformation computing, updating surface meshes and generating

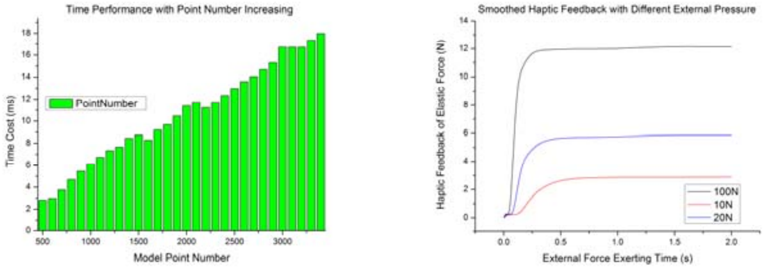

Fig. 6. The left figure illustrates time cost of deformation computing increases linearly with the number of physics points. The right figure shows smoothed elastic response force of the contact point after employing the pressure mask method as in section 4.

haptic feedback. Space grid updating and rendering time are not taken into account. As illustrated in Fig. 6, the time cost meets the real-time requirements well, and increases linearly with the number of points increasing. Comparing with the O(n^2) time complexity of FEM or BEM model, this demonstrates that the speedup of the point-based model in our framework is noticeable even for large number of models.

To evaluate the time performance of different parts of our framework, we extend the previous test to an integrated MIS environment including interaction and rendering (Fig. 5). Then we record the time cost of different parts in each time step as in Table 2.

Table 2. Time performance of different parts in an integrated simulation

Physics-Num	Deformation (ms)	Collision (ms)	Integration (ms)	Rendering (ms)
1000	5.3099	0.7799	0.1422	0.4700
2000	11.3999	1.8800	0.1452	0.4599
3000	17.6499	2.8099	0.1503	0.4700
4000	23.7500	4.0699	0.1540	0.4700
5000	30.1599	5.0000	0.1600	0.6200

The results show that the main computation resource is focusing on physically-based computing, while the time cost of collision handling (including updating uniform grid), integrating and rendering part is tiny comparing with the deformation part. Something worth notice is that the time cost of integration is nearly constant with the same surface mesh. This means that it is easy to couple a fine sampled particle system with a surface mesh to enhance the realism of deformation without increasing the integrating cost. The MIS simulator with our framework could work at 60 fps in average, and this proves to be suitable for real-time applications.

6 Conclusion

In this paper we propose a point-based simulation framework for MIS simulators. We integrate point-based techniques in model construction, deformable simulation, collision handling and haptic rendering into a unified framework to simulate the physics behaviors in MIS system. In this framework, our current work is focusing on simulating organ deformations and handling interactions. Future work will be related to integrating blood simulation into this framework to enhance reality and use GPGPU to improve the time efficiency because most of the point-based algorithms in our framework are parallelizable.

References

1. James, D.L., Pai, D.K.: ArtDefo: accurate real time deformable objects. In: SIGGRAPH 1999: Proceedings of the 26th annual conference on Computer graphics and interactive techniques, pp. 65–72. ACM Press/Addison-Wesley Publishing Co., New York (1999)

2. Becker, M., Ihmsen, M., Teschner, M.: Corotated SPH for Deformable Solids. In: Proc. Eurographics Workshop on Natural Phenomena (2009)
3. Müller, M., Keiser, R., Nealen, A., Pauly, M., Gross, M., Alexa, M.: Point based animation of elastic, plastic and melting objects. In: SCA 2004: Proceedings of the 2004 ACM SIGGRAPH/Eurographics symposium on Computer animation, pp. 141–151. Eurographics Association, Aire-la-Ville (2004)
4. Monaghan, J.: On the Problem of Penetration in Particle Methods. JCP 82, 1–15 (1989)
5. Nesme, M., Marchal, M., Promayon, E., Chabanas, M., Payan, Y., Faure, F.: Physically realistic interactive simulation for biological soft tissues (2005)
6. Pang, W.-M., Qin, J., Chui, Y.-P., Wong, T.-T., Leung, K.-S., Heng, P.-A.: Orthopedics surgery trainer with PPU-accelerated blood and tissue simulation. In: Int. Conf. Med. Image Comput. Comput. Assist. Interv., vol. 10(Pt 2), pp. 842–849 (2007)
7. Solenthaler, B., Schlдfli, J., Pajarola, R.: A unified particle model for fluid–solid interactions: Research Articles. Comput. Animat. Virtual Worlds 18(1), 69–82 (2007)
8. Turini, G., Pietroni, N., Megali, G., Ganovelli, F., Pietrabissa, A., Mosca, F.: New techniques for computer-based simulation in surgical training. International Journal of Biomedical Engineering and Technology, IJBET (2008)
9. Choi, K.-S., Sun, H., Heng, P.-A.: An efficient and scalable deformable model for virtual reality-based medical applications. Artificial Intelligence in Medicine 32(1), 51–69 (2004)
10. Harada, T., Tanaka, M., Koshizuka, S., Kawaguchi, Y.: Real-time Coupling of Fluids and Rigid Bodies. In: APCOM 2007 in conjunction with EPMESC XI, Kyoto, Japan, December 3-6 (2007)
11. Horton, A., Wittek, A., Miller, K.: Subject-specific biomechanical simulation of brain indentation using a meshless method. In: Ayache, N., Ourselin, S., Maeder, A. (eds.) MICCAI 2007, Part I. LNCS, vol. 4791, pp. 541–548. Springer, Heidelberg (2007)
12. Lim, Y.-J., De, S.: Real time simulation of nonlinear soft tissue response in minimally invasive surgical procedures using a meshfree approach. In: Proceedings of the US National Congress on Computational Mechanics, Austin, TX (2005)
13. Adams, B., Pauly, M., Keiser, R., Guibas, L.J.: Adaptively sampled particle fluids. In: SIGGRAPH 2007: ACM SIGGRAPH 2007 papers, p. 48. ACM, New York (2007)

Six Degree-of Freedom Haptic Rendering for Dental Implantology Simulation

Cédric Syllebranque[1] and Christian Duriez[2]

[1] Didhaptic Laval, France
[2] INRIA Lille Nord Europe, University of Lille

Abstract. Training systems for dental implantology that are based on virtual reality need a precise haptic feedback with six Degrees of Freedom (6DoF) This is particularly challenging when using real patient data for the jawbone and during the interactive simulation of drilling. In this paper, we present our simulator and two complementary contributions: The first one is a method for 6DoF haptic rendering of contacts between the drilling tool and the jawbone model issued from a CT-scan. The second one is a fast simulation of the jawbone erosion during drilling which is relevant for 6DoF haptic rendering.

1 Introduction

During a dental implant procedure, the tooth root is replaced by an artificial one, in order to support restorations that resemble a tooth. The technique requires a planning, often based on a 3D CT scan, to identify the vital structures and to chose the appropriate orientation for the implants. The main difficulty during the surgery is the precise drilling of the jawbone.

A first pilot hole in the jawbone is expanded by using progressively wider drills, depending on choosen implant width and length. This must prevent from breaking the jawbone and avoids the elevation of the temperature under too strong drilling constraints, and thus a necrosis of the bone. The holes must be drilled on the accurate direction decided during the planning. However, the density of the bones is non homogeneous. The jawbone, like most of human bones, is composed of two different layers: the core, called spongious bone, is protected by a harder one, the cortical bone. Thus, when the cortical is about to be pierced (cortical breakthrough), the dentist must be careful that he does not apply an excessive force that would drive in the drill tool too deeply. One important skill is to be able to drill a precise hole even while being disturbed by the jawbone inhomogeneities. Moreover, as the view on the operative field is partially obstructed by the tools and cooling irrigation, the surgeons naturally use haptic feedback to perform the procedure.

The surgical placement of implants requires specific formation and the risk of complication decreases with the dentist experience [1]. The training usually begins by acquiring drilling experiences on some artificial jawbones made of plastic. Then, it quickly switches to companionship training on real patients.

F. Bello and S. Cotin (Eds.): ISBMS 2010, LNCS 5958, pp. 139–149, 2010.
© Springer-Verlag Berlin Heidelberg 2010

Some expensive centers provide training on a cadaver head. The benefit of a training system based on virtual reality is to propose an alternative to training on cadaver. It would allow a repetitive rehearsal, and a wide choice of clinical cases.

To allow for acquiring the drilling skills described above, our simulator satisfies the following technical specifications. It includes a comprehensive virtual environment displaying important visual obstructions and anatomical obstacles due to the cheeks and the tongue. The data comes from real patients, so that the teacher can propose a large variety of pathologic cases. The interactions between the dentist tools and the jawbone, such as the collision response and the drilling, are simulated using a physics based approach. The system includes a haptic device with six Degree-of-Freedom (6DoF) (3 translation forces and 3 rotation torques) for rendering all forces that are applied to the drilling tool.

To satisfy these specifications, we have two contributions that are presented in this paper. We extend 6DoF god-object method proposed by [2] (see following section for details) to voxel based collision where the voxel map is issued from a CT-scan. Moreover, we propose a new method for the haptic rendering of a drilling task based on an efficient way of updating the CT-scan volume data.

The remainder of this paper is organized as follows. Section 2 summerizes previous work on 6 DoF haptic rendering and on drilling simulations. Section 3 presents the new algorithm for 6DoF haptic rendering of contacts based on jawbone models from CT-scan. The new method for the drilling simulation and haptic rendering is presented in section 4. Results are shown and discussed in section 5. Finally, we conclude in Section 6.

2 Previous Work

In this section, we only give a brief overview of previous work on haptic rendering of volumetric data including rendering of bone erosion and haptic rendering with 6 DoF. For more details, we refer a recent book on haptic rendering [3].

Voxel based haptic rendering with 6DoF was introduced in [4] with the Voxmap PointShell (VPS) software by Boeing. This pioneer work shows the efficiency of voxel-based collision detection. However, the proposed collision response, which is based on a computation of simple penalty forces, suffers from a lack of precision and stability. Several improvements (i.e. virtual coupling with pre-contact braking force) were proposed to avoid instabilities and improve haptic rendering (see also [5]) but the precision problem remains: the geometrical interpenetration at the end of the collision response depends on the stiffness of the contact springs which is limited by stability issues. In [6], authors propose to overcome the deficiencies of haptic hardware by augmenting perceptual rendering of forces associated to events. To improve precision and haptic rendering quality, [2] proposed a constraint-based approach which is an extension of the god-object method proposed in [7] to 6DoF haptic interaction. This algorithm is able to produce visually convincing non-penetrating configurations and thus improves the perceived stiffness of the objects [3]. However this method is based on continuous collision detection algorithm between triangle meshes and is not applicable in conjunction with voxel-based collision detection. Several other works proposed the use of discrete distance fields in haptic rendering [8] [9] [10], but the redering is based on penalty approaches which allows penetrating configurations. In the following section, we present an algorithm that extends 6DoF god-object method, based on constraints, to voxel-based collision method.

Haptic rendering of bone drilling has been studied in several papers. Augus *et al.* [11] developed an analytical model for bone erosion that can be parametrized with experimental data [12]. Their model is simple, fast to compute and fits quite well with experimental data. The geometry of the drill is assumed to be a sphere but Morris *et al.* [13] proposed a more complete erosion rate model based on sample points on the drill tool. An other milling model is also proposed in [14]. In [15] a discrete marching cube is performed in real-time to evaluate the contact forces. In [16] and [17] they propose a simulation of dental implantology based on FreeForm© software (from Sensable). However, in all these papers, haptic feedback is limited to 3DoF and is derived from elastic contact forces that are similar to penalty forces. In [18], drilling forces are derived from constraints and in [19] drilling forces are computed to ensure stable haptic feedback, but both methods are still limited to 3DoF rendering. In section 4, we propose a similar model of bone erosion but we couple it with a constraint-based approach for haptic feedback.

3 6DoF God-Object Simulation on CT-Scan Model

The method described here extends the 6DoF constraint-based method proposed by Ortega [2] that was inspired by the pioneer work of Zilles and Salisbury [7]. The god-object method employs an idealized reference frame of the haptic device that is constrained to remain on the surface of the environment obstacles when the real haptic device can not prevent from penetrating the environment obstacles. At each time step, the algorithm computes the configuration that minimizes the distance between the real and the idealized reference frames, while meeting the constraints. The virtual object (here, the virtual drill) is attached to the idealized reference frame and the constraints are given by the collision between its geometry and the virtual environment geometry. This way, the user only sees realistic non-penetrating configurations between the virtual object and its environment. We provide an improvement to the method: our algorithm does not need continuous collision detection so that we can use voxel-based collision detection. Moreover, to include friction, we use another solving process.

3.1 Collision Detection between Jawbone and Drill Models

Our method relies on a 3D distance map of the jawbone. This map is precomputed off-line and updated on-line at high rates during drilling. It is extracted from a CT-scan of a real patient and discretized homogeneously using voxel

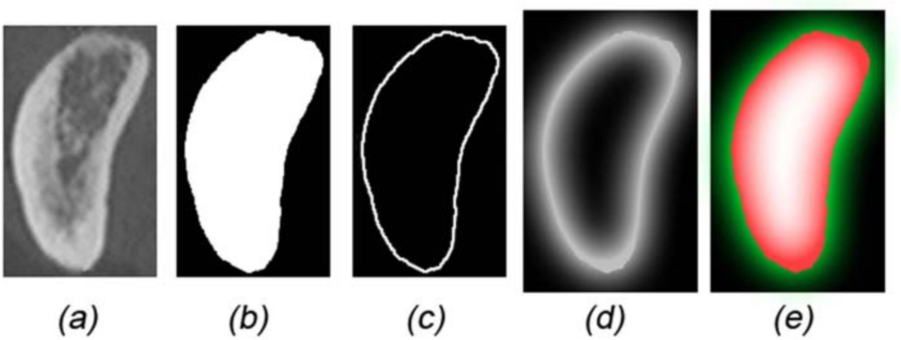

Fig. 1. Illustration of 3D distance map extraction from CT-scan datas (here for one slice): (a) Original CT-scan slice - (b) Binarization - (c) Border extraction - (d) 3D distance map to surface - (e) Signed 3D distance map to surface (blue = outside, positive, and green = inside, negative)

samples of a size about $0.2mm$[1]. First, we binarize each CT-slice to obtain an inside/outside map. We assemble those binarized slices to get a volume block and then extract borders.Finally, for each of these border voxels, we compute a distance field in neighborhood (within a given distance d). Inside the volume, minimal distance are inverted. This process is illustrated by the figure 1. The result is a discrete potential field holding minimal distance to the object's surface that can be interpolated inside each voxel using a tri-linear interpolation. Using this approach, we obtain an implicit surface of the jawbone that can be evaluated very quickly (if χ is the potential function evaluated at point P, $\chi(P) < 0$ if and only if the point P is inside the jawbone).

For the collision detection with the virtual drill, we use the method proposed in [4]. The drill is modeled using pointshells: a set of surface point samples associated with inward-pointing surface normals. The collision computation consists in a simple evaluation of the potential function and the contact normal is token from the pointshell normal. For each colliding point we associate a point on the jawbone surface, which is a *probable* entry point in the model of the jaw. The position of this surface point P_s is computed by raytracing technique between its colliding position P_c and its position P_{go} in the reference frame of the god object (with $\chi(P_{go}) \geq 0$).

As the collision technique is not continuous, we could miss some collision events. To avoid this problem we limit the possible displacement of the drill between two collision computations. We compute an in-between position for the drill tool, at the begining of each time step, when the distance between the position of the god-object and the position of the interface exceeds a given threshold distance (in our case, the threshold equals the size of 6 voxels). The colliding position P_c of each pointshell is computed in the in-between reference. Let $\mathbf{X}_{go}$ and $\mathbf{X}_r$ denote the 4×4 matrices describing, respectively, the position

---

[1] CT-Scan resolutions vary from $0.1mm$ to $1mm$. If necessary, we resample the CT-Scan using trilinear interpolation.

of the god-object frame and the real position of the interface. To obtain the in-between position $\mathbf{X}_c$, we interpolate the rigid displacement by using the same ratio for the interpolation of the translation and the rotation[2].

3.2 Collision Response Based on Friction Contact

The way contacts are handled plays a very important role in the overall behavior of the interacting objects. The inclusion or not of a friction model highly influences the relative motion of the interacting objects and the haptic rendering. For each colliding pointshell, we compute a gap vector δ between the surface point P_s and the colliding position P_c. δ is projected along the normal n_p and tangential directions t_p and s_p. Along the normal, Signorini's model is used and along the tangential directions, Coulomb's law is applied.

Our solving process is close to the one described in [20]. The mechanical coupling between pointshells comes from a mapping of a unique 6DoF damped spring[3] $(\mathbf{K}, \mathbf{B})$ that links the god-object frame $\mathbf{X}_{go}$ to the real device frame $\mathbf{X}_r$ in the haptic control loop. $\mathbf{H}$ provides the 3DoF motion dx of the pointshells due to a 6DoF motion $d\mathbf{X}$ of the god-object: $dx = \mathbf{H}d\mathbf{X}$. The compliance matrix of the pointshells $\mathbf{W}$ is provided by: $\mathbf{W} = \mathbf{H}(\mathbf{K} + \mathbf{B}\mathrm{dt})^{-1}\mathbf{H}^T$.

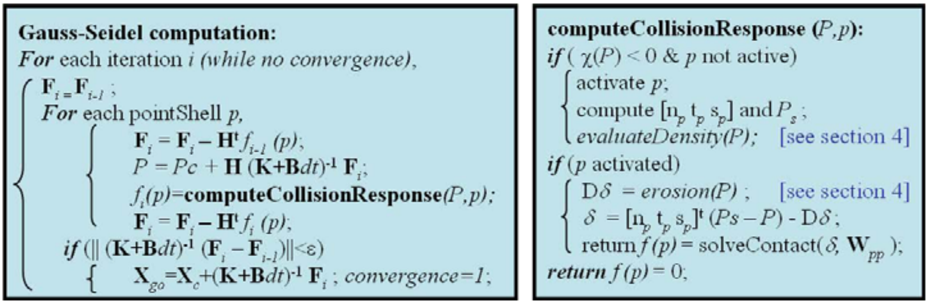

```
Gauss-Seidel computation:
For each iteration i (while no convergence),
    $\mathbf{F}_i = \mathbf{F}_{i-1}$ ;
    For each pointShell p,
            $\mathbf{F}_i = \mathbf{F}_i - \mathbf{H}^t f_{i-1}(p)$;
            $P = Pc + \mathbf{H}(\mathbf{K}+\mathbf{B}dt)^{-1}\mathbf{F}_i$;
            $f_i(p)$=computeCollisionResponse$(P,p)$;
            $\mathbf{F}_i = \mathbf{F}_i - \mathbf{H}^t f_i(p)$;
      if $(\|(\mathbf{K}+\mathbf{B}dt)^{-1}(\mathbf{F}_i - \mathbf{F}_{i-1})\| < \varepsilon)$
            $\mathbf{X}_{go} = \mathbf{X}_c + (\mathbf{K}+\mathbf{B}dt)^{-1}\mathbf{F}_i$ ; convergence=1;
```

```
computeCollisionResponse (P,p):
if ( $\chi(P) < 0$ & p not active)
    activate p;
    compute $[\mathrm{n}_p\ \mathrm{t}_p\ \mathrm{s}_p]$ and $P_s$ ;
    evaluateDensity(P);   [see section 4]
if (p activated)
    $\mathrm{D}\delta$ = erosion(P) ;   [see section 4]
    $\delta = [\mathrm{n}_p\ \mathrm{t}_p\ \mathrm{s}_p]^t (Ps - P) - \mathrm{D}\delta$;
    return $f(p)$ = solveContact($\delta$, $\mathbf{W}_{pp}$ );
return $f(p) = 0$;
```

Fig. 2. Left: Gauss-Seidel algorithm. Right: collision response for each pointshell. $\mathbf{W}_{pp}$ is the diagonal block of $\mathbf{H}(\mathbf{K} + \mathbf{B}dt)^{-1}\mathbf{H}^T$ for pointshell p.

We obtain a non-linear complementarity problem and the solving process is based on the iterative Gauss-Seidel algorithm. To optimize the computation, we do not compute the whole compliance matrix $\mathbf{W}$ (that has a quadratic computational complexity): we only compute the diagonal blocks $\mathbf{W}_{pp}$ and we use operators $\mathbf{H}$ and $\mathbf{H}^T$ to evaluate, at each iteration and at each pointshell the influence other pointshells forces. The solving process is based on a Gauss-Seidel algorithm that is described in figures 2 and 3.

---

[2] Translation interpolation is linear. For interpolating the rotation, we use slerp.

[3] The values in the 6 × 6 matrices **K** and **B** are tuned to optimize the haptic device mechanical stiffness and to ensure stability. The value of these matrices are given by the controller of the Virtuose haptic interface.

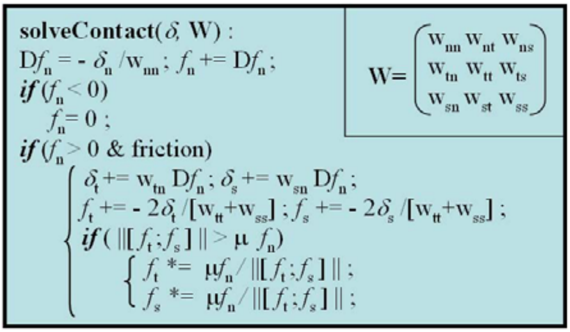

```
solveContact($\delta$, W) :
$Df_n = -\delta_n / w_{nn}$ ; $f_n$ += $Df_n$ ;
if ($f_n < 0$)
    $f_n = 0$ ;
if ($f_n > 0$ & friction)
    $\delta_t$ += $w_{tn} Df_n$ ; $\delta_s$ += $w_{sn} Df_n$ ;
    $f_t$ += $-2\delta_t / [w_{tt}+w_{ss}]$ ; $f_s$ += $-2\delta_s / [w_{tt}+w_{ss}]$ ;
    if ( $\|[f_t;f_s]\| > \mu f_n$ )
        $f_t$ *= $\mu f_n / \|[f_t;f_s]\|$ ;
        $f_s$ *= $\mu f_n / \|[f_t;f_s]\|$ ;
```

$$W = \begin{pmatrix} W_{nn} & W_{nt} & W_{ns} \\ W_{tn} & W_{tt} & W_{ts} \\ W_{sn} & W_{st} & W_{ss} \end{pmatrix}$$

Fig. 3. Computation of the contact force for one point-shell

4 Drilling

In this section, we present a new method for haptic rendering of virtual drilling based on CT-scan data and compatible with the contact algorithm previously described. The outline of the method is illustrated in figure 4.

4.1 Erosion Computation

Using a CT-Scan of a real patient jawbone and the method presented in [21], we compute a volumetric density map. The storage of the density map is optimized to shorten the time access using a sparse matrix indexed by 3 integers (i,j,k) to provide a direct memory access (a global transformation matrix which also includes scaling is used to position it in the virtual environment). We use this map to estimate the local density, i.e. the quantity of material that has to be removed to erode one voxel.

Like the contact algorithm, during the Gauss-Seidel iteration, we compute a collision detection by evaluating $\chi(P)$. We activate the pointshells that are colliding the jawbone and we compute their contribution to the drilling. The local erosion follows an analytical model that is close[4] to the one proposed by [11]. After the integration of the erosion analytical model, we store a new density for each concerned voxel (in `evaluateDensity(P)` function in figure 2). If the density on a voxel vanishes, then we shrink the interpenetration distances by the size of this voxel (in `erosion(P)` function). Then we compute the Gauss-Seidel algorithm and the God-Object position the same way than for contact algorithm, except that the Coulomb's friction coefficient is canceled when drilling. As the interpenetration distances were eroded, the solution do not provide a collision-free configuration: the drill tool penetrates the jawbone surface according to the erosion computation.

During drilling, the drill tool rotates itself and its surface never sticks on the tooth surface. The friction is no more a stick-slip friction but a friction due to the erosion of the tooth surface by the drill tool. Coulomb's friction model is

---

[4] It only differs because the shape of our drill tool models are different.

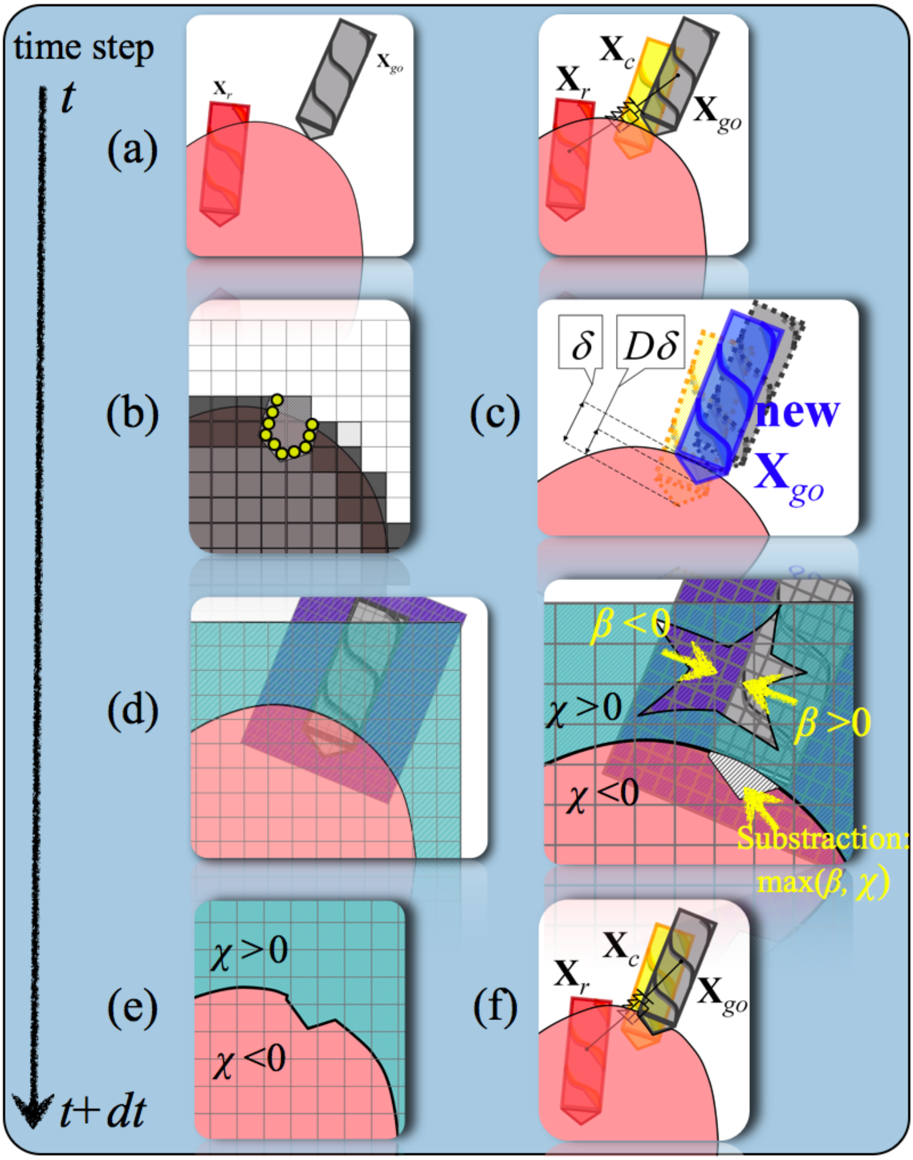

Fig. 4. Computation process for one time step: (a) In-between position $\mathbf{x}_c$ is computed and collision is computed for the pointshells, - (b) For each colliding pointshell, an erosion rate is computed. - (c) The associated interpenetration distance is eroded. The computation continue with the Gauss-Seidel algorithm except that the drill tool can penetrate the jawbone inside with a depth equal to the shrinkage of δ. - (d) Afterwards, the distance map is updated using an algorithm close to the CSG substraction. - (e) We obtain fast and precise geometrical results on the implicit surface. - (f) Finally, the algorithm restarts for a new time step.

then replaced by a simple torque that is applied on the drill tool axis and is proportionnal to the quantity of eroded material.

4.2 On-Line Updates of the Distance Field

When the jawbone is eroded, we update the distance field map that we use for the collision computation and interpenetration evaluation. This process is performed as follows: we precompute another distance field map β for the the drilling tool[5] (see figure 4), but we inverse the values of this map (positive values become negative and vice-versa). We then compute a bounding box around the drill map. For the voxels of the jawbone distance map that are inside this bounding box, we project their center in the tool inversed map. Let's $\beta(P)$ be the value found in the tool inversed map and let's $\chi(P)$ be the current value stored for this voxel. We take the maximum value and assign it to the voxel: $\chi(P) = \max(\chi(P), \beta(P))$. The obtained isosurface on the distance field map models precisely the erosion shape of the drill inside the jawbone. The algorithm can loop for a new time step.

5 Results

The presented algorithms are implemented on our virtual surgery training simulator solution. The haptic system is composed of an implantology hand-piece fixed on a *Haption 6DoF Desktop* device. The controller of the device is based on a virutal coupling scheme between the god-object frame and the real device frame. The virtual environment includes a volumetric jawbone, several different drills and a 3D patient in a 3D dental office (cf Fig. 5). We obtain precise and stable haptic feedback in 6DoF: to illustrate the precision, we focus on the force computation results and for stability, we show the computation time.

Haptic rendering. The figure 6 (b) shows the behaviour of our algorithm under a given user force (in red) applyied on a synthetic jawbone. This synthetic jawbone is made of a box of $1.1g/cm^3$ bone with a top cortical layer of $2.1g/cm^3$ (in (a) before drilling). The drilling depth (in blue) shows the contact/drilling algorithm resulting depth trough all the operation time. We can see that in the cortical part, the bone is hard to drill as it takes 6 seconds to pass through this $2.0mm$ layer, even when the user applies an increasing force reaching $15.0N$. However, after this layer's breakthrough, the drill goes faster and deeply in the soft spongious bone ($5.0mm$ in $0.5s$) while the feedback force felt by the user decreases quickly. This example shows the ability of our algorithms to reproduce the *cortical breaktrough* which must be avoided by the surgeon to prevent from cutting facial nerve passing into the bone.

Computation times. The computation times in the synthetic jawbone example are illustrated by the same figure (Fig. 6 (c)). The contact algorithm (in magenta) takes between $2ms$ and $3ms$ to converge on a 2.4 GHz Quad Core processor. At

---

[5] We use a method similar to the one we developed for the jawbone (cf Fig. 1), except that binarization step is made from the tool profile.

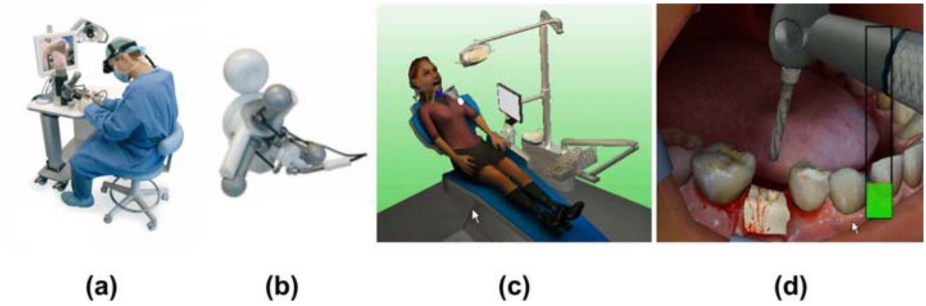

Fig. 5. Our surgery training simulator solution **VirTeaSy Implant Pro - Didhaptic**: (a) global view - (b) haptic device - (c) Virtual environment - (d) Virtual working zone closeup

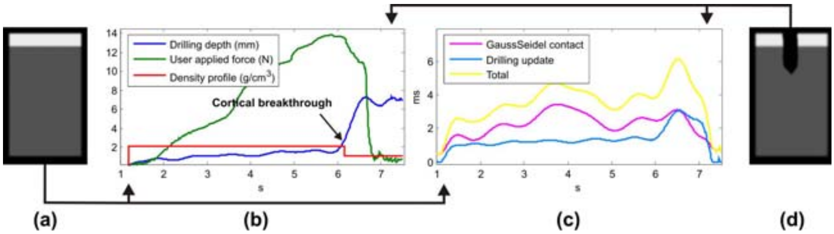

Fig. 6. Haptic rendering and comptuing times during drilling a synthetic jawbone with a 1.9mm drill. (a) a slice of the synthetic jawbone CT-scan before drilling. (b) drilling depth under a user force applied toward the bottom of the jawbone, with density profile. (c) computing times. (d) the same slice as (a) after the drilling.

this maximum computation time, 63 pointshells were detected in collision. The rate obtained by the drilling part is related to the number of voxels involved in the distance map update. In the worst case, about 10000 voxels are in intersection with the tool and are updated in $3ms$. Thus, the minimum total rate is near $166Hz$ for the simulation. To maintain a good stability, the control loop of the haptic device is still computed at $1000Hz$. It uses the last position obtained for the god-object and the new position for the device and between these two positions, the 6DoF damped spring is recomputed to obtain the new haptic force to display.

Precision. This contact algorithm rate is constrained by the precision needed for our application. Indeed, a drill must not be able to enter a hole made by a smaller one. The global convergence criterion must then be small enough to ensure such behaviour. In our tests, we achieve a precision of $10^{-2}mm$ with $0.2mm$ square voxels.

6 Conclusion and Future Work

This paper presents two technical contributions for haptic rendering in a training simulator of dental implantology. We presented an extension of the 6DoF god-object method to voxel-map collision and to contact with friction. We also proposed a new method for the 6DoF haptic feedback of drilling. Both methods are processed in a common manner and are totally compatible.

We plan to improve the performance by parallelizing the update of the distance map. In a more long term, we consider using a multi-threaded approach for the implementation of the Gauss-Seidel algorithm.

References

1. Binon, P.P.: Treatment planning complications and surgical miscues. J. of Oral and Maxillofacial Surgery 65(7, Suppl. 1), 73–92 (2007)
2. Ortega, M., Redon, S., Coquillart, S.: A six degree-of-freedom god-object method for haptic display of rigid bodies. In: IEEE Virtual Reality Conf., pp. 191–198 (2006)
3. Lin, M.C., Otaduy, M.A. (eds.): Haptic rendering: Foundations, algorithms and applications. AK Peters (2008)
4. McNeely, W.A., Puterbaugh, K.D., Troy, J.j.: Six degree-of-freedom haptic rendering using voxel sampling (1999)
5. Petersik, A., Pflesser, B., Tiede, U., Hoehne, K.H., Leuwer, R.: Haptic volume interaction with anatomic models at sub-voxel resolution (2002)
6. Edmunds, T., Pai, D.K.: Perceptual rendering for learning haptic skills. In: Proceedings of the Symposium on Haptic Interfaces for Virtual Environment and Teleoperator Systems, Reno, Nevada, USA (2008)
7. Zilles, C.B., Salisbury, J.K.: A constraint-based god-object method for haptic display (1995)
8. Kim, L., Sukhatme, G., Desbrun, M.: A haptic-rendering technique based on hybrid surface representation. IEEE Computer Graphics and Applications 24(2), 66–75 (2004)
9. McNeely, W.A., Puterbaugh, K.D., Troy, J.: Voxel-based 6-dof haptic rendering improvements. Haptic-e 3(7) (January 2006)
10. Barlit, A., Harders, M.: Gpu-based distance map calculation for vector field haptic rendering. In: WHC 2007: Proceedings of the Second Joint EuroHaptics Conference and Symposium on Haptic Interfaces for Virtual Environment and Teleoperator Systems, Washington, DC, USA, pp. 589–590. IEEE Computer Society, Los Alamitos (2007)
11. Agus, M., Giachetti, A., Gobbetti, E., Zannetti, G., Zorcolo, A.: A multiprocessor decoupled system for the simulation of temporal bone surgery. Computing and Visualization in Science (5), 35–43 (2002)
12. Agus, M., Brelstaff, G.J., Giachetti, A., Gobbetti, E., Zanetti, G., Zorcolo, A., Picasso, B., Franceschini, S.S.: Physics-based burr haptic simulation: Tuning and evaluation. In: International Symposium on Haptic Interfaces for Virtual Environment and Teleoperator Systems, pp. 128–135 (2004)
13. Morris, D., Sewell, C., Barbagli, F., Salisbury, K., Blevins, N.H., Girod, S.: Visuohaptic simulation of bone surgery for training and evaluation. IEEE Computer Graphics and Application (6), 48–57 (2006)
14. Wang, S.M., Chiou, C.H., Cheng, Y.M.: An improved dynamic cutting force model for end-milling process. Journal Mater. Process. Technol. 148, 317–327 (2004)
15. Marras, I., Papaleontiou, L., Nikolaidis, N., Lyroudia, K., Pitas, I.: Virtual dental patient: a system for virtual teeth drilling. In: 2006 IEEE International Conference on Multimedia and Expo, July 2006, pp. 665–668 (2006)

16. Kusumoto, N., Sohmura, T., Yamada, S., Wakabayashi, K., Nakamura, T., Yatani, H.: Application of virtual reality force feedback haptic device for oral implant surgery. Clin. Oral Impl. Res. (17), 708–713 (2006)
17. Ohtani, T., Kusumoto, N., Wakabayashi, K., Yamada, S., Nakamura, T., Kumazawa, Y., Yatani, H., Sohmura, T.: Application of haptic device to implant dentistry - accuracy verification of drilling into a pig bone. Dental Materials Journal 28(1), 75–81 (2009)
18. Kim, L., Hwang, Y., Park, S., Ha, S.: Dental training system using multi-modal interface. Computer-Aided Design and Applications 2, 591–598 (2005)
19. Liu, G., Zhang, Y., Wang, D., Townsend, W.T.: Stable haptic interaction using a damping model to implement a realistic tooth-cutting simulation for dental training. Virtual Reality 12(2), 99–106 (2008)
20. Duriez, C., dubois, F., Andriot, C., Kheddar, A.: Realistic haptic rendering of interacting deformable objects in virtual environments. IEEE Transactions on Visualization and Computer Graphics 12(1), 36–47 (2006)
21. Sjogreen, K., Ljungberg, M., Strand, S.E.: An Activity Quantification Method Based on Registration of CT and Whole-Body Scintillation Camera Images, with Application to 131I. J. Nucl. Med. 43(7), 972–982 (2002)

Haptic Simulator for Prostate Brachytherapy with Simulated Ultrasound

Orcun Goksel and Septimiu E. Salcudean

Department of Electrical and Computer Engineering
University of British Columbia, Vancouver, Canada

Abstract. This paper presents a medical simulator for prostate brachytherapy procedure. Needles are inserted in deformable tissue models using a haptic device while the force feedback computed using a needle-tissue interaction model is rendered on the user's hand. Transrectal ultrasound images of the region of interest are also displayed in real-time using an interpolation scheme accounting for the mesh-based tissue deformation. Employing a 3D ultrasound volume data reconstructed *a priori*, this simulation method achieves realistic ultrasound feedback coupled with immediate tissue deformation. Models for simulating tissue deformation using the finite element method are obtained by segmented the relevant anatomy on MR slices. These models are rigidly registered to the ultrasound voxel volume using the prostate surface. The presented simulation system is suitable for brachytherapy training using haptic control/feedback. It can also be used for treatment planning.

1 Introduction

Minimally invasive procedures often lack a direct visual feedback and therefore are performed using guidance from various medical imaging modalities. In the operating room, physicians have to rely on these images along with the haptic feedback from the medical tools. Therefore, in order to replicate procedures successfully, medical simulators for training, planning, and rehearsal require realistic rendering of both images and haptics, while also taking into account tissue deformation. Furthermore, for rehearsal and planning applications patient-specific models are essential since the tissue mesh and surrounding boundary constraints play a significant role on the outcome of the procedure [1].

Ultrasound is a real-time, cost-effective, non-ionizing, and hence widely-used medical imaging technique. In order to improve the realism of medical training simulations involving this imaging modality, synthesized images realistically mimicking actual procedural ultrasound images are required. For this simulation of ultrasound images, several *generative* methods have been proposed. However, even the most sophisticated generative methods do not capture the realism and complexity of actual B-mode images. Recent work proposes employing actual B-mode volumes to synthesize deformation-coupled images using an *interpolative* scheme in the mesh [2]. This method, which was validated through phantom studies, is adopted and integrated into our needle insertion framework.

F. Bello and S. Cotin (Eds.): ISBMS 2010, LNCS 5958, pp. 150–159, 2010.
© Springer-Verlag Berlin Heidelberg 2010

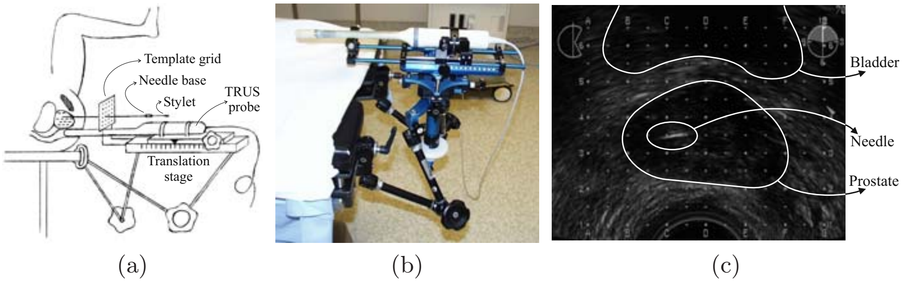

Fig. 1. (a) The brachytherapy procedure setup, (b) a picture of the probe and its stage, (c) and an intra-operative ultrasound image

There exist several studies in the literature on modeling tool interaction with deformable tissue. See [3] for a review. A subcategory of these methods motivated by training, especially laparoscopic procedure simulators, target graphical rendering of simulated camera images as the visual feedback. However, during procedures involving real-time medical imaging, e.g. ultrasound, our simulation system becomes essential for imaging slices within the deformed tissue volume.

Prostate brachytherapy is the permanent implantation of radioactive seeds in and around the prostate to treat cancer. In brachytherapy, the seeds are delivered using long, flexible needles inserted through a *template grid* according to a pre-plan as seen in Fig. 1(a). Meanwhile, a transrectal ultrasound (TRUS) probe mounted on a translation stage is used by the physician to image the anatomy and the needles. Figure 1(b) shows a picture of the probe and the stage. During the procedure, a knob on the side of this stage is used to translate it to image the anatomy at different depths. A sample ultrasound image from the procedure can be seen in Fig. 1(c). Brachytherapy received significant attention from the research community targeting tissue deformation and needle interaction simulations [4,5]. However, haptic and ultrasound feedback, which are both essential in a training setup, have not been provided in any previous work.

2 Methods

2.1 Online Simulation Components

The components described below are illustrated in Fig. 2. At the heart of the simulation lies the needle-tissue interaction model, which runs in a separate thread at high-priority. A low-level haptic process running at 1 KHz reads the haptic device position to control the needle base location and provides force feedback computed in the simulation to user's hand. This process also handles other low-level control tasks achieving a coupling between the device and the simulated needle.

Tissue deformation is modeled using linear-strain FEM and is coupled to the needle shaft using a stick-slip friction model [4]. The flexibility of brachytherapy needles is modeled similarly to the bending of a cylindirical rod. This model is

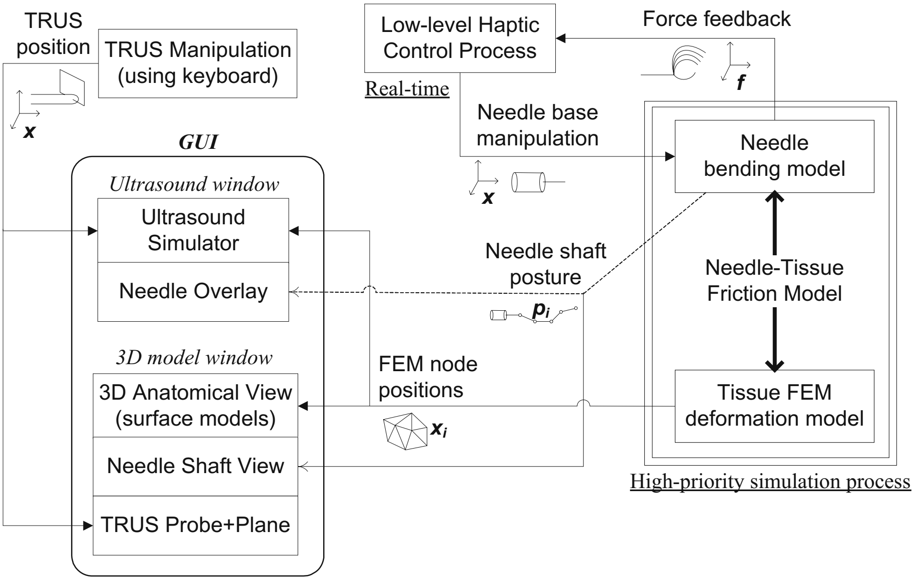

Fig. 2. The online simulation components and their data interaction

discretized as a set of linear rod segments connected via torsinal springs that force the segments to align modeling flexibility [6]. Using the needle posture and the forces exerted on the needle shaft by the tissue at a time instant, the torques at each segment joint and the corresponding spring deviations (hence a new needle posture) are found.

For imaging feedback, real-time B-mode TRUS images are shown to the user using an interpolative ultrasound simulation technique [2]. The nominal 3D voxel volume of the prostate region is collected by sweeping the transrectal probe within the volume of interest. After having registered this image volume to the FEM model in an offline step, the simulated real-time displacements of the mesh nodes caused by needle forces are used to deform this 3D voxel volume. The synthesized B-mode images are generated in real-time, by slicing this deformed voxel volume. In order to accelerate the slices, our technique maps the 2D imaging slice pixels back to the nominal undeformed volume where their intensities are obtained by interpolation on the regular voxel grid. For the details of this method, please refer to [2]. The depth of the transversal imaging plane can be changed by user input, currently using the keyboard, although a probe mockup with a position sensor can also be used.

B-mode needle appearance is also synthesized on the presented ultrasound images. The needle-image simulation method of [7] is adopted, which interpolates an ultrasound needle appearance for arbitrary relative spatial arrangement of the ultrasound image slice and the needle shaft/tip. A large set of needle images, collected *a priori* in water, are used in a multi-dimensional tensor-product interpolation scheme and the simulated needle images are then blended with the

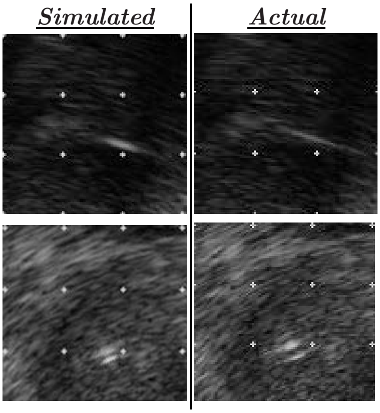

Fig. 3. Comparison of simulated (left) and actual (right) needle images on trasversal TRUS images from a brachytherapy procedure (reprinted from [7])

simulated ultrasound images. This generates realistic-looking needle images in ultrasound as seen in Fig. 3.

An additional 3D view of the anatomy is also displayed, since the data required for such visualization is already available in the simulation. In this work, the immediate deformed anatomy surfaces are rendered in this display along with the needle, TRUS probe, and other visual cues that facilitate the comprehension of the 3D layout. In certain training scenarios such as for evaluating a trainee, this view can be disabled using the interface.

2.2 Patient Model Generation

Each patient model is generated using two sets of imaging data: (*i*) pre-operative TRUS images and (*ii*) pre- or post-operative MRI of the prostate region. The TRUS images are used to reconstruct a 3D B-mode voxel volume for the on-the-fly ultrasound simulation. The MR volume is used to generate a mesh representation of the relevant anatomy. These two modalities are registered using the prostate surface. An outline of the model generation steps described below can be followed in Fig. 4.

First, the prostate, the pelvic bone, and the bladder are segmented in MR images as seen in Fig. 5(a) using the Stradwin software, where the anatomy surfaces seen in Fig. 5(b) are interpolated from these cross-sections [8]. The tissue inside and around these surfaces are then meshed using the TetGen volume meshing tool [9]. Since most meshing applications taking explicit surface representation do not modify the given surface vertices, depending on the desired mesh resolution, these anatomical surface models are resampled at a lower resolution using *fast-marching geodesic farthest-point sampling* [10] prior to meshing. This reduced model as seen in Fig. 5(c) also accelerates the meshing process.

Next, the prostate is segmented on TRUS images. Accordingly, the mesh generated above and seen in Figs. 6(a)-(b) is registered rigidly to the TRUS image

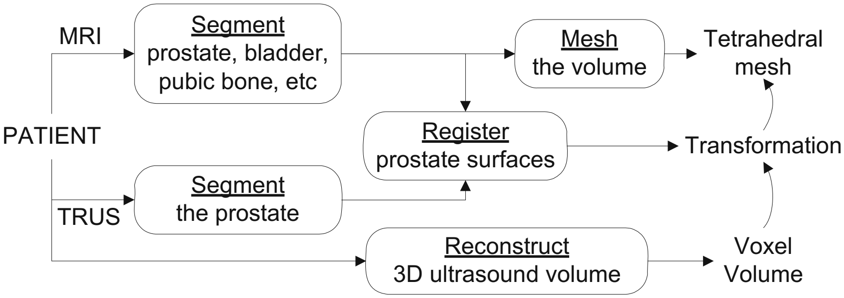

Fig. 4. Patient-specific model generation procedure

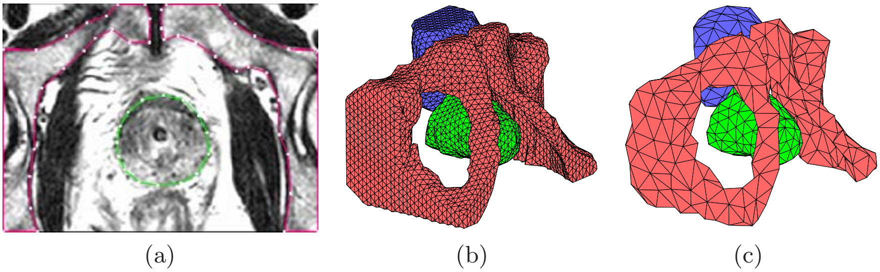

Fig. 5. (a) A segmented MR slice, (b) the fine surface meshes generated from segmented contours, and (c) coarser surface models after farthest point sampling

volume using the prostate surface models from both imaging modalities. *Iterative closest point* (ICP) method is used to match the point clouds of the prostate models. The registered surfaces are seen in Fig. 6(c). For the FEM deformation simulation, a tissue stiffness matrix is computed and inverted in an offline model generation step. The pelvic bone is used as a zero-displacement boundary constraint for the deformation of the tissue mesh. This inverse tissue stiffness matrix and other required mesh vertex/connectivity information computed offline are later employed in real-time by the needle-interaction model.

The ultrasound image simulation also requires certain mesh-related data structures, such as node-element and element-element neighbourhood lists, in order to accelerate its online processing [2], so these are also compiled offline and saved for online use. For a given probe and given imaging parameters, the needle-image simulation employs interpolation from a set of needle images acquired *a priori* at certain position/orientation intervals. The image dataset acquired in [7] for a brachytherapy TRUS probe is used for the needle-image component in this paper.

In order to use in the *3D anatomical view*, the mesh faces corresponding to anatomical surfaces are identified offline. The stick-slip interaction model parameters on such surfaces are adjusted in order to simulate different tissue characteristics such as an increased tip cutting threshold simulating the prostate capsule, that is typically harder to penetrate than the surrounding tissue. Such

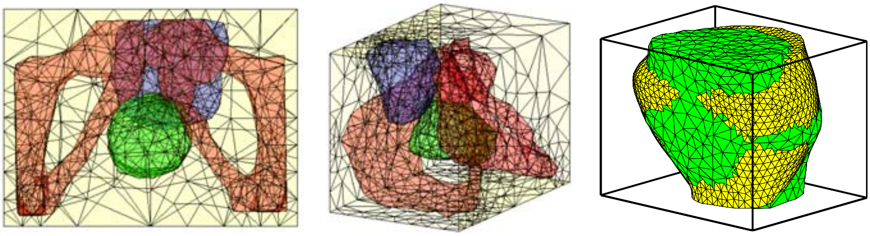
(a) (b) (c)

Fig. 6. (a)-(b) The volume mesh generated from segmentation of MRI and (c) the rigidly registered prostate surface models from MRI and TRUS

friction and cutting parameters of the interaction model are currently set using empirical values. Young's modulus and Poisson's ratio of different tissue layers are assigned from approximate values in the tissue biomechanics literature.

3 Results and Discussion

Haptic interaction is currently implemented using a Novint Falcon device, that has three degrees-of-freedom for both position control and force feedback. Simulating the template grid that constraints the lateral motion of the needle, the device is fixed in those two axes using a PID controller once the insertion point on skin is selected in the ultrasound interface. Subsequently, the device controls the needle base in the insertion axis and provides feedback in the same axis during the simulation. In practice, the needle bending is relevant only beyond the *template grid*. This can be simulated by simply neglecting/zeroing the bending angles of the deformable needle model segments at and before the template location. The discrete angular-springs bending model uses the flexural modulus previously identified for a brachythrapy needle through experiments [6]. In this simulation, a symmetric needle tip is modeled.

The corresponding components of the system run at real-time haptic and visual rates. Refresh rates of the needle interaction and ultrasound simulations can be set in the interface at run-time with typical values being 250 Hz and 10 Hz, respectively. The ultrasound image pixels that are mapped back from the immediate deformed mesh to the nominal time-zero mesh at each iteration are interpolated using tri-linear interpolation in that nominal image dataset. The image simulation takes a large portion of the processing time, therefore the interface including this ultrasound view is isolated in a separate thread running at a lower priority than the insertion model. The graphical interface to the simulation software is seen in Fig. 7.

This brachytherapy simulation can also be used as part of a treatment planning system. For given needle-base trajectories, read from a file or commanded in the interface, the simulation finds the needle tip/shaft after the insertion. For example, assuming that this location is where a seed is implanted during the

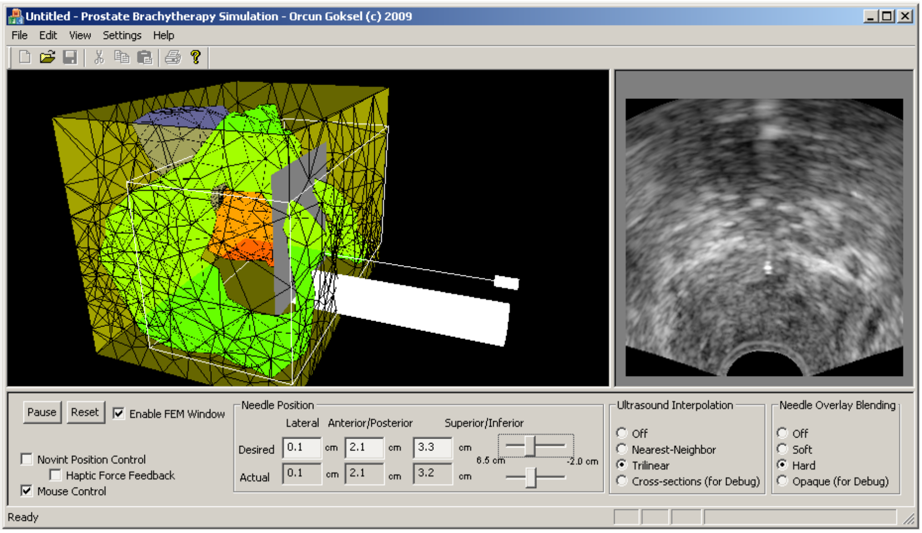

☑ Enable FEM Window
☐ Novint Position Control
☐ Haptic Force Feedback
☑ Mouse Control

Needle Position

	Lateral		Anterior/Posterior		Superior/Inferior	
Desired	0.1	cm	2.1	cm	3.3	cm
Actual	0.1	cm	2.1	cm	3.2	cm

Ultrasound Interpolation
○ Off
○ Nearest-Neighbor
● Trilinear
○ Cross-sections (for Debug)

Needle Overlay Blending
○ Off
○ Soft
● Hard
○ Opaque (for Debug)

Fig. 7. The graphical interface to the simulation displaying the anatomical surface models on the left and the simulated ultrasound window on the right

retraction, optimization techniques can be used for path planning [11]. Figure 8 demonstrates an insertion targeting the needle tip at the *circled* spatial location without taking into account deformation. Consider a seed is implanted when the needle arrives to this position in the nominal frame as in Fig. 8(a) with the seed shown with *plus*, which at the time coincides with the nominal targeted location. However, this implanted seed is actually in the deformed tissue configuration and it will end up at a different location once the needle is retracted and the tissue returns to its nominal configuration as seen by the mismatch between the seed and its original target in Fig. 8(c). Note that the ultrasound simulation components are not essential in this treatment planning/targeting operating mode.

During the needle insertion simulation, the conformity of the FEM mesh and the needle model is ensured by *remeshing* the tissue model on-the-fly as new elements are intercepted by the needle tip [4]. This allows for the use of coarser tissue meshes, however induces a computational overhead on the order of hundreds of milliseconds at the time of remeshing. This is acceptable for the use of this simulation in treatment planning. For simulation scenarios where a coarse mesh is used with haptic feedback, a pre-insertion is performed in the background once the insertion template location is chosen. This completes in a few seconds and ensures that the nodes are created/moved on the needle path. Consequently, a subsequent insertion with haptic feedback does not require remeshing and hence does not involve any time-steps possibly exceeding haptic feedback rate.

The deformation of the prostate due to the existence of TRUS probe is assumed minimal and hence the pre-operative MR and the intra-operative TRUS volumes are registered rigidly in the offline registration step that brings the ultrasound images in the FEM model frame. In the future, deformable registration

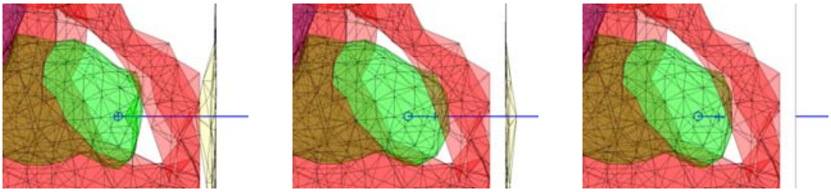
(a) (b) (c)

Fig. 8. Simulation of the seed placement error due to tissue deformation. The circle denotes the pre-plan target, whereas the plus sign marks the actual implanted seed location (a) at the time of insertion, (b) during needle retraction, and (c) after the needle leaves the tissue. The trajectory followed by the seed (plus sign) during retraction is also plotted in these figures.

options will be investigated for this offline step to model deformation caused by the placement of the TRUS probe. Indeed, given that the pelvic bone is also (partially) segmented in TRUS images, it is possible to register these models and consequently the corresponding TRUS voxel volume using well-known deformable registration techniques. Note that FEM-based registration approaches can be of value in this context, since the generated mesh readily provides a good deformable model for registration. Furthermore, such models with element elasticity values obtained from measurements can be automatically derived using elastography techniques [12].

The interaction of the TRUS probe with the tissue, which is not modeled in the current simulation and therefore is not taken into account in the mesh, may be significant during the prostate biopsy or the initial pre-/intra-operative ultrasound registration phase of the brachytherapy. However, during the later needle insertion phase, the probe is often manipulated merely in the superior-inferior axis using the knob on the translational stage. Probe-tissue friction during this manipulation is also currently neglected considering the lubrication of the probe encapsulating balloon. Nevertheless, it is theoretically possible to simulate an accurate probe-tissue interaction using a stick-slip model similar to the needle-tissue interaction.

There exist methods in the literature for finding both the biomechanical properties of the prostate region [12] and the parameters of needle interaction [13,14]. Acquiring such simulation parameters non-invasively is still a challenging research problem. Once acquired, the validation of a simulation using these estimated parameters is a further challenge due to their dependency on a multitude of factors that may change during a procedure such as bleeding and swelling. These issues may have a lesser significance in a training scenario, however should certainly be addressed prior to a planning application of the method.

4 Conclusions

In this paper, a novel needle insertion simulation with simulated ultrasound feedback is presented for the prostate brachytherapy procedure. This is the first real-time deformable tissue interaction model for brachytherapy in the literature that also provides coupled realistic deformable ultrasound feedback. The visual realism of the simulated ultrasound is ensured intrinsically by the use of actual TRUS images as input. The needle in the developed simulation is controlled using one of various methods including a haptic device, allowing for utilization in training, rehearsal, or planning applications. A patient-specific model generation procedure for this simulation is also presented in this paper.

The simulator components *ultrasound image simulation* (also validated experimentally in [2]) and *needle interaction simulation* (implemented with haptics in 2D in [15]) have received excellent feedback. The integrated system for brachytherapy has not yet been tested by physicians. A future study is aimed to evaluate the usefulness of this simulator and to identify any shortcomings. Tissue/needle parameter identification and the validation of the presented system will be studied next. Models for beveled-tip needles will also be explored.

References

1. Misra, S., Macura, K.J., Ramesh, K.T., Okamura, A.M.: The importance of organ geometry and boundary constraints for planning of medical interventions. Medical Engineering and Physics 31(2), 195–206 (2009)
2. Goksel, O., Salcudean, S.E.: B-mode ultrasound image simulation in deformable 3-D medium. IEEE Transactions on Medical Imaging 28(11), 1657–1669 (2009)
3. Misra, S., Ramesh, K.T., Okamura, A.M.: Modeling of tool-tissue interactions for computer-based surgical simulation: A literature review. Presence: Teleoperators & Virtual Environments 17(5), 463–491 (2008)
4. Goksel, O., Salcudean, S.E., DiMaio, S.P.: 3D simulation of needle-tissue interaction with application to prostate brachytherapy. Computer Aided Surgery 11(6), 279–288 (2006)
5. Chentanez, N., Alterovitz, R., Ritchie, D., Cho, L., Hauser, K.K., Goldberg, K., Shewchuk, J.R., O'Brien, J.F.: Interactive simulation of surgical needle insertion and steering. ACM Transactions on Graphics 28(3), 1–10 (2009)
6. Goksel, O., Dehghan, E., Salcudean, S.E.: Modeling and simulation of flexible needles. Medical Engineering and Physics 31(9), 1069–1078 (2009)
7. Zhu, M.: Real-time B-mode ultrasound image simulation and artifacts modelling of needles and brachytherapy seeds. Master's thesis, University of British Columbia (2009)
8. Treece, G., Prager, R., Gee, A., Berman, L.: Surface interpolation from sparse cross sections using region correspondence. IEEE Transactions on Medical Imaging 19(11), 1106–1114 (2000)
9. Si, H.: TetGen, a quality tetrahedral mesh generator and three-dimensional delaunay triangulator. Technical Report 9, WIAS, Berlin, Germany (2004)
10. Peyré, G., Cohen, L.D.: Geodesic Methods for Shape and Surface Processing. In: Advances in Computational Vision and Medical Image Processing: Methods and Applications, pp. 29–56. Springer, Heidelberg (2008)
11. Dehghan, E., Salcudean, S.E.: Needle insertion parameter optimization for brachytherapy. IEEE Transactions on Robotics 25(2), 303–315 (2009)

12. Salcudean, S., French, D., Bachmann, S., Zahiri-Azar, R., Wen, X., Morris, W.: Viscoelasticity modeling of the prostate region using vibro-elastography. In: Larsen, R., Nielsen, M., Sporring, J. (eds.) MICCAI 2006. LNCS, vol. 4190, pp. 389–396. Springer, Heidelberg (2006)
13. Hing, J., Brooks, A., Desai, J.: Reality-based estimation of needle and soft-tissue interaction for accurate haptic feedback in prostate brachytherapy simulation. In: Robotics Research. STAR 28, vol. 28, pp. 34–48 (2007)
14. Okamura, A., Simone, C., O'Leary, M.: Force modeling for needle insertion into soft tissue. IEEE Transactions on Biomedical Engineering 51, 1707–1716 (2004)
15. DiMaio, S.P., Salcudean, S.E.: Interactive simulation of needle insertion models. IEEE Transactions on Biomedical Engineering 52(7), 1167–1179 (2005)

A Shell Model for Real-Time Simulation of Intra-ocular Implant Deployment

Olivier Comas, Stéphane Cotin, and Christian Duriez

INRIA, Alcove team, Lille, France

Abstract. With 30 million interventions a year worldwide, cataract surgery is one of the most frequently performed procedures. Yet, no tool currently allows teaching all steps of the procedure without putting patients at risk. A particularly challenging stage of this surgery deals with the injection and deployment of the intra-ocular lens implant. In this paper we propose to rely on shell theory to accurately describe the complex deformations of the implant. Our approach extends the co-rotational method used in finite element analysis of in-plane deformations to incorporate a bending energy. This results in a relatively simple and computationally efficient approach which was applied to the simulation of the lens deployment. This simulation also accounts for the complex contacts that take place during the injection phase.

1 Introduction

According to the latest assessment of the World Health Organization, age related cataract is responsible for 48 % of world blindness, which represents about 18 million people. Cataract is the clouding of the lens of the eye which impedes the passage of light. Its treatment is a surgical operation, where the opaque lens is removed and replaced by an artificial intra-ocular lens. As people live longer, more surgical interventions are needed. However, current methods of teaching are not compatible with increasing demands of training for this procedure, and also expose patients to complications inherent to the inexperience of the operator. A cataract surgery simulator can offer an efficient alternative teaching method for ophthalmologists, as illustrated in recent reports such as [1]. The work presented in this paper focuses on the simulation of a crucial step of cataract surgery: the injection and deployment of an artificial lens. To reach this objective, we propose an efficient yet simple formulation for triangular shells, as well as a physically accurate model of the complex (self-)contacts that occur during the injection and deployment of the artificial lens.

1.1 Related Work

Although various shapes of intra-ocular lens implants exist they all share common properties: they are three-dimensional structures, usually made of acrylic material, and are much thinner in one direction (0.13 mm) than in the two other

F. Bello and S. Cotin (Eds.): ISBMS 2010, LNCS 5958, pp. 160–170, 2010.
© Springer-Verlag Berlin Heidelberg 2010

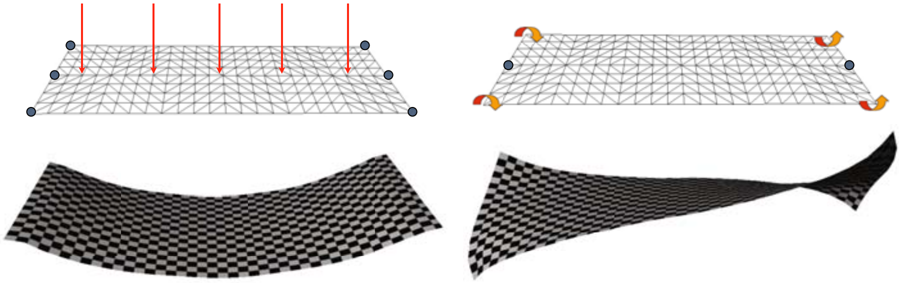

Fig. 1. Illustration of a key difference between various models of thin objects. While thin plate theory allows to describe bending (left), it cannot represent more complex deformations such as twist (right) which is captured by shell theory.

ones (6 and 13 mm). This last characteristic is what classifies these lenses as thin objects, i.e. three-dimensional objects that can be abstracted as two-dimensional structures. Numerous models are available in the literature to describe physics of thin objects, from fairly simple and naive approaches to more complex and thorough representations. Continuum mechanics provides many formulations able to accurately describe stresses occurring within thin objects. Most of them fall into one of the following two categories: plate theory or shell theory. Those theories have been a subject of interest in the mechanical community for decades. The difference between these two kinds of structures is very well explained by Liu *et al.* [2] and can be summarized by the fact that plate bending elements can only carry transversal loads while shells can undergo more complex deformations. For instance, if we consider the horizontal board of a bookshelf, that board can be approximated as a plate structure and the transversal loads are the weight of the books. A typical deformation of the board is illustrated in figure 1 left. Conversely, a shell structure can carry loads in all directions, and therefore can undergo bending, twisting and in-plane deformation (see Figure 1 right). Considering the folded shape of the implant within the injection device (see Figure 3), a thin plate model would not correctly capture the deformation and therefore a shell formulation was retained to model the intra-ocular lens behaviour.

Development of a satisfactory physical model that runs in real-time but produces visually convincing animation of thin objects has been a challenge in Computer Graphics, particularly in the area of cloth modelling. Rather than resorting to shell theory which involves the most complex formulations in continuum mechanics, previous works have often relied on discrete formulations. Early approaches to cloth modelling only considered in-plane deformation, and often relied on mass-spring models (see [3], [4] or [5] for instance). More recent works have considered adding bending through angular springs. For instance Taskiran *et al.* [6] have chosen to use a linear representation of angular springs to supply bending and torsion effects in hair modelling, which allowed them to simulate curly hair with good realism. Wang *et al.* [7] successfully used a network of linear and angular springs to describe bending and twisting of catheters and guidewires in an interventional radiology simulator. Yet, such models are limited in their ability to describe certain behaviour, as they do not rely on continuum mechanics. Another limitation of such models is the difficulty to derive spring stiffness (in particular for angular springs) from elastic properties (Young's modulus and Poisson's ratio). For these reasons, other approaches have been proposed. Among the different models introduced recently we can mention the work of Choi *et al.* [8] and Bridson *et al* [9]. Choi *et al.* proposed a real-time simulation technique for thin shells undergoing large deformations. The authors adopt the energy functions from the discrete shells proposed by [10]. For real-time integration of the governing equation, they adapted a modal analysis technique, called modal warping. The resulting simulations run in real-time even for large meshes, and the model can handle large bending and/or twisting deformations with acceptable realism. Bridson *et al.* followed the same energy approach to derive their bending model but improved the resolution of the equations by suggesting a novel mixed implicit/explicit integration scheme. They also presented a post-processing method for treating cloth-character collisions that preserves folds and wrinkles. Pabst *et al.* improved the bending modelling used by Bridson *et al.* to allow the integration of measured material data. A method to use thin shell dynamics with point sampled surfaces for efficient animation was recently proposed by Wicke *et al.* [11] where the curvature of the shell is measured through the use of fibers.

In this paper we consider the problem of lens implant folding, unfolding and deployment within a very constrained space. An important difference with previous works is that the ratio stiffness / mass of artificial lenses is very high compared to many material (such as fabric), resulting in added difficulties to obtain a numerically stable simulation. Indeed, if the mass density of cotton and acrylic is about the same, the stiffness of intra-ocular implants is three orders of magnitude higher. The closest work to what we propose is the one of Thomaszewski *et al.* [12] who derive their formulation from thin shell analysis in a co-rotational framework. However, the authors use very soft and deformable material (Young's modulus $E = 5000\,Pa$ and Poisson's ratio $\nu = 0.25$).

2 Co-rotational Triangular Shell Model

We propose to define a triangular shell element by combining a two-dimensional in-plane membrane energy, with an off-plane energy for describing bending and twist (see figure 2). To allow for real-time simulation, a computationally efficient formulation is needed. We therefore propose to extend the co-rotational idea introduced by Fellippa in [13]. Indeed co-rotational approaches have been successfully applied to real-time simulation of volumetric objects over the last few years [14]. They offer a good trade-off between computational efficiency and accuracy by allowing small deformations but large displacements. We propose to improve and extend a plate model first introduced by Przemieniecki [15] to a co-rotational formulation. Once combined with an in-plane membrane formulation we obtain an accurate, yet computationally efficient, shell finite element method featuring both membrane and bending energies.

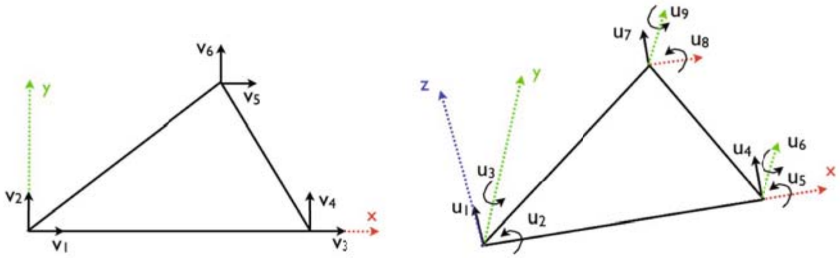

Fig. 2. A triangular shell element can be defined as a combination of a triangular in-plane membrane element (left) and a triangular thin plate in bending (right). The different degrees of freedom v and u of both models are illustrated above.

2.1 Triangular Elastic Membrane

The computation of the triangular elastic membrane stiffness matrix can be derived from previous works dealing with tetrahedral co-rotational elements (see Muller *et al.* [14] for instance). The element stiffness matrix $\mathbf{K}_e$ can be computed as follows:

$$\mathbf{K}_e = \int_v \mathbf{J}\boldsymbol{\chi}\mathbf{J}^T dV \tag{1}$$

where $\mathbf{J}$ is the strain-displacement matrix and $\boldsymbol{\chi}$ embodies the material's behaviour. The implant is very stiff and we therefore assume that the local deformations remain limited during the deployment and a linear constitutive law is sufficient. Thus in the simple case of Hooke's law we have:

$$\boldsymbol{\chi} = \frac{E}{12(1-\nu^2)} \begin{bmatrix} 1 & \nu & 0 \\ \nu & 1 & 0 \\ 0 & 0 & \frac{1}{2}(1-\nu) \end{bmatrix} \tag{2}$$

The stiffness matrix in the global frame is eventually obtained using the rotation matrix of the element: $\mathbf{K} = \mathbf{R}\mathbf{K}_e\mathbf{R}^T$ where $\mathbf{R}$ describes the rotation of the (triangular) element with respect to its initial configuration.

2.2 Triangular Plate Bending

To calculate the stiffness matrix for the transverse deflections and rotations shown on figure 2, we start with the assumed deflection u_z of the form

$$u_z = c_1 + c_2 x + c_3 y + c_4 x^2 + c_5 xy + c_6 y^2 + c_7 x^3 + c_8 xy^2 + c_9 y^3 \tag{3}$$

where $c_1, \ldots, c_9$ are constants. Equation 3 solves an issue of symmetry which was observed with the deflection function proposed by Przemieniecki in [15]. These constants can be evaluated in terms of the displacements and slopes at the three corners of the triangular plate using

$$\mathbf{u} = \mathbf{C}\mathbf{c} \tag{4}$$

where $\mathbf{u} = \{u_1 u_2 \dots u_9\}$ and $\mathbf{c} = \{c_1 c_2 \dots c_9\}$. Matrix $\mathbf{C}$ derives from equation 4:

$$C = \begin{bmatrix} 1 & 0 & 0 & 0 & 0 & 0 & 0 & 0 & 0 \\ 0 & 0 & 1 & 0 & 0 & 0 & 0 & 0 & 0 \\ 0 & -1 & 0 & 0 & 0 & 0 & 0 & 0 & 0 \\ 1 & x_2 & 0 & x_2^2 & 0 & 0 & x_2^3 & 0 & 0 \\ 0 & 0 & 1 & 0 & x_2 & 0 & 0 & 0 & 0 \\ 0 & -1 & 0 & -2x_2 & 0 & 0 & -3x_2 & 0 & 0 \\ 1 & x_3 & y_3 & x_3^2 & x_3 y_3 & y_3^2 & x_3^2 & x_3 y_3^2 & y_3^3 \\ 0 & 0 & 1 & 0 & x_3 & 2y_3 & 0 & 2x_3 y_3 & 3y_3^2 \\ 0 & -1 & 0 & -2x_3 & -y_3 & 0 & -3x_3^2 & -y_3^2 & 0 \end{bmatrix} \tag{5}$$

The notations

$$u_1 = (u_z)_{x_1,y_1} \qquad u_2 = \left(\frac{\partial u_z}{\partial y}\right)_{x_1,y_1} \qquad u_3 = -\left(\frac{\partial u_z}{\partial x}\right)_{x_1,y_1} \tag{6}$$

and so on for the two other vertices, were used.

We can calculate the strains from the flat-plate theory using:

$$e_{xx} = -z\frac{\partial^2 u_z}{\partial x^2} \tag{7}$$

$$e_{yy} = -z\frac{\partial^2 u_z}{\partial y^2} \tag{8}$$

$$e_{xy} = -2z\frac{\partial^2 u_z}{\partial x \partial y} \tag{9}$$

Hence, using the above equations and equation (3), we have

$$\begin{bmatrix} e_{xx} \\ e_{yy} \\ e_{xy} \end{bmatrix} = -z \begin{bmatrix} 0 & 0 & 0 & 2 & 0 & 0 & 6x & 0 & 0 \\ 0 & 0 & 0 & 0 & 0 & 2 & 0 & 2x & 6y \\ 0 & 0 & 0 & 0 & 2 & 0 & 0 & 4y & 0 \end{bmatrix} \mathbf{c} \tag{10}$$

or symbolically $\mathbf{e} = \mathbf{Dc}$ where $\mathbf{D}$ stands for the 3×9 matrix in equation 10, including the pre-multiplying constant $-z$. Noting from equation (4) that $\mathbf{c} = \mathbf{C}^{-1}\mathbf{u}$, we have:

$$\mathbf{e} = \mathbf{DC}^{-1}\mathbf{u} = \mathbf{bu} \tag{11}$$

where $\mathbf{b} = \mathbf{DC}^{-1}$. Knowing that the stiffness matrix $\mathbf{K}_e$ for an element is obtained from

$$\mathbf{K}_e = \int_v \mathbf{b}^T \boldsymbol{\chi} \mathbf{b} dV \tag{12}$$

where $\boldsymbol{\chi}$ is the material matrix, the substitution of $\mathbf{b}$ into this expression yields

$$\mathbf{K}_e = (\mathbf{C}^{-1})^T \int_v \mathbf{D}^T \boldsymbol{\chi} \mathbf{D} dV \mathbf{C}^{-1} \tag{13}$$

The integration is carried out numerically using Gauss points located at the middle of each edge of the triangle.

2.3 Implementation

In practical terms, the different computations associated with each triangular shell element can be described as follows:

1. Compute the rotation matrix $\mathbf{R}$ from global to triangle (local) frame
2. Compute the local displacement vector $\mathbf{u} = \{v_1, v_2, 0, u_2, u_3, v_3, v_4, 0, u_5, u_6, v_5, v_6, 0, u_8, u_9\}$ for each of the 3 nodes of the triangle (the nodes have 6 degrees-of-freedom). As we are in a co-rotational framework the normal displacements u_1, u_4, u_7 of all 3 nodes are null in the local frame of the triangle.
3. Compute matrix $\mathbf{D}_i$ at each Gauss point i
4. The strain-displacement matrix at each Gauss point i is computed with $\mathbf{J}_i = \mathbf{D}_i \mathbf{C}^{-1}$
5. Compute the local stiffness matrix $\mathbf{K}_e$ of the element as $\mathbf{K}_e = \sum_{i=1}^{3} \mathbf{J}_i \boldsymbol{\chi} \mathbf{J}_i^T$
6. Transform the local element stiffness matrix into the global frame and add it to a global stiffness matrix

The co-rotational shell formulation has been successfully implemented into the open-source framework SOFA [16].

2.4 Validation

We compared our model with some theoretical results reported by Zhongnian [17] to assess its quality in modelling bending. The test that we carried out uses a square shape mesh clamped on all four edges. A uniform load is then applied on the square and the maximum deflection z_{max} at the centre can be calculated. Several simulations are performed with increasing load values q (ranging from 1 to $5 N/m^2$) and the following parameters were used: Young's Modulus $E = 1.092 \times 10^6\, Pa$, Poisson's ratio $\nu = 0.3$, square edge length $L = 10\, m$, thickness $h = 0.1\, m$. Using these particular values it can be shown that $z_{max} = 0.126\, q$. The maximum deflection obtained in our simulations are reported in table 1. In average we found $z_{max} = 0.1248\, q$, resulting in a $0.93\,\%$ error between our model and theoretical results on that test.

3 Simulation of the Intra-ocular Lens Injection

Cataract surgery consists in three main steps: capsulorhexis, phacoemulsification, and implantation of an intra-ocular lens. Prior to starting the surgery, a viscoelastic fluid is introduced into the capsule to facilitate capsulorhexis creation and provide protection during phacoemulsification. This fluid remains in the capsule for the duration of the surgery, including the injection of the implant.

Table 1. Comparison of our shell model with theoretical results on the bending of a square plate. An error of less than 1 % was found between our simulation and theoretical results.

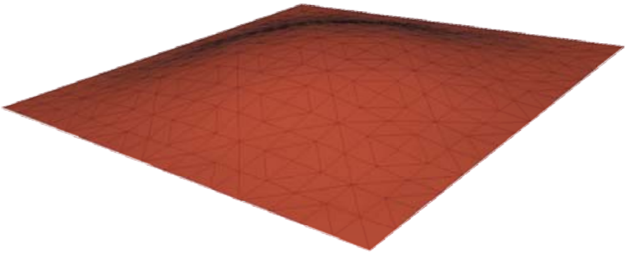

q	z_{max}
1	0.1218
2	0.2475
3	0.3747
4	0.5050
5	0.6374

Capsulorhexis is the technique used to remove a part of the anterior lens capsule. Phacoemulsification consists in using a surgical device which tip vibrates at an ultrasonic frequency to emulsify the natural lens material and then aspirate the fragments of the cortical material. After the removal of the diseased lens, an intra-ocular lens is implanted into the eye, through a small incision (about 2 mm) using a foldable intra-ocular lens (see figure 3). The foldable lens, usually made of acrylic material, is then implanted within the lens capsule through the incision used during phacoemulsification. In some cases the implant can be flipped or the hooks (also called *haptics*) can break. Therefore the simulation of the insertion and deployment of the implant is crucial for achieving a successful surgery.

To simulate the insertion and deployment of an intra-ocular lens, we first created a triangulation of the lens surface. Particular care was given to the mesh, to ensure that areas where large stresses occur contain a higher density of elements (figure 4). This was done by noting the constraints applied by the surgeon to the haptics while inserting the implant within the injection device. During this stage, the haptics are folded onto the implant body, leading to high stresses at the junctions. The lens mesh contains 743 triangles and 473 nodes. Models of the injection device and the entire eye anatomy were also created.

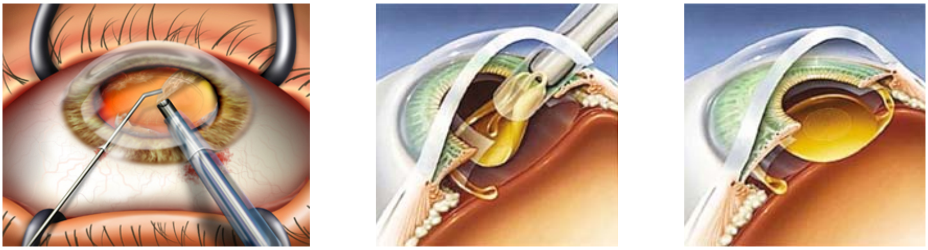

Fig. 3. Left: removal of the opacified lens by phacoemulsification. Center: insertion of the lens implant which is folded inside the injection device and then deploys within the lens capsule. Right: the lens in place in the capsule.

Table 2. Physical parameters of the intra-ocular implant (source: Alcon)

Young's modulus	Poisson's ratio	Mass density
$1MPa$	0.42	$1.2g/cm^3$

Physical parameters of the lens implant have been provided by the manufacturer Alcon and they are presented in table 2.

The first difficulty is to obtain the folded geometry of the lens within the injection device. This step is not important for the training process and does not need to be interactive. Indeed the surgeon does not always have to prepare the implant as some injection devices are readily available with a folded implant already in place. We simulate the folding process by first folding the haptics onto the implant body. The body was then bent while keeping the haptics inside to obtain the shape described in figure 5. The whole process was carried out by applying the necessary forces and boundary conditions on the body and haptics of the implant. The folded implant was then placed into the injection device. The simulation of the injection consists in pushing the intra-ocular implant within the injection device into the lens capsule. During these stages of the simulation, complex contacts occur and consist of self collisions of the lens as well as collisions between the lens and the injector and later with the capsule. To solve the contacts we use the contact warping method proposed Saupin *et al.* [18] as it offers an efficient way to compute physically correct contact responses in the case of co-rotational models. As adhesions between the haptics and the body is often observed in surgery, friction is also taken into account in the contact response process.

Results of our simulation are illustrated in figure 6. We can notice the progressive deployment of the implant when it exits the injector. The shape of the intra-ocular lens remains very close to that of a real one during all stages of the simulation: within the injector, during the ejection phase, and when in place

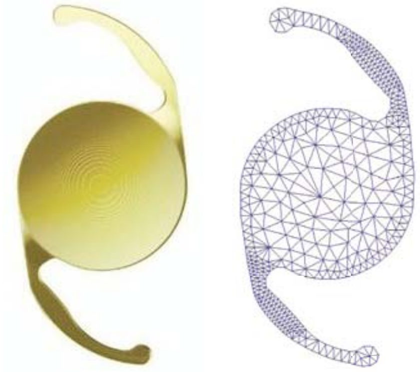

Fig. 4. An actual intra-ocular implant and the triangular mesh used in our simulations. Notice the higher density of elements in areas where large deformations will take place.

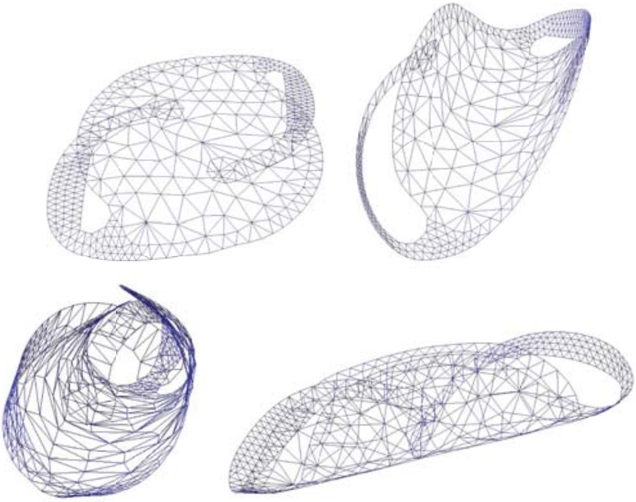

Fig. 5. Top: intermediary steps of the intra-ocular implant folding. Bottom: fully folded implant ready to be placed into the injection device.

Fig. 6. Three steps of the simulation of the intra-ocular lens implant injection and its deployment within the lens capsule. Top: images from a real cataract surgery, courtesy of Dr. Tarek Youssef, ophtalmologist in Canada. Below: our simulation of the implant's deployment.

within the capsule. Due to the high stiffness and low mass of the lens, a direct sparse solver was used at each time step (dt $= 0.01\,\text{s}$) rather than an iterative solver, resulting in a more accurate and more stable simulation, to the detriment of computation times (about 5 FPS for the complete simulation, and about 10 FPS for the deformation only, on a 2.4 GHz processor).

4 Conclusion

We proposed a co-rotational formulation for shell elements by extending a classical in-plane triangular finite element approach. This simple shell element can efficiently handle both membrane, bending and twist forces. The validity of our approach has been demonstrated though comparison with theoretical results. It was then applied it to a rather complex application: the simulation of intra-ocular lens implant deployment in a cataract surgery simulation. These preliminary results are very encouraging and show the potential of such models. Examples include the modelling of hollow anatomical structures (stomach, colon, etc.), the simulation of cardiac valve leaflets, and blood vessels. Regarding improvements of our current model and simulation, we plan to account for the interaction with the viscoelastic fluid (currently approximated by a high damping). Computation times also need to be improved through the use of more optimised meshes and by porting our parallelisable algorithm to Graphics Processing Units.

Acknowledgments

We are very grateful to Jérémy Ringard for his invaluable help in improving the eye anatomical model, to Jérémie Dequidt and Damien Marchal for understanding Blender, to Fréderick Roy for his help with SOFA, and Nadia Boubchir for her persistence in motivating us to obtain these results in time.

We would also like to thank INRIA and the SOFA project, as well as CSIRO Preventative Health National Research Flagship, ICTC, The Australian e-Health Research Centre for their fundings.

References

1. Feudner, E., Engel, C., Neuhann, I., Petermeie, K., Bartz-Schmidt, K., Szurman, P.: Virtual reality training improves wet-lab performance of capsulorhexis: results of a randomized study. Graefes. Arch. Clin. Exp. Ophthalmol. 247, 955–963 (2009)
2. Liu, G., Quek, S.: Finite Element Method: A Practical Course. Butterworth (2003)
3. Provot, X.: Deformation constraints in a mass-spring model to describe rigid cloth behavior. In: Graphics Interface 1995, pp. 147–154 (1995)
4. Hammer, P.E., Perrinb, D.P., del Nidob, P.J., Howe, R.D.: Image-based mass-spring model of mitral valve closure for surgical planning. In: Proc. of SPIE Medical Imaging, vol. 6918 (2008)
5. Yu, H., Geng, Z.: An improved mass-spring model to simulate draping cloth. In: IEEE International Conference on Intelligent Computation Technology and Automation, vol. 1, pp. 568–571 (2008)
6. Taskiran, H.D., Güdükbay, U.: Physically-based simulation of hair strips in real-time. In: WSCG (Short Papers), pp. 153–156 (2005)
7. Wang, F., Duratti, L., Samur, E., Spaelter, U., Bleuler, H.: A Computer-Based Real-Time Simulation of Interventional Radiology. In: The 29th Annual International Conference of the IEEE Engineering in Medicine and Biology Society (IEEE-EMBS), pp. 1742–1745 (2007)

8. Choi, M.G., Woo, S.Y., Ko, H.S.: Real-time simulation of thin shells. In: ACM SIGGRAPH/Eurographics symposium on Computer animation, pp. 349–354 (2007)
9. Bridson, R., Marino, S., Fedkiw, R.: Simulation of clothing with folds and wrinkles. In: Symposium on Computer Animation, pp. 28–36 (2003)
10. Grinspun, E., Hirani, A.N., Desbrun, M., Schröder, P.: Discrete shells. In: Proceedings of the Symposium on Computer Animation, pp. 62–67 (2003)
11. Wicke, M., Steinemann, D., Gross, M.: Efficient animation of point-sampled thin shells. In: Computer Graphics Forum (Eurographics 2005), vol. 24, pp. 667–676 (2005)
12. Thomaszewski, B., Wacker, M., Strasser, W.: A consistent bending model for cloth simulation with corotational subdivision finite elements. In: ACM SIGGRAPH/Eurographics Symposium on Computer Animation, pp. 107–116 (2006)
13. Felippa, C.A.: A systematic approach to the element independent corotational dynamics of finite elements. Technical Report CU-CAS-00-03, Center for Aerospace Structures (2000)
14. Muller, M., Gross, M.: Interactive virtual materials. In: Proceedings of Graphics Interface (GI 2004), pp. 239–246 (2004)
15. Przemieniecki, J.: Theory of matrix structural analysis. McGraw-Hill, New York (1985)
16. Allard, J., Cotin, S., Faure, F., Bensoussan, P.J., Poyer, F., Duriez, C., Delingette, H., Grisoni, L.: Sofa - an open source framework for medical simulation. In: Medicine Meets Virtual Reality, pp. 13–18 (2007)
17. Zhongnian, X.: A simple and efficient triangular fem for plate bending. Acta Mechanica Sinica 2(2), 185–192 (1986)
18. Saupin, G., Duriez, C., Cotin, S., Grisoni, L.: Efficient contact modeling using compliance warping. In: Proceedings of Computer Graphics International Conference (2008)

Endovascular Guidewire Flexibility Simulation

Vincent Luboz[1], Jianhua Zhai[2], Peter Littler[3], Tolu Odetoyinbo[3], Derek Gould[3],
Thien How[2], and Fernando Bello[1]

[1] Division of Surgery, Dept. of Surgery and Cancer,
Imperial College London – St Mary's Hospital, London, W2 1NY, UK
`{vluboz,f.bello}@imperial.ac.uk`
[2] University of Liverpool, School of Clinical Sciences, Liverpool, UK
[3] Royal Liverpool Hospital, Radiology Department, Liverpool, UK

Abstract. Endovascular clinicians use guidewires to navigate within vessels during angiography or angioplasty. In mastering this core skill, an alternative to the traditional apprenticeship in patients is provided by virtual training environments though these require a faithful replication of complex guidewire behaviours inside the vasculature. This paper presents the integration of realistic flexibilities into our guidewire model that simulates the stiffness of seven commonly used guidewires. Each virtual instrument is represented as a mass-spring model replicating their flexibility and shape, especially at the flexible end. The bending coefficients were determined by comparing of the behaviour of real guidewires in a transparent silicone rubber vascular phantom to that of virtual guidewires in the virtual representation of the phantom. As a result, our representation captures the required range of behaviour and enables accurate deformation.

Keywords: Flexibility, guidewire model, mass-spring simulation, interventional radiology, endovascular surgery.

1 Introduction

Endovascular surgery and interventional radiology (both noted as IR in the rest of the paper) use medical imaging to guide minimally invasive techniques involving needles, wires and catheters to access and treat vascular pathology. The manipulation of these instruments is considered a core skill, acquired during training to ensure a safe and positive outcome for patients. Mostly, this training still relies on an apprenticeship on real patients, though this is expensive and carries a risk of complications [1]. Computer-based simulation proposes a safe framework to practice specific skills as often as needed and is now beginning to be used as an alternative to improve IR core skills training [2].

Several commercial vascular IR environments have been developed (e.g. VIST - www.mentice.com; and Angiomentor - www.simbionix.com) and integrate different IR instruments, pathologies and simple datasets. Their main drawback is that they lack realism of instrument behaviour since little physics-based modelling is involved in the computation of the instrument motion. This could potentially lead to incorrect core skills training.

F. Bello and S. Cotin (Eds.): ISBMS 2010, LNCS 5958, pp. 171–180, 2010.
© Springer-Verlag Berlin Heidelberg 2010

Several academic research groups have recently described development of simulator models that aim to replicate accurate instrument behaviour. A real time non linear deformable beam model resulting in an accurate simulation has been introduced in [3]. A Cosserat model which simulates a guidewire as a set of straight, non-bendable, uncompressible beams with perfect torque control, is presented in [4]. Although the simulation was accurate, it could not be achieved in real time. Another system using multiple flexible finite element bodies is used to simulate several types of IR instruments in [5]. Recently, we proposed a novel mass-spring approach [6] modelling a guidewire in real time while navigating in a very detailed vasculature, with visually correct accuracy. So far, only one guidewire was available in our framework, severely limiting the options for the trainee to use a guidewire with a different flexibility or shape as dictated by the needs of the target vasculature.

Since flexibility and shape variations are key to guidewire navigation, we have improved the realism of our simulator model by developing and integrating new virtual guidewires. Our aim is to model their behaviour as closely as possible to reality in terms of shape and flexural modulus. Section 2 describes briefly our mass-spring model and the seven different guidewires integrated into our simulator. Determination of the characteristics and behaviours of virtual guidewires, using a trial and error process, is presented in section 3 along with the validation of the virtual flexural modulus.

2 Methods

This work is part of a project conducted in the CRaIVE network (http://www.craive.org.uk/) aiming to train IR core skills: navigating medical instruments within the vasculature. Here, we concentrate on the guidewire since it is the first instrument used within the vessels.

The simulator is programmed in Visual C++ and the interface uses FLTK library (http://www.fltk.org/) while graphics are handled by VTK library (http://www.vtk.org/). The Vascular Simulation Platform (VSP) haptic device, developed by Mentice / Xitact, is used in our simulator to manipulate a real wire. A 2GB RAM, 2.10GHz Intel® Core™2-Duo desktop was used for the simulations.

2.1 Guidewire Modeling

We introduced a visually realistic model for the guidewire in complex vasculatures in real time simulation in [6]. This section summarizes our mass-spring model and the interactions with the vessel walls. The vasculature is modelled as a surface made of triangular polygons and segmented by the methods presented in [7].

Our guidewire model is composed of a set of particles ($X_0..X_N$) connected by stiff springs of equal length (λ). The wire tip is distinguished from its body to facilitate force propagation during a rotation and to allow different tip shapes. The instrument's tip consists of the first ($X_0..X_{tlength}$) particles of the instrument while the body is composed of the subsequent particles ($X_{tlength+1}..X_N$).

The instrument can be pushed or pulled and each direction is handled differently. When the guidewire is pulled, the last particle X_N is pulled first and the motion is then propagated along the body axis to all the body particles and the tip particles. This approach is not suitable when the instrument is pushed as the tip would be hard to control at bifurcations. In consequence, a different approach is used in this case: first, the tip of the instrument is pushed, then, the body follows.

When the guidewire is rotated, the particles are rotated by the angle φ starting with the last particle X_N on the body axis. It is then propagated to all the other particles, going towards the tip. If a collision occurs, a new rotation axis is defined at the colliding particle and the next particles (up to the tip) are rotated of φ along this new axis. More details are presented in [6].

To avoid perforating the vasculature, our simulator runs a collision detection test when the guidewire is translated or rotated. The algorithm presented in [6] and based on encapsulating the vasculature in an Axis Aligned Bounding Box tree and each guidewire particle in a bounding sphere was not modified since it proved to be time efficient and accurate.

Each time a collision is detected, the simulator computes a collision response step. It ensures all the colliding particles stay inside the vasculature, providing that the user does not apply too much force on the guidewire which could lead to perforation. In our case, four forces are involved: external force, spring force, and 2D and 3D bending forces. The external force moves particles away from vessel wall triangles and is controlled by an external force coefficient, k_e. The spring force ensures that the spring length remains close to λ and is controlled by a spring force coefficient, k_s.

The instrument shape is conserved by the 2D bending force, using a bias angle conservation constraint. For the i^{th} particle, it is defined as:

$$F_{bending} = -k_b(\theta_i - \theta_b) \cdot u_{\{i-1\}} \tag{1}$$

Where k_b is the bending factor representing the flexural modulus, θ_i is the bending angle for the i^{th} particle, θ_b is the bias bending angle for the i^{th} particle, and $u_{\{i-1\}}$ is the vector perpendicular to the v_1 vector lying on the same surface as vector v_2 (Fig. 1). The instrument's body being initially straight, the bias angle of its particles is

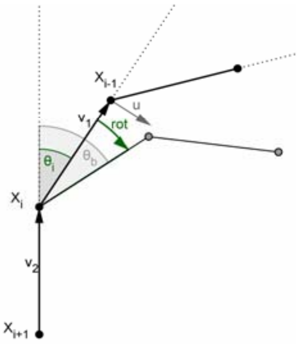

Fig. 1. 2D bending force applied at X_i leads to a translation of X_{i-1} along $u_{\{i-1\}}$

null. Thus, this force contributes to straighten them when the body is deformed, depending on the flexibility of the instrument. In the case of the tip, the bias angle will tend to move back to the wire initial shape since it is different from zero.

The 2D bending force effect is only along the plane defined by v_1 and v_2. External forces might create a deviation of the tip particles out of this plane. We therefore introduced a 3D bending force which constrains all tip particles in this original plane as defined in the following equation for the i^{th} particle:

$$F_{3D\_bending} = -k_{b3D} \cdot \alpha \cdot w_{\{i-1\}} \tag{2}$$

Where k_{b3D} is the bending factor, α is the bending angle between the body plane π_2 and the tip plane π_1, $w_{\{i-1\}}$ is π_2 plane's normal applied at the $i\text{-}1^{\text{th}}$ particle, as shown in Fig. 2. The body plane is determined by the first two particles of the tip and the first body particle. The tip plane is composed by the particle where the 3D bending force is being defined and the two neighbouring particles.

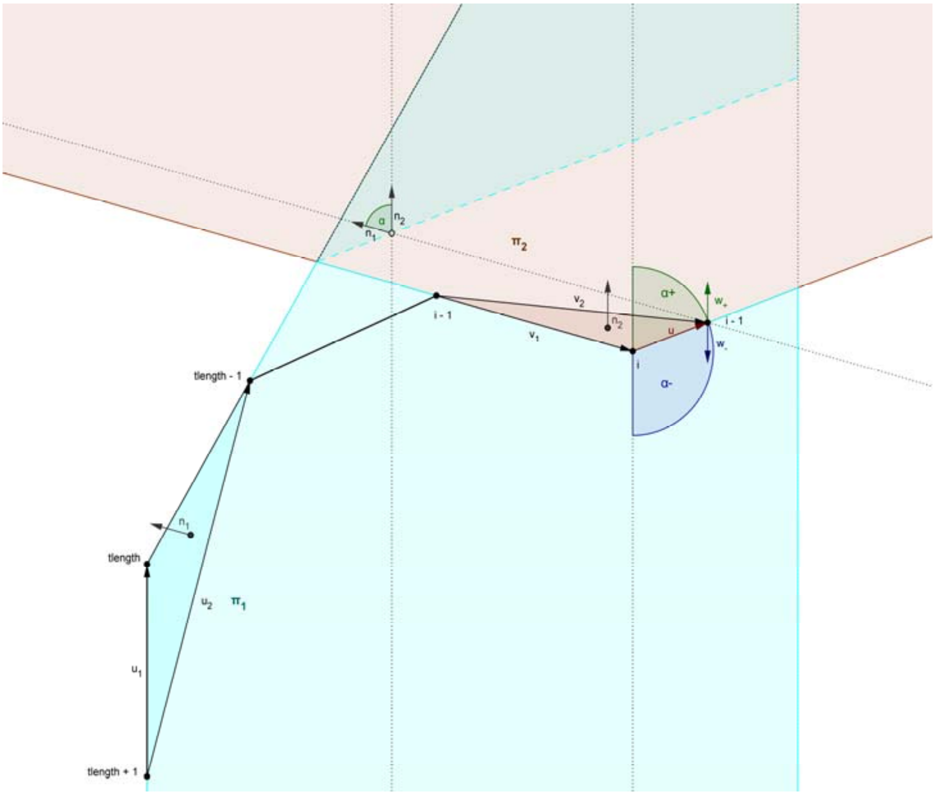

Fig. 2. Definition of the 3D bending force for the tip particle i

A 2D (or 3D) bending coefficient smaller than one leads to a flexible behaviour, while values greater than one make the guidewire stiffer.

2.2 Guidewire Selection

There is a wide variety of IR guidewires with different length, diameter, surface coating, material, stiffness, tip configuration, etc. They can be classified according to their mode of use e.g., access, selection and exchange [8]. For *access* into a vessel, a guidewire requires an atraumatic, 'floppy' tip to avoid damage to the vessel wall, often with a J-shaped tip configuration that approximates the diameter of the accessed vessel. *Selective* guidewires use an angled or curvable, soft tip, often with a more solid mandril to permit steering, thereby cannulating vascular side branches or crossing stenosed or tortuous vessel segments. An *exchange* guidewire is used to exchange one catheter for another, hence these require greater length and stiffness to deliver a diagnostic catheter or therapeutic medical device over the wire.

Based on these considerations, seven commonly used guidewires were chosen: *Access*: Fixed Core Straight and Fixed Core Safe-T-J-Curved (Cook, Bloomington, In, USA), Bentson (Boston Scientific); *Selective*: Terumo Angled and Stiff Angled wires (Terumo, Somerset, NJ, USA); *Exchange*: Rosen-Curved (Cook, Bloomington, In, USA), Amplatz Super Stiff (Boston Scientific, Natick, MA, USA).

In our mass-spring model, the guidewire tip and body are treated separately to allow replicating each wire shape. Even the straight wires have different numbers of tip particles, depending on their flexibility. For example, the Amplatz super stiff wire has a longer flexible tip than the Cook Straight wire. Curved wires also have a different number of tip particles to better fit the real shape. For example, the curved tip of the Terumo wires is composed of: (1) six particles, 2mm apart, with a curvature following a circle of radius 9.5mm and (2) four other tip particles are initially in the same axis of the body particles and take into account the transition of flexibility values between the tip and the body (the body being stiffer than the tip), as shown in Fig. 3.

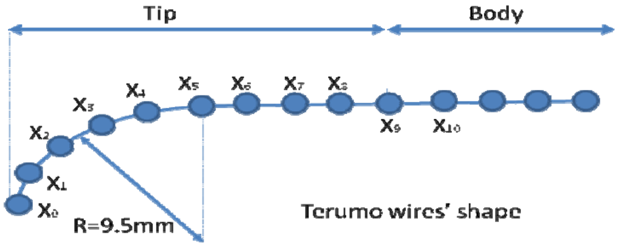

Fig. 3. Shape of the Terumo guidewires: the six first tip particles are following a 9.5mm radius curve while the four last tip particles are in a straight line with the body particles

2.3 Estimating Guidewire Flexibility

Estimating the values of the coefficients used in our mass-spring model was a key step to avoid instability and to reach a realistic behaviour. The external force being applied equally on each particle, a k_e of 1 was chosen for the body particles. A slight

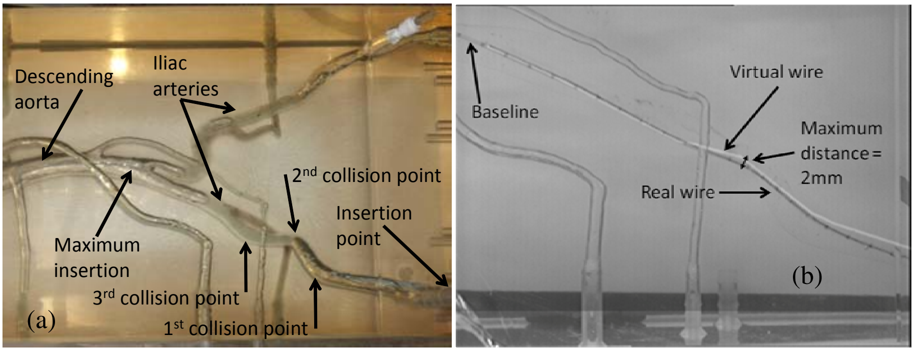

Fig. 4. (a) The four reference positions of the validation in the vascular phantom made of silicon: 1st, 2nd and 3rd collision points, and maximum insertion point. (b) Digital image on the bottom iliac artery with the 1cm marked catheter, the real guidewire in black, and the virtual one in white.

attenuation of the external force was introduced for the tip particles and their k_e was set to 0.9. Because the spring forces are the same along the wire, a k_s of 1 was set for every particle to maintain the overall length of the wire as constant as possible. The 3D bending force being applied only to the tip, a k_{b3D} of 1 was applied to the tip, to stabilize it, and 0 to the body.

The flexibility of the seven guidewires was translated represented by the 2D bending coefficient of the mass-spring model. To estimate the variations of this coefficient between each wire, videos were recorded as the real guidewires were inserted and manipulated, at room temperature, by the same operator within a silicone rubber vascular phantom, Fig. 4 (a). This phantom was built from a patient CT scan by Elastrat (Geneva, Switzerland) and models real vessels (abdominal aorta and first order branches, iliac and common femoral arteries) with their real dimensions (2mm to 15mm diameter). To take into account the change of flexibility due to the hydrophily of the guidewires and to minimize optical distortion when viewing the wire through the silicone rubber phantom, an aqueous solution of glycerol (40% by weight) was used to fill the phantom tubing. Wire flexibility also tends to change with in vivo temperatures after several minutes. To address this and because the fluid filling the phantom was at room temperature, we limited each test to 30 seconds, in order to avoid any variations.

To compare the real guidewire behaviour with the one in our simulator, the phantom geometry was first imported as a virtual vascular model. It was imaged in a CT scanner with dilute contrast medium instilled into its vascular structure to provide sufficient anatomical detail. The corresponding virtual vascular model was then extracted from these imaging data using a level set method [7]. Virtual guidewires were inserted in the virtual phantom to compare them with their real counterparts. Four reference positions were recorded, as seen in Fig. 4 (a) for the real phantom: the first, second and third collision points between the wire and the vessel walls, and the maximum insertion point at the bifurcation of the aorta. A fifth position was also recorded: the configuration of the wire at the end of a rotation of 360 degrees applied to the proximal end of the guidewire at the maximum insertion point. Digital images of both real and virtual guidewires at those reference positions were finally overlaid on the same images to compare their path. A simple rigid registration was applied to overlay the images, matching the contour of the silicon and virtual vessels. When the paths diverged, the bending coefficient was changed to reach the best possible match between real and virtual guidewires according to the criteria described below.

2.4 Evaluation Methodology

Two measurements were used in order to evaluate the behaviour of the virtual guidewire for a specific 2D bending coefficient: the maximum distance between the centers of the two wires in the 2D images and the Dice Similarity Coefficient (DSC).

The maximum distance was estimated visually by overlaying a 1cm marked catheter baseline (Fig 4. (b)) on the image representing the real and virtual guidewires. This baseline is a simple catheter with markers every centimetre to give an idea of the distances in the images. To avoid disturbing the guidewire paths, the marked catheter was not present in the phantom during the tests.

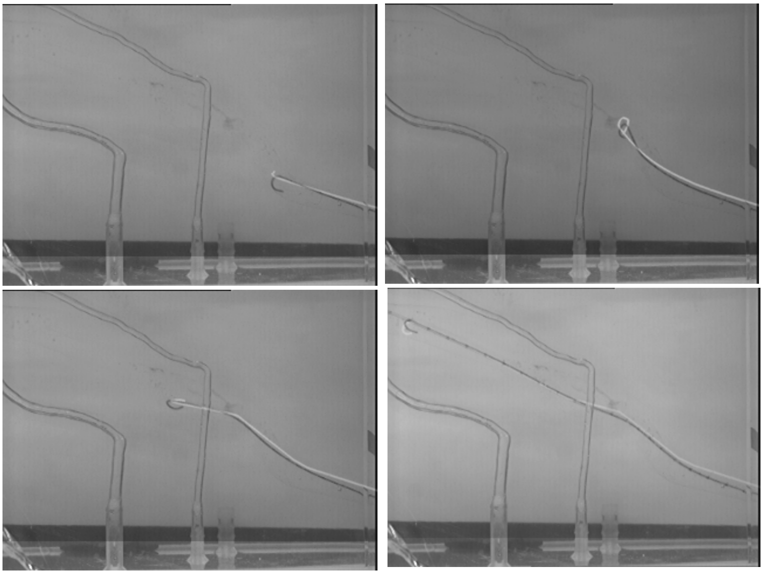

Fig. 5. The three first collision points and maximum insertion point for the Cook TJ guidewire

The DSC is a widely used similarity measure, S, defined as the ratio of twice the common area to the sum of the individual areas of both images of the real (R) and of the virtual (V) guidewires [9]:

$$S = \frac{2|R \cap V|}{|R| + |V|} \tag{5}$$

The DSC was applied to segmentations of the digital images outlining the wires (automatic for the virtual guidewire and manual for the real guidewire). According to [10], a DSC value of 70% indicates excellent agreement.

3 Results

Using the process described above, the 2D bending coefficients of the seven guidewires were chosen and integrated into our mass-spring model. Table 1 summarizes for each guidewire the DSC and the maximum distance between the real and the virtual wires.

Table 1. DSC and maximum distance estimated between the real and virtual guidewires

	1st collision point	2nd collision point	3rd collision point	Max insertion	360 rotation
Cook Straight guidewire (Kb body = 1.0, Kb tip = 0.9)					
DSC in %	12	13	21	47	40
maximum distance in mm	4	3	2	2	2
Amplatz Super Stiff guidewire (Kb body = 1.2, Kb tip = 0.8)					
DSC in %	36	12	20	37	38
maximum distance in mm	0.5	5	3	1	1
Terumo Angled guidewire (Kb body = 0.8, Kb tip = 0.8)					
DSC in %	32	48	38	33	31
maximum distance in mm	2	4	3	2	3
Terumo Stiff guidewire (Kb body = 1.1, Kb tip = 0.8)					
DSC in %	39	21	28	41	28
maximum distance in mm	1	3	3	2	3
Bentson guidewire (Kb body = 1, Kb tip = 0.7)					
DSC in %	44	28	32	44	30
maximum distance in mm	1	3	3	2	2
Cook Rosen Curved guidewire (Kb body = 1.05, Kb tip = 1)					
DSC in %	60	29	38	44	45
maximum distance in mm	2	5	4	2	2
Cook TJ guidewire (Kb body = 1.0, Kb tip = 0.9)					
DSC in %	41	20	30	46	39
maximum distance in mm	5	3	3	2	5

Fig 4. (b) gives an example of the comparison for the Cook Straight guidewire, while Fig. 5 is for the Cook TJ guidewire. The curved tip does not match exactly at most collision points because of the external force coming from the virtual vascular

phantom surface and applied to the virtual guidewire. Nevertheless, the body of the wire matches very well at each reference position.

4 Discussion and Conclusion

This paper presents the integration of realistic guidewire flexibilities into our simulator to improve the wire behaviour and to propose an environment able to accurately train instrument navigation. We used our mass-spring model presented in [6] to represent seven commonly used guidewires. Their behaviour depends on four parameters, influencing the collision response forces. The spring, external force, and 3D bending coefficients are constant for all guidewires while the 2D bending coefficient is responsible for the flexibility of the wire. Its variation was estimated through comparison of virtual simulations with videos of real guidewires in a vascular phantom.

The results section shows the similarity between the real and virtual guidewire behaviours. Fig. 5 demonstrates how close the virtual Cook TJ guidewire is to the real one. On average, at the maximum insertion, the real and virtual guidewires have a DSC of 42%. For example, the real and virtual Cook Straight guidewires are 47% similar. Although these values are significantly below 70%, the real and virtual guidewires match closely, as shown by the distance measurements which demonstrate a maximum separation of 2mm at the maximum insertion point. The low DSC is likely due to the fact that it is difficult to entirely match two wires of 0.9mm diameter. However, these results suggest that our virtual guidewires are similar to the real ones and behave accurately and realistically.

Current improvements include measurement of the real flexural modulus and its integration into the simulator in the form of the 2D bending coefficient. An evolving bending coefficient along the tip is also being investigated to model the variations of the wire flexural modulus.

Future work will focus on improving the evaluation of guide-wire similarity by recording real wires in the phantom with several view points. We are also considering applying this method during real patient fluoroscopy but the associated low resolution and spatial limitations might impact on accuracy. Finally, we aim to study the influence of incorporating different flexural modulus on core skills training methodology.

Acknowledgements

This work was partially funded by EPSRC, the UK's Engineering and Physical Sciences Research Council.

References

1. Seymour, N.E., Gallagher, A.G., Roman, S.A., O'Brien, M.K., Bansal, V.K., Andersen, D.K., Satava, R.M.: Virtual reality training improves operating room performance: results of a randomized, double-blinded study. Annals of Surgery 236(4), 458–463 (2002); discussion 463-4

2. Dawson, S., Gould, D.A.: Procedural simulation's developing role in medicine. The Lancet 369, 1671–1673 (2007)
3. Cotin, S., Duriez, C., Lenoir, J., Neumann, P., et al.: New approaches to catheter navigation for interventional radiology simulation. In: Duncan, J.S., Gerig, G. (eds.) MICCAI 2005. LNCS, vol. 3750, pp. 534–542. Springer, Heidelberg (2005)
4. Alderliesten, T., Konings, M.K., Niessen, W.J.: Modeling Friction, Intrinsic of Curvature, and Rotation Guide Wires for Simulation of Minimally Invasive Vascular Interventions. IEEE Transactions on Biomedical Engineering 54(1) (January 2007)
5. Chui, C., Li, Z., et al.: Training and pretreatment planning of interventional neuroradiology procedures – initial clinical validation. MMVR 2002 85, 96–102 (2002)
6. Luboz, V., Blazewski, R., Gould, D., Bello, F.: Real-time Guidewire Simulation in Complex Vascular Models. The Visual Computer (2009)
7. Luboz, V., Din, N., Song, Y., King, D., Gould, D., Bulpitt, A., Bello, F.: Segmentations of 3D vasculatures for interventional radiology simulation. In: Workshop of British Machine Vision Association (BMVA) (December 2008)
8. Schneider, P.: Endovascular Skills: guidewire and catheter skills for endovascular surgery, 3rd edn. (December 2008)
9. Dice, L.R.: Measures of the amount of ecologic association between species. Ecology 26(3), 297–302 (1945)
10. Zijdenbos, A.P., Dawant, B.M., Margolin, R.A., et al.: Morphometric Analysis of White Matter Lesions in MR Images: Method and Validation. IEEE Transactions on Medical Imaging 13(4) (December 1994)

Author Index

Adam, Clayton 90
Angelini, Elsa 71
Anquez, Jérémie 71
Azarnoush, Hamed 20

Bajka, Michael 181
Bello, Fernando 171
Bibin, Lazar 71
Bisaillon, Charles-Etienne 20
Bloch, Isabelle 71
Boubekeur, Tamy 71
Boulet, Benoit 20

Choudhury, Nusrat 11
Comas, Olivier 160
Cotin, Stéphane 160

Davidson, Sean R.H. 119
de la Plata Alcalde, Juan Pablo 71
Degrandpre, Christian 20
Delorme, Sébastien 11
Duriez, Christian 139, 160

Fornaro, Jürgen 82

Gertner, Mark 119
Goksel, Orcun 150
Gould, Derek 171
Granero-Molto, Froilan 29
Gu, Lixu 130

Harders, Matthias 82, 181
Hirsch, Sven 38
How, Thien 171

Ilegbusi, Olusegun 98

Jewett, Michael A.S. 119
Jiang, Di 11

Kolios, Michael C. 119

Lamouche, Guy 20
Little, J. Paige 90
Littler, Peter 171
Lloyd, Bryn A. 38, 49
Luboz, Vincent 171

McGregor, Robert H.P. 49
Miga, Michael I. 29
Mora, Vincent 11

Noe, Karsten Østergaard 59

Odetoyinbo, Tolu 171

Pai, Dinesh K. 108
Payan, Yohan 1
Peng, Xiaopeng 130
Pop, Mihaela 119
Promayon, Emmanuel 1

Salcudean, Septimiu E. 150
Schiavone, Patrick 1
Sherar, Michael D. 119
Sørensen, Thomas Sangild 59
Spagnoli, Anna 29
Sueda, Shinjiro 108
Syllebranque, Cédric 139
Szczerba, Dominik 49
Székely, Gábor 38, 49, 82

Tuchschmid, Stefan 181

Valaski-Tuema, Eric 98

Wei, Qi 108
Weis, Jared A. 29

Zhai, Jianhua 171
Zhou, Zhe 130
Zhu, Bo 130

Comparing Automatic Simulator Assessment with Expert Assessment of Virtual Surgical Procedures

Stefan Tuchschmid[1], Michael Bajka[2], and Matthias Harders[1]

[1] Computer Vision Laboratory, ETH Zurich, Switzerland
{tuchschmid,mharders}@vision.ee.ethz.ch
[2] Clinic of Gynecology, University Hospital Zurich, Switzerland
michael.bajka@hin.ch

Abstract. This study focuses on the comparison of expert assessment of virtual surgical procedures through Objective Structured Assessment of Technical Skills (OSATS) with the automatic assessment and feedback provided by a surgical simulator for hysteroscopic procedures. The existing multi-metric scoring system of the simulator was extended to include hysteroscopic myomectomy. The original OSATS was also modified for the examined surgical procedure. OSATS reliability, expert coherence, and interrater agreement with simulator feedback were investigated in a study with eight experts. The same selection of six movies showing virtual procedures performed at a hysteroscopy training course was rated by each expert. For the task-specific checklist, the reliability of the simulator was significantly higher than that of the individual human raters ($p=0.006$). In addition, the ranked order of the overall scores of all movies was the same for both simulator and expert consensus opinion. This is a first step to providing simulator feedback with the same reliability as an expert panel, thus facilitating competency-based surgical education and assessment in the near future.

1 Introduction

The traditional apprenticeship model for surgical education is increasingly put to test with regard to economy, reliability, and ethics [1]. The assessment of proficiency in this model is mainly based on the subjective impression of the surgical educator as well as on the number of performed procedures (e.g. logbooks). This paradigm is currently being replaced by more formal competency-based assessments, at least at the early stages of a surgeon's education [2]. In addition to this, the demand for certified continuous medical education (CME) is also growing, thus further increasing the need for new approaches to training and assessment.

Competency-based education requires objective measures of proficiency. To this end, Reznick et al. [3] have developed in the late 1990s the Objective Structured Assessment of Technical Skills (OSATS) method, which mainly targeted skills assessment on bench trainers. Since first presented, OSATS has been modified and successfully tested for reliability in many different surgical specialties,

F. Bello and S. Cotin (Eds.): ISBMS 2010, LNCS 5958, pp. 181–191, 2010.
© Springer-Verlag Berlin Heidelberg 2010

such as general surgery [4], urology [5], or ophthalmology [6]. In obstetrics and gynecology, a team of the University of Washington has put its focus on the development of customized OSATS for a new hysteroscopy curriculum [7,8].

Virtual Reality (VR) simulators have been reported to be a reliable and valid means of measuring surgical competency, in addition to traditional methods such as direct observation, animal models, or procedure logs [1]. VR trainers track all actions of a user in the virtual environment, with complete knowledge of the state of the procedure. Darzi et al. [9] pointed out in 1999 that *"a system that can provide unbiased and objective measurement of surgical precision (rather than just speed) could help training, complement knowledge based examinations, and provide a benchmark for certification."* Since then, some effort has been made to develop assessment parameters which relate better to the final objective of the given surgery. Rosen et al. used Markov models for the clustering of force/torque signatures in order to reveal the internal structure of a surgical task [10]. Moorthy et al. [11] analyzed the dexterity of a surgeon to provide performance feedback on the psychomotor skills. The CELTS system [12] developed at Harvard University in the early 2000s succeeded in providing objective expert-novice differentiation of procedural skills based on motion tracking of laparoscopic instruments. Ritter et al. [13] showed that time to completion is a poor metric for the objective assessment of intracorporal knot-tying performance, whereas an automated knot quality score could accurately distinguish well-tied knots from poorly tied ones.

However, the development of metrics that evaluate cognitive decision making and compare behaviour to that of experts remains an important research area [14]. Especially the correspondence of any simulator-based metrics with assessments of experts has not been well studied so far.

Therefore, we compared expert assessment through OSATS to the automatic assessment and feedback provided by a surgical simulator. The VR-based Surgical training system used in our study is a simulator for hysteroscopic interventions [15]. The HystSim trainer [16] allows full procedure training of diagnostic and therapeutic interventions and showed high acceptance ratings by experienced and novice surgeons [17].

2 Methods

2.1 Simulator Assessment of Virtual Hysteroscopic Procedures

A number of different assessment metrics for VR diagnostic hysteroscopy have been implemented in the simulator. We have extended a previously existing version of a multi-metric scoring system [18] with new parameters for therapeutic hysteroscopy, e.g. removal of myoma. Construct validity of the applied system has successfully been shown [19].

The simulator assessment parameters are grouped into five modules, namely Myomectomy, Visualization, Ergonomics, Fluid Handling, and Safety (see Table 1). Each parameter is weighted and linearly interpolated between a lower and upper limit. Two expert surgeons, each having performed more than 500

Table 1. Extended multi metric scoring table for therapeutic hysteroscopy on the HystSim VR trainer (adapted from [19])

Scoring & Grading	maximum score	upper value	lower value	target value
Myomectomy	**100**			
removed pathology	100	95 %	60 %	high
Safety	**100**			
tool active without contact	25	10 s	3 s	low
cuts from front to back	25	1	0	low
cutting while view obscured	25	3 s	0.1 s	low
cutting while uterus collapsed	25	3 s	0.1 s	low
Economy	**80**			
procedure time	40	600 s	240 s	low
path length	30	3200 mm	1600 mm	low
camera tilted	10	30 s	10 s	low
Visualization	**60**			
visualized surface	40	85 %	50 %	high
left tube visualized	5	1.0 s	0.0 s	high
right tube visualized	5	1.0 s	0.0 s	high
upper cavum visualized	5	1.0 s	0.0 s	high
time out of focus	5	45 s	5.0 s	low
Fluid Handling	**40**			
time view obscured	20	60 s	10 s	low
time uterus collapsed	10	30 s	5 s	low
distension media used	10	3000 ml	800 ml	low
Overall score	**380**	(100%)		
Grading	A 90-100%, B 80-89%, C 70-79%, D 60-69%, E <60%			

hysteroscopic interventions were responsible for choice, weighting, implementation, and configuration of the metrics into the scoring and grading system. In the resulting feedback report, module scores and the individual metrics for each module are provided to the trainee. In order to group the overall scores, gradings with letters from A (best, $> 90\%$) to E (worst, $< 60\%$) were given.

2.2 Adapted OSATS for Virtual Hysteroscopic Procedures

The OSATS introduced by Reznick et al. [3] consists of a task-specific checklist and a global rating scale (GRS). The checklist is comprised of binary assessment questions and needs to be adapted for each different test station. The GRS has seven items, each evaluated on a 5-point Likert scale. The middle and extreme points are anchored with explicit verbal descriptions. Finally, a Pass/Fail rating is provided for each test. The overall score for OSATS is computed by taking the sum of the checklist score (1 point for each passed/completed item) and the global rating scale (7 items with maximal 5 and minimal 1 point).

The previously presented and validated OSATS for hysteroscopy [8] has been developed for the assessment on bench stations. Specifically, in that study residents were asked to assemble an operative hysteroscope and to resect a large polyp from an inanimate uterine model. Several of the suggested items do not apply for a fully virtual simulated procedure (e.g. “tool assembly”, “placing of obturator”, “removing of specimen”). Therefore, a new checklist was agreed upon by a panel of four experts with broad teaching experience in hysteroscopy. In addition, the panel extended the OSATS of the Toronto group with further items for evaluating video recordings [20]. To this end, GRS categories were removed, which cannot be rated based on video recordings only. These were substituted with points which were more appropriate for the given surgical procedure. We have exchanged the items “Knowledge of Instruments”, “Use of Assistants”, and “Knowledge of Specific Procedure” with the categories “Resection Skills”, “Visualisation”, and “Fluid Handling”. The task specific checklist of the resulting OSATS is shown in Figure 1 and the GRS in Figure 2.

2.3 Study Setup

An important element of our study is the movies of the simulated procedures to be assessed. In order to avoid any bias which potentially could be introduced by artificial generation of such movies (e.g. by asking our expert panel to act like novices and perform common mistakes), we decided to obtain recordings during a hysteroscopy training course. The recordings were acquired during a course with 62 participants in Lugano, Switzerland from June 25 - 27, 2009, organized by gynecologie suisse (Swiss Society of Obstetrics and Gynecology). Virtual training sessions were carried out on the hysteroscopy simulator, focusing on myoma removal. The training setup used in the course is depicted in Figure 3. Thereafter, six representative movies were selected from all recordings for our

Task-Specific Checklist for Hysteroscopic Myomectomy

Instructions to candidates: Cervix is already dilated. Perform first a diagnostic hysteroscopy and then safely remove myoma.

Item	*Not done or incorrect*	*Done correctly*
Performs complete diagnostics before cutting	0	1
Clearly visualizes left and right tubal ostia	0	1
Visualizes upper fundus by 180^0 rotation	0	1
Only starts cutting when view is clear	0	1
Only starts cutting when loop close to pathology	0	1
Always pulls activated loop toward scope rather than away	0	1
Completely removes pathology	0	1
Does not cut into myometrium	0	1
Does not perforate	0	1
Always keeps horizon stable	0	1
Completes task within 5 min	0	1

Fig. 1. Task-specific checklist, adapted for hysteroscopic removal of myoma

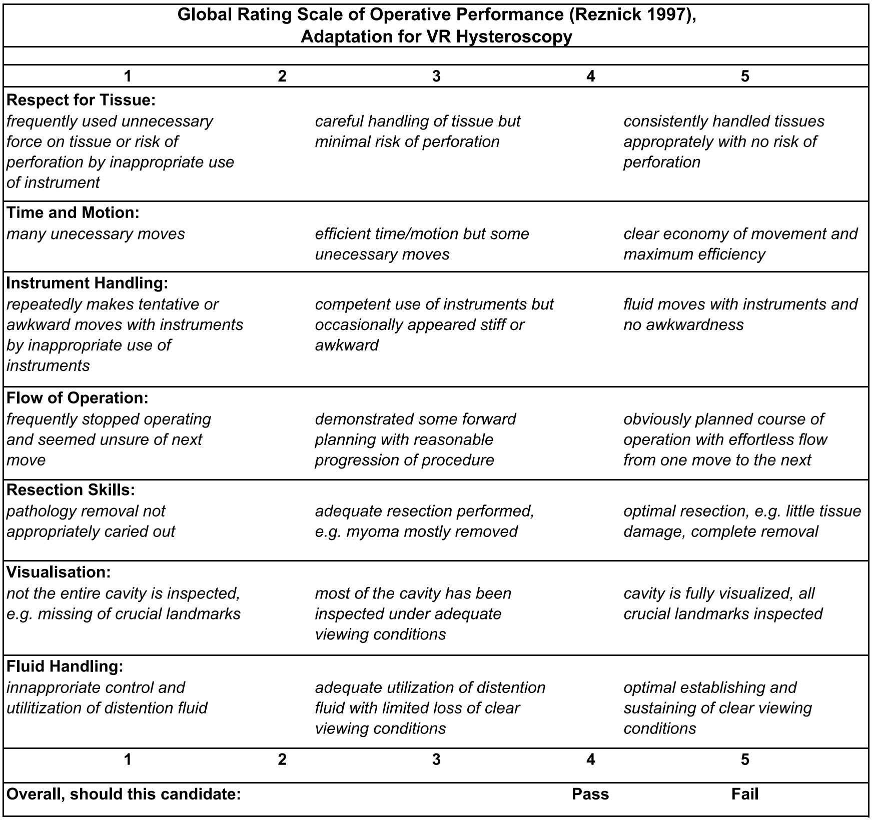

Global Rating Scale of Operative Performance (Reznick 1997),
Adaptation for VR Hysteroscopy

1	2	3	4	5
Respect for Tissue:				
frequently used unnecessary force on tissue or risk of perforation by inappropriate use of instrument		*careful handling of tissue but minimal risk of perforation*		*consistently handled tissues approprately with no risk of perforation*
Time and Motion:				
many unecessary moves		*efficient time/motion but some unecessary moves*		*clear economy of movement and maximum efficiency*
Instrument Handling:				
repeatedly makes tentative or awkward moves with instruments by inappropriate use of instruments		*competent use of instruments but occasionally appeared stiff or awkward*		*fluid moves with instruments and no awkwardness*
Flow of Operation:				
frequently stopped operating and seemed unsure of next move		*demonstrated some forward planning with reasonable progression of procedure*		*obviously planned course of operation with effortless flow from one move to the next*
Resection Skills:				
pathology removal not appropriately caried out		*adequate resection performed, e.g. myoma mostly removed*		*optimal resection, e.g. little tissue damage, complete removal*
Visualisation:				
not the entire cavity is inspected, e.g. missing of crucial landmarks		*most of the cavity has been inspected under adequate viewing conditions*		*cavity is fully visualized, all crucial landmarks inspected*
Fluid Handling:				
innapproriate control and utilitization of distention fluid		*adequate utilization of distention fluid with limited loss of clear viewing conditions*		*optimal establishing and sustaining of clear viewing conditions*
1	**2**	**3**	**4**	**5**
Overall, should this candidate:			**Pass**	**Fail**

Fig. 2. Global Rating Scale, adapted for therapeutic hysteroscopy

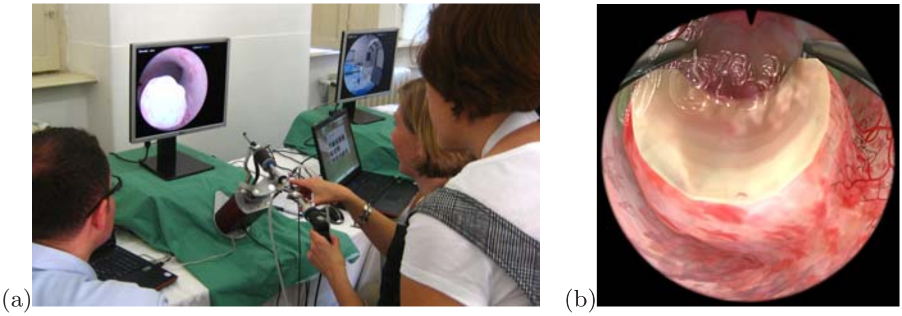

Fig. 3. Hardware configuration during recording (a) and example simulation screenshot(b) of setup used in this study

study together with an expert. Selection criteria were set such as to cover a wide range of performances. The selected movies reflected varying prior exposure and experience with hysteroscopy. In addition, one movie was including during which a uterus perforation occurred – one of the main complications in hysteroscopy. In the scoring system of the simulator, these movies covered the whole scoring range from grade A through E.

Next, the movies were provided online in random order to national and international experts with teaching function for residents. The experts were provided with the OSATS form and asked to carefully review the movies consecutively on the webpage. Thereafter, they were asked to fill out first the task-specific checklist and then the GRS. Finally, the Pass/Fail rating had to be provided for each case. The first eight expert responses were used in this study. All participants completed the questionnaire with checklist, GRS, and Pass/Fail score for all movies.

3 Results

In the first step we verified the reliability of the OSATS itself. We calculated Cronbach's α for the eight experts. According to [21], a test should have at least a Cronbach α of 0.7 to be reliable. We obtained 0.841 for the checklist, 0.894 for the global rating scale, and 0.858 for the Pass/Fail criteria. This is in line with other OSATS studies, where Cronbach α values in the range of 0.71 [3] to 0.97 [8] were reported.

Next, we examined the coherence of the experts' opinions. To this end, we first defined the consolidated expert panel opinion for the checklist. The majority decision of all eight experts on every item of the checklist for all six movies was determined. In a sense, this can be seen as an "expert panel" assessment. This expert panel decision was termed "consensus opinion". If the consensus opinion was tied on an item, it was treated as "passed". Note that treating such a tie as "failed" did not significantly change the results. In 25.7% of the items, the decision was unanimous. One or two experts disagreed in 22.8% and 22.7% of the items, respectively. In 18.2% the decision was with 5 to 3 votes, and in 10.6% experts were tied on an item. The obtained consensus report was then used as a measure of interrater variability for each expert.

Several methods for establishing interrater differences were presented in the literature [21]. We consider interrater agreement as the number of observations in agreement with the consensus opinion, divided by the total number of observations. Values above 80% are generally considered sufficiently high for reliable assessment [21]. Table 2 shows the results of comparing each of the individual experts to the consensus opinion for the eleven checklist items of each movie (N=11) and for all the six movies together (N=66). Depending on the movie, the mean interrater agreement for the checklist was in the range between 0.68 (Movie F) and 0.93 (Movie D). It can be seen that in the checklist ratings there are sometimes large discrepancies between experts on single movie assessments. Interrater agreement values as low as 0.45 resulted.

A similar trend is also visible when analyzing the results of the GRS for the different procedures. While there was wide agreement on some aspects of the procedures (e.g. Movie C and D provided unsatisfactory visualization), the 95%

Table 2. Interrater agreement in checklist rating of 6 procedures (Movies A - F) between individual experts and consensus opinion as well as between simulator and consensus opinion. In addition, the mean of all experts' agreement with consensus opinion is shown.

Movie	*A* [N=11]	*B* [N=11]	*C* [N=11]	*D* [N=11]	*E* [N=11]	*F* [N=11]	*All* [N=66]
Expert 1	0.91	0.82	0.91	0.91	0.73	0.73	0.83
Expert 2	0.91	0.82	0.82	0.82	0.91	0.64	0.82
Expert 3	0.82	1.00	0.64	1.00	0.64	0.73	0.80
Expert 4	0.91	0.91	0.64	1.00	0.73	0.36	0.76
Expert 5	0.82	1.00	0.73	1.00	0.55	0.64	0.79
Expert 6	0.91	0.91	0.91	0.82	0.64	0.82	0.83
Expert 7	0.91	0.82	0.82	0.91	0.91	1.00	0.89
Expert 8	0.45	0.64	0.55	1.00	0.55	0.55	0.62
Mean Experts	0.83	0.86	0.75	0.93	0.70	0.68	0.79
Simulator	1.00	0.91	0.73	1.00	0.73	0.91	0.88

confidence interval of the median value is usually quite large (see Figure 4). As an example, the difference between upper and lower limit for the checklist item "Flow of Operation" was ranging from 0.747 points of the Likert scale (Movie A; 95% confidence interval 1.252 - 1.999) to 2.521 points (Movie F; 95% confidence interval 1.989 - 4.51).

We also compared agreement on the Pass/Fail criteria. For Movies A - F, the number of Pass/Fail ratings were 0/8, 7/1, 3/5, 7/1, 1/7, and 3/5, respectively. Movie F was a perforation of the uterine cavity. It is interesting to note that this serious complication was assessed quite differently by the experts in checklist, GRS, and Pass/Fail rating. One reason for this could be that the perforation was not fully realized by some of the experts. It could also be that some experts adjusted their scores for items unrelated to the actual perforation downwards, in order to ensure a low overall score.

In the next step, we compared the expert ratings to the automated assessment of the simulator. In order to compare consensus opinion with the simulator assessment, we defined corresponding checklist values based on the individual metrics of the simulator multi-metric scoring system. This was done by setting appropriate thresholds, and sometimes combining two simulator metrics for one checklist item. As an example, the checklist entry for "Clearly visualizes left and right tubal ostia" was true when both simulator metrics "Left tube visualized" and "Right tube visualized" were larger than one second. For all movies, the agreement between consensus opinion and simulator opinion on the checklist was 0.88 (see last row of Table 2). Comparing all human ratings with simulator assessment for all movies, the simulator agreement with the consensus opinion is significantly higher (p=0.006, Mann-Whitney U-test, two sided, exact). This trend is also visible for the individual experts, where simulator agreement with the consensus opinion is higher than that of the experts in 7 out of 8 cases. Due

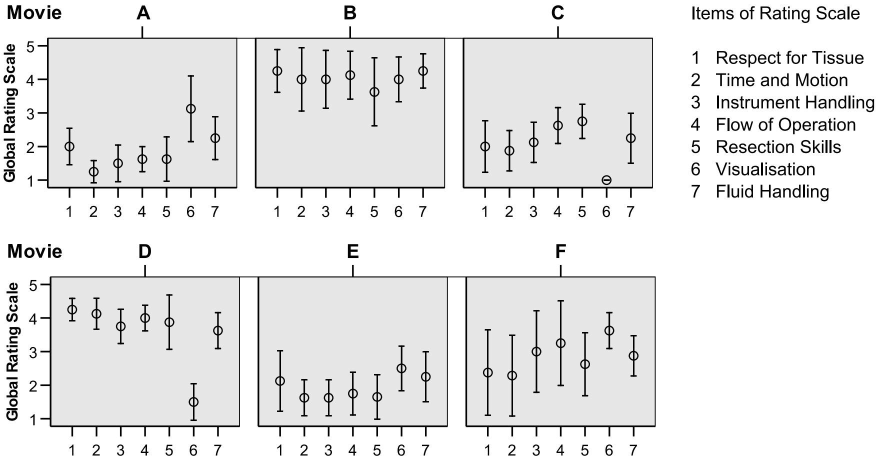

Fig. 4. Results of the global rating scale (GRS) for the 8 different expert raters. The mean scores for all items are shown with 95% confidence intervals represented by the bars. Scores are based on a 5-point Likert scale.

to the small number of movies for each expert this is, however, not statistically significant on the $p<0.05$ level.

Finally, we also investigated how well the overall score of the simulator feedback correlated with that of the OSATS. The average ratings of the eight experts on the GRS were rounded to the nearest Likert value from 1 to 5. Direct comparison of the score numbers is not straightforward since the simulator does not provide categories matching the GRS. Moreover, the simulator feedback is set on a different scale. Therefore, we examined the ranked order of the movies according to the scores. We computed the Spearman-Rho correlation of the overall scores for Movies A - E. This was done between experts, as well as between simulator and experts. We excluded Movie F in this analysis since the simulator does not provide an overall score for a perforation, but labels it as an emergency scenario. Interrater correlation between experts was in the range from 0.4 to 1.0 (mean 0.77). In contrast to this, the agreement between consensus opinion and simulator reached 1.0. Thus, the simulator ranked the movies in exactly the same order as the expert panel opinion.

4 Discussion and Conclusions

We have introduced an adapted OSATS for VR hysteroscopic myomectomy and investigated expert opinion coherence in the assessment of six movies of simulated interventions. Comparing ratings of the checklist items showed that the simulator provided more consistent ratings than 7 out of the 8 experts. It is also interesting to note that a large part of the disagreement between simulator and expert consensus was due to a single item ("Only starts cutting when view is clear"). Thus, there is potential to further increase rating reliability by adjusting simulator metrics.

The challenge of comparing simulator with OSATS assessments is the very different nature of the two rating systems. While the OSATS has been specifically created for efficient and reliable scoring by a human rater, the multi-metric scoring system of the simulator was designed for optimal feedback for performance improvement [19]. Nevertheless, the ranked order of the overall scores was the same for both simulator and the consolidated expert opinion based on OSATS.

A major limiting factor of integrating OSATS into a training and assessment program is the limited availability of staff surgeons to observe the performance of trainees [1]. A simulator providing OSATS with the same reliability as an expert panel consensus for each individual procedure has the potential to make competency-based training possible, regardless of busy operating room schedules or the availability of cadavers or patients.

Our current plan is to extend the simulator feedback system to directly generate the full OSATS report as a complement to the multi-metrics feedback report. While items of the GRS such as "Respect for Tissue", "Instrument Handling", or "Flow of Operation" will be more difficult to implement with high specificity than checklist items, the high correlation between the ranked order of the overall scores indicates that such an endeavour could be successful. In addition, the availability of the full OSATS on the simulator would also facilitate meaningful transfer studies between VR and operation room.

In general, tests are considered reliable with Cronbach α>0.7, however important decisions about an individual's future should not be made unless α is >0.9 [21]. Current OSATS studies with human raters seldom reach this reliability level. Based on the initial results presented in this paper, we believe that the automatic generation of OSATS on a virtual reality simulator with adequate reliability is feasible. This would be especially important for high-stake assessment which may decide about a surgical career. While the past decades have seen a significant shift towards evidence-based clinical medicine, such development would support and accelerate a similar shift in education, training, and assessment of surgeons in the very near future.

Acknowledgment. This work has been performed within the NCCR Co-Me supported by the Swiss National Science Foundation.

References

1. Moorthy, K., Munz, Y., Sarker, S., Darzi, A.: Objective assessment of technical skills in surgery. BMJ 327(7422), 1032–1037 (2003)
2. Gallagher, A., Ritter, E., Champion, H., Higgins, G., Fried, M., Moses, G., Smith, C.D., Satava, R.M.: Virtual reality simulation for the operating room: proficiencybased training as a paradigm shift in surgical skills training. Ann. Surg. 241(2), 364–372 (2005)

3. Reznick, R., Regehr, G., MacRae, H., Martin, J., McCulloch, W.: Testing technical skill via an innovative "bench station" examination. Am. J. Surg. 173(3), 226–230 (1997)
4. Grantcharov, T.P., Kristiansen, V.B., Bendix, J., Bardram, L., Rosenberg, J., Funch-Jensen, P.: Randomized clinical trial of virtual reality simulation for laparoscopic skills training. Br. J. Surg. 91(2), 146–150 (2004)
5. Matsumoto, E.D., Hamstra, S.J., Radomski, S.B., Cusimano, M.D.: The effect of bench model fidelity on endourological skills: a randomized controlled study. J. Urol. 167(3), 1243–1247 (2002)
6. Cremers, S.L., Lora, A.N., Ferrufino-Ponce, Z.K.: Global rating assessment of skills in intraocular surgery (GRASIS). Ophthalmology 112(10), 1655–1660 (2005)
7. Mandel, L.P., Lentz, G.M., Goff, B.A.: Teaching and evaluating surgical skills. Obstet. Gynecol. 95(5), 783–785 (2000)
8. Van Blaricom, A.L., Goff, B.A., Chinn, M., Icasiano, M.M., Nielsen, P., Mandel, L.: A new curriculum for hysteroscopy training as demonstrated by an objective structured assessment of technical skills (OSATS). Am. J. Obstet. Gynecol. 193(5), 1856–1865 (2005)
9. Darzi, A., Smith, S., Taffinder, N.: Assessing operative skill. Needs to become more objective. BMJ 318(7188), 887–888 (1999)
10. Rosen, J., Hannaford, B., Richards, C.G., Sinanan, M.N.: Markov modeling of minimally invasive surgery based on tool/tissue interaction and force/torque signatures for evaluating surgical skills. IEEE Trans. Biomed. Eng. 48(5), 579–591 (2001)
11. Moorthy, K., Munz, Y., Dosis, A., Bello, F., Darzi, A.: Motion analysis in the training and assessment of minimally invasive surgery. Minim. Invasive Ther. Allied Technol. 12(3), 137–142 (2003)
12. Stylopoulos, N., Cotin, S., Maithel, S.K., Ottensmeye, M., Jackson, P.G., Bardsley, R.S., Neumann, P.F., Rattner, D.W., Dawson, S.L.: Computer-enhanced laparoscopic training system (celts): bridging the gap. Surg. Endosc. 18(5), 782–789 (2004)
13. Ritter, E.M., McClusky, D.A., Gallagher, A.G., Smith, C.D.: Real-time objective assessment of knot quality with a portable tensiometer is superior to execution time for assessment of laparoscopic knot-tying performance. Surg. Innov. 12(3), 233–237 (2005)
14. Sewell, C.: Automatic Performance Evaluation in Surgical Simulation. PhD thesis, Stanford University (2007)
15. Harders, M., Bachofen, D., Bajka, M., Grassi, M., Heidelberger, B., Sierra, R., Spaelter, U., Steinemann, D., Teschner, M., Tuchschmid, S., Zatonyi, J., Szekely, G.: Virtual reality based simulation of hysteroscopic interventions. Presence: Teleoperators and Virtual Environments 17(5), 441–462 (2008)
16. Website: VirtaMed HystSim (2009), `http://www.simbionix.com/HystSim/HystSim.html`
17. Bajka, M., Tuchschmid, S., Streich, M., Fink, D., Szekely, G., Harders, M.: Evaluation of a new virtual-reality training simulator for hysteroscopy. Surg. Endosc. 23(9), 2026–2033 (2009); Epub Apr 24, 2008
18. Tuchschmid, S., Bajka, M., Bachofen, D., Szekely, G., Harders, M.: Objective surgical performance assessment for virtual hysteroscopy. Stud. Health Technol. Inform. 125, 473–478 (2007)
19. Bajka, M., Tuchschmid, S., Fink, D., Szekely, G., Harders, M.: Establishing construct validity of a virtual reality training simulator for hysteroscopy via a multi metric scoring system. Surg. Endosc. (2009); (Epub ahead of print, June 24)

20. Dath, D., Regehr, G., Birch, D., Schlachta, C., Poulin, E., Mamazza, J., Reznick, R., MacRae, H.M.: Toward reliable operative assessment: the reliability and feasibility of videotaped assessment of laparoscopic technical skills. Surg. Endosc. 18(12), 1800–1804 (2004)
21. Gallagher, A.G., Ritter, E.M., Satava, R.M.: Fundamental principles of validation, and reliability: rigorous science for the assessment of surgical education and training. Surg. Endosc. 17(10), 1525–1529 (2003)